

HafenCity University Hamburg

**A Vessel-Based Mobile Mapping System –
From Sensor Integration to Multipurpose Products**

a Master Thesis submitted to
HCU Hamburg
for the degree of
Master of Science

presented by
Dipl.Ing.(FH) Thomas Thies
28.02.2011

1st Evaluator

Prof. Dr.-Ing. Volker Böder
HafenCity University Hamburg

2nd Evaluator

M.Sc. Frank Köster
Hamburg Port Authority

Declaration (§22(4) PSO)

I declare, that this Master Thesis – in the case of group work the respective marked parts of the work – has been completed independently without outside help and only the defined sources and study aids were used

Literally or copied passages or passages analogous in sense from different text sources are marked by referencing the respective sources.

Hamburg,

.....
Dipl.Ing.(FH) Thomas Thies

Abstract

For several years terrestrial laser scanners were used in multiple geodetic survey applications. These electro-optical measurement sensors which are based on further developments of LiDAR systems and total stations provide high accurate area based and contact-free object detection by using laser devices. For this reason laser scanner as relatively young mapping sensors have a solid position on the surveying market. Because of the rising demand on area based high resolution geo-data in the public and private sector whereas resolution means geometric but also time resolution, mobile mapping systems have been developed to combine the advantages of high speed terrestrial laser scanning and accurate positioning in kinematic and therefore also economic survey applications. At the moment these land vehicle mobile mapping systems were mainly used for road or railway track monitoring or inventory surveys and 3D city models.

In the hydrographic branch vessel based mobile mapping systems which usually consist of a SONAR sensor, a positioning device and attitude and heading sensors were used for several decades. Multibeam echosounders provides area based depth information of the seabed by using hydro-acoustic measurement methods. The integration of hydrographic mapping sensors, positioning and attitude devices on one survey platform enables the kinematic determination of the seabed topography. Since hydrographic surveys usually are bordered by the coast line because of the measurement principle, the combination of laser scanning and echosounding provides seamless transition between “wet” and “dry” datasets.

The main objective of this thesis is even the integration of different mapping sensors to set up a vessel based mobile mapping system which fulfils the requirements of multiple survey applications in the Port of Hamburg. The focus of the work is split into three key aspects, the configuration of a mobile mapping system containing laser scanning and echosounding sensors, an accuracy analysis for the established system and practical test projects where the performance of the system in real-life conditions is evaluated.

The configuration of the multisensor system covers the sensor installation, integration and interfacing in the sensor network of the survey vessel whereas the main focus is on the spatial and temporal relationship between the systems. The determination of lever arms and angular misalignments between the sensors but also the time synchronization of all systems are mandatory to set up such a system.

The second part of the work is defined by an accuracy analysis of the established mobile system. In this context a *a priori* uncertainty estimation shows the possible performance of the survey system with respect to the individual sensor accuracies summarized by using the law of error propagation. A comparison of mobile measured datasets with a reference dataset determines the achieved absolute accuracy.

The final part of this investigation covers several performed survey projects in the Port of Hamburg which were done on the one hand to demonstrate potential port related applications for such a mapping system and on the other hand to present workflows to process recorded datasets in order to produce multipurpose products.

ABSTRACT

Zusammenfassung

Seit einigen Jahren werden im Rahmen von ingenieurgeodätischen Vermessungen terrestrische Laserscanner eingesetzt. Diese Sensoren, welche eine Weiterentwicklung von LiDAR Systemen und elektrooptischen Totalstationen darstellen, ermöglichen eine hochgenaue und flächenhafte Erfassung der Umgebungssituation und haben sich daher bereits in vielen geodätischen Anwendungsgebieten als Datenerfassungstechnik durchsetzen können. Aufgrund des steigenden Bedarfes an räumlich und zeitlich hochaufgelösten Geodaten sowohl im öffentlichen als auch privaten Sektor werden seit einiger Zeit mobile Datenerfassungssysteme entwickelt, die die Vorteile von terrestrischen Laserscannern und aktuellen Positionierungssystemen in kinematischen Messanwendungen vereinen. Diese Systeme, die auch als Mobile Mapping Systeme bezeichnet werden, werden bereits in verschiedenen Anwendungen hauptsächlich zur Bestanderfassung und Überwachung im Straßen- und Gleisbereich eingesetzt.

Im der Hydrographie existieren hingegen seit vielen Jahren mobile Messsysteme, die nach dem Messprinzip der hydroakustischen Tiefenmessung die flächenhafte Erfassung der Gewässergrundtopographie ermöglichen. Durch die Integration von sogenannten Fächerecholoten, aktuellen Satellitennavigationslösungen und Lagewinkelmesssensoren auf Vermessungsschiffen wird die mobile Erfassung des Gewässergrundes ermöglicht. Da die hydrographische Vermessung im Allgemeinen am Übergang zwischen Wasser und Land aufgrund des angewendeten Messprinzips endet, bietet sich eine Kombination von elektrooptisch und hydroakustisch messenden Sensoren auf einer Plattform an.

Die Zielsetzung der vorliegenden Arbeit ist es durch Integration der verschiedenen Messsensoren ein schiffsbasiertes mobiles Datenerfassungssystem aufzustellen, welches den Anforderungen der verschiedenen Anwendungsgebiete im Hamburger Hafen gerecht wird. Hierbei wird vor allem auf drei Schwerpunkte eingegangen, den Aufbau eines mobilen Datenerfassungssystems für Über- und Unterwasseranwendungen, eine Genauigkeitsanalyse für das erstellte Messsystem sowie die Darstellung von verschiedenen Anwendungsbeispielen im Hamburger Hafen.

Der Aufbau des Mobile Mapping Systems umfasst die Installation und Integration der verschiedenen Messsysteme auf einem Vermessungsschiff, wobei vor allem die räumliche und zeitliche Zuordnung der Sensorik berücksichtigt wird. Hier sind insbesondere die Bestimmung der Lagewinkel der einzelnen Messinstrumente zueinander und die einheitliche Zeitsynchronisierung zu nennen, die letztendlich die Güte eines Multisensorsystems bestimmen.

Der zweite Teilbereich dieser Arbeit stellt eine Genauigkeitsuntersuchung des aufgestellten Messsystems dar. Mittels einer a priori Genauigkeitsabschätzung wird das erreichbare Genauigkeitspotential der Messanlage evaluiert. Durch einen anschließenden Vergleich von mobil erfassten Daten mit Referenzdatensätzen sind Aussagen über die tatsächlich erreichte Genauigkeitsgüte möglich.

Im abschließenden Teil dieser Untersuchung werden potentielle Anwendungsgebiete für das Mobile Mapping System aufgezeigt und anhand von ausgewählten Messprojekten näher analysiert.

ZUSAMMENFASSUNG

Contents

Abstract	vii
Zusammenfassung	ix
1 Introduction	1
2 Basic Principles	5
2.1 Hydrographic Depth Measurement	5
2.1.1 Basics of Echo Sounding	6
2.1.2 Principles of Echo Sounding	7
2.2 Terrestrial Laser Scanning	11
2.2.1 Principles of Measurement	13
2.2.2 Deflection System and Field of View	17
2.3 Inertial Navigation Systems	21
2.3.1 From mechanical Gyroscope to Fiber Optic Gyro	21
2.3.2 Basics of Inertial Navigation Systems	26
2.4 Mobile Mapping Systems	29
2.4.1 Characteristics of Mobile Mapping Systems	29
2.3.3 Overview of existing Mobile Mapping Systems	35
3. Realization of a Mobile Mapping System	39
3.1 Survey Platform and Sensors	39
3.2 Sensor Integration and Interfacing	44
3.3 Determination of Lever Arms	46
3.4 Calibration of Angular Misalignments	47
3.4.1 Angular Offsets between IMU and Vessel Frame	48
3.4.2 Angular Offsets between Scanner and Vessel Frame	51
3.5 First Mobile Mapping Results	56

4. Data Processing	61
4.1 Online Processing QPS QINSy	61
4.2 Post Processing QPS QINSy	66
4.2.1 Post Processing QINSy - GNSS Trajectory	65
4.2.2 Post Processing QINSy - INS Trajectory	67
4.3 Post Processing RIEGL RiPROCESS	69
4.3.1 Post Processing RiPROCESS - INS Trajectory	69
4.3.2 Post Processing RiPROCESS - Scan Data Adjustment	71
4.4 Summary	75
5. Accuracy Analysis	77
5.1 Uncertainty of Mobile Mapping	77
5.2 Reference Measurement	89
5.3 Inner Accuracy between Processing Methods	92
5.4 Inner Accuracy between multiple Survey Lines	98
5.5 Absolute Accuracy between Reference and Mobile Data	101
5.6 Summary of Accuracy Considerations	106
6. Test Surveys and Examples of Multipurpose Products	107
6.1 Building „Dockland“ - Object of 3D Port Model	107
6.2 Embankment „Koehlbrand“ - Bathymetric Chart	111
6.3 Harbor „Grasbrookhafen“ - Electronic Navigational Chart	114
6.4 Summary	117
7. Conclusion and Outlook	121
I List of Figures	123
II List of Tables	127
III Bibliography	129

A	Appendix.....	133
A.1	Data Sheets – Used Sensors.....	135
A.2	Initial Lever Arm Measurement.....	149
A.3	Uncertainty Computations.....	153
A.4	QPS QINSy Calibration Results.....	157
A.5	RIEGL RiProcess Calibration Results.....	161
A.6	GEOMAGIC 3D Comparison Results	187
A.6	Product “Dockland” - Object of 3D Port Model.....	221
A.7	Product “Koehlbrand” - Bathymetric Chart.....	225
A.9	Product “Grasbrookhafen” - Electronic Navigational Chart.....	229

1. Introduction

The Port of Hamburg is at the moment on position fifteen of the world-wide leading ports of container transshipment and the third behind Antwerp and Rotterdam in Europe. Although the depression in 2008/2009 has deeply affected the international economy, the container transshipment rates in Hamburg already have started to rise. Whereas in 2008 9.7 million TEU's were handled, the rates decreased down to 7.0 million TEU in 2009. In 2010 a container transshipment of almost 8 million TEU's was reached. But to be able to handle millions of containers and additionally millions of tons of bulk and mixed cargo the port facilities and the whole port infrastructure has to be improved continuously. The Hamburg Port Authority meets these challenging tasks for the Port of Hamburg and is therefore responsible for the strategic port planning, the real-estate management, the maintenance and further development of waterway, railway and corresponding land infrastructure and the safety of navigation in the port area.

One major task of the waterway infrastructure is the maintenance of the water depths in the port. Every year several dredgers have to maintain the required depths in the fairway of the river Elbe but also in many harbour basins in order to provide sufficient under-keel clearance for the vessel traffic. Because of sedimentation and erosion effects in the tide influenced port area the seabed topography changes continuously which is monitored by the four survey vessels of the hydrographic department of the HPA. These vessels are equipped amongst other measurement sensors with multibeam echosounders and perform all-the-year hydrographic measurements to determine the water depths area based in the whole port. The results of these surveys were not only used to plan and to control the dredging activities in the port but also to receive information about sedimentation and erosion processes. Especially critical erosion effects at constructions directly located at the waterside like quay walls, buildings, bridge pylons etc. have to be detected by the hydrographic measurements.

Another task of the hydrographic department of the HPA is to monitor the embankments of the ports waterways. Because of external causes based on strong erosion effects, vessel groundings, over-dredging activities etc. the stability of steep slopes can be endangered and lead to slope ruptures. These critical damages of the embankment affect not only the safety of navigation in this area but also the stability of buildings and constructions close to the bank. For this reason the most endangered embankments of the port have to be monitored in certain intervals by hydrographic measurements. Unfortunately hydrographic echosounding measurements are only able to map the underwater part of the slopes, although the dry part is of equal importance.

Since hydrographic surveys usually are bordered by the coast line because of the measurement principle, a survey system is needed, which provide not only kinematic echosounding but also above-water mapping capabilities. One of these "dry" mapping sensors can be a terrestrial laser scanner. Terrestrial laser scanners are active, optical measurement sensors which are based on contact-free and area based object detection by using laser devices. These sensors scan automatically the environment either grid based or similar to multibeam echosounders profile based with high speed in order to map the surrounding area as a point cloud.

A combination of echosounding and laser scanning would provide seamless transition between “wet” and “dry” datasets in order to map not only the underwater seabed structure but also port facilities like quay walls, flood protection walls, dykes and bridges. Both measurement methods on one survey platform would complement one another in order to support decision making processes for the maintenance of the port infrastructure with high resolution geo-datasets.

For these reasons the topic of this master thesis is to conceive of and to practical realize a vessel based mobile mapping system whereas the main objective is the integration of different mapping and positioning sensors. The thesis task is split into three key aspects, the configuration of a mobile mapping system containing laser scanning and echosounding sensors, an accuracy analysis for the established system and practical test projects where the performance of the system in real-life conditions has to be evaluated.

The configuration of the multisensor system has to cover the sensor installation, integration and interfacing in the sensor network of the survey vessel whereas the main focus should be on the spatial and temporal relationship between the systems. The determinations of lever arms and angular misalignments between the sensors but also the time synchronization of all systems have to be assured.

The second part of the task is to perform an accuracy analysis of the established mobile system. In this context a *a priori* uncertainty estimation shall show the possible performance of the survey system. A comparison of mobile measured datasets with a given reference dataset has to be used to determine the achieved absolute accuracy.

The final part of this investigation shall demonstrate the performance of the mapping system by carrying out test surveys in the Port of Hamburg. This should present exemplarily some port related applications of such a mapping system and in addition their corresponding multipurpose products.

This thesis is organized according to the following chapters:

- Chapter 2: Basic Principles

A mobile mapping system consists of several totally different sensors whereas each of these sensors is based on different measurement principles which will be introduced in this chapter. At first the term hydrographic depth measurement will be discussed and the measurement principle will be explained. The second part will present the laser scanning and the third will give an introduction to inertial navigation systems. Finally the basics of mobile mapping systems including components and already existing systems will be presented.

- Chapter 3: Realization of a Mobile Mapping System

This chapter presents the initial steps of setting up a mobile mapping system and starts with the selection of survey platform and sensors. Furthermore the calibration procedure which was performed to determine the spatial relationship between sensors and platform is described in detail. Finally first survey results will be discussed from the point of remaining systematic problems.

- Chapter 4: Data Processing

This chapter describes different approaches for processing the data recorded by the mobile mapping system and presents proposed processing workflows and their pros and cons. The differences between online and post-processing but also between different post-processing software packages will be discussed.

- Chapter 5: Accuracy Analysis

This chapter deals in the first part with *a priori* computations of the systems uncertainties with respect to the law of error propagation and reflects the possible performance of the whole mobile mapping system. The second part will present the results of practical accuracy analysis with real data. Different datasets collected by mobile, but also by static terrestrial laser scanning will be compared with each other in order to determine values for precision and absolute accuracy.

- Chapter 6: Test Surveys and Examples of Multipurpose Products

In this chapter several performed survey projects will be presented and the workflows to derive multipurpose products will be described. The potential demand on products based on mobile mapping will be discussed from point of a port authority.

- Chapter 7: Conclusion and Outlook

This final chapter summarizes the results of this thesis and gives an outlook to future work.

2. Basic Principles

The mobile mapping system which was briefly mentioned before consists of several totally different sensors which were integrated to compute high accurate measurement results. Each of these sensors is based on different measurement principles which will be introduced in this chapter. At first the term hydrographic depth measurement will be discussed whereas the measurement principle will be explained but also different applications are presented. Although the echo sounding part of this thesis is small in comparison to the laser scanning part the basic principles have to be introduced to be able to compare both approaches. The second part will present the laser scanning and the third will give an introduction to inertial navigation systems. In this section not only the principles of rotation and acceleration measurements will be explained but also the integration of these sensors into an inertial measurement unit will be presented. Finally the basics of mobile mapping systems including components and already existing systems will show the complexity of such a system.

2.1 Hydrographic Depth Measurement

Depth measurements were performed over millennia by the human mankind similar to navigational measurements. Navigation is the process of monitoring and controlling the movement of a vessel from one place to another. The mariner has to find a safe route to the desired destination which also means that he has to know the water depths of this route. If one considers the Egyptians who sailed along the river Nile, the Vikings on their raids or Columbus at his discovery of America. All of them used a kind of lead lines, lead or stones weighted ropes, to determine the depth under the keel of their ships. Until the beginning of the 20th century this was the only method to measure water depths. With the invention of the first echo sounder by Alexander Behm the period of lead line measurements had been started to end. Behm recognized during his experiments that the decrease of sound intensity of a sound wave during the path through the water column is a function of the water depth. To create sound waves Behm had used fire guns which gave a constant sound source. Because of different problems with the sound source he changed his echo sounding equipment in the way that not the sound intensity was measured but the time which was needed by the sound wave to travel to the seabed and back. The approach was to measure the time difference between transmitting and receiving of sound waves which is directly related to the water depth. This first echosounder was the beginning of sonar technology (WDR, 2007). The world wars had forced the development of the sonar technology in order to create systems to detect and localize sound sources in the water. The introduction of digital signal processing methods in the 60's of the 20th century has started a technological revolution initiated by computer engineering. From this time a lot of hydrographic applications have been invented. For example the side scan sonar which is used to map the seabed with acoustic images became the most important tool in the field of marine geology. With the emergence of multibeam echosounders in the 70's it was possible not only to create sound images but also to survey the seabed area based. Today combinations of multibeam echosounder and sidescan sonar were used to map the seabed topography and its acoustic properties.

2.1.1 Basics of Echo Sounding

The principle of depth respectively range determination with echosounders is based on time measurements of acoustic waves. Acoustic waves can be described as the propagation of mechanical perturbations which are local compressions and dilations in particular. The sound wave is a longitudinal wave or pressure wave that propagates away from the source. In case of an echosounder the wave is initiated by a transducer which creates locally directed perturbations in the water column. The sound wave travels through the water column and strikes an impedance layer, a layer which separates two mediums with different density and velocity properties, for example at the seabed. The acoustic signal is then partially absorbed but to a certain amount also reflected in the direction of the transducer. The measured time difference between transmission and reception of the acoustic wave is even a function of the water depth and the sound velocity.

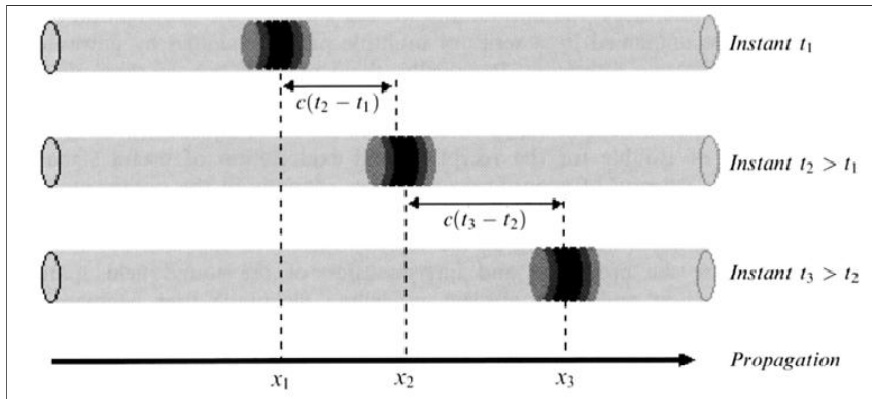


Figure 2.1: Principle of one dimensional propagation of sound waves as a function of time (LURTON, 2010)

From this relationship the water depth can be calculated with respect to following equation:

$$H = \frac{c \cdot \Delta t}{2} \quad (2.1)$$

where: H = water depth
 c = sound velocity
 Δt = time difference

As sound source a transducer is used to convert an electronic impulse into a pressure wave when transmitting energy into the water, but also to convert the sound wave reflected at the seabed and finally received into an electronic impulse. A transducer therefore contains additional to a transmitter also a receiver to make the depth measurement possible.

For the conversion of electronic signals into sound waves and vice versa there exist several physical processes whereas in the hydrographic area the properties of some piezoelectric crystals are mostly used. The physical effect is that when an electric field is applied to these crystals a change in polarization will occur which is directly related to a deformation of the material. If this deformation takes place in a certain medium an acoustic wave is created. In contrast to the transmission the reception process uses the fact that when a piezoelectric crystal is stressed in this case by sound waves it will generate an electric potential which lead to an induced voltage. Figure 2.2 show the physical effect of piezoelectricity and its realization in a Tonpilz transducer.

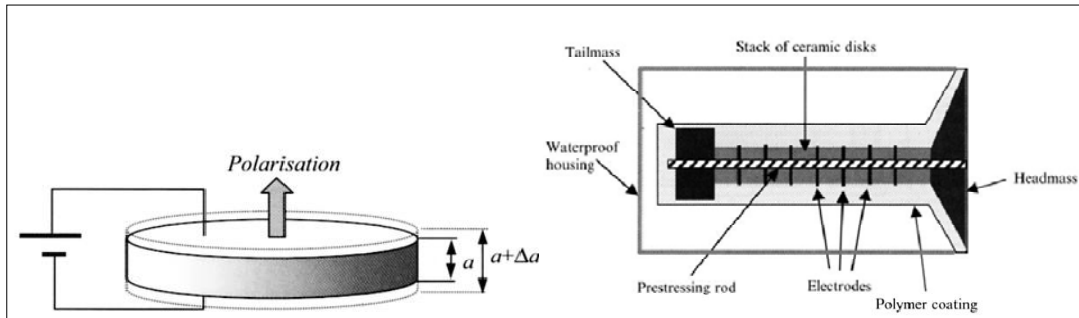


Figure 2.2: Physical principle of piezoelectricity (Left) and the realization of this effect in a transducer (Right); When the piezo element is excited by a strong electric field it change polarization which leads to a deformation of the element (LURTON, 2010)

The Tonpilz technology is the most common used technology for hydrographic transducers. As shown in figure 2.2 the piezoelectric elements are separated by electrodes which induce the driving electric field to the arrangement. When such an electric field is applied to the elements they start to swing at their resonance frequency which produces acoustic waves at the headmass of the transducer. The size of the piezoelectric elements which were used in a transducer determines the resonance frequency. But also the size of the headmass, thickness and diameter, influence the resonant frequency of the transducer which is directly linked to the directivity of such a system.

2.1.2 Principles of Echo Sounding

A transducer of a single beam echosounder transmits the sound wave with a certain frequency and transducer dependent beam width of for example 5-15 degree into the water column. The sound wave travels to the seabed, is then reflected at the bottom and travels back to the receiver unit off the transducer. The first significant received echo from the point of signal to noise ratio is then used for the time measurement. This procedure ensures that always the shallowest depth will be measured.

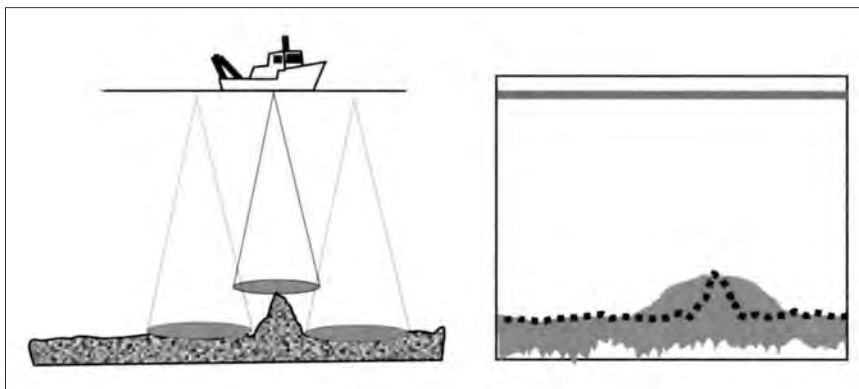


Figure 2.3: Principle of measurement of a single beam echosounder (Lurton, 2010) The beam geometry with respect to the seabed (Left) and the corresponding echogram in contrast to the true topography (Right)

Figure 2.3 depicts the principle of measurement of a single beam echosounder. It is obvious that the horizontal resolution of the measurement is directly related to the beam width of the transducer.

Because of the fact, that always the first good echo is used for the depth measurement it is also clear that the wider the beam width the higher the vertical error can be at slopes or obstacles. This is based on the depth depending increase of the size of the footprint, which is the ensonified area at the seabed.

The vertical resolution on the other hand depends only on the time period where one signal will be transmitted, the pulse length. The relationship between beamwidth, pulse length and the values for horizontal and vertical resolution are described as follows:

$$\delta x = 2 \cdot \tan\left(\frac{\theta}{2}\right) \cdot H \quad (2.2)$$

where: H = water depth
 θ = beam width
 δx = horizontal resolution
T = pulse length
c = sound velocity
 δz = vertical resolution

$$\delta z = c \cdot \frac{T}{2} \quad (2.3)$$

If one tries to improve the horizontal resolution by decreasing the beam width one has to keep in mind that with same frequency the size of the transducer has to increase in order to make the beam width smaller which can be described by the following expression:

$$d = \frac{0,7 \cdot c}{\sin \theta \cdot f} \quad (2.4)$$

where: d = transducer diameter
 θ = beam width
f = frequency
c = sound velocity

From the equation above it is possible to derive the relationship that with increasing frequency and same beam width the diameter of the transducer decreases. In other words with increasing frequency and the same transducer diameter the beam width decreases as well.

Because of the physical properties absorption and penetration depth of sound waves the used frequencies of single beam echosounder depends on the desired application. For deep water surveys transducers with low frequencies of for example 15kHz were used because of less loss of energy. For shallow waters transducer with frequencies of about 200 – 400 kHz were used.

The multibeam echosounder combines the advantages of single beam echosounders and sidescan sonar systems. Sidescan sonar systems are used as mentioned before to map the underwater topography by creating intensity images of the seafloor. The sensor is towed above the seabed and transmits a very narrow sound fan to both sides of the sensor to the bottom. Because the system ensonifies a wide swath over a certain time period a lot of echoes will be received by the sensor, which measure the time of arrival but also the echo intensity for each of these echoes. Similar to a single beam echosounder the first of these echoes is then used to compute the water depth below of the sensor. With the assumption of a horizontal seabed for each of the echoes the distance to the sensor can be calculated.

The distance of each echo to the towfish is calculated as follows:

$$y = \sqrt{\frac{c^2 \cdot \Delta t^2}{4} - T^2} \quad (2.5)$$

where: y = horizontal distance of echo

c = sound velocity

Δt = time difference

T = water depth below the sensor

With the calculated distance to the sidescan sensor and the measured intensity of the echo a grayscale picture of the seabed can be created strip by strip whereas the gray value directly related to the intensity. From this intensity image the user can draw conclusions about potential obstructions at the seafloor but also about different materials with different reflection parameters which allows a seabed classification for example.

Multibeam echosounders are in general an extension of single beam systems. But instead transmitting and receiving only one vertical beam a multibeam projector transmits a wide fan and the receiver array receives a fan of beams across the ship. Although the individual beams are created at the receiver side of the system where the beam forming procedure is done, the multibeam principle can be pictured as in figure 2.4. It is obvious that because of the wide fan with swath angles of for example 75deg to both sides of the sensor a width of up to 7.5 times the water depth can be surveyed.

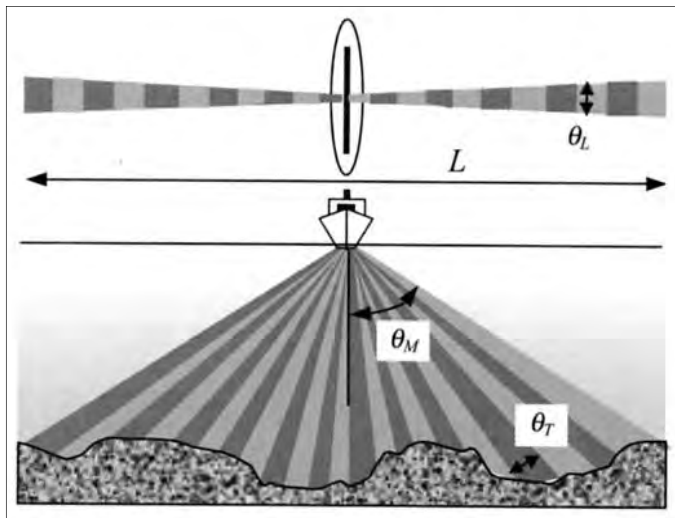


Figure 2.4: Principle of depth measurement of a multibeam echosounder (LURTON, 2010) At a certain swath angle the fan covers a distance on the seabed of 7.5 times the water depth.

Similar to sidescan systems a multibeam is able to measure the intensity of each beam which can be used to create a pseudo sidescan image of the seabed which is called backscatter. Additionally by using different processing algorithms a multibeam is also capable to create true sidescan image. Because of the worse geometry of a multibeam arrangement fixed at a vessel in comparison to a towed sidescan sensor but also by using different frequencies the multibeam sidescan image contains a lower resolution but can be corrected by true depths instead of the flat bottom assumption. However, the purpose of such a multibeam is in general to measure time differences and angles for all beams of a swath. With respect to LURTON (2010) every pair of beam angle and time of flight (t, θ) is used to compute coordinates in the sensors reference system.

The mathematical relations between both measurements of a multibeam echosounder are shown in figure 2.5.

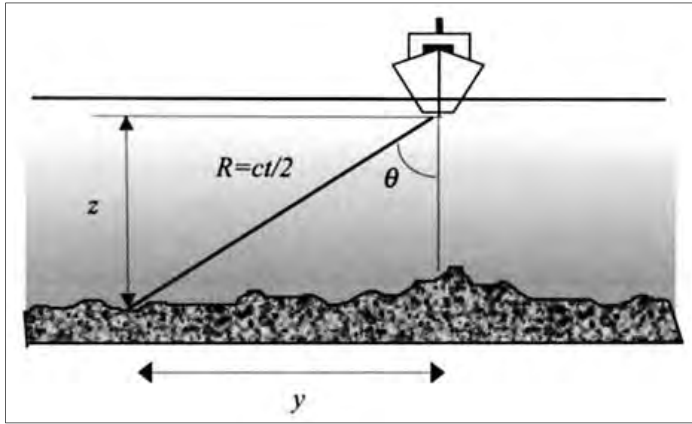


Figure 2.5: Relationship between measured variables beam angle θ and time of flight with respect to the sensor reference system (LURTON, 2010)

If one assumes the simple case that the sound velocity is constant over the whole water column, that the fan is perfectly perpendicularly aligned to the vessel axis and additionally that the vessel is not tilted because a roll issue, one can describe the position of sounding with respect to the sensor with the following expressions:

$$y = R \cdot \sin \theta = \frac{c \cdot t}{2} \cdot \sin \theta \quad (2.6)$$

where: R = Range
 θ = beam width
t = time of flight
c = sound velocity

$$z = R \cdot \cos \theta = \frac{c \cdot t}{2} \cdot \cos \theta \quad (2.7)$$

with: $R = \frac{c \cdot t}{2} \quad (2.8)$

For the more realistic case where the sound velocity changes over depth, the position of the corresponding sounding has to be computed by taking ray-tracing algorithms into account. The horizontal and vertical resolution of a multibeam measurement is equal to single beam echosounding depending on the beam width and the pulse length. Because of longer ranges and the grazing angles of the outer beams at the seabed the horizontal resolution is lower than for nadir beams because of the increasing size of the footprints of this soundings.

A multibeam echosounder has to be part of a complete survey system in order to compute the position and depth of a sounding in a certain horizontal and vertical reference frame correctly in kinematic survey conditions. Not only the attitude and heading of the sensor has to be known precisely but also the absolute position has to be measured. Therefore different sensors like GNSS, attitude and heading sensor, sound velocity probe etc. have to be integrated and time synchronized to build up a complete mobile mapping system for hydrographic purposes. The term mobile mapping system will be discussed in detail in chapter 2.4 but it has to be pointed out that mobile mapping systems in the hydrographic field exist over decades.

2.2 Terrestrial Laser Scanning

With the invention of the laser in the 60's of the last century and the start of the computer age new electronic technologies like electronic tachometer have replaced old optical devices on the survey market. The emergence of LiDAR systems in the late 70's which were initially developed for scientific reasons and not to map topography, but also the availability of reliable GNSS and INS systems in the 90's have lead to an accelerating demand of high density LiDAR point data. As a combination of total station and LiDAR the first terrestrial laser scanner were presented to the market in the late 90's. This relatively young technology nowadays has got solid position in the surveying sector.

Terrestrial laser scanners (TLS) are active, optical measurement sensors which are based on contact-free and area based object detection by using laser devices. Similar to the measurement principle of a total station, the terrestrial laser scanner determines two angles and a range in order to derive three dimensional coordinates of the measurement point. In difference to tachometers which are designed to measure discrete points TLS sensors automatically scan the environment grid based with high speed in order to map the surrounding area as a point cloud which is pictured schematically in figure 2.6. Additional to the spatial information a measure for reflectance, which depends on the material properties of the target object, will be determined for each point. In combination with digital cameras which are plugged to the scanner system not only intensity values but also true color values can be applied as an attribute to a measurement point.

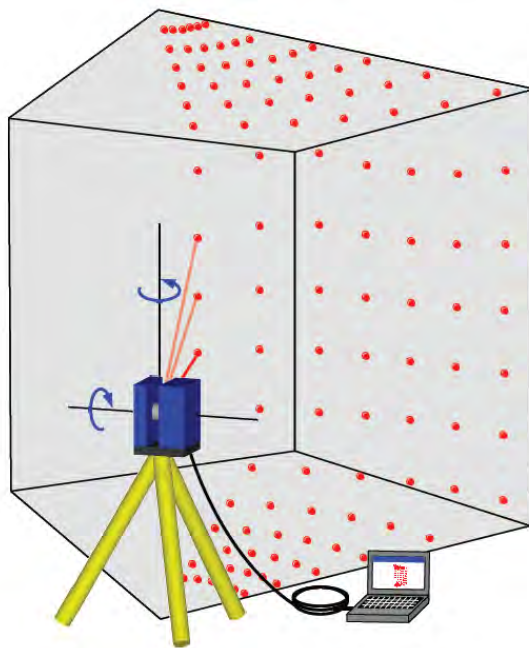


Figure 2.6: Principle of measurement of a terrestrial laser scanner (GORDON, 2008); The topographic environment is automatically scanned area based. For each measurement point two angles and a range are determined to create a 3D coordinate.

Laser scanner measurements have become a wide spread surveying technique for multipurpose applications in industrial surveying with reverse engineering tasks, in the area of archeological research, in crime scene investigations and so on. For these tasks different scanner devices are available which differ in field of view, maximum range, principle of distance measurement and accuracy.

The differentiation of laser scanner systems leads to following three groups of sensors. At first scanners for close-up range measurements which provide ranges up to 25 meters at maximum are usually based on triangulation distance determination which is the most accurate method and therefore mostly used in the industrial surveying sector. The second class of sensors serves the medium range market. The principle of distance measurement of these midrange sensors are based on amplitude or frequency modulated continuous waves which are described in detail later. The maximum range of 100 meters is delimited by the ambiguity solution method which measures phase shifts of waves with different frequencies respectively wave lengths. The maximum range is therefore defined by the lowest frequency whereas the accuracy depends on the highest frequency of the range measurement device. The third class of laser scanners operates in ranges from 400 to more than 1000 meters. The distance measurement in this case is based on the time of flight method which determines the travel time of an laser impulse from the scanner to the target object and back. The accuracy of the measured distance depends on the accuracy of time measurement which leads to a lower accuracy compared to the other distance measurement methods. It is obvious that the accuracy which is required for a special task determines the sensor in particular the distance measurement device which is needed to achieve the requirements. The following schematic referring to ELING (2009) shows different scan survey applications with respect to measurement ranges.

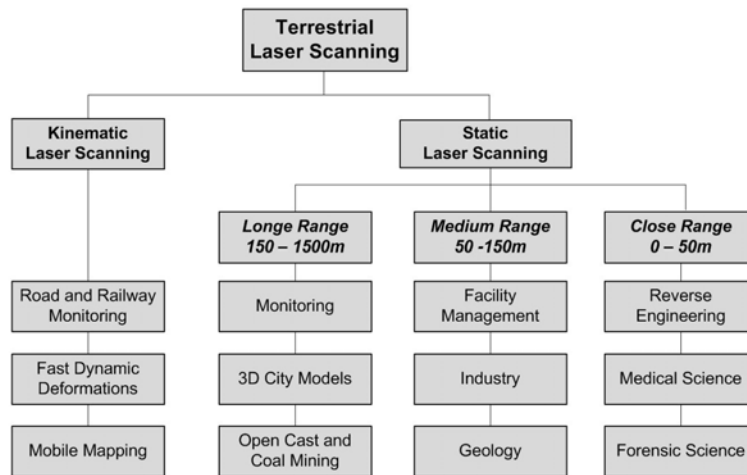


Figure 2.7: Fields of application for terrestrial laser scanners divided by measurement range, for kinematic laser scanning only the mid- and long-range devices are used (based on ELING, 2009)

Table 2.1: Overview of different laser scanning systems and their properties (SCHULZ, 2007)

Laser Scanner	Manufacturer	Distance Technique	Range [m]	Frequency [kHz]
CPW 8000	Callidus	direct TOF	80	28
LS 880	FARO	AMCW	76	120
HDS 3000	Leica Geosystems	direct TOF	300	1.8
LMS-Z420i	Riegl	direct TOF	800	12
GX	Trimble	direct TOF	350	5
Imager 5003	Zoller+Fröhlich	AMCW	53	625

2.2.1 Principles of Measurement

As shown before in figure 2.7 the most significant difference of existing laser scanner systems is the method of distance measurement which influences the accuracy and defines the application of such a system. The distance measurement methods can be distinguished in:

- Triangulation
- Direct Time-of-Flight
- Amplitude-Modulated Continuous Wave (AMCW)

At first the different distance measurement principles will be presented briefly whereas the triangulation method is omitted because it is a non-polar distance measurement method which is explained in detail by ELING (2009). The second part introduces the principles of angle measurements.

The **direct time-of-flight (TOF)** method measures the travel time of a transmitted, reflected and received laser impulse whereas the distance between sensor and target object can be described as follows:

$$s = \frac{c}{2} \cdot \Delta t \quad (2.9) \quad \begin{array}{l} \text{where: } s = \text{target distance} \\ c = \text{speed of light} \\ \Delta t = \text{time of flight} \end{array}$$

In contrast to the hydrographic depth measurement which is based on the same time-of-flight principle the accuracy of time measurement of a laser scanner has to be 200.000 times better than of an echosounder to reach a similar precision. This is only related to total different propagation speeds of both methods. If a scan distance resolution of 1 millimeter is required the time resolution should be at least:

$$\Delta t = \frac{2 \cdot \Delta s}{c} = \frac{2 \cdot 0.001m}{3 \cdot 10^8 m/s} \approx 6.7 \cdot 10^{-12} s = 6.7 ps$$

It is obvious that the accuracy of the measured distance is theoretically independent of the range but is based on the timing accuracy of the measurement device. In general it can be stated that an accuracy of a single distance measurement of 1 centimeter is hardly reachable. To improve this several pulses were used to create an averaged value for the distance. Below the measurement principle is pictured in figure 2.8.

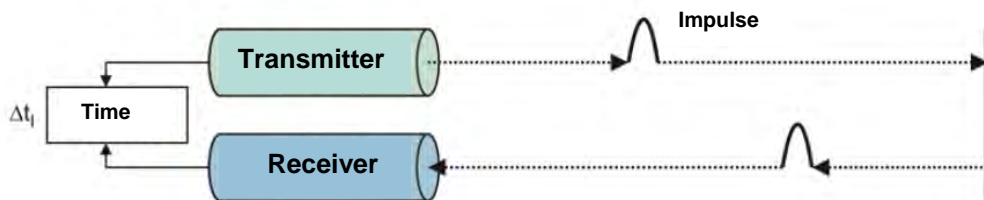


Figure 2.8: Direct time-of-flight measurement principle (HESSE, 2007); The transmitting unit emits the laser impulse which is largely reflected at the target object and received at the receiver unit; The time difference between transmitting and receiving is measured precisely

In contrast to figure 2.8 one transmitted laser impulse can lead to multiple echo pulses that reach the receiver unit of a scanner. Similar to LiDAR systems laser scanners using the TOF technique are able to distinguish between at least the first and the last pulse. With respect to latest RIEGL scan systems it is nowadays possible to measure multiple targets with one laser pulse by performing wave form analysis (RIEGL, 2009) as pictured below. The functionality avoids problems at edges, where multipath effects can potentially bias the measurement, if the distance between two echoes is sufficient enough to distinguish between signals.

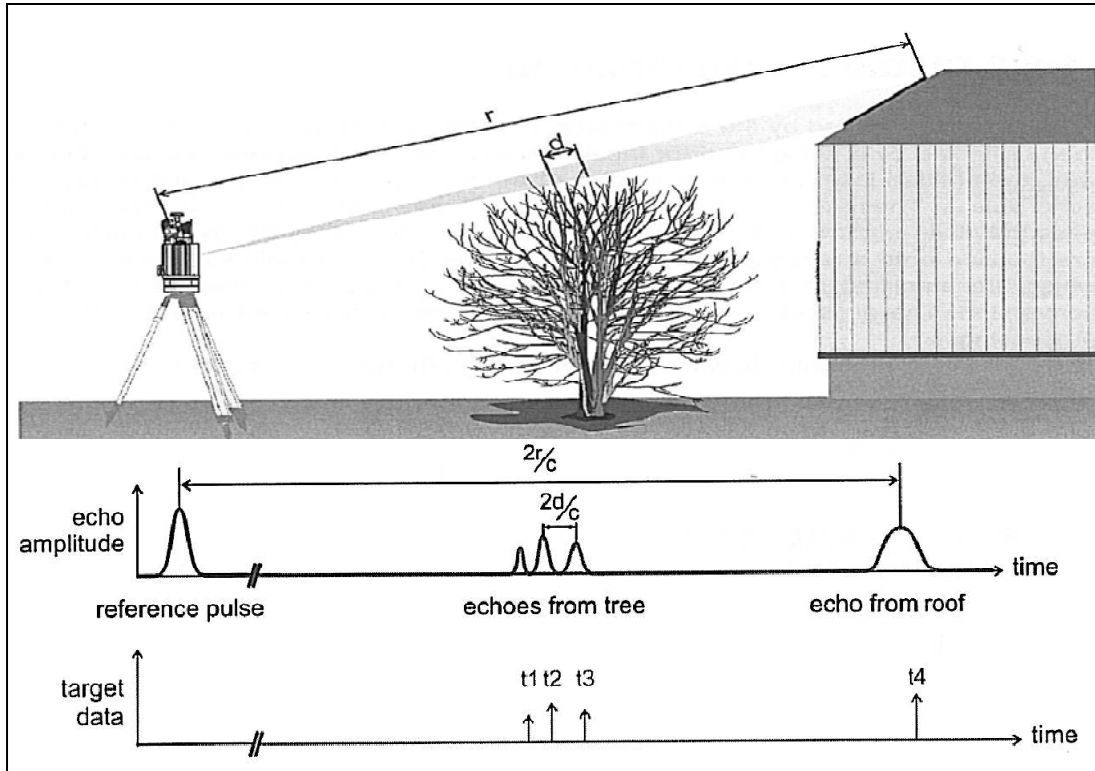


Figure 2.9: Multiple target capability of laser scan systems (RIEGL, 2009); On the way from the scanner to the building parts of the laser pulse strikes the tree in between but also the roof of the building; All received echoes are digitized

The **amplitude-modulated continuous wave (AMCW)** method, which is mainly used as distance measurement method in tacheometers, is based on the continuous modulation of the carrier. The carrier is heterodyned with a second wave with a different wavelength by amplitude modulation. The modulated signal is transmitted and received back after reflection on the target containing a difference in phase which is proportional to a certain time difference respectively to the distance of flight. This only works unambiguously if the double distance between the scanner and the target is smaller than the wavelength of the modulated wave, which can be described as:

$$s = \frac{c}{2} \cdot \frac{\Delta\phi}{2\pi f} \quad (2.10)$$

where: s = target distance
 c = speed of light
 $\Delta\phi$ = phase shift
 f = frequency of modulated wave

The relationship between phase shift and time difference can be expressed by:

$$\Delta t = \frac{\Delta \phi}{2\pi f} \quad (2.11)$$

where: Δt = time of flight
 $\Delta \phi$ = phase shift
 f = frequency of modulated wave

Assuming a more complex case where the double distance between sensor and target exceeds the wavelength of the modulated wave, the number of full multiple waves have to be determined in order to compute the distance correctly which is pictured in figure 2.10.

$$s = \frac{1}{2} \cdot \left(N \cdot \lambda + \lambda \cdot \frac{\Delta \phi}{2\pi} \right) \quad (2.12)$$

where: s = target distance
 $\Delta \phi$ = phase shift
 λ = modulated wave length
 N = multiples of λ

Practically this ambiguity is avoided by using different modulation frequencies which were applied additionally to initially modulated waves. It has to be kept in mind that the phase can be measured with an accuracy of 1/4000 up to 1/8000 of the wavelength. Therefore the lowest frequency respectively the largest wavelength defines the maximum range and higher frequencies improve the accuracy of phase measurements and indirectly the distance measurement as well (SCHULZ, 2007).

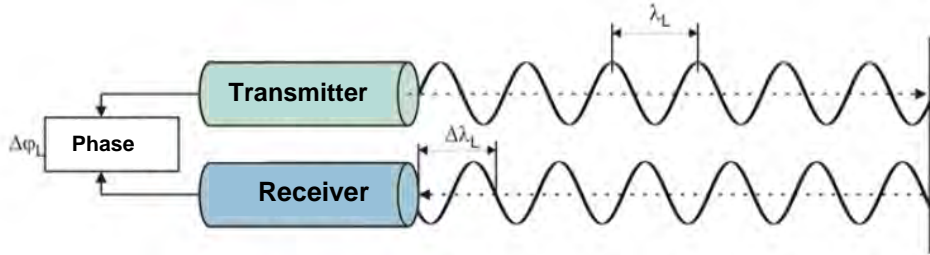


Figure 2.10: Amplituded-modulated continuous wave measurement principle (HESSE, 2007)
 The carrier is modulated sinusoidally and at the receiver the phase is measured and the phase shift is determined. The ambiguities of multiple wavelengths are solved by using different frequencies for modulation.

Referred to SCHULZ (2007) the maximum operation range of AMCW systems is limited to around 100 meters, because of the intensity loss of modulated waves which leads to problems during phase measurements. With respect to HESSE (2007) the maximum range can be shifted by taking some additional conditions like minimum object distances into account. The advantages of those systems are based on the higher accuracy of only a few millimetres and on the higher sampling rate which can reach values of up to 700 kHz.

Contrary to the TOF method AMCW is not capable to detect multiple targets with one measurement which is the reason that systematic problems at edges and corners because of the grazing angles and multipath effects can bias the data.

The three values irrespective of intensity and time which were measured by the laser scanner device consist of a distance and two angles. To achieve accurate scan results not only the distance measurement system is of importance but also the angle measurement method. In former times the determination of angles with theodolites were based on analogue measurements.

The reference circles, glass arcs with angular numbering, were observed by the surveyor using coincidence microscopes. Nowadays digital encoders determine electro-optically the orientation of the laser beam with respect to vertical and horizontal direction. In general two different techniques can be distinguished which will be presented here briefly:

- Incremental Encoding
 - Static Incremental Encoding
 - Dynamic Incremental Encoding
- Binary Encoding
 - Parallel Binary Code
 - Serial Binary Code

Incremental encoding techniques uses glass arcs which are incrementally coded by transparent and opaque strips of equal width. The distance between two adjacent strips of overall usually 10000 is called grid constant and is well known. Emitted light from a fixed light source passes through the rotating vertical or horizontal disk and irradiates a CCD sensor or photodiode which counts not only the on/off states but measures also continuously the intensity of the light that can be described as a sinusoidal wave. The number of periods of this wave is proportional to the angular rotation. Because the angles were determined relatively to the light source, absolute angle measurements require an initialization where an additional code on the disk triggers the angle measurement. This code describes the zero angle position and provides absolute angle measurement. To improve the angular resolution of such a system the disk is observed by two light sources and photo diode devices which enclose an angle of 90 degree. This arrangement leads to a double number of on/off states. In difference to the static mode the dynamic system consists of two independent light barriers and a continuously rotating coded disc. One light device is fixed with the body of the sensor and one is mounted at the alidade of the system. The trigger code starts the angle measurement when passing the alidade light device and stops at the second light barrier. Additional to the coarse measurement by counting the on/off a fine measurement is applied by measuring the phase shift as pictured in figure 2.11. An additional method to improve the angular resolution is the use of the Moire effect which is described in detail by MÖSER et al. (2000).

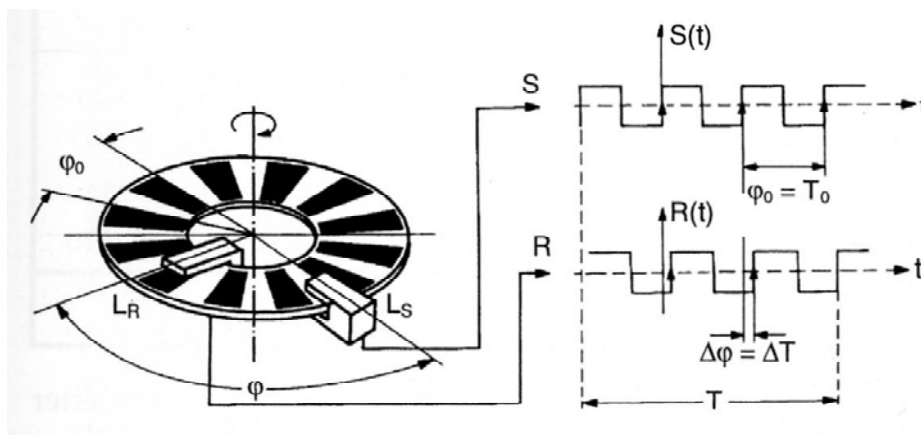
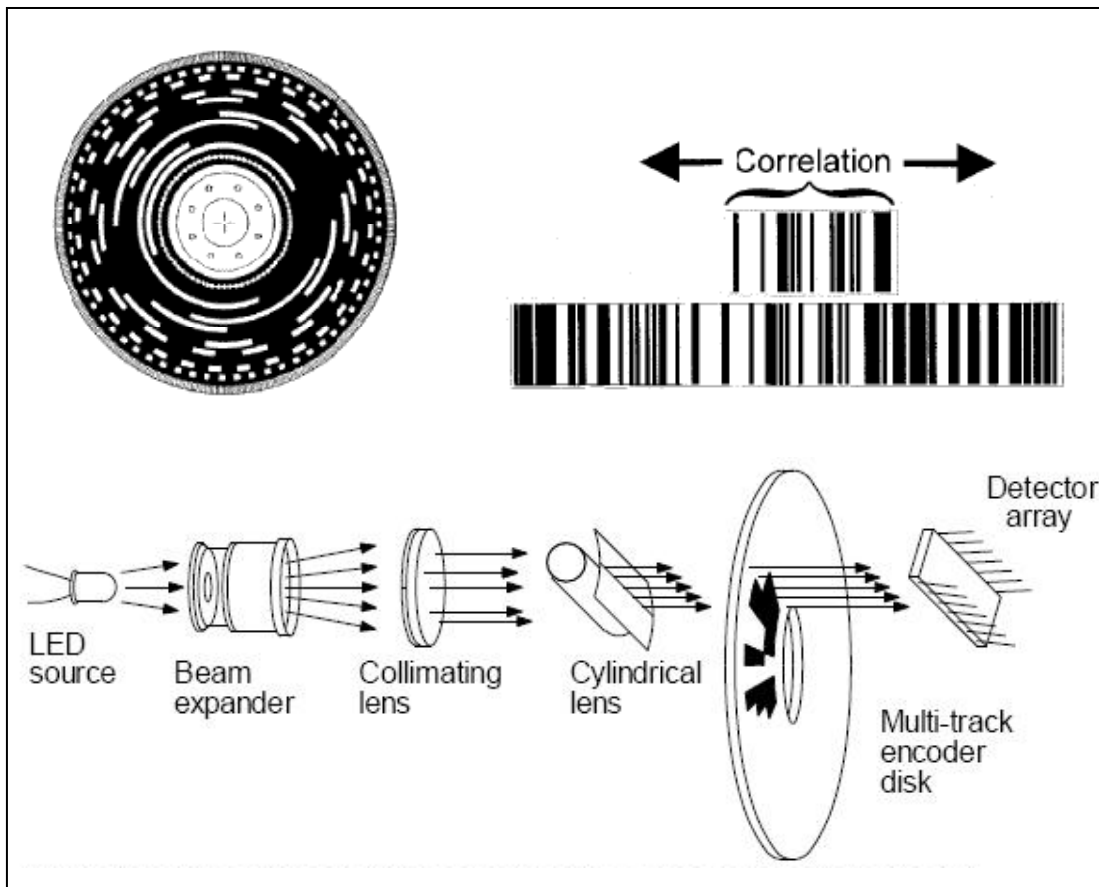


Figure 2.11: Principle of dynamic incremental encoding by measuring the phase shift (MÖSER et al., 2000)

The **binary encoding** method uses glass discs which contain a binary code either as coded rings (parallel binary code) or as absolute code (serial binary code) as shown in figures 2.12. The code describes absolute angle values – this is why the method is also known as absolute encoding. In general the code is divided into coarse sections and subsections which can easily be converted in numeric values. Light from an optical light source passes through the coded glass disc and maps a certain sector of the disc to an CCD sensor which perform at first a coarse measurement by digital image processing methods. The fine measurement is based on several interpolation procedures which are performed automatically and described in detail by KAHMEN (1997) and MÖSER et al. (2000).



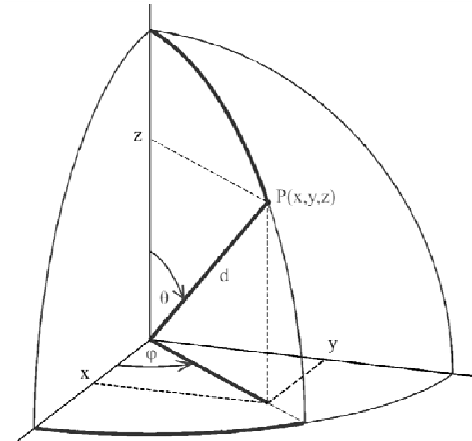
Figures 2.12: Examples of parallel (Top left) and serial (Top right) binary codes for angle encoding; The binary code is translated by digital image processing methods in order to determine numeric values for horizontal and vertical angles (SCHULZ, 2007); The optical path of light from LED source to the CCD sensor (ELECTRYSKY, 2011)

2.2.2 Deflection System and Field of View

The prior differentiation of terrestrial laser scanners was based on differences in the distance measurement methods and corresponding measurement ranges. But in general it can be stated that deflection system, field of view and also the distance measurement method are correlated with each other. For example a system with sampling frequencies in distance measurement of 700kHz requires a sufficient method to deflect laser beams with same speed.

In this section different realizations in field of view and deflection system will be presented and compared before finally the error sources of a laser scanning system will be summarized.

The results of laser scanning consist of two angles and a range which were determined with respect to the scanners own coordinate system SOCS. A measured point can be described either in spherical coordinates where d is the distance, θ is the tilt respectively zenith angle and φ is pan angle which defines the horizontal direction of a target point, or in cartesian coordinates X , Y and Z . The relationship between both of them is pictured and expressed mathematically below:



$$\begin{bmatrix} x \\ y \\ z \end{bmatrix} = \begin{bmatrix} d \cdot \sin \theta \cdot \cos \varphi \\ d \cdot \sin \theta \cdot \sin \varphi \\ d \cdot \cos \theta \end{bmatrix}$$

$$\begin{bmatrix} d \\ \theta \\ \varphi \end{bmatrix} = \begin{bmatrix} \sqrt{x^2 + y^2 + z^2} \\ \arccos\left(\frac{z}{d}\right) \\ \arctan\left(\frac{y}{x}\right) \end{bmatrix} \quad (2.13)$$

Figure 2.13: Relationship between spherical and cartesian coordinates with respect to the scanners own coordinate system SOCS (ELING, 2009)

Although the SOCS allows to describe each point in space, the field of view of a scanner delimits this capability. Referred to HESSE (2007) the scanners inherent property, the field of view can be distinguished in three different classes. The camera view is designed to scan only in very limited window without the capability to rotate around the vertical axis which can be useful in the medical or industrial sector. The panorama view enables the user to scan the complete 360 degree object space except for the sensor position whereas hybrid systems are a combination of both which are restricted only in vertical angles. In panorama and hybrid systems the horizontal rotation is managed by servomotors and the vertical rotation by rotating mirrors. Figure 2.14 describes all classes of field of view schematically.

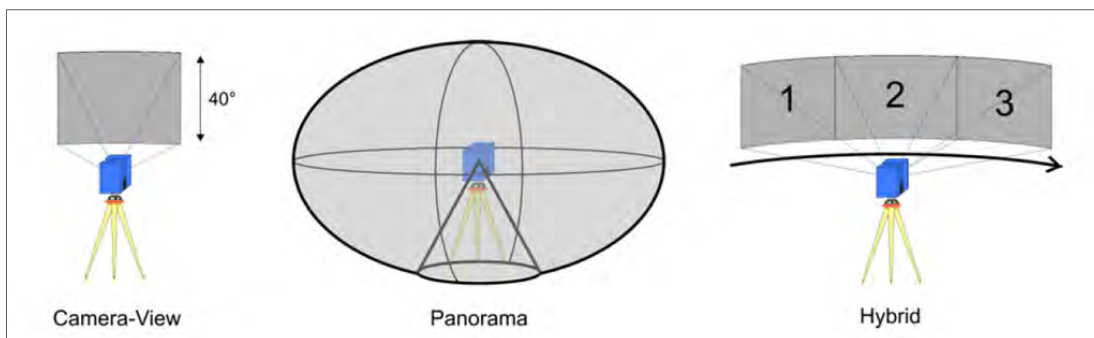


Figure 2.14: Classification of laser scanning devices by the field of view; Camera view(Left), panorama view (Middle) and hybrid system (Right) (HESSE, 2007)

Another differentiation of laser scanners is given by the deflection method. Figure 2.15 shows the methods of laser deflection schematically. In a oscillating mirror deflection system the laser signal is emitted in horizontal direction and deflected by two perpendicularly to each other rotating planar mirrors. In this arrangement one mirror is responsible for the horizontal direction of the laser beam and the other for the vertical direction. A rotation by servomotors around vertical axis is usually not implemented in those systems. The rotating mirror principle is based on a orthogonal deflection of the horizontal emitted laser beam at the 45 degree angled plane mirror. The rotation of the mirror leads to a deflection of the laser beam in vertical directions. The change in horizontal directions is performed by servomotors which rotate the scanner in incremental steps around the vertical axis. The third principle deflects the vertical emitted laser beam in vertical directions by using rotating polygon mirrors. The vertical angle of the deflected beam depends on the angular rotation of the polygon mirror whereas the horizontal direction is based on the rotation around the vertical axis of scanner similar to the rotating mirror technique.

Table 2.2: Overview of different scanners classified by deflection system (SCHULZ, 2007)

Laser Scanner	Manufacturer	Deflection Technique
CPW 8000	Callidus	rotating mirror
LS 880	FARO	rotating mirror
HDS 3000	Leica Geosystems	oscillating mirror
LMS-Z420i	Riegl	rotating polygonal mirror wheel
GX	Trimble	scanning optical system (patented)
Imager 5003	Zoller+Fröhlich	rotating mirror

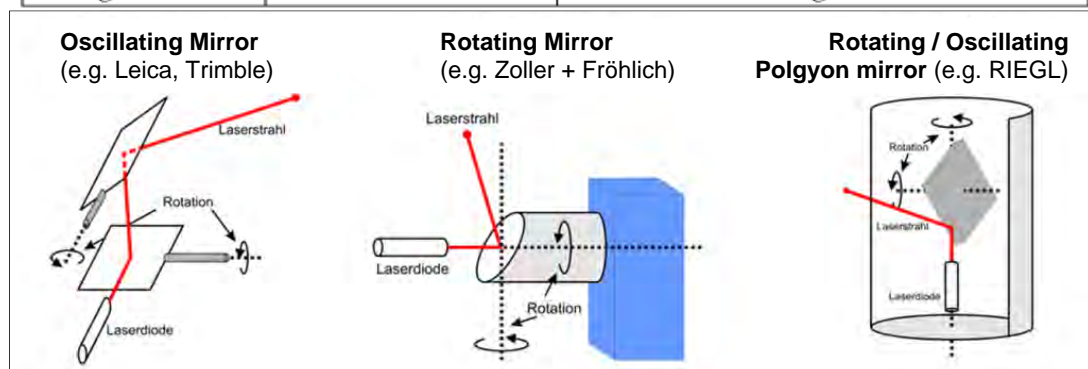


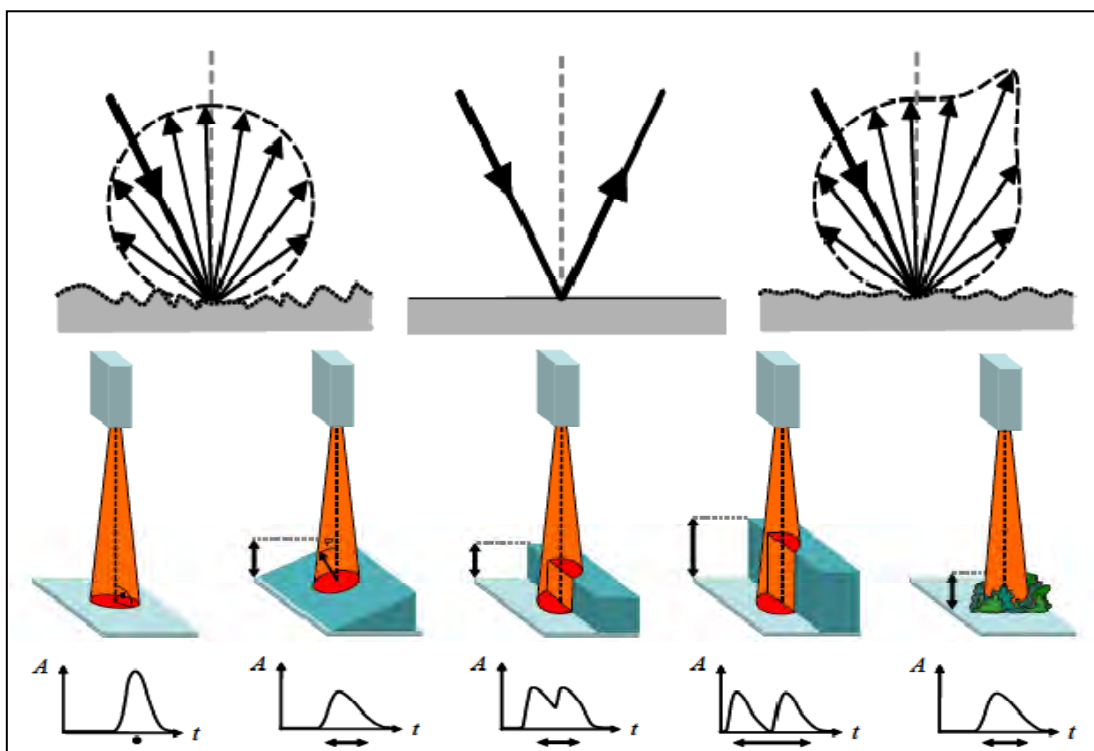
Figure 2.15: Classification of laser scanning devices by deflection system; oscillating mirrors (Left), rotating angled mirror (Middle) and rotating polygon mirror (Right) (HESSE, 2007)

To summarize the prior considerations one can state that laser scanners which support only the camera field of view usually are based on the oscillating mirror concept in combination with the TOF distance measurement method. Panorama scanners which are mostly based on AMCW distance measurements in general use the rotating mirror concept because the deflection rotation is only delimited at the position of the scanner because of the shadowing effects by the scanner itself. Hybrid scanners are only delimited in vertical directions because of the rotating polygon mirror principle and provide often the TOF distance measurements. For kinematic laser scanning respectively mobile mapping applications only panorama and hybrid laser scanner can be used.

It is obvious that a laser consists of several high technology sensors and components. Only the proper physical but also mathematical combination of these instruments is the base of a laser scanner. But as one can imagine each component underlies systematic effects and produce a certain bias. Although the major part of error sources of a laser scanner were calibrated extensive by the system developer there exist different non instrumental errors which are worthy to mention. Error sources related to laser scanning can be distinguished in:

- instrumental errors:
 - eccentricity of scan centre
 - wobble of vertical axis
 - error of collimation axis
 - error of horizontal axis etc.
- non instrumental errors:
 - intensity of laser beam
 - angle of incidence
 - footprint of laser beam
 - surface properties
- atmospheric errors:
 - errors in temperature, air pressure, humidity

Just as an example, the intensity of a laser beam influences the accuracy of distance measurement highly but depends on the one hand on surface properties like color and roughness of the scanned object which influence the reflectivity but also on the beam-object-geometry like angle of incidence and size of footprint. Figure 2.16 describes exemplarily the relationship of these non instrumental errors.



Figures 2.16: 1.Types of reflection (Top): diffuse reflection (Left), specular reflection (Middle) and a combination of both (Right) 2. Different scenarios of laser beam - object geometry (Bottom) whereas the ideal case is shown on the left side; The angle of incidence but also the footprint of the laser beam creates biases in distance measurement which is based on the evaluation of signal patterns of the reflected laser pulses (JUTZKI, 2007)

2.3 Inertial Navigation Systems

Since human mankind has used boats and vessels to sail over the oceans they have to navigate their platforms over sea in order to reach the desired destination. With respect to BOWDITCH (1995) the term of navigation is defined as "...the process of monitoring and controlling the movement of a craft or vehicle from one place to another". This definition contains not only the positioning by for example sighting of land marks or celestial bodies but also the monitoring of movement by measuring the speed and the direction of the vessel.

From the navigational point of view the first instrument to determine the direction or respectively the heading of a vessel was a magnetic needle floating in a bowl of water - the magnetic compass, invented by the Chinese one millennium ago. Only roughly one century ago at the beginning of the 20th century the first full functional gyroscope was developed by Hermann Anschuetz-Kaempfe (GREWAL, WEILL, ANDREWS, 2007). This instrument is based on the earlier invented momentum wheel gyroscope and provides a lot of advantages in contrast to a magnetic compass. Gyros had their breakthrough in the military world of the 20th century where they replaced magnetic compasses, which do not work on iron ships. Over the years the technology behind the gyros has been improved to a certain stage until in the early 70's the optical fibre was developed for the telecommunications industry. This material was the base to apply the Sagnac principle to the development of fiber optic gyros (FOG). Nowadays optical gyros have displaced the mechanical gyroscopes almost completely because of abrasion and precision reasons. This chapter introduces briefly the basic principles and error sources of a mechanical gyroscope and the development to fiber optic gyros. The second part describes the technical background of inertial navigation systems including the used sensors and the combination with GNSS.

2.3.1 From mechanical Gyroscope to Fiber Optic Gyro

In contrast to magnetic compasses a mechanical gyroscope is not influenced by the Earth's magnetic field. In general a gyroscope consists of a balanced and high speed rotating wheel which is mounted in a special gimbals arrangement which allows the wheel to rotate freely around three axes as shown in figure 2.17.

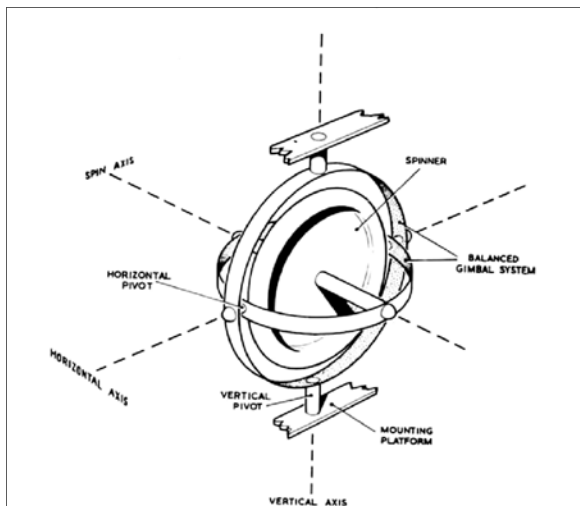


Figure 2.17: The free gyroscope (TETLEY, CALCUTT, 1988) containing three freedoms of rotation around the spin axis, the horizontal and vertical axis. The arrangement of the gimbals defines these axes.

One of the fundamental properties of a free gyroscope is the gyroscopic inertia which is related to one of the basic laws of motion described by Isaac Newton. Newton's first axiom points out that "a body will remain in its state of rest or uniform motion in a straight line unless a force is applied to change that state". With reference to a gyroscope it is clear that a spinning mass will only leave its plane of rotation when an external force will be applied to the system. In this case the gyroscope opposes a force to the external force which is called gyroscopic inertia. This physical effect is well known from a spinning top. This educationally valuable toy rotates around the vertical axis balancing on a point and remains in the state of rest until the rotation rate decreases. If one tries to push the top perpendicular to the rotation axis one recognizes a force which tries to keep the rotating mass vertically, the gyroscopic inertia. For a spinning rotationally symmetric body the angular momentum is defined as the product of the torque respectively the momentum of inertia and the angular velocity.

With respect to the fact that an acting force to an object with certain mass creates an acceleration, for a rotating system it is clear that an external acting momentum introduces an angular acceleration to the spinning system. Because the angular momentum of a spinning system is directly proportional to the angular velocity, this change of velocity with respect to time changes the angular momentum to a certain amount. The acting momentum changes not only the absolute value but also creates a continuously changing direction of the angular momentum which is also known as the term precession. In other words the torque induced precession describes the movement of a gyroscope axis under the influence of an external force as shown below in figure 2.18.

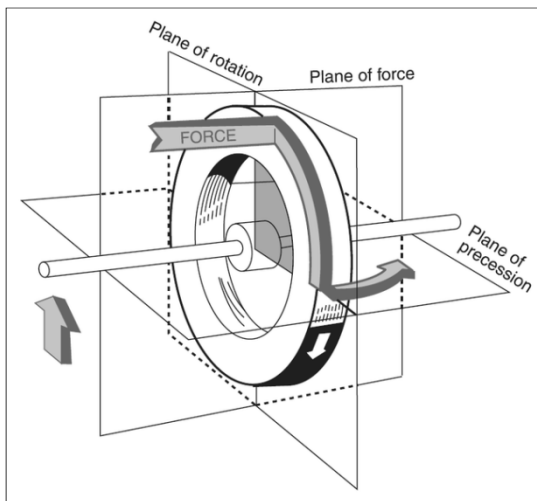


Figure 2.18: Precession of a gyroscope (FAA, 2008) under the influence of an external force. A force is applied to the rotor by lifting one end of the rotation axis. This result is a displacement at an angle of 90 degrees to the applied force. The plane of rotation has moved around the vertical axis although the force was applied in horizontal direction.

Coming back to the example of a spinning top where the axis of this spinning object "wobbles" when a torque is applied to it. Generally when a top will be started it will at first wobble a while until it is forced to be upright. After a while the rotation rate and therefore also the angular momentum will decrease. The now introduced precession is indirect proportional to the angular momentum and increases until the top will turn over.

To use the principle of precession of a gyroscope to find the geographic north direction the gyros spin axis can be made meridian seeking. In this case the gyro uses the Earth rotation to maintain its spin axis parallel to rotation axis of the Earth.

With respect to figure 2.19 a north seeking gyro doesn't contain three freedoms of rotation because the vertical axis works as a pendulum under the influence of the gravity of the Earth. To assign the principle of the pendulum effect to a gyro one has to add a certain weight to the vertical pivot point (TETLEY, CALCUTT, 1988). Then the Gravity causes a vertical force which influences the gyro in a way that it will start to perform a horizontal precession. This precession is the reason why the gyroscope becomes north seeking. The gravity forces the spin axis into the vertical direction which induces a horizontal precession of the rotor with the effect that the rotating axis points to true north.

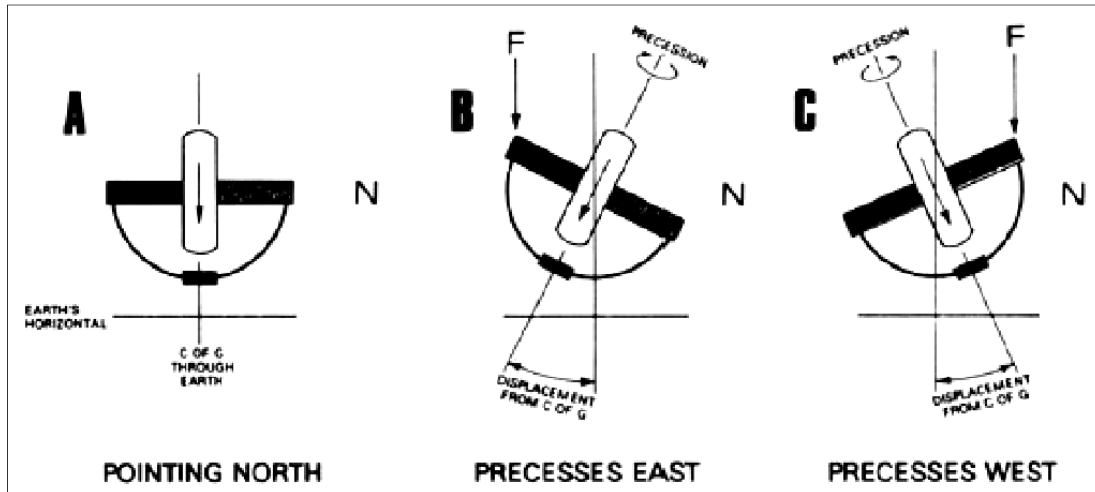


Figure 2.19: Principle of a bottom heavy north seeking gyro (TETLEY, CALCUTT, 1988); Whereas the state A describes a stable north pointing gyro, B and C describe the precession direction when the gyro is tilted with north end below (B) and above (C) of the horizontal plane because of earth rotation.

If only the gravity and earth rotation will be taken into account the precession of the gyro produce a continuously elliptical precession around the meridian which means that the gyro will not settle on the meridian. TETLEY and CALCUTT (1988) explain that the extent of the ellipse depends to major part on the initial displacement of rotating axis of rotor to the meridian. Therefore in addition to the gravity a second force is needed which will produce a damping torque to the system. This additional torque will reduce the extent of precession until the spin axis is oriented not only horizontally but also is settled in the meridian. In latitudes between the equator and the poles even the centrifugal force can produce this damping torque because its direction differs to the direction of gravity.

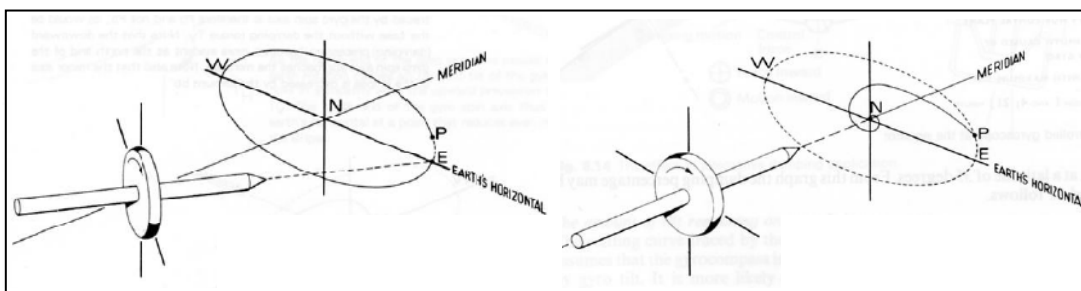


Figure 2.20: Principle of a precessing gyro only influenced by the gravity (Left) and a gyro damped by an external torque (Right). The damping effect of the centrifugal force doesn't work at the equator (TETLEY, CALCUTT, 1988)

At the equator the centrifugal force is parallel to the gravity and therefore a different force is needed to create an “anti-tilt” precession which enables the gyro to settle in the meridian. Practically there are different approaches to create this damping force by applying weights to the gyro with a fixed offset to the vertical axis as pictured in figure 2.21. TETLEY (1988) point out that the point where the weight is attached to is precisely calculated to tune the damping procedure so that the gyro will settle in meridian. The effect of gyro damping is shown in figure 2.20 (Right) and explained completely by TETLEY and CALCUTT (1988). Instead of an ellipse the precession describes a spiral figure with decreasing extent.

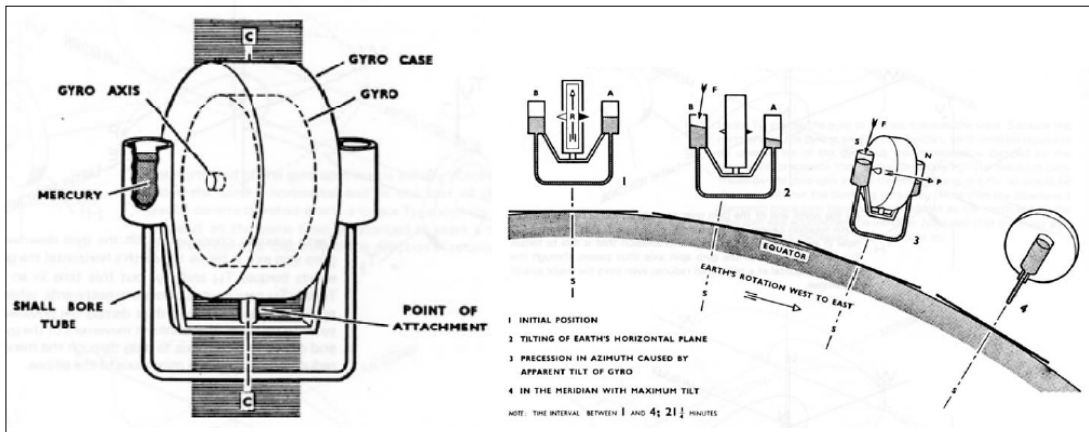


Figure 2.21: Example of gyro damping by using the principle of communicating vessels; The construction of such a unit (Left) and the principle of operation (Right) (TETLEY, CALCUTT, 1988)

By using a gyro compass there are different significant error sources worthy to mention:

- Fixed error: -alignment error between the indicated heading and vessels lubber line
- Variable errors: -dynamic error by roll and pitch movements of the vessel
- dynamic error by speed and course of the vessel path

A full description of these errors can be found in FABECK (1980) and in TETLEY (1988). In general it can be stated that all of these errors can be reduced to a minimum by for example adequate damping procedures to reduce the effect of the vessels motion. In this context the Schuler tuning should be mentioned which has improved the pendulum period of the suspended mass in order to eliminate this error sensitivity. The speed and course error can be computed directly in modern gyros when the gyro is GNSS added. The GNSS provides not only the needed positional information but also values for speed over ground and course over ground, which are essentially for the computation of the error. The heading value is then automatically corrected by the error and output to the user.

With the development of laser devices and the improvement of optical fiber with low signal loss in the sixties the base was found for non mechanical but optical gyroscopes. These so called lightwave gyroscopes use the fact that a phase coherent light travelling around a closed planar path will experience a certain phase shift which is directly proportional to the rotation rate of the planar path which is called the Sagnac effect or Sagnac interference.

With respect to figure 2.22 the Sagnac experiment is as follows. A beam of light is emitted at point O and split at point j into two beams R and T. By an arrangement of mirrors M1 to M4 these beams were forwarded in opposite direction around the grey shaded area S. When both beams have finished their journey through the arrangement they were redirected at point j in order to leave the system in direction of point c. At this point c the resulting interference pattern of both light beams is obtained. The interference pattern changes with the rotation velocity of the setup whereas the arrangement has to be located on a rotatable platform. This setup is called Sagnac interferometer.

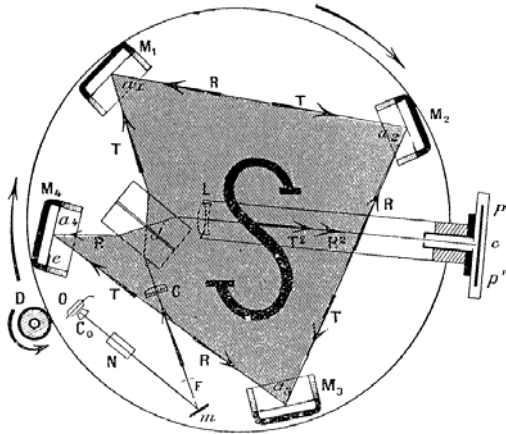


Figure 2.22: The Sagnac interferometer (WIKIPEDIA, 2011)

When the system is rotating and again a beam is emitted into it, one of the split beams has to travel a shorter distance than the other one which creates a different interference pattern than a non-rotating system. From this relationship the angular velocity of a system can be derived by comparing interference patterns. This fundamental principle is used by optical gyroscopes. In contrast to a mechanical gyro these new optical gyros measure their own angular velocity with respect to the inertial frame without any mechanical component. This fact and the difference in size of such a system make optical gyros more attractive to many user groups.

In general optical gyros can be divided in two common types of laser gyroscopes, the ring laser gyroscopes (RLG) and the fiber optic gyroscopes (FOG). The ring laser gyroscopes use a lasing segment within the closed polygonal light path with mirrors at the corners and can be described as digital rate integrating gyroscopes. They are based on the same relativistic effect that was described by Sagnac where the phase rate between two in opposite direction travelling laser beams is proportional to the rotation rate of the inertial system. These gyroscopes were directly developed after the first practical laser was invented. The first gyros of this type had faced problems at low rotation speeds which were improved by the implementation of vibrating components in order to create a pseudo rotation of the inertial system.

The base for fiber optic gyroscopes was not only the invention of the laser but also the improvement of optical fiber in the 70's of the last century. A fiber optic gyroscope is a ring interferometer using thousands of turns of optical fiber to create a fiber coil which surrounds a certain area. Similar to the ring laser gyro light is emitted into the interferometer and splitted into two counter propagating directions through the fiber coil. When the system is rotated the Sagnac effect creates a difference in travel time between both light waves which can be measured interferometrically.

Today high performance FOG's are at least equivalent to RLG's from the point of performance. Due to the fact that ring laser gyros use mirrors to guide the light the production process is more complex. Additionally as mentioned before RLG's use a dithering process to avoid problems at low rotation speeds. Because of these vibrating components the lifetime of such a sensor is less than a fiber optic gyro (IXSEA, 2009). Below both types of optical gyros are pictured in figure 2.23.

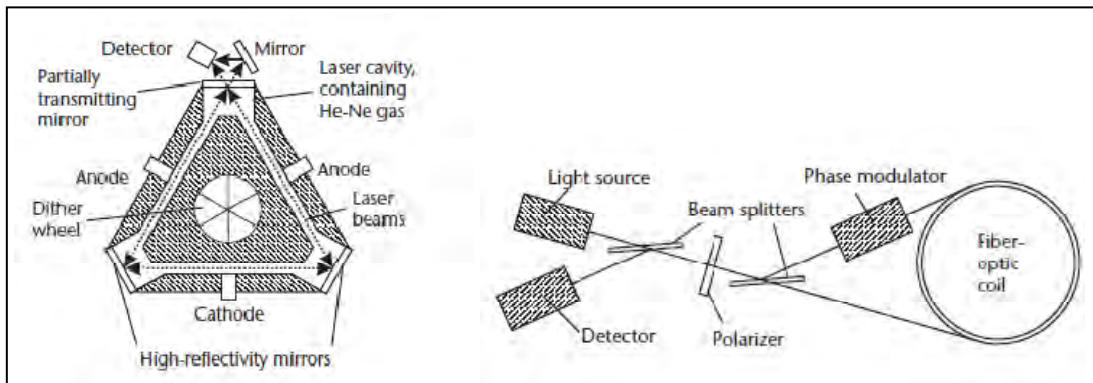


Figure 2.23: Principle of measurement of a ring laser gyroscope (Left) and a fiber optic gyroscope (Right); Both are based on the fundamental Sagnac effect (GROVES, 2008)

In the hydrographic society fiber optic gyros have become accepted for the use in inertial navigation systems because of several reasons. More and more applications need more accurate heading and motion data whereas the space on board for such a system decreases. But not only the performance and size is important but also the lifetime becomes relevant. Fiber optic gyros don't contain mechanical components and provide low maintenance. This seems to be the reason why optical gyros replace other systems on the hydrographic market.

2.3.2 Basics of Inertial Navigation Systems

With respect to the definition found by BOWDITCH (1995) which points out that navigation is "...the process of monitoring and controlling the movement of a craft or vehicle from one place to another", inertial navigation can be described as an autonomous process to determine the position and attitude of a moving object in space precisely only by utilizing the effect of inertia when the initial state of the object is well known. The inertial measurement is based on the determination of external acting forces by acceleration measurements, which are used to derive movements of the body. In general an inertial measurement unit, the system which makes inertial navigation possible, consists of three gyroscopes oriented perpendicular to each other and accelerometers to provide rotation and acceleration measurements in all three coordinate axes. These measurements describe six freedoms, three rotations and three translations which is enough to determine the position and attitude of an object in space.

The need for those systems was born in the military sector during the Second World War. The first practical system which is worthy to call IMU was implemented in German V2 rockets. After the WW2 the knowledge moved to the USA where the developments were forced because of the Cold War.

At this stage not only long-range bombers but also nuclear submarines were equipped with inertial measurement units. The most attractive advantage of such a system is that it works autonomously without adding any external signals which are potentially endangered for jamming. With the raising computer development in the 60's IMU's were put together with navigational microcomputers on all Apollo and Lunar expeditions. The inertial measurement unit has been improved over decades but in general the configuration of an IMU is described by the figure 2.24 below.

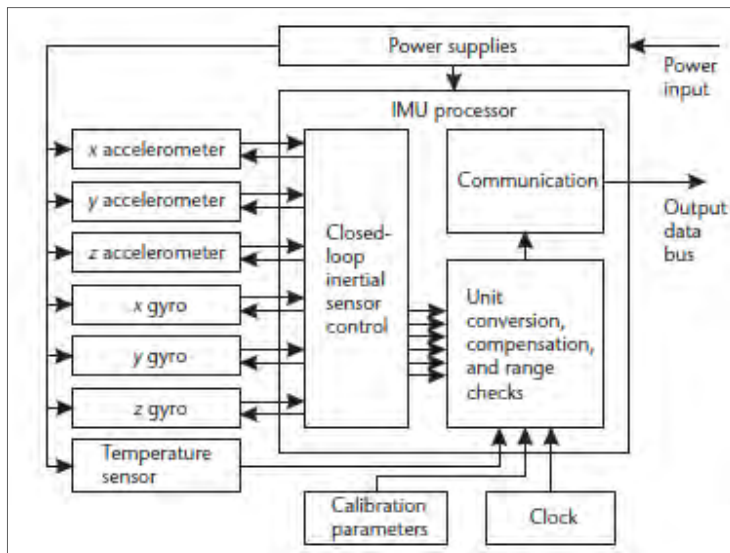


Figure 2.24: Configuration of a common inertial measurement unit IMU (GROVES, 2008)

Common IMU's consist of three accelerometers and three single-degree-of-freedom gyros mounted perpendicular to each other. Furthermore the system is equipped with the IMU processor, a store for the calibration parameters, communication interfaces for input and output and finally the power supply.

With respect to IXSEA (2009) the inertial computation consists of two different processes. At first the measurements of the gyroscopes and accelerometers are integrated and compensated for non-linear corrections. The resulting attitude update is based on a quaternion algorithm where the elementary angle variations are integrated. For the velocity and position updates the gravity and the Coriolis force are taking into account. The accuracy of all these computations depends on the accuracy respectively bias of contained gyroscopes and accelerometers but also on the initial start values for attitude, velocity and position. Below the biases of the sensors for different IMU grades are presented in table 2.3.

Table 2.3: Biases for common gyroscopes and accelerometers distinguished by IMU grade (GROVES, 2008)

IMU Grade	Accelerometer Bias		Gyro Bias	
	mg	$m s^{-2}$	$^{\circ} hr^{-1}$	$rad s^{-1}$
Marine	0.01	10^{-4}	0.001	5×10^{-9}
Aviation	0.03–0.1	$3 \times 10^{-4} - 10^{-3}$	0.01	5×10^{-8}
Intermediate	0.1–1	$10^{-3} - 10^{-2}$	0.1	5×10^{-7}
Tactical	1–10	$10^{-2} - 10^{-1}$	1–100	$5 \times 10^{-6} - 5 \times 10^{-4}$
Automotive	>10	$>10^{-1}$	>100	$>5 \times 10^{-4}$

The errors respectively biases introduced by the inertial sensors increase continuously because the gyroscopes and accelerometers data are integrated over time and the computations of attitude, position and velocity form a loop. All errors propagate with time and influence each other, which will lead to a certain drift in all of these values.

In contrast to inertial navigation global navigation satellite systems GNSS provides high long-term position accuracy especially in differential RTK mode. GROVES (2008) points out that by integrating inertial and GNSS data the advantages of both technologies can be combined to give a continuous high precision navigation solution with high long- and short term accuracy. While GNSS measurements avoid the drifting effects of an INS, the inertial solution smoothes the noisy GNSS solution. The integration algorithm which is pictured as diagram in figure 2.25 is usually based on the Kalman filter which compares INS and GNSS solution and computes corrections for inertial attitude, position and velocity in order to create an integrated navigation solution.

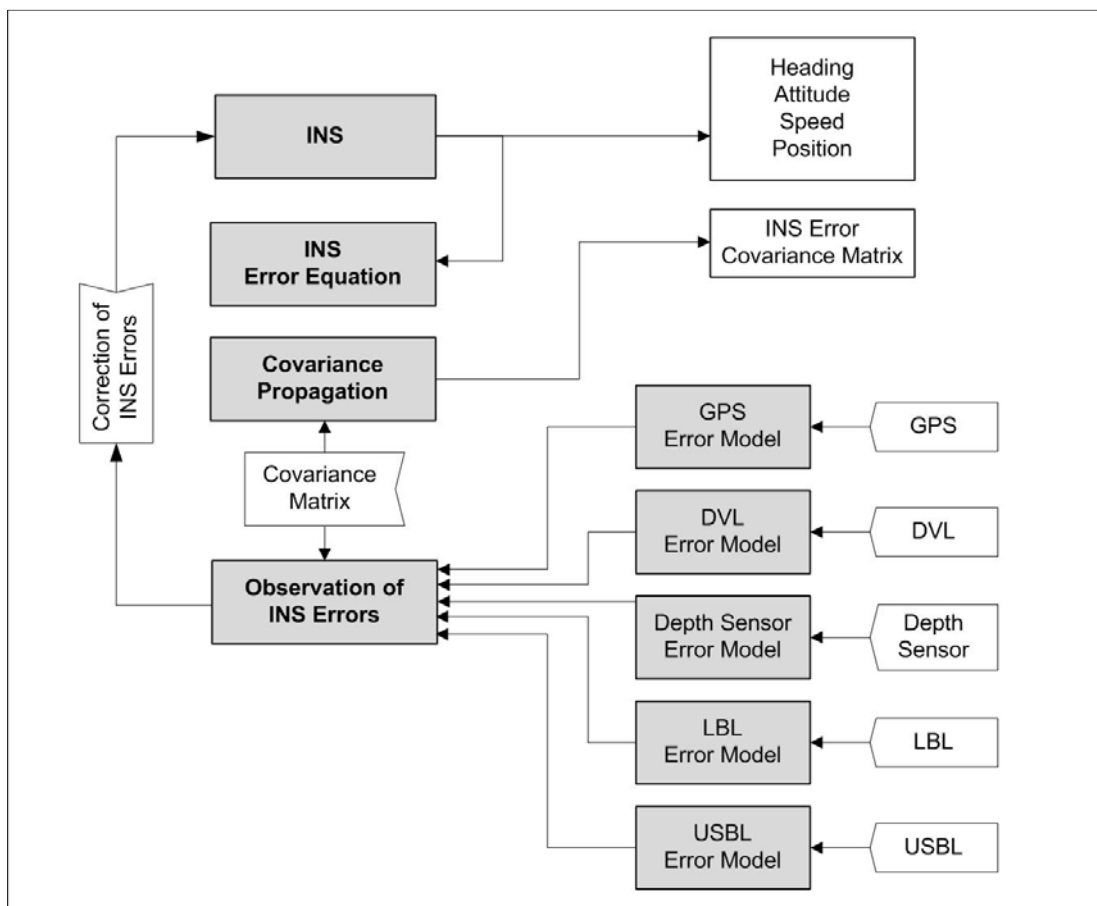


Figure 2.25: Schematic of the IXSEA Kalman filter; The Kalman filter uses external sensor data to improve the pure inertial system; The key component of this algorithm is the covariance matrix which contains all error estimates and correlations between different errors (based on IXSEA, 2009)

The combination of INS and GNSS which can be described as an integrated navigation system is one of the key components of a hydrographic mobile mapping system. It computes a high accurate and high dense trajectory containing position and attitude data which is needed to register measurements of echosounding and laser scanning systems as described in the next chapter.

2.4 Mobile Mapping Systems

The demand on high dense spatial 3D geo data rises exponentially with the availability of mapping sensors like multibeam echosounders, LiDAR systems, terrestrial laser scanners, and photogrammetric sensors. Also the corresponding IT architecture has to enable the user to handle the huge amount of data to derive the needed information or product. For several years LiDAR systems have been used to derive height and elevation models of the Earth's surface. They emerged in the 90's of the last century when the performance of GNSS and INS systems had achieved a sufficient accuracy to use them for geodetic surveys. At the same time the first multibeam echosounders were used in the hydrographic sector to map the wet part of the Earth. Both of these applications have shown the advantages of kinematic area based surveying techniques from an economic point of view and can be seen as pioneers of mobile mapping systems.

In general a mobile mapping system consists of different sensors for on the one hand the determination of the trajectory of a moving platform and on the other hand the detection of target objects (LI, 1997). Mobile platforms can be water vehicles, land vehicles or aircrafts which were moved above or along the target object. As navigation sensors often a combination of GNSS and INS systems are used which can be aided by external devices like Doppler velocity logs for hydrographic applications or odometers for land surveys. The object detection is usually done by photographic devices like CCD cameras and laser scanners. By the integration of navigation sensors that provide the trajectory of the platform and detection sensors that describe spatial attributes of the object, geo-referenced data can be derived immediately or in post-processing. Key roles in such a system play the time synchronization of all used sensors and the determination of spatial relationship, the lever arms and angular offsets between these sensors.

This chapter will discuss briefly the characteristics of mobile mapping systems and present some selected existing mobile mapping applications.

2.4.1 Characteristics of Mobile Mapping Systems

In the last decade a lot of different land vehicle MMS were developed for e.g. road monitoring and inventory surveys, 3D city models and railway track monitoring. Although the sensors which were used to build up a MMS are manifold one can summarize the key features of a mobile mapping system as follows:

- one platform arrangement for navigation and detection sensors
- determination of misalignments between sensors and platform
- time synchronization between all affected measuring devices
- determination of trajectory containing position and attitude of the platform
- time stamped detection of target objects and attributes
- data integration and georeferencing by transformations in time frame

Figure 2.26 shows a possible configuration of a mobile mapping system. In this case the object detection is performed by a 2D laser scanner which is connected to a GNSS receiver for supporting the scanner with a time signal for synchronization issues. The final trajectory is based on GNSS and INS measurements and computed in a separate computer. The final scan result is computed by merging the scan and trajectory data with respect to the time reference. Several transformations between sensor, body and global reference frames have to be done to receive a georeferenced 3D point cloud. Additional to the main components aiding sensors like CCD camera and odometer can be integrated in the system as well.

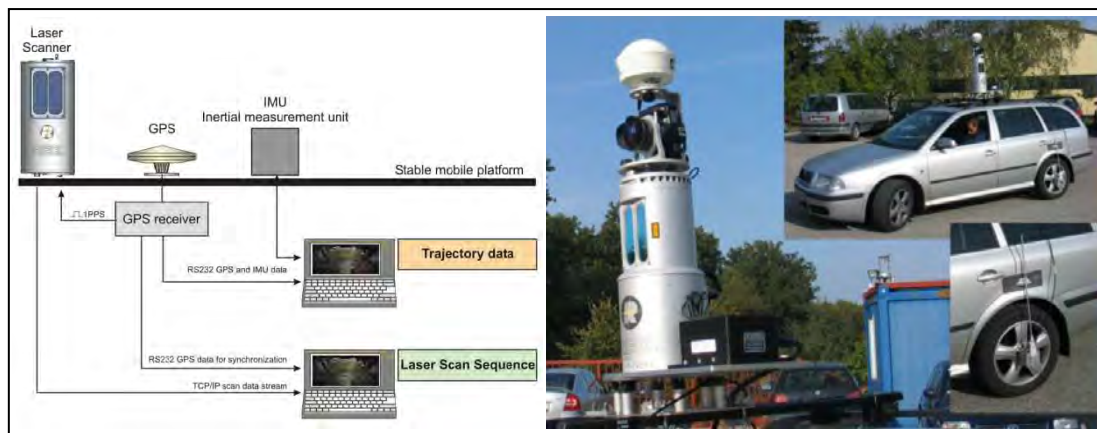


Figure 2.26: Schematic of a possible mobile mapping system (Left) and an example of a practical realization of a car based MMS (Right) (RIEGER et al., 2008)

The different sensors for positioning and attitude determination but also for the detection of target object parameters can be classified by their measurement principle and corresponding accuracy as shown in table 2.4.

Table 2.4: Different potential sensors of a mobile mapping system classified by accuracy and measurement dimension (based on HESSE, 2007)

Sensor Class / Sensor	Accuracy	Dimension	Type of Measurement
Position and Attitude			
GNSS - stand alone	Low	3D	kinematic Position
Differential GNSS	Medium	3D	kinematic Position
Precise Differentiell GNSS	High	3D	kinematic Position
Tacheometer	Medium-High	3D	local, kinematic Position
INS - true inertial	High→Low	3D	relativ, kinematic Position and Attitude Data
GNSS added INS	High	3D	kinematic Position and Attitude Data
Gyro compass	Medium	1D	Heading Information
Motion sensor	Medium	3D	Attitude Information
Odometer	High	1D	relative Distance/ Speed Information
USBL - Ultrashort Baseline	Low	2D / 3D	kinematic Position
DVL - Doppler Velocity Log	Medium	2D	Speed over Ground / Speed through Water
Object Detection			
CCD-Camera	Medium-High	2D	Picture Coordinates
Profile Laser Scanner	Medium-High	2D	local Object Coordinates
Terrestrial Laser Scanner	Medium-High	3D	local Object Coordinates
Multibeam Echosounder	Medium-High	2D	local Object Coordinates
Sidescan Sonar	Medium-Low	2D	local Object Coordinates

In contrast to static surveying methods where the position of the detection sensor is clearly defined, kinematic surveying e.g. mobile laser scanning is based on a moving platform where the position changes with time. It is significant to mention that the term “kinematic” means a relative motion between the surveying instrument and the target object, which also implements a static sensor and a moving target object. In the context of mobile mapping the sensor platform is moving whereas the target object is usually static.

As shown in figure 2.27 and table 2.4 a mobile mapping system can contain different sensors. To compute highly accurate geo-referenced datasets all sensors have to work in the same time frame which means that they have to be time synchronized. Usually the GNSS time scale is used for synchronization issues because of the high accuracy and stability of this method. GNSS receivers provide not only the output of time messages and the corresponding PPS pulses but support mostly an event marker input for external sensors. Nowadays a lot of sensors have interfaces to receive the PPS pulse and the time message of the GNSS receiver in order to synchronize their clock to an external clock. If they do not support the PPS pulse they usually output an event marker pulse which can be recorded and time stamped by the GNSS receiver. These time-stamped events can later be used to synchronize the external data in post-processing. Referring to HESSE (2007) there are different approaches to perform time synchronization which can be classified by the host of synchronization. With respect to figure 2.27 method A is based on the integration of external data into the data stream of the laser scanner. In this case the time reference is the scanner's internal time. Another method B can be an external realtime computer which is connected to a GNSS receiver, the laser scanner and all other external sensors. With the PPS pulse and the UTC message the GNSS receiver synchronizes the PC clock whereas the data of the other sensors is time stamped by the real-time computer. The third method C is based as initially described either on the processing of UTC message and PPS pulse by the scanner or the scanners event marker output to the GNSS receiver.

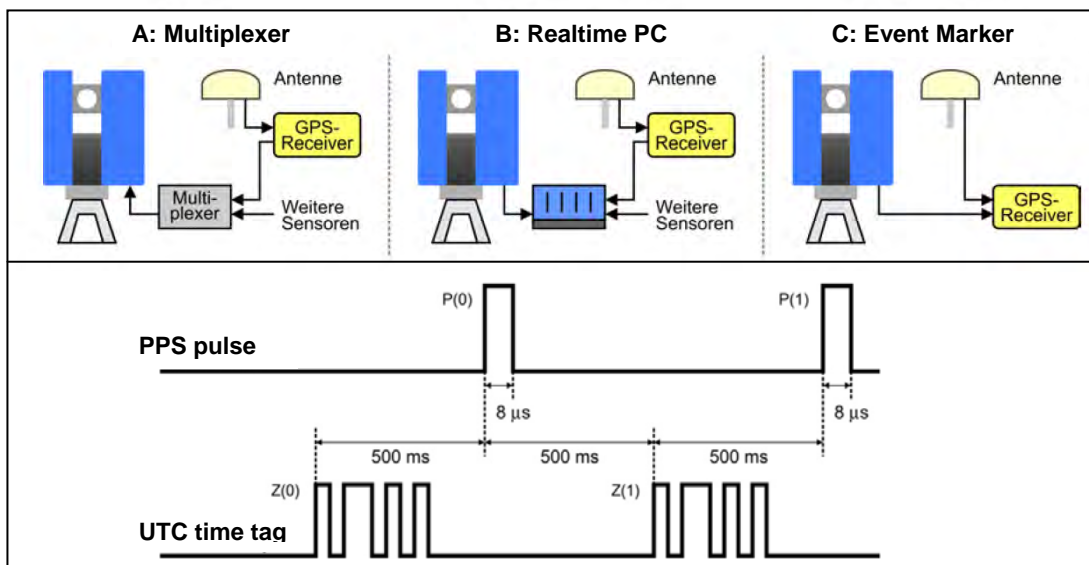


Figure 2.27: Different approaches of time synchronization between GNSS, laser scanner and external sensors (Top) and the relationship between a GNSS receivers PPS pulse and the corresponding UTC time message (Bottom) (HESSE, 2007)

Besides the time synchronization, a major role for the performance of a mobile mapping system plays the accuracy of the trajectory. Trajectory is defined as the path a moving object follows through space as a function of time and can be described as 3D positions and attitude information with respect to a certain reference frame. Figure 2.28 shows an example of a trajectory and the derived corresponding laser scan point cloud

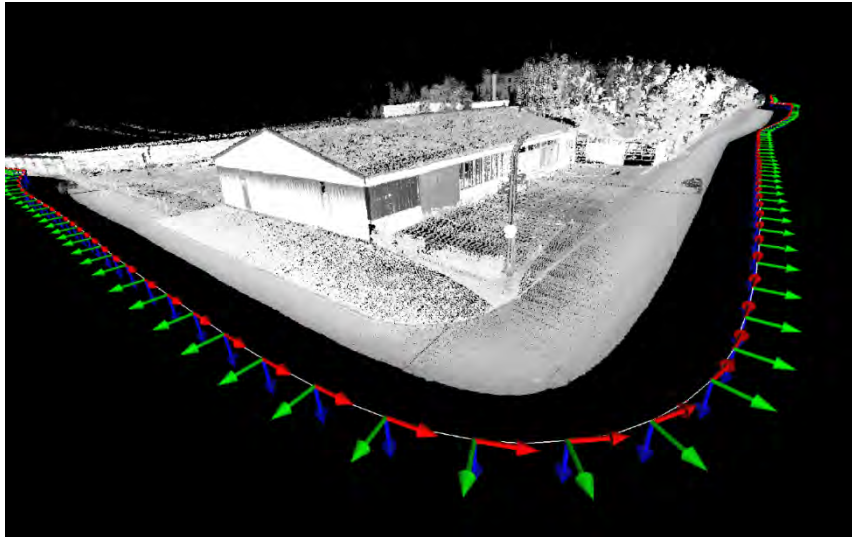


Figure 2.28: Geo-referenced scan data and trajectory (STUDNICKA et al., 2007)

For each measurement of a mapping sensor the absolute orientation of the sensor respectively of the sensor platform has to be known precisely in order to georeference this dataset correctly. Especially for the data processing of laser scanning and multibeam echosounding datasets the trajectory should meet following requirements (GRÄFE, 2007):

- absolute orientation for all mapping sensors with high frequency
- high accuracy in position and attitude data
- high consistency without data gaps or jumps

For these reasons the trajectory is mostly based on GNSS added INS measurements whereas GNSS measurements provide high long-term position accuracy especially in differential RTK mode and avoid the drifting effects of an INS. The high short-term accuracy of an INS is used in this constellation to smooth the noisy GNSS solution. As mentioned in chapter 2.3 the integration of GNSS and INS is usually based on the Kalman filter which compares INS and GNSS solution and computes corrections for inertial attitude, position and velocity in order to create an integrated navigation solution. The Kalman filter is a recursive filter and is mostly used to combine data measured by different sensors with different accuracies. In general the Kalman filter algorithm is divided in two steps. The first one estimates the system state, which consists of position, velocity, attitude etc., at a future time and is therefore called time update. The second step is called measurement update and consists of obtaining measurements and comparing them with the estimates. Whereas the time update looks into the future and estimates the state vector and its error behavior, the measurement update brings new obtained values of the state vector into the filter and improves the prior estimates (SCHULZ, 2007).

The Kalman filtered trajectory can be improved by applying the filter in forward and also in backward direction. This approach only works in postprocessing because all measurements of the trajectory have to be known by the filter. During the forward algorithm data is chronologically integrated and filtered by the Kalman filter whereas each calculated state vector is the result of treatment of all previous state vectors. The backward algorithm integrates the data anti-chronologically where each calculated state vector is the result of treatment of all state vectors that follow. After this procedure the results of both computations were merged and smoothed as shown in picture 2.29.

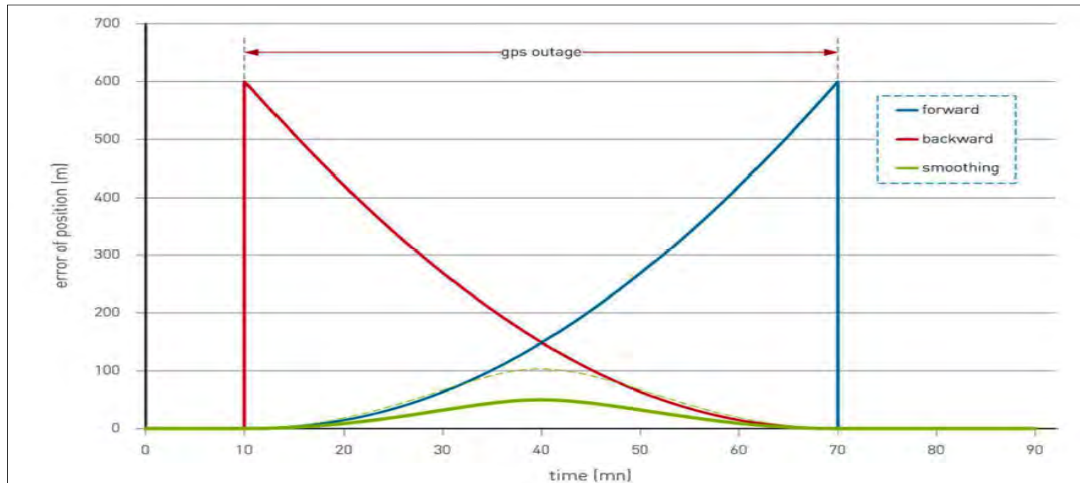


Figure 2.29: Example of the results of an combined forward and backward Kalman filter. A GNSS outage of one hour is simulated where the INS is in true inertial. The drift in position increases exponentially with time. The merged solution of both filter directions minimizes the error. (IXSEA, 2010)

To use the computed trajectory in order to geo-reference scan data as shown in figure 2.28, the relationship between the sensors reference frame and the global reference frame has to be known. Following reference frames have to be distinguished:

Table 2.5: Different coordinate reference frames in mobile mapping applications (based on GRÄFE, 2007)

Reference Frame	Point of Origin	Orientation of Coordinate Axes
Sensors Own Coordinate System - SOCS	Sensors center of measurement e.g.: acoustic center of echo-sounder, optical center of laser scanner	Depends on the principle of measurement e.g.: laser scanner: Z axis is axis of secondary sensor rotation, X axis is perpendicular to Z and points to horizontal zero orientation
Body Coordinate System - BODY	Defined point of origin on the mobile platform: on survey vessels the center of gravity	X axis points in the direction of movement Y axis is perpendicular to X and points to the starboard side of the platform, Z points in vertical direction either up or down
Topocentric Coordinate System - ENU/END	Defined point on the Earth's surface	X axis points to north, Y axis generally points to east, Z axis points in the direction of the ellipsoids normal vector
Global Coordinate System - ECEF	Origin of a geocentric ellipsoid	Axes of the reference ellipsoid, Z axis is the mean rotation axis of the earth, X axis points to the meridian of Greenwich

The relationship between these different coordinate reference frames is pictured in figure 2.30. To geo-reference data of a mapping sensor, it has to be brought into the same reference frame than the trajectory is based on. Then for each measurement epoch the information of the trajectory can be applied to the sensor measurements.

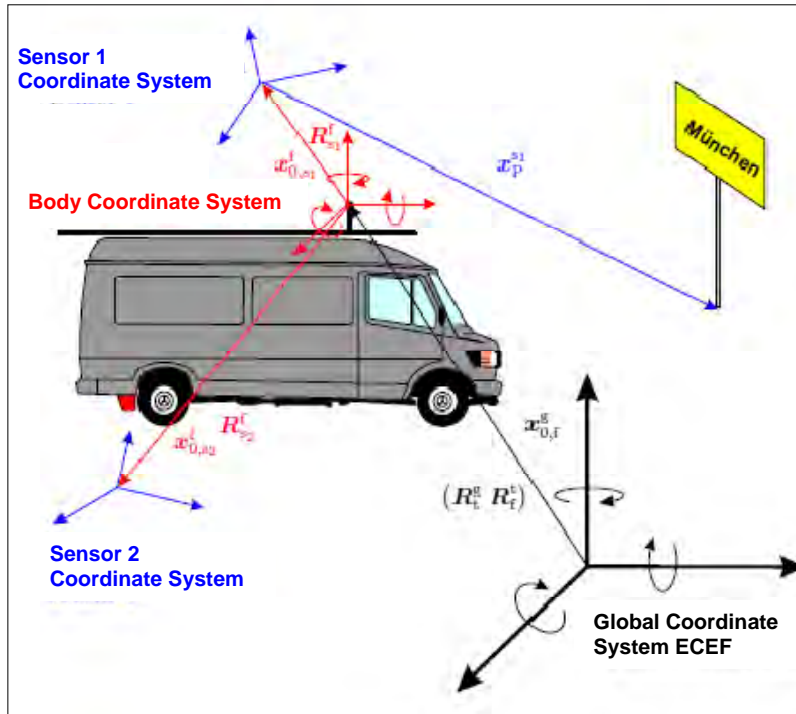


Figure 2.30: Relationship of different reference frames used in mobile mapping applications for geo-referencing sensor data in a global reference frame (GRÄFE, 2007)

The transfer of sensor coordinates into a global reference frame contains several transformations between the effected coordinate systems can be summarized whereas the lever arms and the angular misalignments between the sensors and the platform were taken into account.

- Transformation of sensor coordinates into the body reference frame contains the translations between the different points of origin which are derived on the initial measurement. Additionally the angular misalignments between the sensor and the body system in heading roll and pitch direction have to be applied as rotations in order to receive object coordinates in the body reference frame.
- The next transformation is designed to transfer the body coordinates into a local topocentric reference frame. For this computation the attitude data of the trajectory is used to reduce the coordinates by the determined heading, roll and pitch values of the platform. After this step the object coordinates are given in local east-north-up (ENU) System.
- The last transformation is then performed to transfer the object coordinates from the ENU system into the global reference frame ECEF system by using the position information of the trajectory.

The geo-referenced mapping results are mostly transformed into projected coordinates with respect to a local reference frame which makes further processing steps more feasible.

2.4.2 Overview of existing Mobile Mapping Systems

Over the last decade much effort was performed to set up and to evaluate different mobile mapping systems in the road and railway construction and monitoring sector. Nowadays different system developers offer all-in-one packages which consist of an integrated navigation and mapping solution including data acquisition software. However a countless number of customized mapping solutions have been developed in the scientific but also commercial sector. Many survey companies offer the full spectrum of mobile measurements. This chapter should give a rough overview of published existing MMS whereas some of these systems should be presented. HESSE (2007) has summarized the latest developments in mobile mapping systems classified by mapping system and publication as follows:

Table 2.6: Overview of developed and published mobile mapping systems classified by mobile platform (based on HESSE, 2007)

MMS	Mobile Platform	Mapping principle	Publications
MoSES	Car based	videogrammetric / profile scanner	Heister and Graefe (2004); Graefe (2003); Graefe (2007)
KISS	Car based	videogrammetric	Hoch et. al. (1995); Heister et. al. (1995); Sternberg et. al. (2001)
Visat	Car based	videogrammetric	El-Sheimy and Schwarz (1993); Schwarz et.al. (1993); Schwarz and El-Sheimy (1996)
GPSVan	Car based	videogrammetric	Novak (1990); Toth and Grejner-Brzezinska (2001); Grejner-Brzezinska and Toth (2002);
TeleInfo	Car based	photogrammetric	Tele-Info AG (2004)
Geomobil / GeoVAN	Car based	profile scanning	Alamus et. al. (2004); Talaya et. al. (2004); Alamus et. al. (2005)
CityGrid Scanner	Car based	profile scanning	GeoDATA (2005); Wack et. al. (2003); Sevcik and Studnicka (2006)
Road Scanner	Car based	profile scanning photogrammetric	Gandolfi et.al. (2008)
TruckMMS	Car based	profile scanning photogrammetric	Glennie (2007); Glennie (2009)
StreetMapper	Car based	profile scanning	Kremer and Hunter (2007); Haala et.al. (2009)
VISIMIND	Car based	profile scanning photogrammetric	Baz et.al. (2008); Kersten et.al. (2009)
miniUAV	Helicopter based	profile scanning photogrammetric	Jaakkola et.al. (2010)
LYNX Mobile Mapper	Multi platform	profile scanning	Ussyshkin (2008)
SwissTrolley	Rail based	profile scanning	Wildi and Glaus (2002); Glaus (2006)
SpaceTec	Rail based	profile scanning	SPACETEC (2007)
Fraunhofer Inst.	Rail based	profile scanning	Wirth (2007)
BoMMS	Vessel based	profile scanning	Alho et.al. (2009); Flener et. al. (2010)
Bay Hydrographer	Vessel based	profile scanning videogrammetric	van Rens et.al. (2007)

It is obvious that most work was done for car based applications in contrast to the vessel based systems. From these developments three selected applications will be presented in more detail.

The **Road-Scanner** is a car based mobile mapping system initially developed from point of road inventory surveys by the University of Bologna. The used van is equipped with an Applanix POSLV 220 navigation solution containing IMU and GNSS receivers.

For object detection there are four photogrammetric digital cameras and a FARO LS880 installed on the platform as shown in figure 2.31. The main task was to survey an urban area for underground project planning initiated by the municipality of the city of Bologna. The requirements on the survey result but also the permitted time frame was only affordable with a mobile mapping system. All inventory features like road signs, traffic lights, trees, buildings, private accesses etc. of the effected streets over a length of 7.5 kilometers had to be measured with sub-decimeter accuracies and documented comprehensively. The survey was conducted with speeds of up to 20km/h whereas the scanner with a maximum profile sampling frequency of 30Hz has created scan lines every 18 centimeters. Every 3 meters images have been taken by the photogrammetric cameras. To evaluate the mobile mapping results overall 60 discrete control points were measured additionally by classic methods like RTK GNSS and tacheometers. The results of the comparison between mobile and static datasets have shown the capabilities of the Road-Scanner in areas with good GNSS conditions without shadowing effects. Here mean differences of at maximum 5 centimeters have been reached. In certain street sections especially in the historic district of Bologna with urban canyons and resulting GNSS loss, the mean differences especially in the height component exceed 50 centimeters.

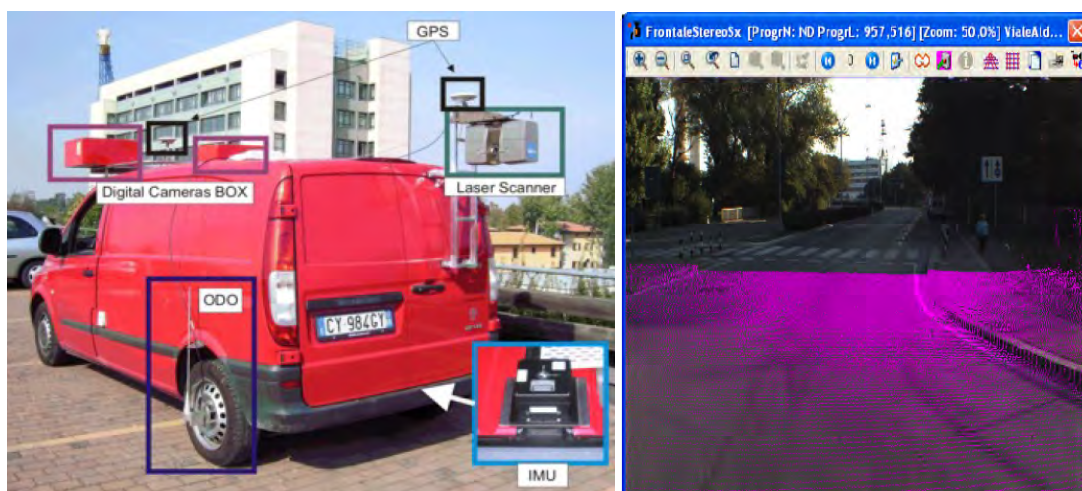


Figure 2.31: The mobile mapping system Road-Scanner (Left) and survey results as a combination of laser scanning and photogrammetry (Right) (GANDOLFI et al., 2008)

At totally different approach was used in Finland with the **mini-UAV** (unmanned aerial vehicle) platform for mobile mapping. In this research the Finnish Geodetic Institute has used a remotely controlled helicopter supplied with low-cost navigation and mapping sensors for topographic surveys. Especially from the point of forest measurements where the characteristics of individual trees have to be used to derive tree species, trunk and canopy characteristics and determination of biomass, this field of mobile mapping can be of importance for the Finnish economy which is based to a major part on the export of wood and paper.

The mini-UAV is equipped with a modular FGI Sensei which consists in this case of a NovAtel SPAN-CPT GNSS added INS navigation system, an Ibeo Lux and in addition a Sick LMS151 profile scanner. The laser scanners were selected because the combination of low costs and relatively high sampling rates and corresponding high dense data acquisition.

In addition the helicopter was equipped with a CCD camera for true color coding of the point clouds and a spectrometer supporting a spectral range between 397-1086nm for detecting changes in biomass. Although the helicopter is able to carry a payload of 7 kilograms, not all instruments can be used simultaneously during one flight. To evaluate the absolute accuracy of the mobile system reference data based on static terrestrial laser scanning has been acquired. This reference data set was also used to carry out the boresight alignment to determine the angular misalignments between scanner and IMU by comparing the mobile and reference data. After this alignment the absolute planimetric accuracy of the system was evaluated at 72 control points which consists of building corners and small single object like lampposts. Mean planimetric deviations of 35 centimeters with a standard deviation of 22 centimeters were calculated. The vertical accuracy is determined by the mean deviation in elevation of 3 centimeters with a standard deviation of 9 centimeters.

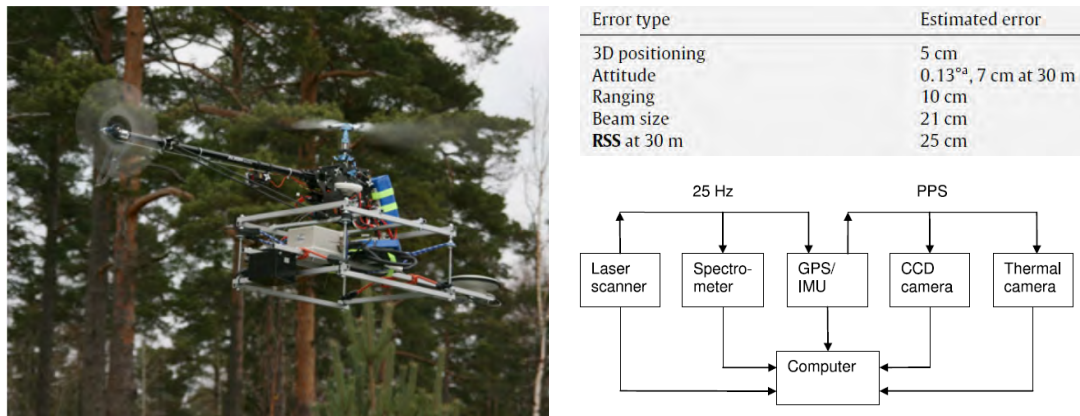


Figure 2.32: The mobile mapping system mini-UAV(Left), the error budget of this MMS (Top right) and a schematic of system components (Bottom right) (JAANKOLA et.al., 2010)

With this research which also covers automatic tree pole detection algorithms it was shown that also low cost sensors can reach sufficient results for the corresponding application. Especially the approach of multi-sensoral measurements to map not only 3D point but also special object attributes like biomass shows the potential of the cost saving mini-UAV.

One of the first vessel based mobile mapping applications which used video-grammetry and profile laser scanning was installed on the NOAA survey vessel **Bay Hydrographer** a few years ago. The approach was to setup a mobile system to map near-shore features like piers, rock, aids to navigation and coastline with two different technologies. The aim was the integration of video and laser scanning systems into a hydrographic sensor system to receive a continuous stream of geo-referenced image data and point clouds.

A complete package of two cameras (1600x1200 pixel resolution), a POSMV 320 GNSS-INS integrated navigation solution, a RIEGL LMS420i 3D laser scanner and data acquisition software were installed aboard of the survey vessel. The sensors were interfaced and time synchronized. As shown in figure 2.33 all sensors were mounted as close to each other as possible on a fixed stable platform on the port side of the vessel roof.

A calibration was carried out by using 23 land surveyed control points at the shoreline in order to determine the angular misalignments sufficient enough. The first part of the test had dealt with automatic video recognition of buoys alongside a channel. The software was trained to recognize the aids to navigation by their reflectivity signature which worked well during the tests. The second part was conducted to evaluate the performance of a long range laser scanner in profile mode. The maximum measurement range is 1000 meters with a corresponding measurement rate of 8000 points per second. The proper time synchronization was guaranteed by interfacing the POSMV unit with the scanner.



Figure 2.33: The vessel based mobile mapping system Bay-Hydrographer (Top left), the mounting bracket and mapping sensors (Top right) and first survey results of the battleship Wisconsin (Bottom) (VAN RENS et al., 2010)

The data of the navigation system and the scanning system were recorded separately and afterwards post-processed. The trajectory was computed by the post-processing software of the POSMV and merged with the scan data in POSPC.

This first investigation of mobile laser scanning in combination with videogrammetry on a survey vessel has shown the capabilities in the hydrographic sector. The integration of additional sensors into a existing multi-sensor system like a survey vessel is straight forward due to the fact that also multibeam echosounders or side scan sonar are used over years as wet mobile mapping systems. The combination of classic hydrographic sensors like echosounders and new optical devices like laser scanners can be used to support the total hydrographic survey solution.

3. Realization of a Mobile Mapping System

As shown in chapter 2 a mobile mapping system consists of a mobile platform where several high technology sensors are mounted on. The sensors have been integrated and calibrated to build up a complete survey solution. This chapter presents these initial steps and starts with the introduction of the mobile platform the survey vessel “Deepenschriewer III” and the sensors which were used for this thesis. The following sections show the calibration procedure which was performed to determine the spatial relationship between sensors and platform and consists of lever arm measurements and boresight alignment. Finally first survey results will be discussed from the point of remaining systematic problems which establish the bridge to chapter 4 where the data processing will be presented.

3.1 Survey Platform and Sensors

Since this thesis is originated in cooperation between Hamburg Port Authority (HPA), HafenCity University (HCU) and Northern Institute of Advanced Hydrographics (NIAH) a certain repertory of survey vessels and sensors were available to choose from.

The HPA as the authority of the Port of Hamburg is responsible for the maintenance of the land and water infrastructure of the port area. This contains not only the construction of port facilities like e.g. quay walls, berthing areas, bridges etc. but also the vessel traffic management and the water depth maintenance. For this reason four survey vessels equipped with different multibeam echosounders, RTK GNSS equipment and inertial navigation systems perform all-the-year hydrographic surveys to monitor the change of water depths based on sedimentation and erosion. Additionally all routine dredging activities in the port area are monitored and controlled by these surveys.



Figure 3.1: Survey vessels *Deepenschriewer I – IV* (numbered from top left to bottom right) of the Hamburg Port Authority

The vessels pictured in figure 3.1 differ in size and in draught because the different port areas respectively survey conditions require different vessel properties. Whereas the smallest vessel Deepenschriewer IV with a length of 11.5 meters, a width of 3.7 meters, a draught of 80 centimeters and height above water level of 2.5 meters is well suited to survey narrow canals and very shallow areas, the Deepenschriewer II with dimensions of 27.5 meters in length, 8.60 meters width and 1.40m draught is designed to survey in more rough sea conditions which can be found on the river Elbe.

The NIAH which was established in 2006 is a public private partnership between the HCU and different private companies, offers services for public and private institutions in the fields of hydrographic research, training and consulting. With a wide spread range of hydrographic sensors and software applications NIAH performs by order special survey tasks on an international level. At the HafenCity University which offers an IHO certified Level-A master course NIAH supports the hydrographic education with equipment and know-how. Maybe for this reason one of two survey boats is called Level A and is shown in figure 3.2 below. The vessel is characterized by its small size 8 meters length, 2.5 meters width and a draught of only 35 centimeters and the capability to equip the platform modularly, dependant on the survey task different sensors can be mounted and integrated to setup a multi-sensor platform.



Figure 3.2: Survey boat "Level A" of the NIAH during a survey. As a standard sensor a RESON Seabat 8101 multibeam echosounder is bow-mounted

The requirements on a survey vessel with respect to this thesis can be summarized as follows, respectively the vessel should:

- Provide a stable behavior in waters with rough survey conditions
- Provide enough space on the roof to mount different sensors
- Be small enough to reach also secluded port areas
- Be available during the test period

At the end the decision was to use the Deepenschriewer III as mobile mapping platform because on the one hand this vessel provides the best behavior in water and enough space for the sensors to mount and on the other hand the size and draught is a suitable for most survey tasks in the port. The dimensions of the vessel are 17.2 meters length, 4.9 meters width and 1.4 meters draught.

As sensors for this investigation two different laser scanners, one INS and two attitude and heading sensors were available to setup a system. The major properties of both laser scanners are summarized below whereas the complete data sheets are attached in annex A-1.



Figure 3.3: RIEGL VZ400 laser scanner

RIEGL VZ-400

Type of Laserscanner:	3D hybrid scanner
Distance Measurement:	Direct-TOF
Range:	300m in high speed mode 500m long range mode
Range Accuracy:	5mm at 100m range
Field of View:	100° vertical / 360° horizontal
Effective Meas. Rate:	125000 meas./sec in high speed mode 42000 meas./sec in long range mode
Scan Speed:	3 lines/sec to 120 lines/sec
Vertical Angular Steps:	$0.0024^\circ \leq \Delta\varphi \leq 0.288^\circ$
Horiz. Angular Steps:	$0.0024^\circ \leq \Delta\varphi \leq 0.5^\circ$
Beam Divergence:	0.3mrad



Figure 3.4: Z+F IMAGER 5006h laser scanner

Z+F IMAGER 5006h

Type of Laserscanner:	3D panorama scanner
Distance Measurement:	AMCW
Range:	79m (ambiguity interval)
Range Accuracy:	ca. 2-3mm (range noise at 50m)
Field of View:	310° vertical / 360° horizontal
Effective Meas. Rate:	up to 1Mio meas./sec
Scan Speed:	up to 50 lines/sec
Vertical Angular Steps:	$0.0018^\circ \leq \Delta\varphi \leq X$
Horiz. Angular Steps:	$0.0018^\circ \leq \Delta\varphi \leq X$
Beam Divergence:	0.22mrad

Although the IMAGER 5006 system provides more accurate distance measurements, higher angular resolutions and a panorama field view the deciding properties for hydrographic applications are the maximum measurement range in combination with the scan speed described by scan lines per second. Both delimiting factors influence a survey planning drastically. For these reasons the RIEGL system was used for this thesis. From point of navigation systems the decision was either to use a GNSS added INS solution or a GNSS solution combined with an attitude and heading sensor. Following systems were available for the tests:



Figure 3.5: TSS MAHRS-Surface attitude and heading sensor

TSS MAHRS-Surface

Type of Unit:	Attitude and heading sensor
Technology:	Mechanical gyros and pendulum accelerometers
Heading Accuracy:	$\pm 0.2^\circ$ secant latitude
Roll / Pitch Accuracy:	$\pm 0.03^\circ$
Output Rate:	up to 200Hz



IXSEA OCTANS

Type of Unit:	Attitude and heading sensor
Technology:	Fiber optic gyros and pendulum accelerometers
Heading Accuracy:	$\pm 0.1^\circ$ secant latitude
Roll / Pitch Accuracy:	$\pm 0.01^\circ$
Output Rate:	up to 200Hz

Figure 3.6: IXSEA OCTANS
Attitude and heading sensor



IXSEA HYDRINS

Type of Unit:	Inertial Navigation System
Technology:	Fiber optic gyros and pendulum accelerometers
Position Accuracy:	0.6 Nm/hr = 0.01° /hr (free inertial) 1m after 2min no GNSS aiding 20m after 5min no GNSS aiding GNSS aided: 3 times better than GNSS
Heading Accuracy:	$\pm 0.02^\circ$ secant latitude
Roll / Pitch Accuracy:	$\pm 0.01^\circ$
Output Rate:	up to 200Hz

Figure 3.7: IXSEA HYDRINS
Inertial navigation system

As shown in chapter 5.1 the performance of a mobile mapping system from point of measurement point accuracies depends to a major part on the heading accuracy of the platform. But also the position and height accuracy is of high importance. Only a navigation system which combines the advantages of each contained sensor reach the highest possible performance. For this reason a combination of IXSEA HYDRINS (figure 3.7) and the RTK-GNSS solution is used for this work instead of the attitude and heading systems shown in the figures 3.5 and 3.6. The GNSS system which is shown in figure 3.8 consists of a geodetic dual frequency receiver in rover mode combined with a geodetic antenna and supports GPS as well as GLONASS signals. Together with Trimble VRS-Now differential correction service the system provides centimeter accuracies.



TRIMBLE SPS851, Zephyr II

Horizontal Accuracy:	$\pm <1\text{m}$ SBAS positioning $\pm 0.25\text{m} + 1\text{ppm}$ (code differential pos.) $\pm 0.01\text{m} + 1\text{ppm}$ (RTK)
Vertical Accuracy:	$\pm <5\text{m}$ SBAS positioning $\pm 0.50\text{m} + 1\text{ppm}$ (code differential pos.) $\pm 0.02\text{m} + 1\text{ppm}$ (RTK)
Position Output Rate:	up to 20Hz
Data Outputs:	NMEA, GSOFF, 1PPS Time Tags

Figure 3.8: TRIMBLE SPS851 GNSS receiver and TRIMBLE Zephyr II antenna

Since the Deepenschriewer III was already equipped with a RESON Seabat 8101 multibeam echosounder, which is shown in figure 3.9 this system was also used for all depth measurements related to this thesis.



RESON Seabat 8101

Technology:	Beamformer with phase and amplitude bottom detection
Additional Features:	SideScan capability
Operating Frequency:	240kHz
Swath Coverage:	150°
Number of Beams:	101 equiangular
Beamwidth – along:	1.5°
Beamwidth – across:	1.5°
Measurement Rate:	up to 40 pings/sec

Figure 3.9: RESON Seabat 8101 multibeam echosounder

As discussed in chapter 2.4 the main features of a mobile mapping system should be mounted close to each other on a stable single bracket. This procedure improves not only the accuracy of lever arm determination, additionally the spatial relationship between the sensors especially the angular misalignments will not be disturbed when the platform is unmounted for example at the evening and remounted again at the next morning. As shown in figure 3.10 a customized bracket was produced which spent enough space for the laser scanner, INS and GNSS antenna.

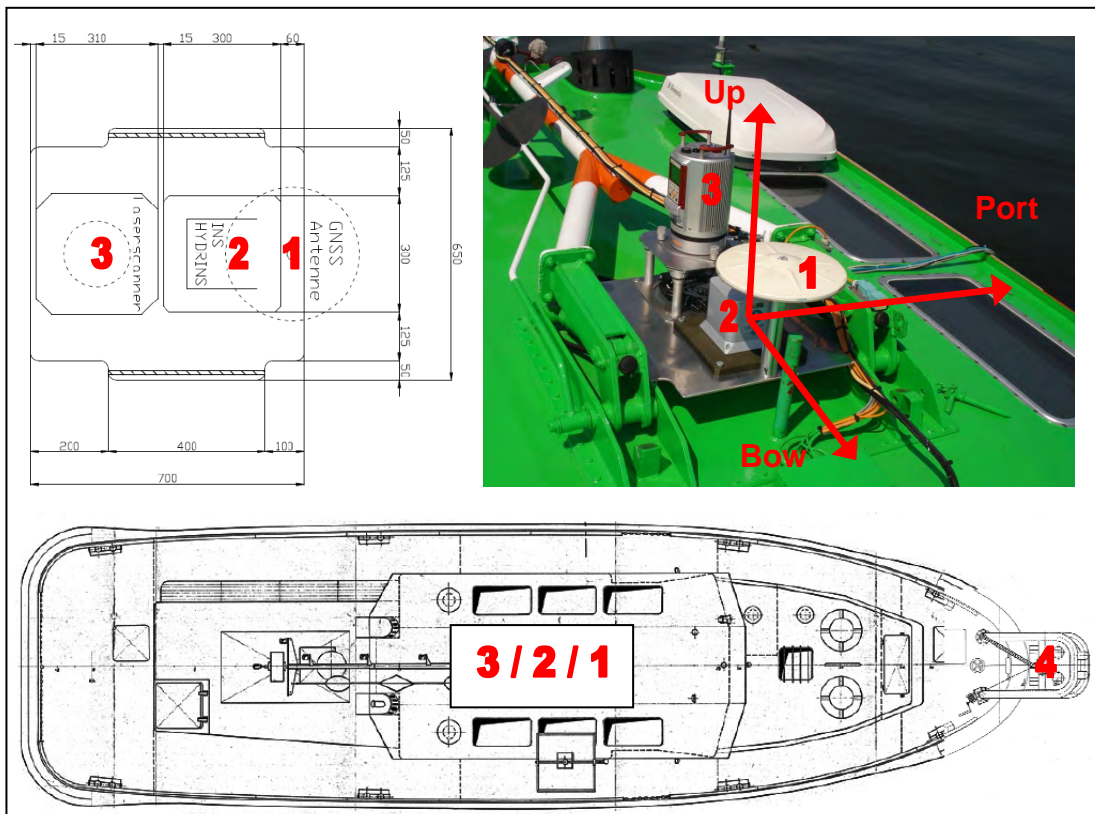
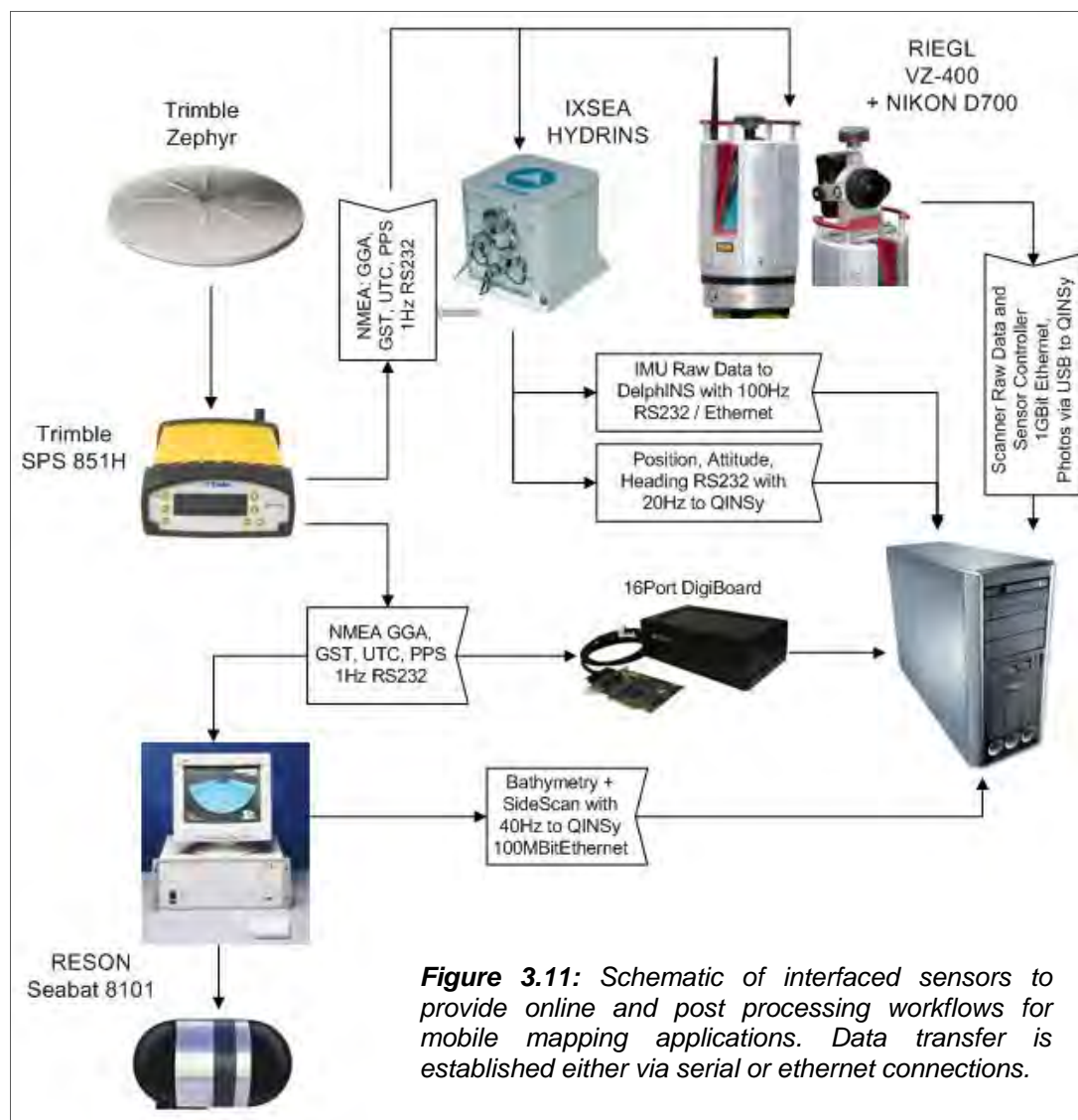


Figure 3.10: Sensors for mobile mapping mounted on a single bracket on the roof of the Deepenschriewer III, 1-GNSS antenna, 2-INS, 3-Laser scanner, 4-Multibeam transducer; (Top left) Construction drawing of the bracket; (Top right) Photograph of the installation; (Bottom) Construction drawing survey vessel – top view

The bracket was mounted on the roof of the vessel near the vessels center line and almost vertical above the vessel's center of gravity at a height of 3.5 meters above water level. The transducer of the multibeam echosounder is bow mounted and located 80 centimeters below water line.

3.2 Sensor Integration and Interfacing

After the sensors were mounted they had to be properly interfaced with each other in order to assure time synchronization and data acquisition of all sensors. The main focus was to setup a system which provides online data processing respectively online mapping. To evaluate the online results a workflow had to be established which also supports postprocessing of navigation and laser scan data. Figure 3.11 shows schematically the data transfer between the sensors. The GNSS receiver provides the PPS signal and corresponding time messages to keep the multibeam, the laser scanner, the INS and the heart of the system, the data acquisition PC in the same time frame.



The online processing part is done by the powerful data acquisition software QPS QINSy. QINSy provides hundreds of drivers to interface sensors from hydrographic, dredging and positioning applications. Furthermore for some sensors QINSy offers special controllers for changing sensor and measurement parameters during the survey out of the data acquisition tool.

Although the processing part is presented in the next chapter one has to keep in mind that every effected sensor has to provide its data twice, first for the online processing and second for post processing.

As an example the GNSS aided INS was configured to output a binary protocol called “Seapath MRU binary format 11 (UTC)” to QINSy with 50 Hz. This data message contains information about position, attitude, heading and time of course. QINSy uses this information to compute the trajectory and to register multibeam and laser scan data online. For post-processing the HYDRINS additionally outputs raw data with 100Hz which contain e.g. raw rotation rates and accelerations and is stored separately on the data acquisition PC. This raw data is later used to compute the trajectory in post-processing. The same procedure has to be enabled with the scan data. Although QINSy requires the online data stream of the scanner, the RIEGL processing tools need the scanners raw data which were stored for this thesis directly on the scanners hard disk.

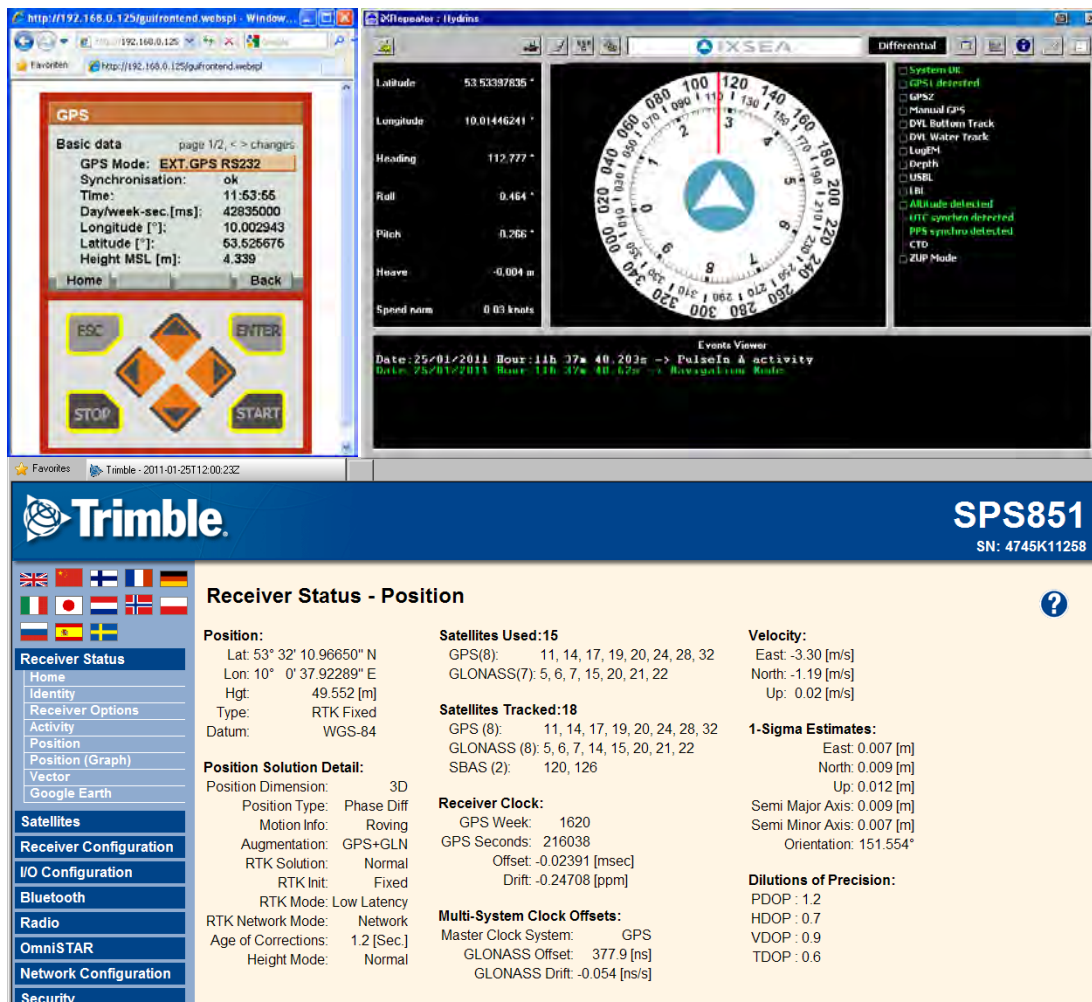


Figure 3.12: User interfaces of RIEGL VZ-400 (Top left), IXSEA HYDRINS (Top right) and TRIMBLE SPS851 (Bottom) either as web interface or controller application

To monitor and to control each measurement device the sensors were connected additionally to the data acquisition PC via network. Almost all new hydrographic sensors offer either a web interface or a controller application to keep track of the sensor's behavior as shown in figure 3.12.

Here all survey relevant parameters can be changed, the I/O dataflow can be monitored and errors or problems can be detected immediately.

The sensor integration and interfacing was finished by performing a test survey although the lever arms and the angular misalignments were only rough estimates at this stage.

3.3 Determination of Lever Arms

As described in chapter 2.4 the measurements of each sensor have been transformed at first from the sensors coordinate system to the body coordinate system. The body respectively vessel coordinate system is generally defined by the vessels center of gravity (COG). The center of gravity is the point at which the whole weight of a body is said to act. Since this theoretical point is usually not known precisely for survey vessels one has to estimate the position as good as possible. Therefore in most cases the COG is defined as a point in the middle of the center or keel line of the vessel at a height near the water line. The X axis is even the vessels center line, the Y axis is perpendicular to X and points to starboard and the Z axis is vertical to X and Y. The plane which is spanned by X and Y should be parallel to the water surface when the vessel is leveled in a stable static state. The locations of all sensors with respect to the vessels coordinate system termed as lever arms have to be determined precisely. This lever arm determination which is also known as initial measurement is usually performed by tacheometric measurements or nowadays by terrestrial laserscanning when the vessel is out of water fixed on a slipway as shown in figure 3.13. By measuring the shape of the vessel the center line and the COG can be computed. Additionally several physical control points were measured which realize and represent the body coordinate system. The positions of all hydrographic sensors were determined with respect to this *a priori* body system.



Figure 3.13: Initial measurement procedure to determine the lever arms off all integrated sensors with respect to the vessel's reference frame; Deepenschriewer III on a slipway in former times (Left); Lever arm measurement in water (Right)

A Priori in this context means that during the land measurements the behavior of the vessel in water is unknown. Because of disadvantageous distribution of mass in the vessel a permanent heel can be produced which causes an angular bias between the vessels coordinate system and a horizontal plane defined by the water surface.

For this reason the initial measurement is partially repeated when the vessel is back in the water and leveled in a stable state. The control points were measured and the results of the land measurements were transformed to this new realization of the body system. Figure 3.14 depicts the results of the initial measurement in combination with the new measured lever arms of laser scanner, INS, and new GNSS antenna. This figure is attached in Annex A-2.

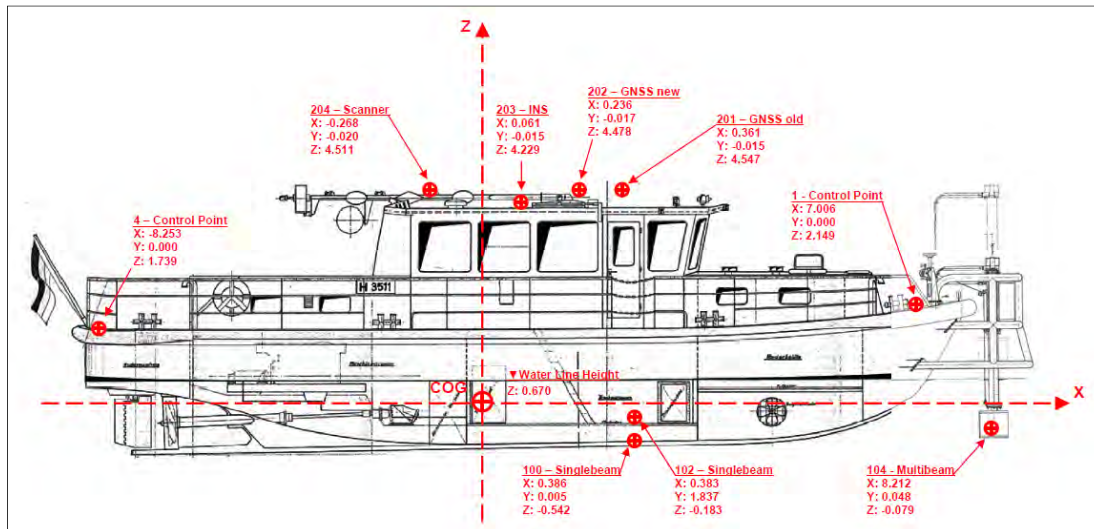


Figure 3.14: Determination of lever arms by initial measurement. The spatial relationship between all sensors to each other is given with respect to the vessels reference frame.

It is important to mention that the positions of laser scanner, INS and GNSS antenna on the mounted bracket were measured when the vessel was in water. As the Deepenschriewer III is in use for several years the COG and all other sensors e.g. multibeam transducer and all control points were determined several times in the past, it was not necessary to repeat the whole procedure to save time and costs. The positions of the “new” sensors have been determined with respect to the vessels coordinate system by placing the tacheometer on the vessel and switching off the internal compensators. The coordinates for each sensor have to be implemented in the data acquisition software QPS QINSy for online processing. At this stage it is essential to determine the angular misalignments in roll and pitch of the attitude sensor, in this case the IXSEA HYDRINS which will be presented in the next sub-chapter.

3.4 Calibration of Angular Misalignments

This chapter deals with the determination of the angular misalignments of the inertial measurement unit and the laser scanner with respect to the vessel's coordinate system. At first the residual angular differences between the body and the IMU frame in roll, pitch and heading have to be determined which is usually performed by a reference measurement combined with the lever arm measurement.

The next step is to calibrate the angular offsets between the scanner's own coordinate system and the body system. This is generally done by a special calibration procedure whereas different laser scan survey lines are measured. The online registered point clouds of these survey lines will be compared with each other and detected angular difference will be used to compute angular misalignments.

3.4.1 Angular Offsets between IMU and Vessel Frame

Once the IMU in this case the IXSEA HYDRINS is mounted and interfaced onboard of the vessel not only the position but also the rough and fine misalignments of the sensor with respect to the vessels reference frame must be determined. This section describes the procedure to evaluate these parameters. There are two different types of misalignment (IXSEA, 2009). The first one is the rough misalignment, means the rough orientation of the IMU reference frame with respect to the vessels reference frame. It is possible to mount the HYDRINS in every position and orientation on the vessel but the sensor has to know the axis inversion. However, as shown in figure 3.10 the IMU X axis is almost parallel to the vessel X axis, means no axis inversion. The second type of misalignment is the fine misalignment which is created by residual angular differences between the vessel reference frame and the HYDRINS reference frame. These angular offsets are defined as roll, pitch and heading misalignments and have to be determined exactly as depicted in figure 3.15.

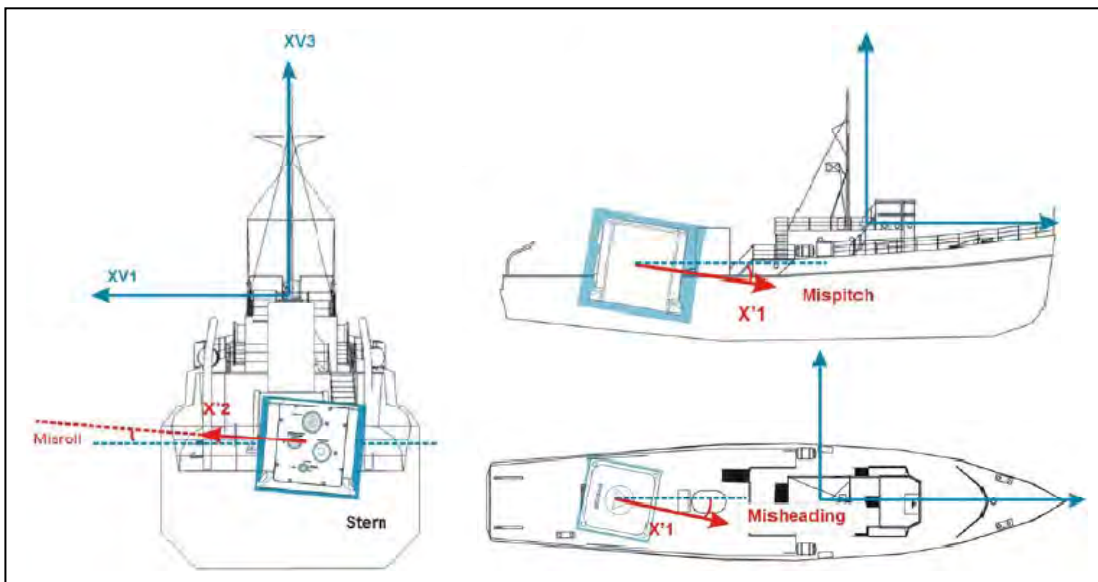


Figure 3.15: Angular misalignments between IMU frame and vessels coordinate system described by Misroll (Left), Mispitch (Top right) and Misheading (Bottom right) (IXSEA, 2009)

IXSEA proposes two different approaches to evaluate the fine misalignment. The direct measurement, which means measuring the three angular offsets of the IMU with respect to the vessel reference frame with e.g. a total station. Alternatively an indirect measurement is possible by using a different IMU. In general these measurements should be done on land by using a dry dock or a slipway to bring the vessel in a fixed position and attitude. Because of logistic and economic reasons as mentioned before it wasn't possible to perform the misalignment measurement on land and therefore the fine alignment was done by two separate measurements in water. At first the heading misalignment was determined. In order to do so the survey vessel was moored directly at a special part of a quay wall in the harbor basin "Hansahafen". The azimuth of the quay wall was previously measured precisely from landside. The straight part of the vessels port side hull was accurately adjusted to the quay wall and over a period of time the heading of the HYDRINS was recorded.

Because of the assumed symmetric vessel hull this procedure was repeated with the starboard side of the vessel. The figures below show the results of both measurements.

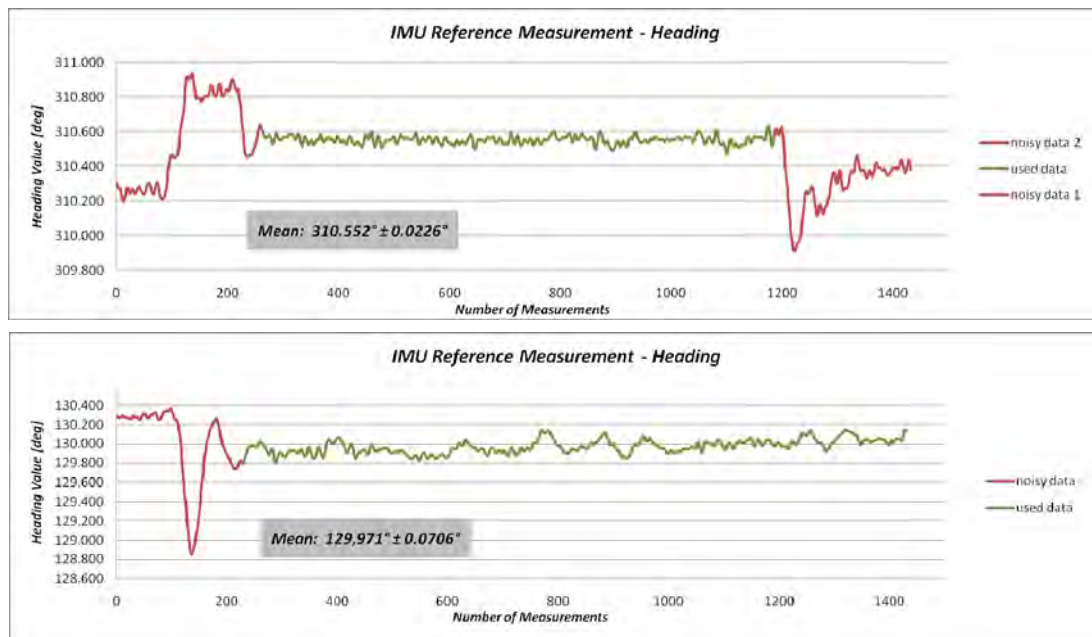


Figure 3.16: Determination of the heading misalignment of the IMU with respect to the vessels coordinate system. The survey vessel is at first orientated in north-westerly direction (Top) and afterwards the vessels bow points to south-easterly direction (Bottom)

Table 3.1: Calculation of the heading misalignment between IMU and vessel frame

	A-O/W [deg]	A-W/O [deg]	Check
Azimuth „Oswaldkai“ =	310.050	130.050	180.000
Mean =	310.552	129.971	180.581
Difference =	0.291		
Mean reduced =	310.262	130.262	180.000
Heading misalignment =	-0.212	-0.212	
Heading reduced =	310.341	129.759	180.581

The diagram on the right shows a vessel's hull (red lines) and the IMU's coordinate system (blue lines). It illustrates the heading misalignment between the two systems, with a misalignment angle indicated.

As pictured in figure 3.16 the measurement where the vessels X axis points to the south-east direction is noisier than the first one which is also shown by the computed mean values and their standard deviations. The problem was caused by changing tide and weather conditions incl. small waves during both measurements. Nevertheless a significant estimate for the heading misalignment is determined.

It is clear that this procedure is not as straight forward as the heading determination on a slipway. Here the azimuth of the keel line can be determined with higher precision whereas the IMU measures a certain heading value without disturbance from waves, tide and wind effects. Both values can be compared with each other in order to calculate the heading misalignment.

However, one has to keep in mind that the heading value measured by the IMU is mainly used to compute the position of a sensor e.g. the laser scanner with respect to the global reference frame. Let assume the distance between the positioning system and the mapping sensor is 10 meters and the heading misalignment was determined with an accuracy of 0.05° , then the absolute position of the sensor is biased around $\pm 9\text{mm}$ in Y direction of the vessels coordinate system.

In the installation used for this thesis the distance between the laser scanner and the GNSS antenna is around 50 centimeters and the distance between multibeam transducer and GNSS antenna is 8 meter, so the effect of a small remaining heading misalignment on the determination of sensor position can be ignored.

It is also clear that the heading value is used to determine the positions of measured target points which can lead to a relatively large bias on object side with ranges of up to 400 meters. But the tiny small residual effect of an IMU heading misalignment is calibrated together with the heading misalignment of the mapping sensor.

Although the calibration procedure is presented in the next sub-chapter it is worth to point out that the determined heading misalignment of the mapping device e.g. multibeam echosounder or laser scanner contains not only the angular offset between the sensors X axis and the vessels X axis but also the small unknown residual angular offset of the IMU. For this reason the heading misalignment was performed accurate enough and the angular offset was set in the HYDRINS to reduce all measured heading values.

A similar approach was used to determine the roll and pitch alignments. In combination with the initial lever arm measurement as described in chapter 3.3 the survey vessel was brought into survey conditions in calmer waters without tide, current, wind and wave effects. The aim was to keep the vessel floating as stable as possible and to decrease the heave, roll and pitch effects to minimum over a certain period of time. During this time period the motion data for roll and pitch were recorded and afterwards processed to get precise mean values for each of them.

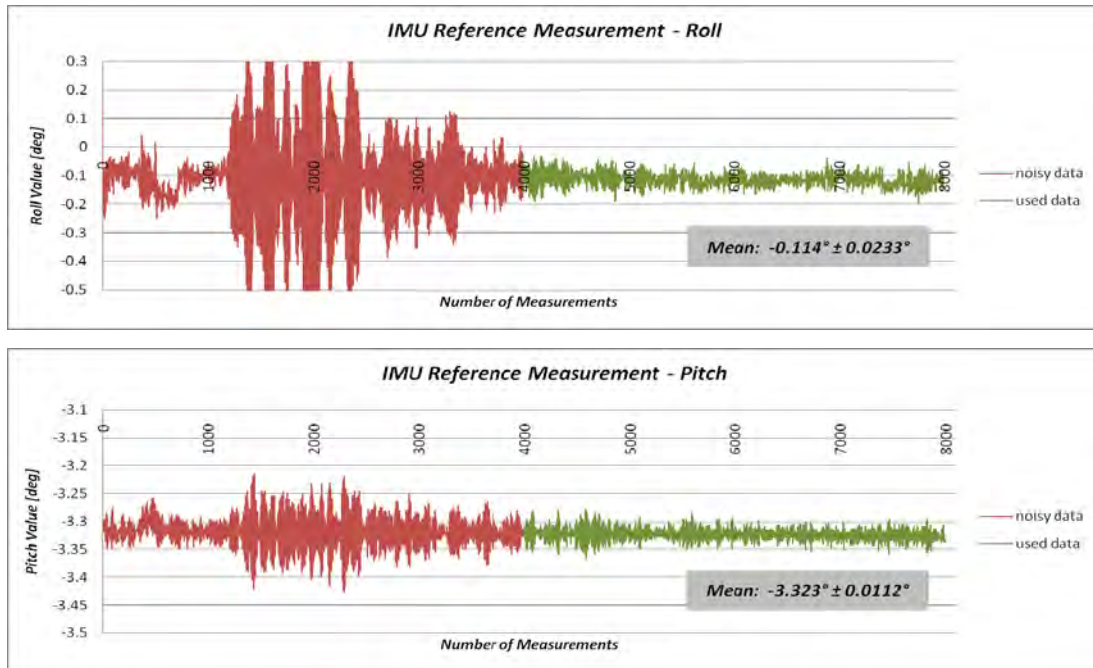


Figure 3.17: IMU reference measurement to determine angular offsets in roll (Top) and pitch (Bottom) direction between the IMU and the vessels reference frame.

By applying the determined mean values for roll and pitch misalignment in the HYDRINS which can be considered as a reset to zero, the IMU's reference frame is aligned to the vessel's reference frame which is realized by the initial lever arm measurement. The following required procedure is called sensor calibration or boresight alignment and is performed to compute the angular misalignments of the mapping sensors with respect to the body frame of the vessel.

3.4.2 Angular Offsets between Mapping Sensor and Vessel Frame

As described in detail in chapter 3.4.1 not only the angular misalignments of the IMU but also of the mapping sensors have to be determined with respect to the vessel reference frame. These small angular offsets in roll, pitch and heading direction describe residual rotations of the scanner or the multibeam transducer around the vessels X, Y and Z axis. To determine each of these misalignments survey lines have to be measured and processed with the data acquisition tool QPS QINSy. For this procedure it is recommended that all lever arms respectively the coordinates of all sensors with respect to the vessel coordinate system are defined in QINSy and the fine alignment of the IMU is finished.

To determine angular offsets of the mapping sensors different already processed point clouds are needed to derive the desired value from. For each of these misalignments a special survey line configuration is needed to detect systematic biases in two or more corresponding point clouds of the laser scanner or the multibeam echosounder. In the following the calibration procedures for roll, pitch and heading misalignment of the laser scanner is presented. Although the determination of angular offsets of the multibeam transducer, which isn't in the focus of this work, was already done by a regular patch test of the survey vessel the differences in procedure for laser scan and multibeam calibrations will be pointed out.

The first procedure is to determine the roll and pitch misalignments of the laser scanner which is similar to a multibeam patch test. Two survey lines with same tracks but in opposite directions have to be measured as shown in figure 3.18. The effects of both biases increase with the distance to the sensor, in this case to the laser scanner. Thus tall objects with plane surfaces containing significant features are needed to derive the boresight angles in roll and pitch.

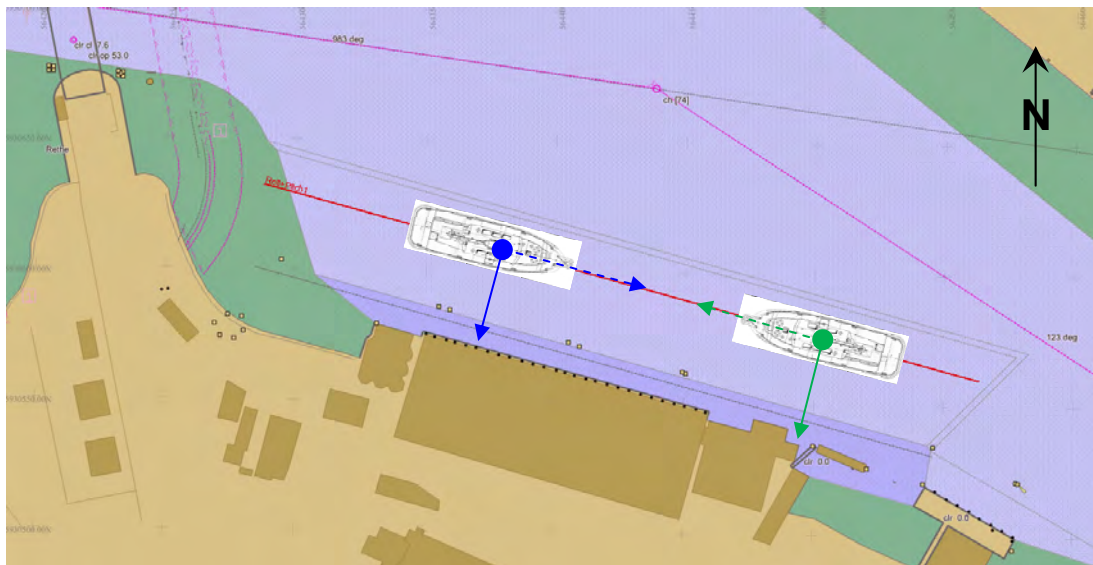
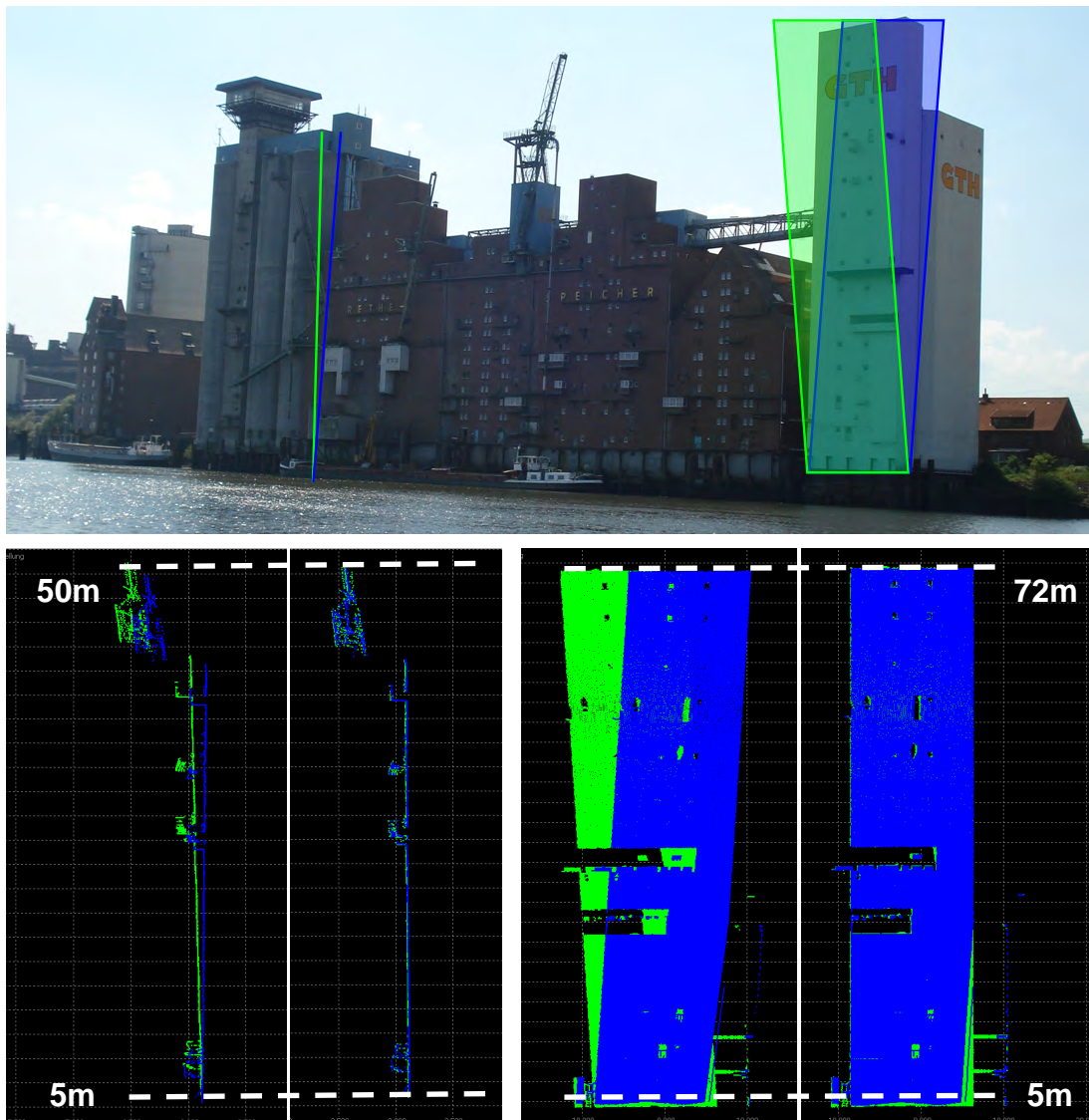


Figure 3.18: Calibration procedure for determination of roll and pitch boresight angles. Two survey lines were measured in opposite directions at the Grain Terminal Hamburg.

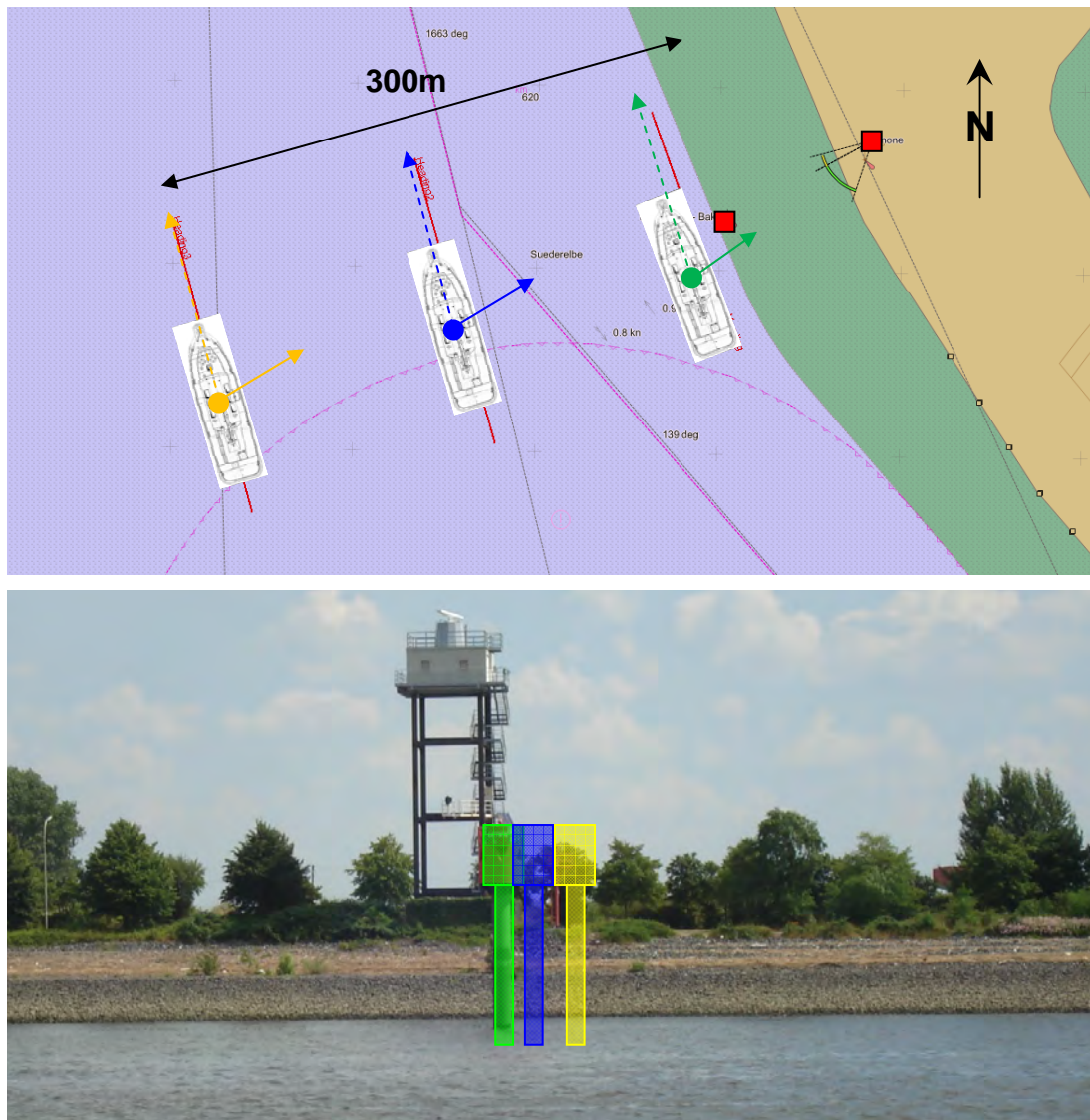
The Grain Terminal Hamburg is well suited for this part of the patch test because it is located directly at the waterside of the Reiherstieg and contains several buildings with different heights up to 70 meters as shown in the pictures of figure 3.19.

Because of countless small features like windows, pipes and gangways on all height levels both point clouds can be used for roll as well as pitch calibration. The boresight alignment is performed in the “Validator” tool of QPS QINSy. The Validator allows to determine each bias by adjusting the angular offsets of the mapping device and was generally designed for multibeam systems. With least square computations the Validator generally calculates angular misalignments by comparing a subset respectively a patch of two different point clouds.

Although QINSy handles a laser scanner as a multibeam sensor the automatic computation is not capable to deal with laser scan data because of the different geometric conditions. Thus the user has to adjust the angle offsets manually and to determine best fitting results visually which is more or less a good estimate for the boresight angles. Figure 3.19 depicts the comparison of patches of point clouds before and after calibration. From this figure one can imagine that the higher the mapped object the more accurate the determination of boresight angles becomes.



Figures 3.19: Calibration procedure for determination of roll and pitch boresight angles with the Validator tool of QPS QINSy. Photograph of the Grain Terminal Hamburg with highlighted patch areas (Top); Before and after comparison of determined and applied boresight angles for roll (Bottom left) and pitch (Bottom right)



Figures 3.20: Calibration procedure for determination of heading misalignment. Three survey lines were measured in same directions at the radar station and light beacon “Kattwyk”(Top); The three colored beacon shapes simulate the expected point cloud results (Bottom)

The determination of the heading offset between the scanner’s and the vessel’s X axis is also similar to a heading patch test of a multibeam. One or more vertical features have to be measured from parallel survey lines in the same direction but with different distances to the object, because the systematic effect of the heading misalignment increases with the distance.

Another survey line configuration is possible when the vertical object can be measured from different locations, means that the object is not located on land but surrounded by water. Then it is possible to arrange both parallel survey lines with same direction enclosing the vertical object in the middle of both lines. The first heading calibration was done near the Containerterminal Altenwerder (CTA) at the radar station and light beacon “Kattwyk”. Three survey lines were measured almost parallel to the coast line with different distances to the light beacon as pictured in figure 3.20. As the object position error based on the heading bias increases with the object distance, the third survey line has produced the largest position error. The angular offset in heading was also determined with QINSy’s validator tool.

After the determination of the angular heading offset the pitch offset has to be recalibrated. Because the angular heading misalignment influences the pitch offset to a certain amount this iterative procedure is needed to improve the accuracy of the pitch offset value. The final results of this first calibration procedure are summarized below. It is important to mention that the angular heading offset at the beacon “Kattwyk” was not determined sufficiently and should only be taken into account as a rough estimate because the distances of the survey lines were not suited to map the object with high dense point data.

Table 3.2: Results of the first calibration procedure

Results 1st calibration			
Roll [°]	<u>0.072</u>	±	0.0060
Pitch [°]	<u>3.512</u>	±	0.0069
Heading [°]	<u>-0.280</u>	±	0.0071

To validate the computed boresight angles respectively to improve the heading calibration the whole procedure was repeated in a different survey area with different survey conditions and calibration objects.

In the area “Waltershofer Hafen” at the quay wall “Predöhlkai” four survey lines were measured in order to confirm the angular misalignments in Roll, Pitch and Heading. Additionally three lines in the “Parkhafen” as shown in figures 3.21 were recorded to get a more precise and more significant value for the angular heading misalignment.

Table 3.3: Results of the second calibration procedure

Results 2nd calibration			
Roll [°]	<u>0.047</u>	±	0.0064
Pitch [°]	<u>3.511</u>	±	0.0054
Heading [°]	<u>-0.167</u>	±	0.0106

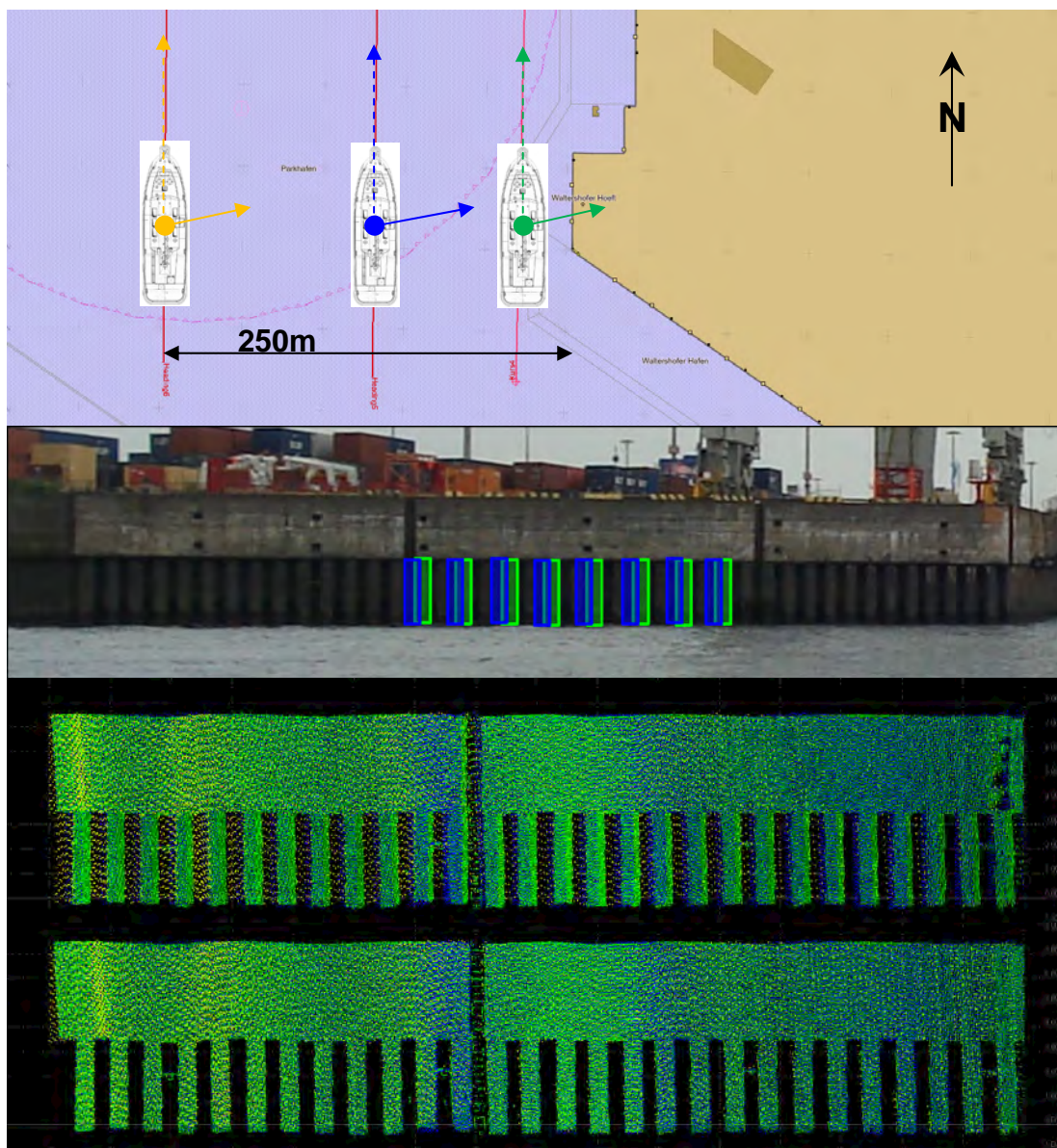
As shown in tables 3.1 and 3.2 above only one angular misalignment, the pitch offset, can be confirmed by the second calibration procedure. The roll offset but most notably the heading misalignments differ from each other to a significant amount. The difference in the roll misalignment can be explained by the accuracy specification of the IMU which is defined as $\pm 0.01^\circ$ (1σ).

Although the heading accuracy (1σ) of the HYDRINS is given with 0.02° secant latitude which is in Hamburg (latitude 53.5°) $\pm 0.034^\circ$, the difference in heading misalignment can be explained by the worse survey line configuration of the first heading patch test at the light beacon “Kattwyk”. One problematic issue is the shape of the light beacon which is a round dolphin and therefore not useful to calibrate the heading. Additionally the distance of the furthest survey line with 300m to the beacon and 400m to the radar station was too large. Only a few not representative measurements from this survey line were recorded on both objects. For calibrating the heading offset at the radar station only measurements of the closest two survey lines were used. Since the results of the calibration can be presented here only in a summarized way the complete calculation is attached as Annex A-4.

The misalignment values for Roll and Pitch were averaged as shown in table 3.4, the final heading offset is a weighted mean whereas the “Kattwyk” value has got a low weight. After the calibration the boresight angles were set in QINSy to be applied during the following surveys in online processing.

Table 3.4: Combined results of both calibration procedures whereas the heading misalignment is more based on the second calibration survey.

Combined results of 1st and 2nd calibration	
Roll misalignment [°]	<u>0.060</u>
Pitch misalignment [°]	<u>3.511</u>
Heading misalignment [°]	<u>-0.190</u>



Figures 3.21: Calibration procedure for determination of heading misalignment. Three survey lines were measured in same directions at a sheet pile wall structure in the “Parkhafen” (Top); Photograph of the calibration area incl. the theoretic shift between the point clouds of two survey lines (Middle); Before and after heading offset calibration (Bottom)

As described in this chapter the whole procedure to setup a system from sensor integration and interfacing, over initial measurement to determine the lever arms in the body system and the extensive calibration procedure to determine the angular misalignments of all contained mapping sensors is complex and at a certain stage not really straight forward. Especially the visual determination of the angular offsets in the validator tool of QINSy, which is not designed to handle such huge laser scan datasets, is laborious and time consuming. Algorithms have to be found to compute the calibration parameters automatically like it is realized for multibeam datasets. The reliability of visual determined angular offsets have to be evaluated by an independent post-processing tool in chapter 4. Nevertheless the mobile mapping system was established and first test surveys had been conducted to evaluate the performance of the system which is presented in the next chapter.

3.5 First Mobile Mapping Results

This chapter will discuss the first survey results whereas the main focus is on detected and terminated systematic artifacts in the mobile scan data. Furthermore considerations on required point densities with respect to vessel speed and object range will be presented..

After the calibration procedure different survey projects have been realized in this thesis whereas the main project was performed for the accuracy analysis which is described in chapter 5. All other projects will be presented in chapter 6. However, during the data processing different remaining systematic problems appeared which were related to this chapter. The first obviously systematic error was found in a port area where three survey lines were measured in opposite directions. As pictured in figure 3.22 the point clouds of two survey lines sailed in equal direction match together whereas the third point cloud is shifted horizontally about 7 centimeters.

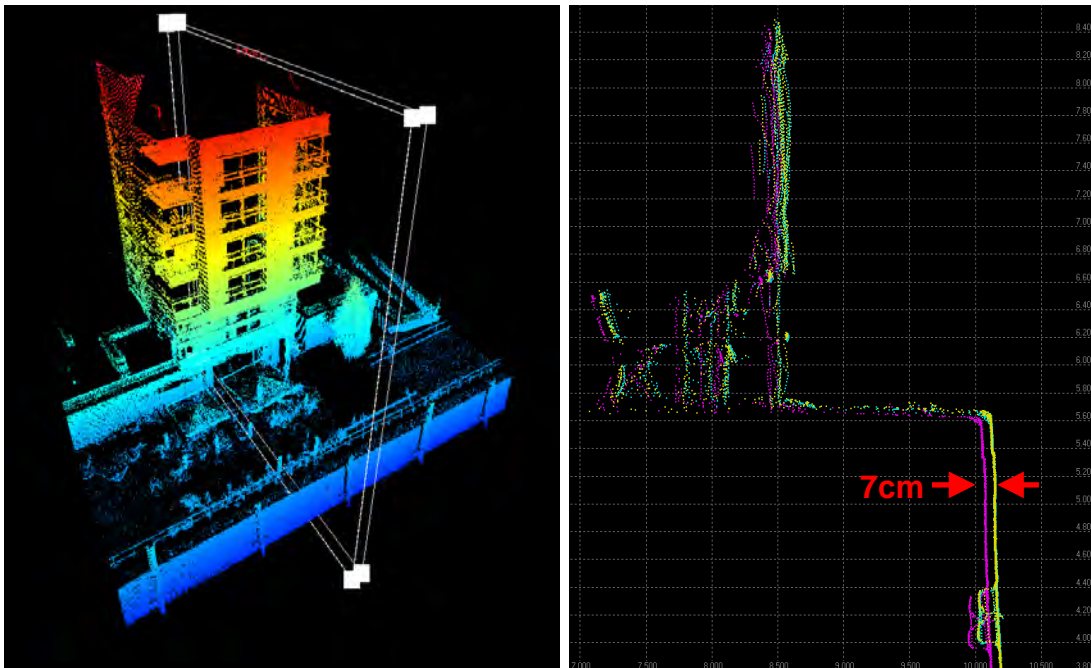


Figure 3.22: Position offset between three reversely sailed survey lines of around 7 centimeters perpendicular to the track of the survey line. (Left) Overview of the survey area and a cross-section through the color coded point clouds (Right)

Although this error can be based on bad positioning e.g. by INS drifting effects during GNSS outtakes, this effect is not only to find locally but the complete survey is affected. The fact that the survey line which is sailed in opposite direction to the other lines produces such offsets suggests a problem in the lever arms. And indeed the position of the INS system with respect to the vessel's coordinate system was set in QINSy erroneously. Fortunately QINSy provides a replay functionality where the lever arms can be corrected and the online processing can be repeated. The next found issue is related to motion data and was found in datasets of a survey to map the building "Dockland" directly located at the river Elbe as shown in the figures 3.23 below.

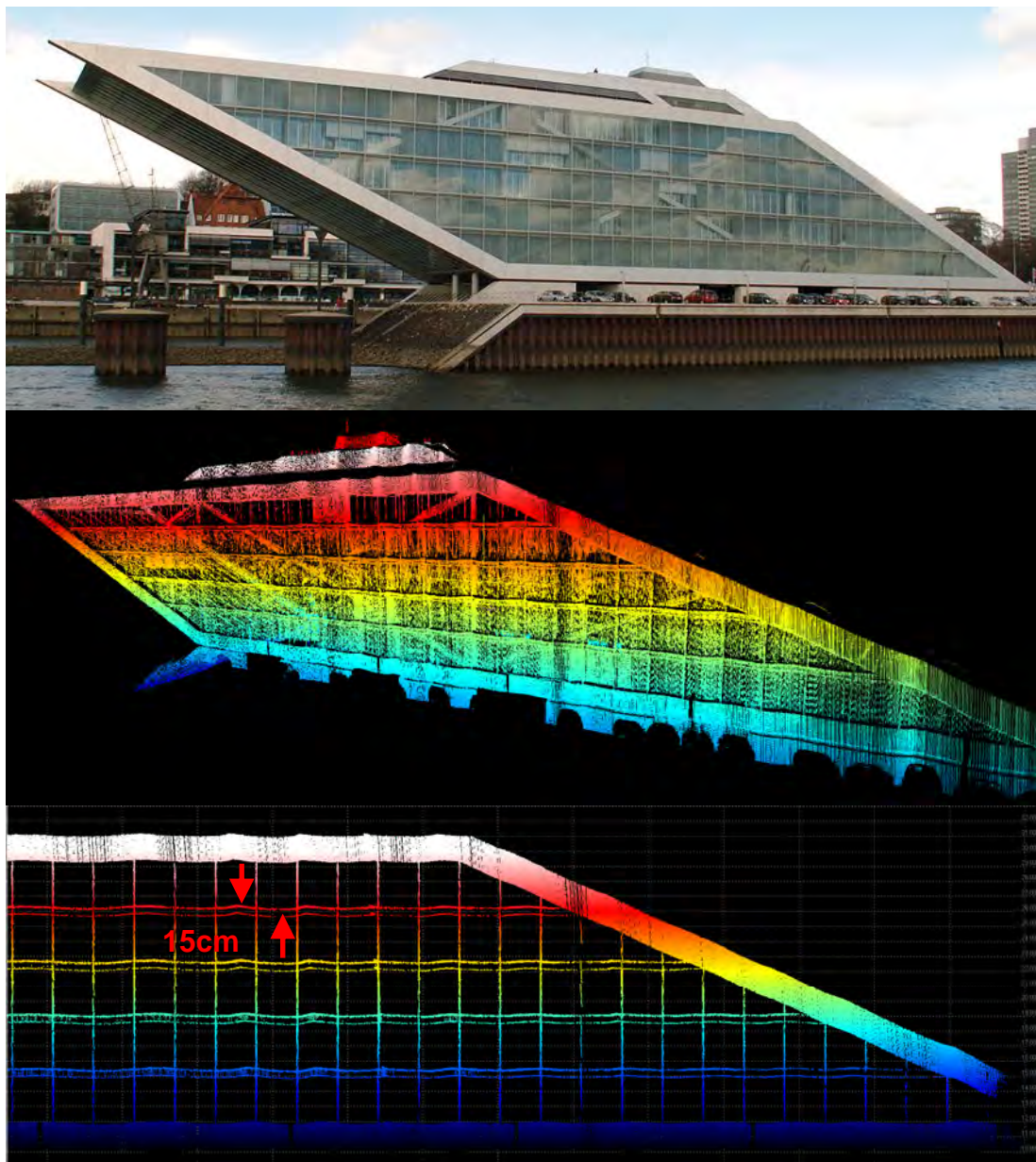


Figure 3.23: Motion artifacts especially in the height component found in point clouds of the project "Dockland"; Photograph of the building "Dockland" (Top); 3D point cloud of one survey line color coded by height (Middle) and a cross section of the building's façade (Bottom); Height variations of up to 15 centimeters with rough survey conditions.

During the measurements the survey conditions were relatively rough. The amplitudes in roll of around $\pm 4^\circ$ and pitch of $\pm 2^\circ$ have led to motion artifacts in the point clouds. The track of the survey was parallel to the building façade, the scanner was oriented almost perpendicular to the building. On the first view the problem seemed to be based on erroneous INS heights because the effect is neither range nor height dependent. But by investigating the problem in more detail not only height variations but also position variations became visible. With increasing object height the height variations are more and more combined with oscillating position offsets which can only be based on dynamic systematics in motion data especially in roll direction. Although the INS which also provides the motion data is time synchronized by PPS and corresponding time message the effect should be caused by a latency. Within the data analysis tool QINSy allows to apply time shifts to sensor raw data whereas the raw data file has always to be replayed when such a change is done in order to check the results. By performing the time shift in incremental steps it was possible to determine the “best fitting” latency of 25ms for motion data as shown in figure 3.24. Since the INS provides QINSy not only with motion data but also with position information it was investigated if the position is also affected by the determined latency. The result was that the position has also a latency but only of around 10ms.

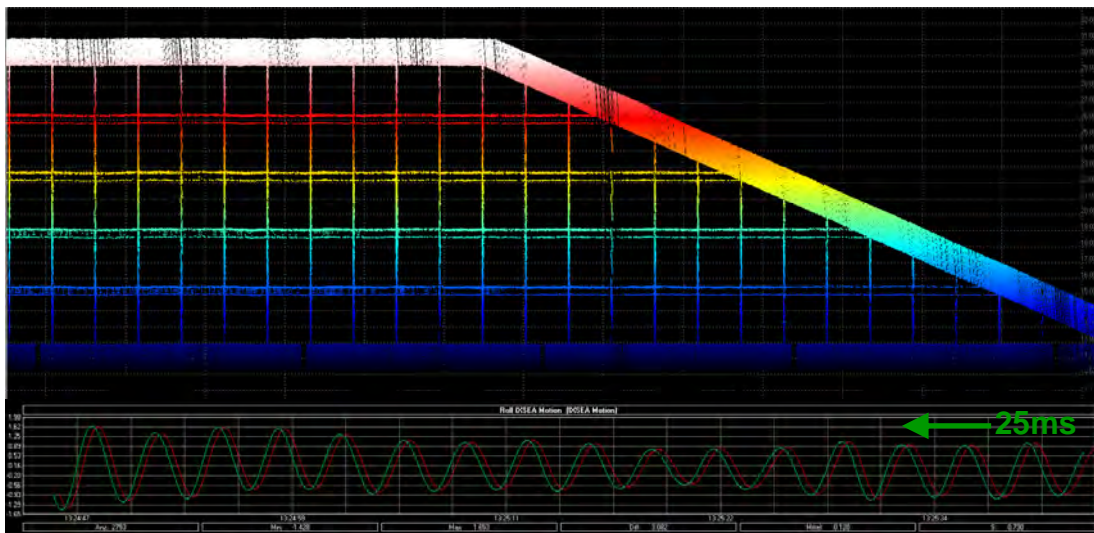


Figure 3.24: The cross section of the building's façade with compensated latency (Top); Graph of the roll values for this survey line, red line display original data and the green one is compensated for 25ms latency (Bottom)

After consulting IXSEA who confirmed that certain data protocols of the HYDRINS in this case the Seapath protocol can have different latencies, a different workflow was tested. As mentioned before in chapter 3.2 not only the seapath protocol was recorded but also INS raw data. With the post-processing tool IXSEA DelphINS which is presented in chapter 4.2 the raw data can be processed to compute a Kalman filtered and smoothed trajectory. If the latency is directly linked to the data protocol, this new computed trajectory should not contain any latency. After the post-processing the computed trajectory was imported in QINSy and indeed a latency was hardly measurable in the data. For this reason IXSEA recommends to use different protocols for position and motion data. At the moment IXSEA and QPS are working on a new data protocol which combines position and attitude data.

In contrast to the systematic effects described before the next considerations have to be done in terms of reachable laser point densities. In mobile laser scanning the achievable point density and point distribution depends on the laser scanners measurement rate, the line scan rate, the used vertical angular stepwidth, the range from scanner to target object and of course from the mobile platform's speed. Generally a mobile scanning is planned and based on the customer's requirements on point density. Figure 3.25 depicts the relationship between these parameters schematically. As shown the vertical point spacing can be roughly derived from the vertical angular stepwidth of the laser scanner and the range to the object. The number of scan lines per second is a function of the maximum effective measurement rate which depends on the scan mode in this case, the angular stepwidth and the vertical scan sector which is used for the survey. Therefore the horizontal spacing between the scan profiles depends on the line scan rate and the vessels speed over ground.

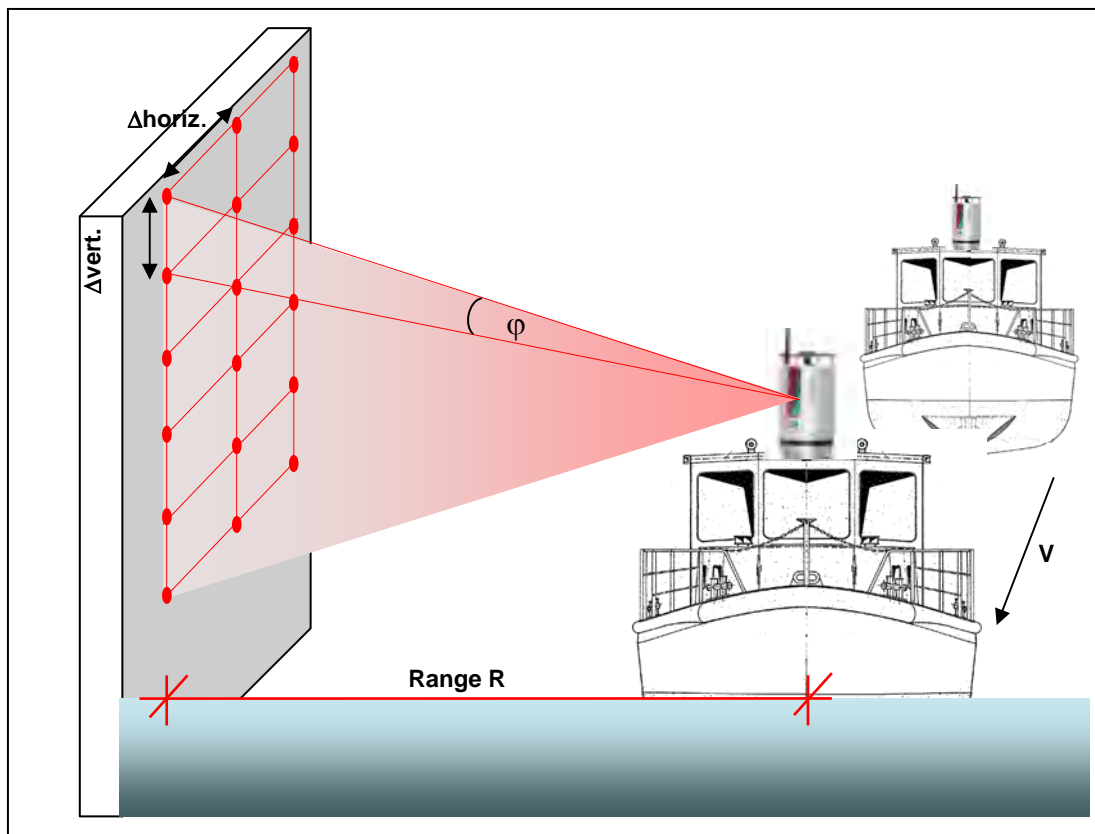


Figure 3.25: Relationship between object range R , vertical angular stepwidth ϕ and vessel speed V with respect to vertical and horizontal laser point spacing

The graphs 3.26 can be used to derive the most suitable combination of scan parameters for each survey in order to achieve a regular grid of scan points with the required point spacing.

As an example a survey has to be performed and point spacing in vertical and horizontal direction of at least 10 centimeters is required. Because of local circumstances the mean object range is around 100 meter. The range determines the maximum vertical angular stepwidth of the scanner of 0.058 degree to be used in order to meet the requirement of 10cm vertical point spacing.

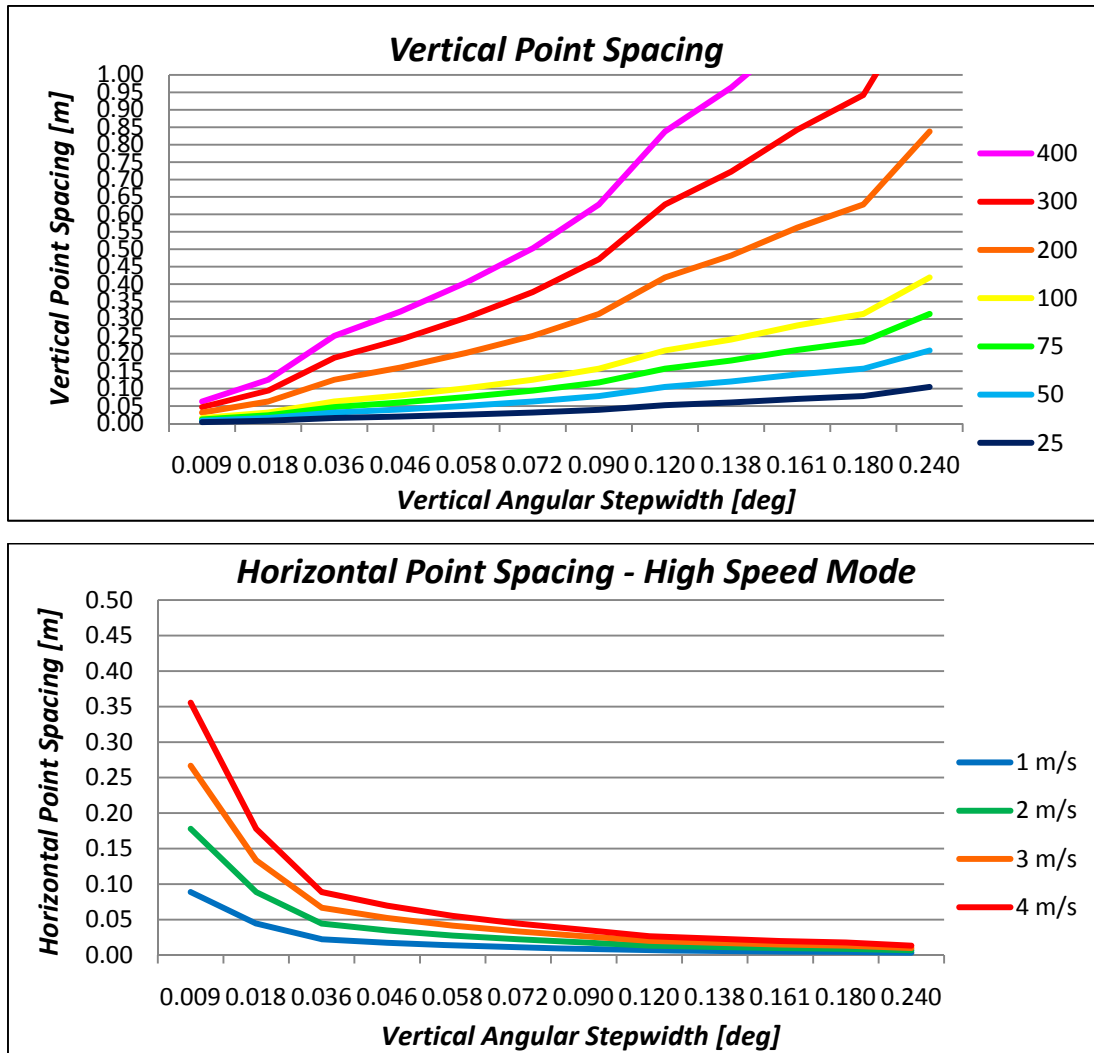


Figure 3.26: Considerations on laser point density for the RIEGL VZ-400 system, the full vertical 100deg sector is used. The relationship between range and vertical angular stepwidth and the resulting vertical point spacing (Top); The relationship between vessel speed and vertical angular stepwidth / line scan rate for long range (Middle) and high speed mode (Bottom)

At ranges of 100 meters the high speed mode of the scanner can be used which increases the line scan rate by factor three in comparison to the long range mode. With the angular stepwidth of 0.058 degree 73 scan lines per second will be measured which leads to a horizontal point spacing of 5.5 centimeter at a vessel speed of 4 m/s. To harmonize the distribution of laser scan points which is at the moment 10.1 centimeters in vertical and 5.5 centimeters in horizontal direction, a smaller vertical angular stepwidth can be used. With an angular stepwidth of 0.046° the vertical point spacing decreases to 8.0 centimeters which causes also a decrease in the scan rate to 58 lines per second. This leads to a corresponding horizontal spacing of 6.9 centimeter at the same vessel speed of 4m/s.

Although this consideration is of theoretic nature it can help to fine-tune a survey from an economic point of view when the mean object range is known. It was assumed that the full vertical field of view of 100 degree is used for a survey. If one decreases this angular sector the line scan rate increases immediately and the horizontal point spacing decreases.

4. Data Processing

The prior chapter 3 has described the sensor interfacing and the data integration. It is the base for all following processing steps. The interfacing of the sensors was designed not only to produce online datasets with QPS QINSy but also to be able to perform post-processing for data of the inertial navigation system and laser scanner. Therefore raw data from both sensors have been simultaneously recorded to make a comparison between online and post-processed datasets. This chapter describes different processing methods their pros and cons and is the base for chapter 5 where the results of these processing methods will be compared with each other. Following data processing workflows can be distinguished by the software package which is used:

- Online Processing – QPS QINSy
- Post Processing – QPS QINSy
 - Post Processing using GNSS Trajectory
 - Post-processing using INS Trajectory
- Post Processing – RIEGL RiPROCESS
 - Post Processing using INS Trajectory
 - Post Processing after Scan Data Adjustment

4.1 Online Processing QPS QINSy

As already mentioned in chapter 3 QPS QINSy is a modular structured software application which consists to the major part of the data integrating, data recording and online processing capabilities but also a powerful data validation and post-processing part. This subchapter focuses of the online processing part of the software. The used sensors are connected to the data acquisition PC via Ethernet, serial connections and sometimes also USB connection. To manage all the interfaces, but also the spatial relationships between the sensors with respect to the vessel reference frame, QINSy needs a setting file where all these information is stored. The structure of such a setting file is depicted in figure 4.1 and is divided into a header which contains geodetic settings like horizontal and vertical reference frames and corresponding datum transformations and map projections and the system settings. The object section of the settings file is divided into the subsections nodes and systems. Whereas the lever arms of each system in vessel coordinates are defined as nodes, the individual system describes each sensor by its interface and measurement properties and the location aboard related to the corresponding node. In the example pictured in figure 4.1 the properties of the laser scanner RIEGL VZ-400 are displayed on the right hand side of the picture. In the upper section the used sensor driver and the corresponding ethernet address is defined. Below of these parameters the location of the scanning sensor is given as the position of node “RIEGL VZ-400” with respect to the vessel reference frame. Additional to these basic settings special measurement parameters can be defined for each measurement system. In this case the boresight angles determined by the calibration procedure are already set in the settings file. So, each contained sensor of the mobile mapping system is defined in the way as described.

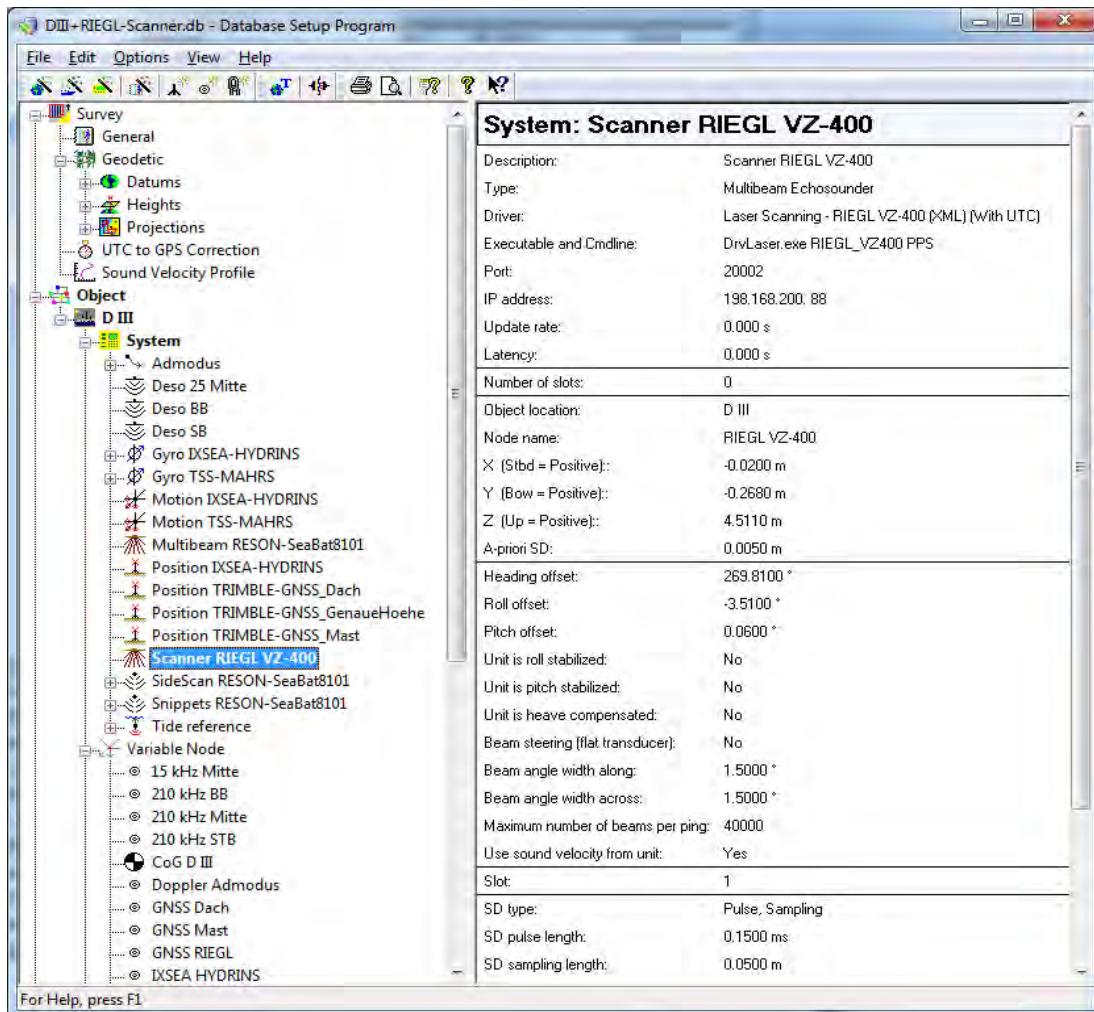


Figure 4.1: A partial overview of the QINSy settings file used for this thesis. On the left side the tree structure with general survey settings and all contained sensors of the survey system are displayed. On the right hand side individual settings for each measurements system can be defined.

One of the most important features is the timing capability of QINSy. Although most of the sensors are already time synchronized by PPS and time message of the GNSS receiver some sensors like the used digital camera are not. QINSy has therefore to handle synchronized and not synchronized data streams of different sensors. For this reason the data acquisition PC is also connected to PPS and time message and QINSy is able to build a time regime where incoming unsynchronized data will be time stamped with respect to UTC.

The online mode of QINSy enables the user to monitor the behavior of each sensor by displaying the sensor raw values in numerical or graphical windows. Certain alarms can be defined to check individual survey and quality relevant sensor parameters for example the position status of a GNSS system which describes the solution of position e.g. RTK mode or stand alone. Figure 4.2 gives an example how the user interface in the QINSy online mode can be configured. In this case raw data displays for motion, scan data and camera data are shown.

An overview window displays the current position of the mobile platform by taking position and heading data into account. An almost countless number of manifold displays can be defined by the user to optimize the user interface.

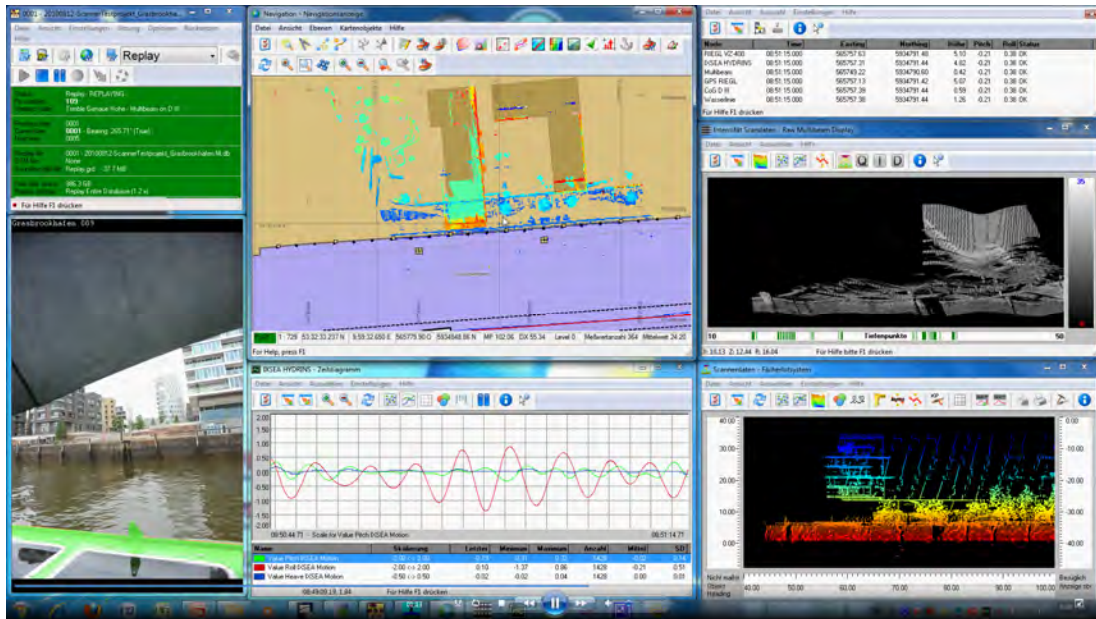


Figure 4.2: A possible configuration of the QINSy online user interface. Different control and overview windows allow the user to control and monitor the online processing

Additional to the one way data reception and display functionality, QINSy provides sensor controller for several measurement devices. With these tools it is possible to communicate with the sensor in order to change measurement properties e.g. the field of view of a laser scanner, scan mode and many more. The controller is embedded in the user interface of QINSy and allows a fast access to all survey relevant parameters of the sensor. Figure 4.3 shows the QINSy control windows for the RIEGL VZ-400 laser scanner and the camera NIKON D700 which is attached to the scanner. Here not only the basic scan pattern can be defined but also atmospheric values and properties for time synchronization.

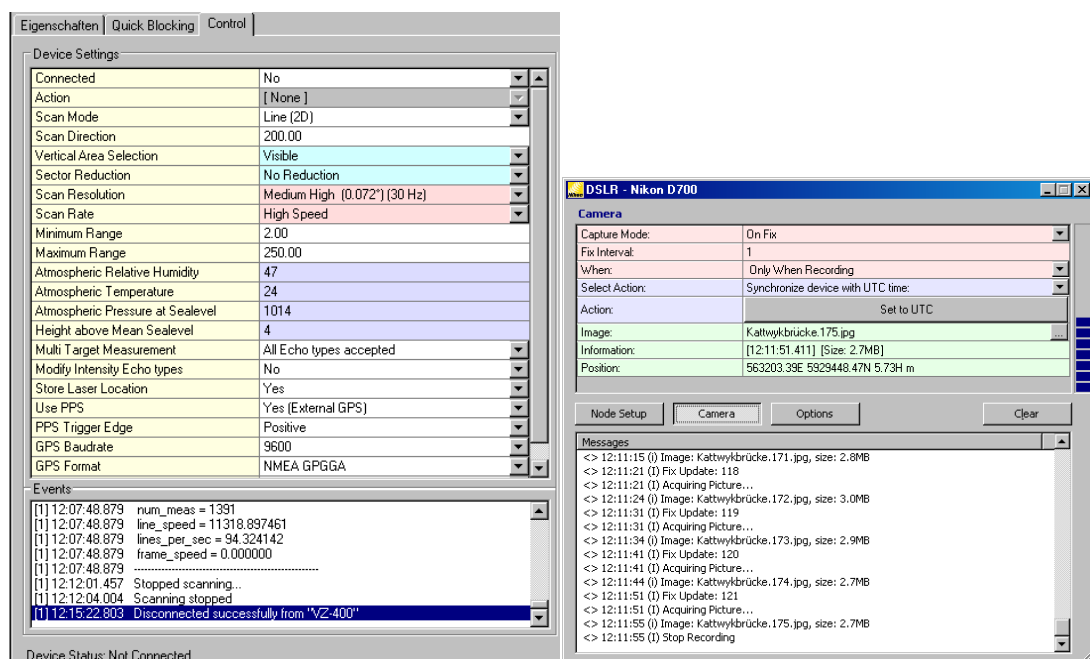


Figure 4.3: QINSy controller for laser scanner RIEGL VZ-400 (Left) and digital camera NIKON D700 (Right). The communication between QINSy and Scanner is based on the RIEGL Data Transfer Protocol (RDTP)

The data transfer between QINSy and the RIEGL scanner is based on the RIEGL Data Transfer Protocol (RDTP). This protocol is TCP based and describes the communication between a server (scanner) and the client (QINSy PC) whereas the client has to send ASCII commands to the scanner which responds by sending status messages and data blocks. During the survey the user's inputs of the controller were translated into RDTP ASCII commands and sent to the scanner which gives a response which is exemplarily shown in figure 4.4.

```

10/08/2010 12:04:49 -> INFO : Stopped scanning...
10/08/2010 12:04:51 -> INFO : Scanning stopped
10/08/2010 12:07:45 -> INFO : Scan Mode: 2D
10/08/2010 12:07:45 -> INFO : Scan Direction: 200.0°
10/08/2010 12:07:45 -> INFO : Vertical Area Selection (XML Scheme): Visible
10/08/2010 12:07:45 -> INFO : Sector Reduction (XML Scheme): No Reduction (0 Sectors defined)
10/08/2010 12:07:45 -> INFO : Scan Rate (XML): High Speed
10/08/2010 12:07:45 -> INFO : Scan Resolution (XML): 0.072°
10/08/2010 12:07:45 -> INFO : Range blocking: min 2.00 - max 250.00 meter
10/08/2010 12:07:45 -> INFO : Multi Target Filter (XML): 15
10/08/2010 12:07:45 -> INFO : Modify Intensity Echo Type: No, Store Laser Location: Yes
10/08/2010 12:07:45 -> INFO : PPS: Yes, Trigger: Positive, Format: GPGL, 9600, PPS Pulse First
10/08/2010 12:07:48 -> INFO : -----
INFO : Start scanning...
INFO : meas_prog = 1
INFO : input_changed = 1
INFO : th_soc_start = 30.000000
INFO : th_soc_stop = 130.000000
INFO : th_soc_incr = 0.071875
INFO : ph_soc_start = 200.000000
INFO : ph_soc_stop = 200.000000
INFO : ph_soc_incr = 0.000000
INFO : num_scans = 0

```

Figure 4.4: QINSy logfile of controller / scanner communication. The scan parameters set in the controller were translated into RDTP commands and sent to the scanner.

The tasks off the online module of QINSy can be divided in two different procedures. On the one hand QINSy has to record raw data from the connected survey sensors in a chronologic order for post-processing issues. On the other hand the raw data of the positioning device, the attitude sensor and the mapping instrument have to be processed and combined with each other to create full registered point clouds in the desired reference frame.

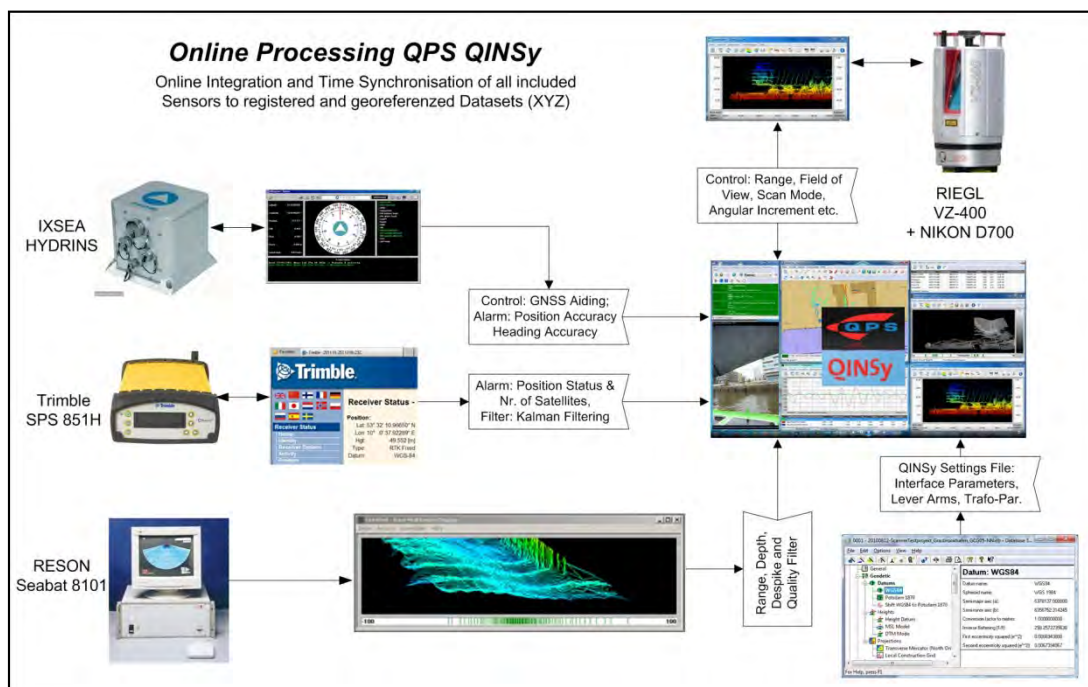


Figure 4.5: Schematic overview of QINSy online processing. The main task of the user is to monitor and to control the sensors. QINSy computes a 3D position in the reference frame for each sounding and laser spot and applies motion and heading data online.

To improve the results of online processing the user can choose between different positioning and height systems e.g. either GNSS positions and heights, or GNSS positions and heights of a tide gauge or just INS positions and heights. By using position filters which are based on Kalman filter algorithms the track of the survey vessel can be smoothed. For echo-sounding systems different depth filters are available to reduce the amount of blunders and outliers. Although the user can influence the quality of online processed data to a certain amount, his tasks are to monitor all contained systems in order to recognize sensor problems and to perform a first quality assurance. QINSy takes over the part of registering the point clouds. For each time stamped sounding or laser spot QINSy determines the values of the trajectory and performs coordinate transformations from the mapping sensors own coordinate system over the body system to the reference coordinate system by taking into account the misalignments and lever arms which are defined in the settings file of QINSy. The results of the online processing are geo-referenced point clouds including sensor typical attributes like intensity values, quality flags and other.

4.2 Post Processing QPS QINSy

As mentioned in the prior chapter 4.1 QPS QINSy offers post processing capabilities to improve the accuracy of mobile recorded datasets. Here it is either possible to edit already processed point clouds or to evaluate and to correct the sensors raw data. This chapter discusses the post processing steps based on raw data whereas the focus is on the used trajectory and the way it is computed.

4.2.1 Post Processing QINSy – GNSS Trajectory

The chapter summarizes the workflow for the post-processing based on sensor raw data by using the GNSS trajectory. Although the HYDRINS has provided QINSy with position data as well it should be shown in chapter 5 if there is noticeable difference between GNSS and INS trajectory. As attitude and heading sensor of course the INS is used. Since the raw data of all sensors were recorded during the online data acquisition it is now possible to evaluate each of them with the QINSy Analyze tool. Here it is possible to check each dataset on inconsistency or raw errors.

As shown in figure 4.6 the position data of the GNSS which is displayed as a time plot contains huge GNSS jumps at the end of the survey line which can be caused by shadowing effects under a bridge for example. These erroneous position and height data can lead to significant errors in the processed laser scan point cloud if they are not corrected. QINSy provides two different approaches to manipulate raw data. The first one allows the user to import a clean trajectory from an external device which is discussed in the next chapter. The second possibility is to interpolate the problematic part of the dataset linearly which is shown exemplarily in figure 4.6 for height component. Although this procedure should be performed with wariness it can be used to get rid of very small GNSS outtakes. Another method can be to smooth the very noisy GNSS height data which is also possible in the raw data analysis tool and shown in figure 4.7. It is important to mention that the real raw data is still maintained and all changes in the datasets are stored in a different file.

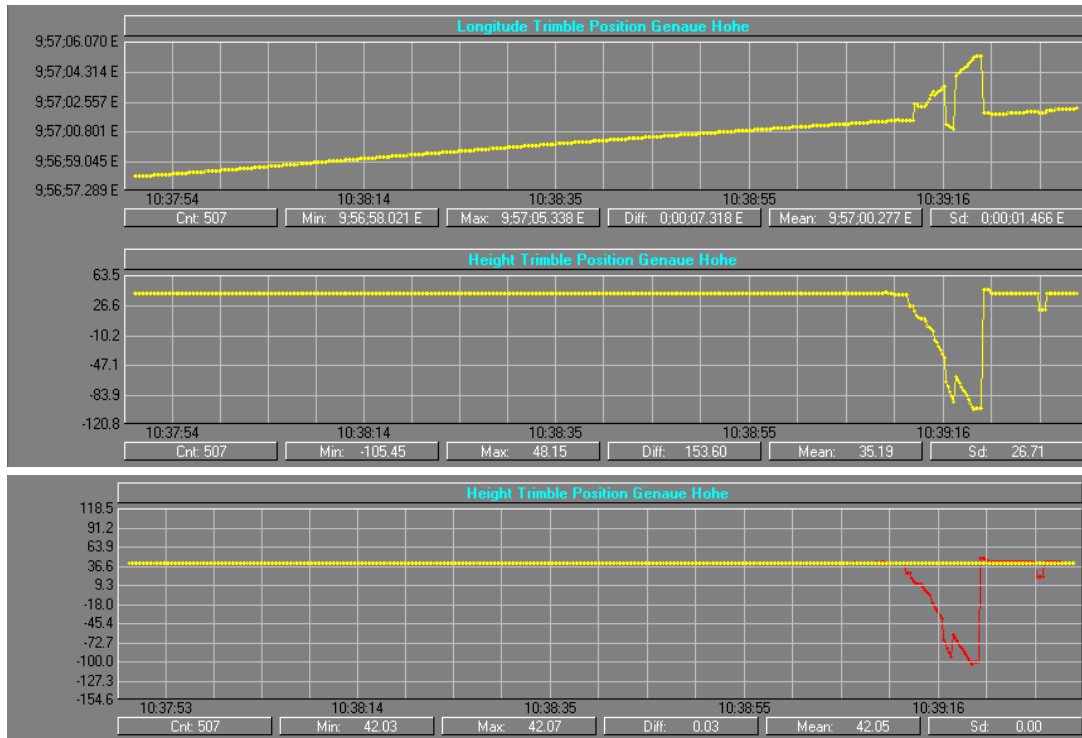


Figure 4.6: QINSy Analyze tool to evaluate and edit sensor raw data; Raw GNSS position data for longitude and ellipsoidal height containing GNSS jumps (Top); The height component is linearly interpolated for a period of 25 seconds.

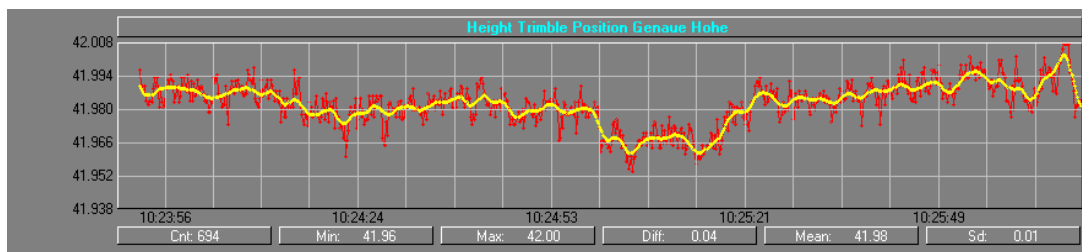


Figure 4.7: QINSy Analyze tool to smooth the very noisy GNSS height data; An average filter is applied to the noisy GNSS height data; The amount of averaging can be user defined

To process the filtered and interpolated datasets a replay of the raw data has to be performed. Thus all sensor data is accurately time stamped QINSy simulates a real survey by playing the data in a chronological order. Although the sensor controllers are not available during the replay almost all online filters can be used to improve the processing results which are again geo-referenced point clouds. The whole procedure of improving raw data and replaying it can be repeated again and again until the results are sufficient enough.

Figure 4.8 shows the general procedure of the raw data post processing capability of QINSy. Additional to this workflow the resulting point clouds usually will be investigated in the Validator tool of QINSy on remaining systematic effects e.g. erroneously determined angular misalignments. By performing a calibration procedure in the Validator tool new determined angular offsets can be set in the raw data file in order to receive recalibrated point clouds after a replay.

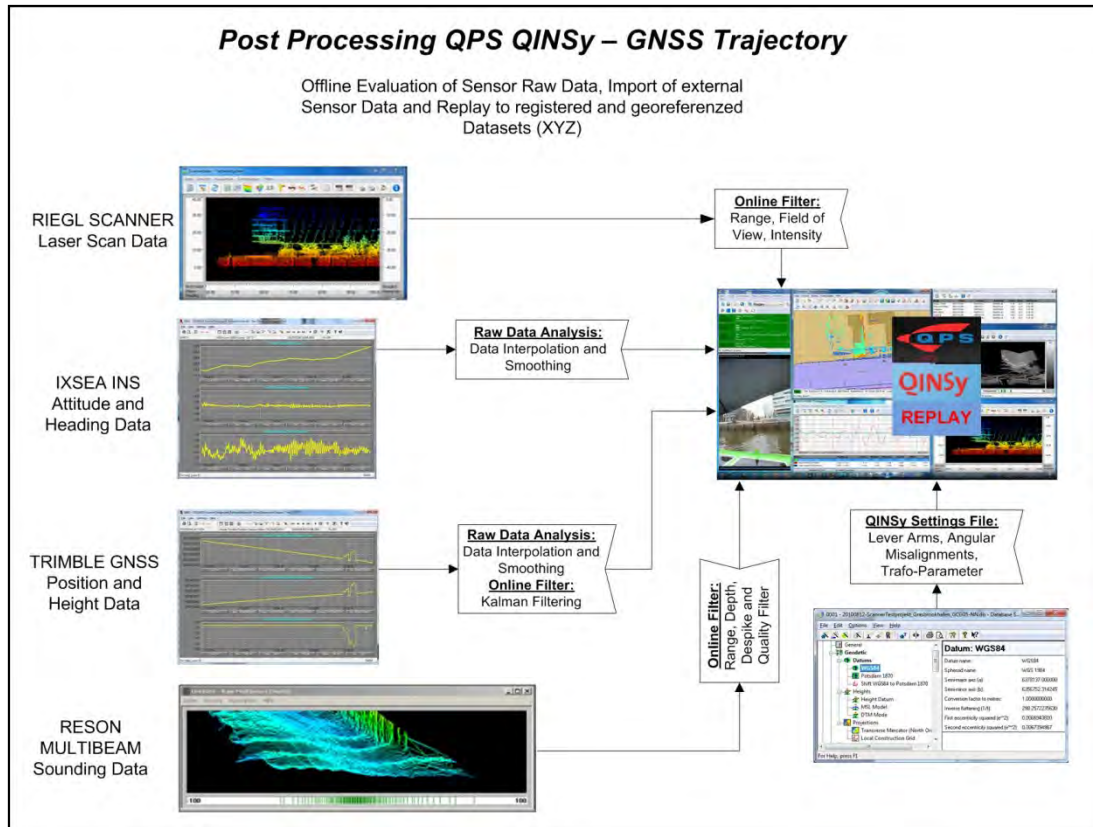


Figure 4.8: Schematic overview of QINSy post processing from the point of raw data evaluation. With the raw data analysis tool gross errors can be detected and partially compensated by interpolation and smoothing procedures.

4.2.2 Post Processing QINSy – INS Trajectory

In contrast to the prior chapter where only GNSS measurements were used for positioning of a mobile mapping system this section summarizes the procedure of integrating post-processed INS trajectories into the post-processing workflow of QINSy. As stated in chapter 3 the binary raw data of the INS were recorded separately to compute a filtered trajectory at a later stage. This is done with the post-processing tool IXSEA DelphINS. The software is designed to improve the INS capabilities by integrating raw INS data with external sensor data to compute a best fitting trajectory. The core component of DelphINS is based on the extended Kalman filter algorithm which is already implemented in the HYDRINS and provides an optimal integration of inertial and external data e.g. GNSS and Doppler Velocity Log (DVL) measurements. In post-processing DelphINS includes a unique feature to reverse time and process data backwards. The results of forward and backward computations are merged to receive an accurate and smooth trajectory (IXSEA 2010). The final exported trajectory can be used to update the QINSy raw data files in order to reprocess the mobile mapping data. Figure 4.9 shows the impressive results of the post-processing computations. In this case the survey vessel had to pass several times the Kattwyk Bridge with the result of serious GNSS outtakes which is indicated in the top graph of figure 4.9. Whereas GNSS height jumps of more than 150m were measured, the online INS solution has maintained the height with a 2 meter error which decreases to only a few centimeters in post-processing.

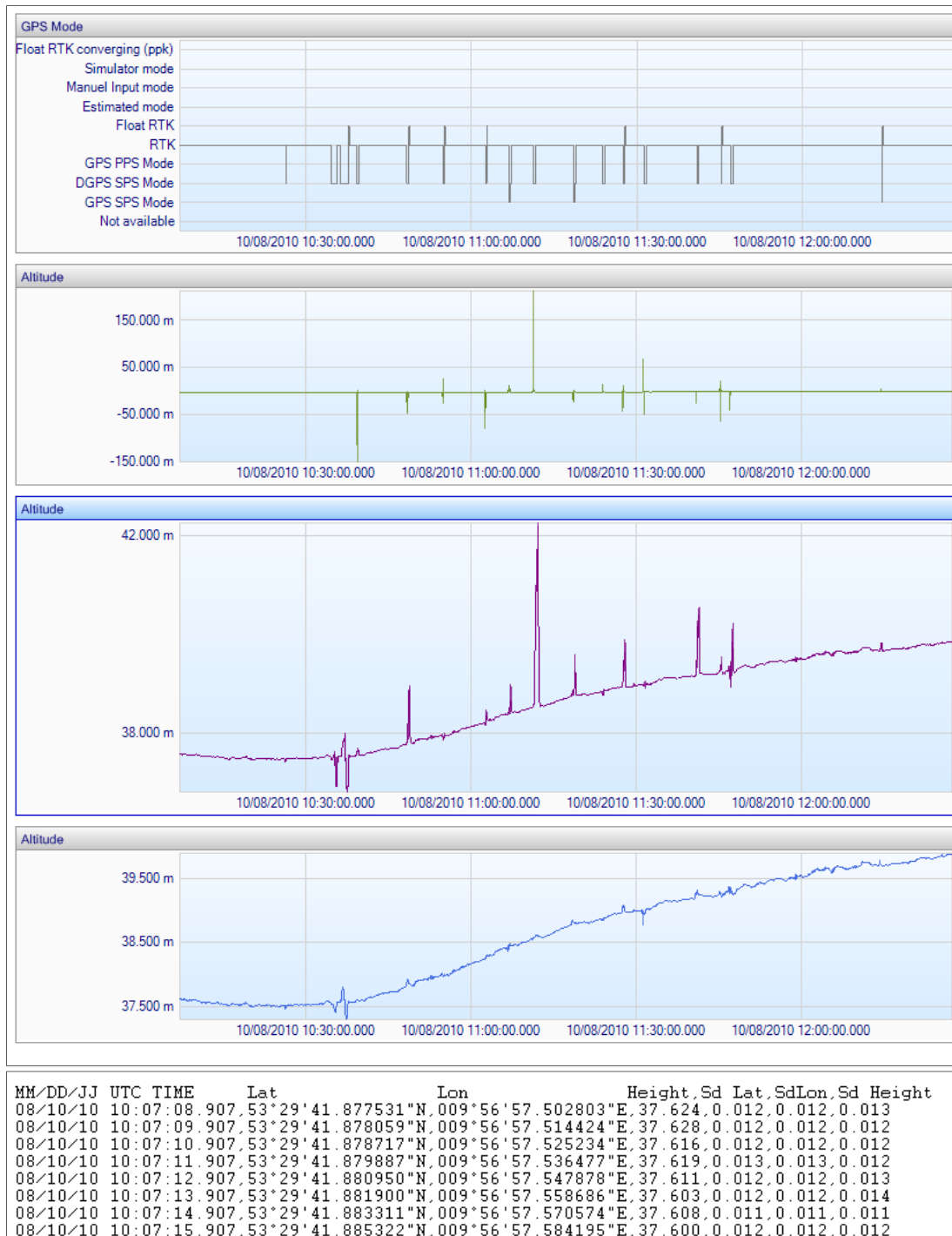


Figure 4.9: Comparison of the height component / altitude of the Trajectory determined with GNSS, INS online mode and INS post-processing mode (Top); Example of an exported trajectory in KOAC-WMD RTK format computed with DelphiINS to be imported in QINSy (Bottom)

With respect to figure 4.9 it is obvious that in the height component of the post-processed trajectory still remaining effects are present. After trajectory import into QINSy these small effects can be interpolated as shown before in chapter 4.2.1. A replay of the updated raw data file will produce proper laser scan point clouds. Figure 4.10 summarizes the described workflow schematically.

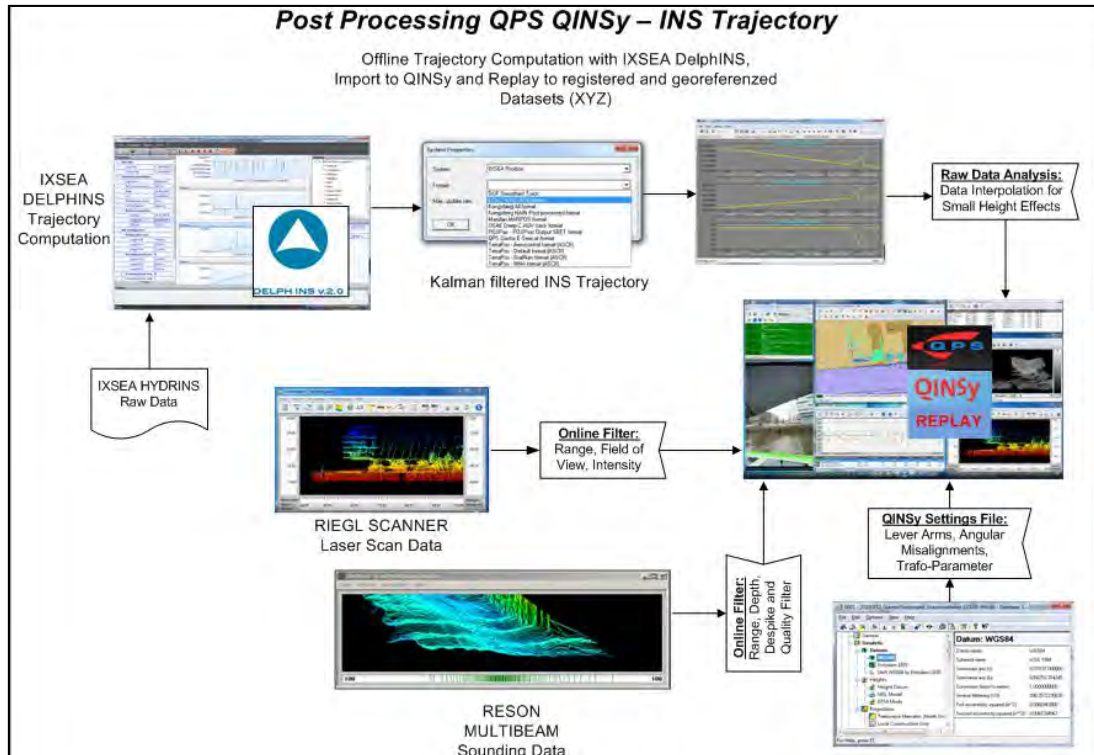


Figure 4.10: Schematic overview of QINSy post processing. In this workflow the trajectory is optimized by an additional post-processing tool which Kalman filters the INS data with forward and backward algorithms. With the raw data analysis tool small rest effects can be detected and compensated by interpolation procedures.

4.3 Post Processing RIEGL RiPROCESS

A total different approach is used by the RIEGL processing software bundle. For mobile mapping applications it is currently not supported to integrate INS and scan data simultaneously in order to perform an online processing to create 3D georeferenced point clouds during the survey. Nevertheless the post-processing combines not only trajectory and scan data but also allows to process image data from a digital camera.

4.3.1 Post Processing RIEGL RiPROCESS – INS Trajectory

The trajectory is as described in chapter 4.2.2 computed with the INS post-processing software DelphINS which provides a forward and backward Kalman filtered trajectory. DelphINS supports two different export formats to be used in the RIEGL application. The first one is the POSpac-POSProc SBET format which was developed to export trajectory data from Applanix post-processing applications. This binary format has been established on the market as a transfer format for trajectory data. The second possible format is the POS format, a generic ASCII format which also contains time stamped position and orientation data.

Heart of the RIEGL post-processing procedure is the application RiPROCESS which was initially designed to process airborne laser scanning data but nowadays also mobile terrestrial laser scan data. The software works project based and integrates laser scanning system information (mounting information, calibration data and laser configuration), navigation device information (position and orientation of the IMU and GNSS unit), original laser data and trajectory data (RIEGL, 2010-1).

The major processing task is the merging of laser scan data and trajectory data which is outsourced to a different tool called RiWORLD. RiWORLD combines the raw laser data which is given in scanner's own coordinate system with the processed trajectory into geo-referenced point clouds with respect to a geo-centered coordinate system e.g. WGS84.

To perform the transformations between the different coordinate systems RiPROCESS has to know, similar to the QINSy's settings file, the lever arms and angular misalignments between the scanner and the IMU data. Because DelphINS has computed the trajectory with respect to the optical center of the scanner there are no lever arms to be applied. The angular offsets of the scanner to the IMU reference frame which is in this case equal to the body reference frame can be used to create a rotation matrix as shown in figure 4.11 (Right).

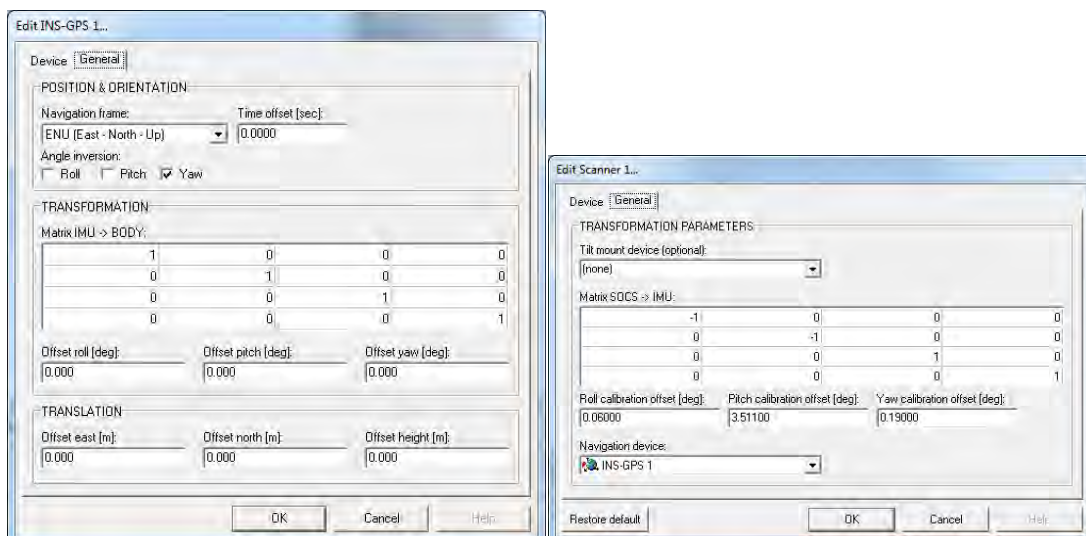


Figure 4.11: Transformation matrices to define the lever arms and angular misalignments of the IMU reference frame (Left) and the scanner reference frame (Right) with respect to the vessel (body) reference frame; Angular offsets are based on the prior QINSy calibration

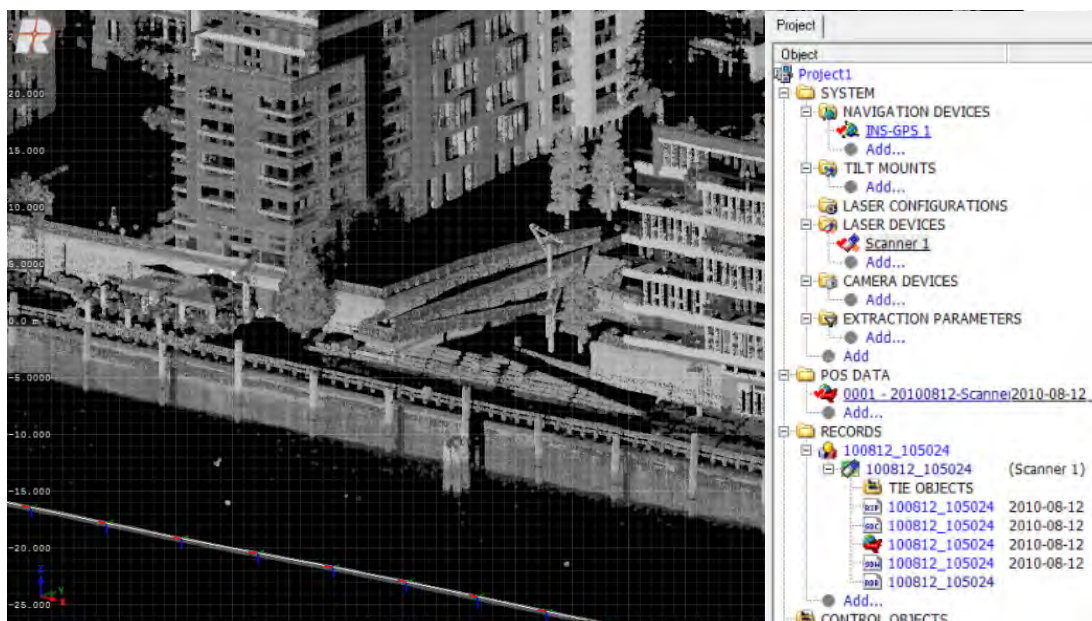


Figure 4.12: User interface of RiPROCESS after post-processing; Results are geo-referenced point clouds incl. intensity information (Left); Project structure contains parameters of INS and laser scanner, trajectory, raw and processed laser scan data (Right)

RiPROCESS uses these transformation matrices to convert the laser data from the SOCS to the IMU system and based on the IMU's transformation matrix finally to the geo-referenced ECEF system. After the processing procedure the scan data is available as geo-referenced point cloud as shown in figure 4.12. To use also the image data taken by the NIKON D700 digital camera for e.g. point cloud coloring the tool RiSCAN PRO has to be used. Although RiSCAN PRO is designed for the whole workflow from data acquisition, data visualization and data manipulation of terrestrial laser scan data it can also handle already processed mobile datasets from RiPROCESS. The images taken by the digital camera can be imported into the project structure of RiSCAN PRO. To geo-reference the photos a mounting and calibration file, which contains not only parameters of the lens but also the lever arms and angular misalignments from the camera with respect to the scanners coordinate system, can be used. Additionally it is possible to determine the outer orientation of the photographs by defining several pairs of picture and scan point coordinates. The picture coordinates can then be transformed to the global reference frame and be used to true-color code the point clouds as shown in the schematic workflow diagram in figure 4.13. Additionally RiSCAN PRO provides the user with tools for data cleaning and modeling which is not in the focus of this work.

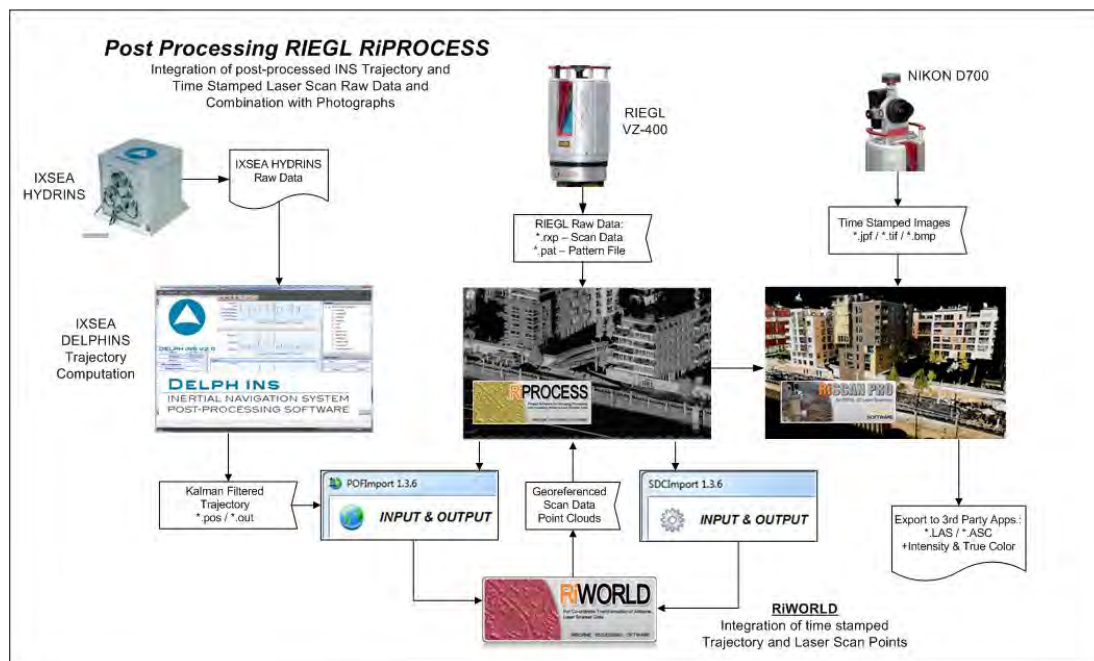


Figure 4.13: Schematic overview of RIEGL post processing. In this workflow the trajectory is based on DelphINS post-processing; Raw scan data and the trajectory are merged with respect to contained lever arms and angular offsets between sensor and body reference frame. Image data can be used in RiPROCESS to true-color code the point clouds.

4.3.2 Post Processing RIEGL RiPROCESS – Scan Data Adjustment

The workflow described in chapter 4.3.1 is based on known angular misalignments between laser scanner and IMU reference frame which were determined during a prior calibration procedure. The calibration was performed with QPS QINSy as described in detail in chapter 3.4 by processing different survey line configurations in order to determine the angular offsets in roll, pitch and heading.

To be independent from third party software RIEGL has implemented an automatic algorithm to compute these three values out of mobile scan datasets. This procedure is implemented in RiPROCESS and is called Scan Data Adjustment. The adjustment is based on several processed survey lines that cover the same objects with at least some common planar surfaces like façades of buildings or walls in all three dimensions. Similar to the manual calibration procedure in QPS QINSy the survey lines have to be sailed in opposite directions and with different scanner orientations. By comparing the point clouds of these multiple survey lines at a common planar surface the angular misalignments appear as pictured in figure 3.19 of chapter 3.4.2. But in contrast to the manual QINSy trial and error calibration procedure RiProcess automatically determines the deviations between corresponding planar surfaces (RIEGER et al., 2009). The corresponding planar surfaces - which are described by their size, location of center of gravity and normal vector - in two or more overlapping datasets were determined by an automated algorithm which can be influenced by user inputs to define e.g. the minimum number of scan points which can produce a planar surface. RIEGER points out that when corresponding planar surfaces in two or more point clouds were detected the scan data adjustment applies an ICP (Iterative Closest Point) algorithm which changes the angular misalignments iteratively in roll, pitch and yaw direction to determine a minimized distance error. As a result of this computation the three angular offsets of the laser scanner with respect to the IMU reference frame are determined and can be applied for reprocessing the datasets in RiProcess. Additionally a measure of accuracy for all used planar surfaces is computed as shown in figure 4.14 (Left).

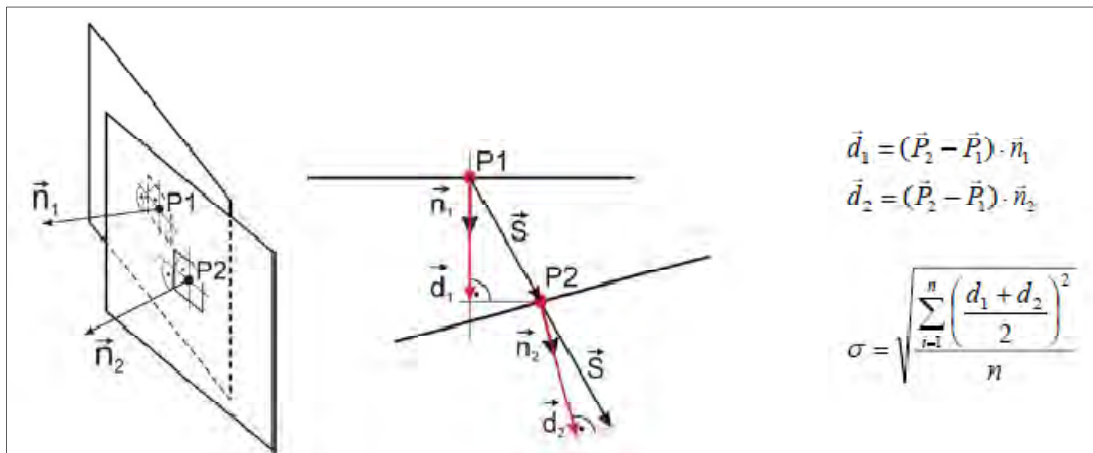


Figure 4.14: Spatial relationship between two corresponding planar surfaces found in at least two overlapping point clouds (Left and middle); The mean squared residual error distance of all used surfaces (Right) (RIEGER et al., 2009)

For a special survey project which will be presented in chapter 5 the scan data adjustment was applied. Eight separate survey lines were measured in the harbor basin “Grasbrookhafen” mapping several building façades and quay walls in opposite survey directions and different scanner orientations as pictured in figure 5.12. For all corresponding survey lines the scan data adjustment has been performed and new values for the angular misalignment have been determined. As mentioned before the parameters to detect a planar surface within the point clouds can be either user defined or default values. The scan data adjustment was performed with two different sets of plane search and matching parameters which is shown in figure 4.15.



Figure 4.15: Plane search and matching parameters for scan data adjustment. (Top) Default values for mobile mapping; (Bottom) User defined

With respect to RIEGL (2010-1) the six independent parameters can be described as follows:

- **Min. plane inclination** angle defines the minimum angle between the planar surface and the horizontal surface
- **Max. plane point deviation** is the maximum distance of a point to the best fitting plane to be used for the plane computation
- **Min. plane point count** defines the minimum number of points which are allowed create a plane
- **Search radius** is the maximum distance between two planes respectively their centers of gravity to be considered as corresponding
- **Angular tolerance** is the maximum angle between two plane normals to be considered as corresponding
- **Max. normal distance** describes the maximum projected normal distance of two corresponding surfaces

The results of each scan data adjustment computation are on the one hand the angular misalignments and on the other hand the mean squared error distance of all used pairs of planar surfaces and a histogram which describes the distribution of the even these distances.

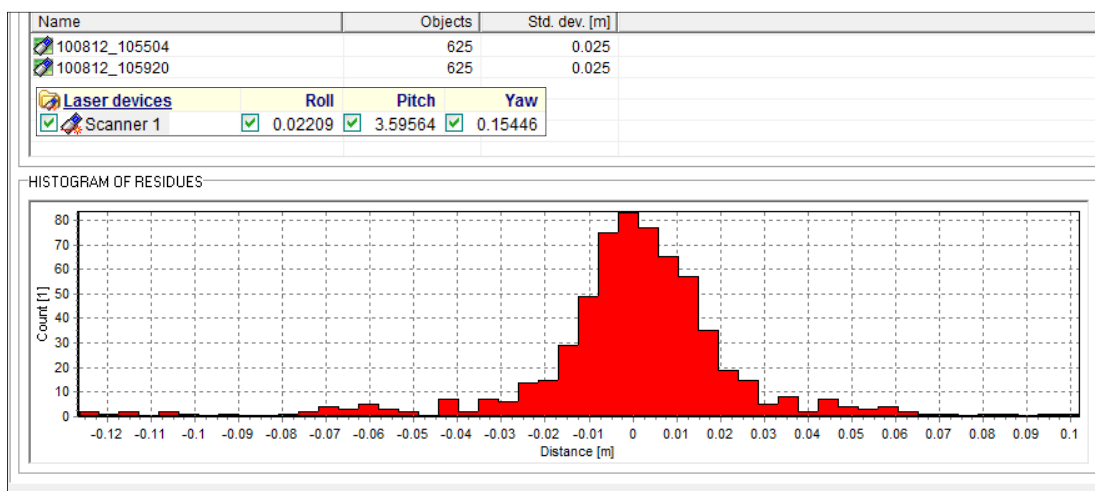


Figure 4.16: Results of a scan data adjustment; The histogram describes the distribution of the remaining distances between corresponding planar surfaces after adjustment

Additionally to the different plane search parameters the scan data adjustment was applied in two iterations. As start values for the angular misalignments in roll, pitch and yaw for the first iteration the QINSy calibration parameters and for the second iteration the mean values of the first iteration were used. Below in table 4.1 the results of all scan data adjustment computations are summarized whereas the complete statistics is attached in annex A-5.

Table 4.1: Results of a scan data adjustment; For each set of plane parameters the scan data adjustment was performed in two iterations; The final averaged values are based on the results of the second iteration

	QINSy	User - 1.1	User - 1.2	Default - 2.1	Default - 2.2	Mean
Rolloffset	0.060	0.0227	0.0210	0.0287	0.0229	0.0219
Pitchoffset	3.511	3.5847	3.5828	3.5766	3.5823	3.5826
Yawoffset	0.190	0.1627	0.1601	0.1647	0.1599	0.1600
Plane StdDev	-	0.0204	0.0202	0.0233	0.0213	-

The determined values were used to process all eight datasets. In an additional scan data adjustment procedure the corresponding point clouds were compared with each other without calculating new boresight angles. In this case only the accuracy measure and the distribution of surface deviations described in figure 4.14 were of interest in order to estimate the precision of mobile datasets. Although this investigation is done in chapter 5 this consideration can be a good estimate for a reachable accuracy. The scan data adjustment result protocols for these computations are attached in annex A-5 as well.

Table 4.2: Final evaluation of determined angular misalignments with respect to the mean squared residual error distance which is a measure for the precision used mobile datasets; Each pair of survey lines shares a certain number of corresponding planar surfaces.

line pair	match. Planes	Error/StdDev.	final Roll	final Pitch	final Yaw
0001+0004	327	0.0208	0.0219	3.5826	0.1600
0002+0003	808	0.0220	0.0219	3.5826	0.1600
0004+0005	428	0.0214	0.0219	3.5826	0.1600
0003+0006	973	0.0216	0.0219	3.5826	0.1600
0002+0007	896	0.0230	0.0219	3.5826	0.1600
0006+0007	1147	0.0197	0.0219	3.5826	0.1600
0001+0008	461	0.0247	0.0219	3.5826	0.1600
0005+0008	686	0.0213	0.0219	3.5826	0.1600
2+3+6+7	5594	0.0220	0.0219	3.5826	0.1600
1+4+5+8	2742	0.0228	0.0219	3.5826	0.1600
Mean Value		0.0219			

As shown in table 4.2 the mean standard deviation of surface differences is calculated of around 2.2 centimeter which has to be evaluated in chapter 5.4. In general it can be stated that the scan data adjustment is a user friendly tool which derives the angular misalignments almost automatically. Different overlapping survey lines have to be surveyed in areas with planar features in all three dimensions like buildings. This is needed to find enough corresponding planar surfaces in the point clouds to perform the calculation properly. Although the accuracy of the determined angular offsets has to be evaluated the whole procedure is straight forward and not user dependent.

With the exception of the values of angular misalignment the postprocessing workflow in RiPROCESS is the same as presented in the chapter before.

4.4 Summary

In the chapters before five more or less different processing procedures were presented. The online processing produces geo-referenced point clouds in the field which enables to user to make first quality control during data acquisition. Although the online trajectory can contain systematic artifacts like GNSS jumps or INS drift effects the online-processed results give a good overview of the performance of the mapping system and can be used to fine-tune the survey configuration e.g. from the point of laser point density and distribution which is not possible in post-processing. Additionally the online integration of all contained sensors can reveal sensor or systematic errors of the whole system configuration. Without question a following post-processing procedure especially the trajectory filtering process improves the accuracy and the reliability of mobile mapped datasets significantly. QINSy's post-processing capabilities enable the user to go back to online recorded sensor raw data but also to implement certain external datasets like a post-processed trajectory. With additional data manipulation tools QINSy can be used to improve the measurement result iteratively. Another advantage of the QINSy package can be the integration of several totally different mapping sensors like multibeam echosounder and sidescan sonar to built up a total hydrographic solution. In contrast to this RIEGL focuses only on the post-processing of laserscan data and does thereby a good job. The software RiPROCESS combines scanner raw data and external trajectory data to process geo-referenced point clouds. With the automated scan data adjustment RiPROCESS provides a tool to compute the angular misalignments of the mapping sensor out of the scan data, whereas in QINSy an extensive calibration procedure is needed to derive these required values manually. Another advantage of the RIEGL approach is the possibility to process camera data together with laser scan point clouds. RiSCAN PRO provides different tools to geo-reference unregistered photographs in order to compute true color point clouds, orthophotos or panorama images. Although QINSy is able to interface different cameras the capabilities are limited to the acquisition mode. Here the absolute orientation is online determined and stored as an attribute file together with the image. Further processing steps can only be performed with third party software.

A combination of both software packages would complement one another's advantages to build the complete mobile mapping processing solution. The online and multisensory capabilities of QINSy ensure a proper sensor integration and a priori quality assurance during the survey whereas the RIEGL software can take over the calibration procedure and the laser scanning processing.

5. Accuracy analysis

As described in chapter 3 the established mobile mapping system consists of different sensors which provide different datasets containing different errors or respectively uncertainties. For example a GNSS receiver (Global Navigation Satellite System) provides the user with at least 3D position information in a certain horizontal and vertical reference frame. The uncertainties of even this horizontal and vertical information differ because of the inherent geometric approach of a GNSS system. It is well known that the accuracy of the GNSS height is less accurate than the horizontal component but both of them propagates their errors to the point of measurement, in this case the laser foot print at the target object. But not only the individual uncertainties of all contained sensors, but also the lever arm measures between the sensors can contain a certain amount of uncertainty.

This chapter deals in the first part 5.1 with the approach of the total propagated error. By performing *a priori* computations of the system uncertainties with respect to the law of error propagation a theoretical error budget will be evaluated. These investigations will reflect the possible performance of the whole mobile mapping system.

Not only the theoretically possible accuracy of the system is of importance, but also the accuracy reached in reality is of high interest. The second part 5.2 to 5.5 will present the results of practical accuracy analysis with real data. Different datasets collected by mobile, but also by terrestrial laser scanning will be compared with each other in order to determine values for relative and absolute accuracy.

5.1 Uncertainty of Mobile Mapping

As described in detail in chapter 3 the system which will be evaluated in this section consists of several independent sensors which were mounted on one platform, the survey vessel "Deepenschriewer III". For each of these sensors the accuracy expressed by their standard deviations are given either by the system developer or by own investigations or assumptions. All these error information have to be summarized and propagated to the point of measurement by applying the law of error propagation. The result of these computations is the *Total Propagated Error*. The total propagated error is a *a priori* accuracy estimation for every measurement point by taking into account every source of error.

For the echo sounding part of a hydrographic mobile mapping system the term „TPE - Total Propagated Error“ was introduced some years ago by the Canadian Hydrographic Service (CHS) and the Ocean Mapping Group (OMG) of the University of New Brunswick (HARE et al., 1995). In this investigation all error sources related to multibeam and multitransducer echosounder systems were evaluated and equations have been established to compute a complete, realistic error budget of such a system. In this study error models for different survey vessels and their sensor configurations were created. It is important to mention that the result of the TPE computation cannot represent systematic errors introduced by a bad calibrated system. For this reason the total propagated uncertainty is always only a good estimate for the real error.

However the approach of the TPE was not only the basis for uncertainty estimation but moreover the basis for automatic cleaning algorithms like *CUBE- Combined Uncertainty and Bathymetric Estimator* (CALDER, 2003) and bathymetric data management approaches like the *Navigation Surface* (SMITH, 2004).

HARE et al. (1995) have classified the different error sources as follows:

Error sources of vertical sounding error:

- Echo sounding: (errors in range and beam angle measurements)
- Roll: (errors in measurement, stabilization and misalignment)
- Pitch: (errors in measurement, stabilization and misalignment)
- Heave: (errors in measurement and induced heave)
- Refraction: (sound speed errors in beam steering and ray tracing)
- Dynamic draft: (squat effects and loading changes)
- Water level: (errors in tide measurement and interpolation)
- Lever arms: (errors in initial measurement)

Error sources of horizontal sounding errors

- Positioning: (DGNSS position error)
- Latency of position: (error by the age of differential correction)
- Echo sounding: (errors in range, beam angle, refraction and motion, footprint)
- Heading: (errors in measurement and misalignment)
- Lever arms: (errors in initial measurement)

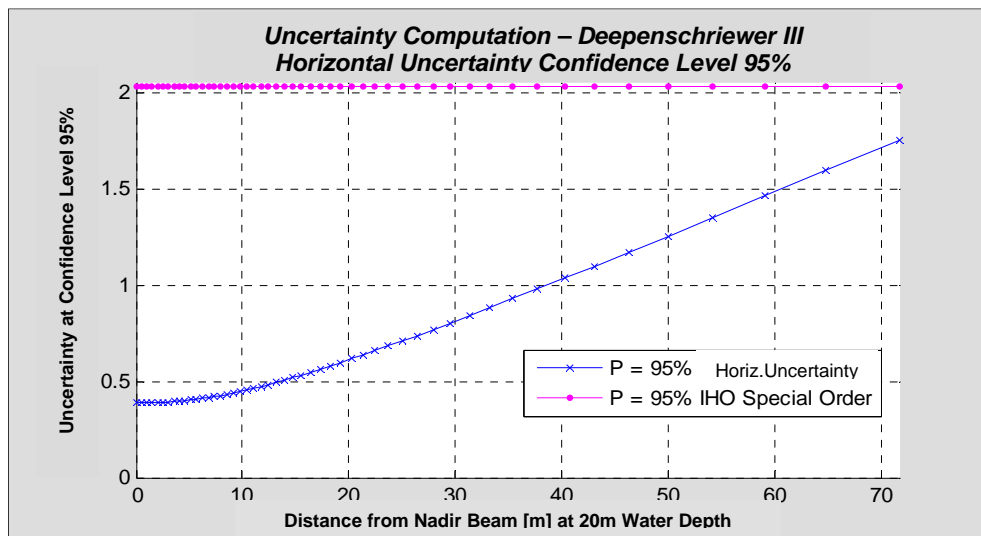
In a prior investigation (THIES, 2007) the error budget of the “Deepenschriewer III” as a multibeam echosounding survey vessel has been evaluated with respect to the error equations of HARE (2001) and the accuracy information of all contained sensors. The former “Deepenschriewer III” contained of following sensors:

- Reson Seabat 8101 multibeam echosounder (150° swath, 1.5° beam width)
- Trimble 5700 RTK-GNSS receiver incl. SAPOS HEPS differential correction
- TSS MAHRS attitude and heading system ($\pm 0.03^\circ$ roll/pitch, $\pm 0.336^\circ$ heading)
- Reson SVP14 sound velocity profiler ($\pm 0.25\text{m/s}$)

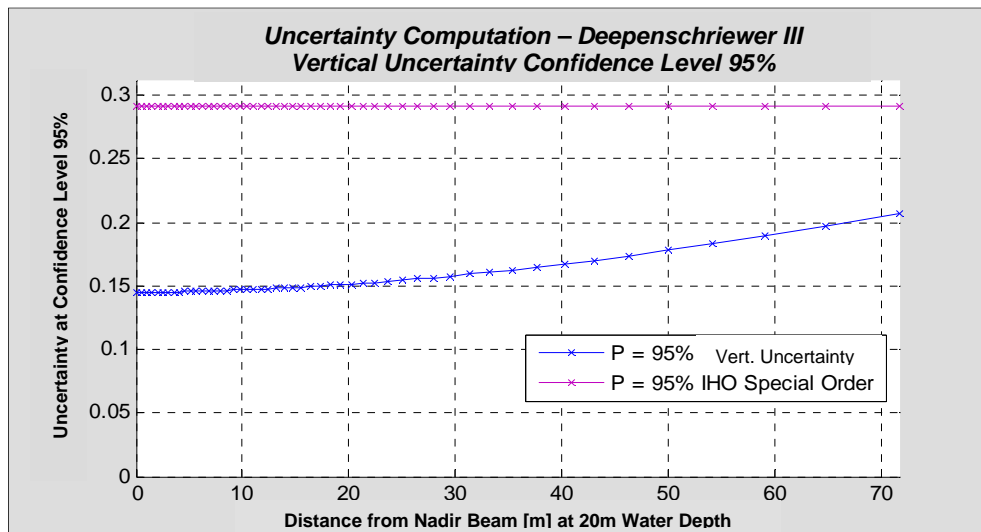
The results of the uncertainty computations are shown in the figure 5.1. The most significant horizontal error source is based on the beam width of the multibeam transducer. On the one hand the size of the footprint depends on the measurement range. But also with increasing distance to the nadir beam the footprint of outer beams and therefore their horizontal uncertainty increases as well because of the grazing angles.

The major effect on the vertical uncertainty is based on the accuracy of the motion sensor and the accuracy of sound speed determination in the water column. It is obvious that the outer beams are less accurate than the beams near to the nadir beam.

The following figures 5.1 show schematically the behavior of the horizontal and vertical uncertainty at water depths of 20m. It is important to mention that in the term of TPE the uncertainty is scaled to a confidence level 95%.



a)



b)

Figure 5.1: a) Uncertainty of a soundings position in water depths of 20m b) Uncertainty of a soundings depth in water depths of 20m; The blue graph displays the uncertainty for the survey system „Deepenschriewer III“; The purple line is with respect to the IHO S-44 the maximum allowed uncertainty for special order areas; The uncertainty is scaled to a confidence level of 95% (THIES, 2007)

As shown above in figure 5.1.a the horizontal uncertainty increases from $\pm 0,40\text{m}$ at the nadir beam with a range of 20m to $\pm 1,75\text{m}$ at the outermost beam with a range of 73m. In contrast to the horizontal uncertainty the vertical TPE increases from almost 15cm up to 21cm.

To improve the uncertainty of such a survey system it has to be upgraded with a high resolution (high frequency) multibeam echosounder producing small beam widths. To increase the vertical part of uncertainty a more accurate motion and heading sensor like an inertial navigation system has to be used.

In comparison to the main error sources the biases because of the uncertainty of RTK-GNSS position and lever arms have less effect to the whole error budget. This will change for the laser scanning part of the mobile mapping system.

Similar to the uncertainty computation of a multibeam system the error sources of mobile laser scanning system can be classified into errors in vertical and horizontal direction with respect to MANSION (2010) and WANG and JIN (2010) as follows:

Error sources of vertical laser point error:

- Laser scanning: (errors in range and angle measurements)
- Attitude: (errors in roll, pitch measurement)
- Lever arms: (errors in determination of lever arms between sensors)
- Positioning: (errors in GNSS/INS height measurement)

Error sources of horizontal laser point error:

- Laser scanning: (errors in range and angle measurements)
- Attitude and heading: (errors in roll, pitch, yaw / heading measurement)
- Lever arms: (errors in determination of lever arms between sensors)
- Positioning: (errors in GNSS/INS position measurement)

It is well known from chapter 2.3 that from point of laser scanning a lot of instrumental and non instrumental errors exist which were not above-mentioned like eccentricity of scan center, errors in collimation and horizontal axis, errors in atmospheric values. For this accuracy estimation all these relatively small error sources will be ignored in order to keep the error computation as simple as possible. Overall twelve parameters as shown in table 5.1 were taken into account for this error estimation.

The scanners own coordinate system (SOCS) is spherical and consists of two angles which describe the two rotations of measurement. As shown below in figure 5.2 the angle Theta describes the vertical rotation of the laser beam whereas the angle Phi stand for the horizontal rotation around axis Z of the SOCS.

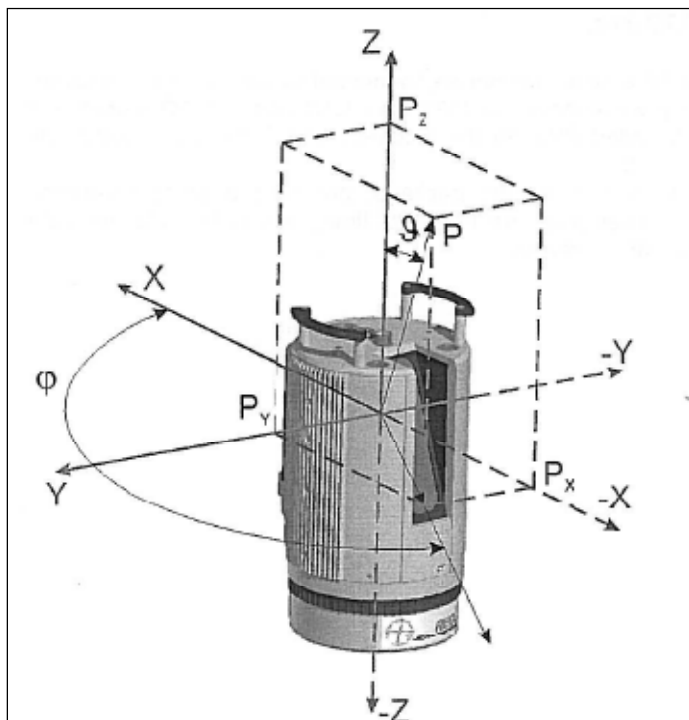


Figure 5.2: The scanners own coordinates system. The spherical coordinates are described by the angles Theta and Phi (RIEGL, 2009)

To describe a point of measurement with respect to the SOCS in Cartesian coordinates following point vector can be used:

$$P = \begin{bmatrix} R \cdot \sin(\Theta) \cdot \cos(\Phi) \\ R \cdot \sin(\Theta) \cdot \sin(\Phi) \\ R \cdot \cos(\Theta) \end{bmatrix} \quad (5.1) \quad \text{with: } \begin{array}{l} R = \text{range} \\ \Theta = \text{laser tilt angle} \\ \Phi = \text{laser pan angle} \end{array}$$

To take the uncertainty of the lever arms between laser scanner and motion sensor and the uncertainty of the INS position into account a translation vector has to be added to the point vector. In order to do so it has to be assumed that the SOCS is perfectly aligned to the IMU reference frame. Otherwise the small angular misalignments, determined by the calibration have to be used to rotate the SOCS to the IMU coordinates system.

$$T = \begin{bmatrix} X_{INS} + \Delta X_{INS-Laser} \\ Y_{INS} + \Delta Y_{INS-Laser} \\ Z_{INS} + \Delta Z_{INS-Laser} \end{bmatrix} \quad P + T = \begin{bmatrix} X_{INS} + \Delta X_{INS-Laser} + R \cdot \sin(\Theta) \cdot \cos(\Phi) \\ Y_{INS} + \Delta Y_{INS-Laser} + R \cdot \sin(\Theta) \cdot \sin(\Phi) \\ Z_{INS} + \Delta Z_{INS-Laser} + R \cdot \cos(\Theta) \end{bmatrix} \quad (5.2)$$

To correct these new coordinates by the three rotations roll, pitch and yaw which were measured by the motion sensor a rotation matrix has to be applied to the vector (5.2). The roll angle θ defines the rotation around the X axis in IMU reference frame. The pitch angle φ is the rotation around the Y axis, whereas the angle ψ stands for the rotation around the Z axis.

$$R_X = \begin{bmatrix} 1 & 0 & 0 \\ 0 & \cos(\theta) & -\sin(\theta) \\ 0 & \sin(\theta) & \cos(\theta) \end{bmatrix} \quad (5.3)$$

$$R_Y = \begin{bmatrix} \cos(\varphi) & 0 & \sin(\varphi) \\ 0 & 1 & 0 \\ -\sin(\varphi) & 0 & \cos(\varphi) \end{bmatrix} \quad (5.4)$$

$$R_Z = \begin{bmatrix} \cos(\psi) & -\sin(\psi) & 0 \\ \sin(\psi) & \cos(\psi) & 0 \\ 0 & 0 & 1 \end{bmatrix} \quad (5.5)$$

The three single rotations have to be summarized according to WANG, JIN (2010):

$$R = \begin{bmatrix} \sin(\psi) \cdot \sin(\theta) \cdot \sin(\varphi) + \cos(\psi) \cdot \cos(\varphi) & \cos(\psi) \cdot \sin(\theta) \cdot \sin(\varphi) - \sin(\psi) \cdot \cos(\varphi) & \cos(\theta) \cdot \sin(\varphi) \\ \sin(\psi) \cdot \cos(\theta) & \cos(\psi) \cdot \cos(\theta) & -\sin(\theta) \\ \sin(\psi) \cdot \sin(\theta) \cdot \cos(\varphi) - \cos(\psi) \cdot \sin(\varphi) & \cos(\psi) \cdot \sin(\theta) \cdot \cos(\varphi) + \sin(\psi) \cdot \sin(\varphi) & \cos(\theta) \cdot \cos(\varphi) \end{bmatrix} \quad (5.7)$$

To rotate the coordinates from the IMU reference frame to the body frame the complete rotation matrix (5.7) has to be applied to the vector (5.2). As a result all coordinates are now defined in the vessels body reference frame corrected by the motion data.

It is important to mention that without the assumption that the laser scanner is perfect aligned to IMU a lot of computations have to be done to take the calibration parameters respectively the angular misalignments into account. All following uncertainty computations were done in the east-north-up (ENU) reference frame instead of the global earth-centered-earth-fixed (ECEF) coordinate system because of reasons of simplicity.

The result vector from the multiplication of the rotation matrix R (5.7) and the position vector $P+T$ (5.2) contains the functions to compute the X, Y and Z coordinates of a laser point in the ENU reference frame. To compute the uncertainty for each of these components the Gaussian law of error propagation of a function with several independent variables has to be applied.

$$\sigma_f(x_1, \dots, x_n) = \sqrt{\sum_{i=1}^n \left(\frac{\partial f}{\partial x_i} \cdot \sigma_i \right)^2} \quad (5.8)$$

A slightly different approach is to compute the maximum absolute error threshold by using the law of linear error propagation in order to compute the total differential of a function with several independent variables.

$$\sigma_{f_{\max}}(x_1, \dots, x_n) = \sum_{i=1}^n \left| \frac{\partial f}{\partial x_i} \cdot \sigma_i \right| \quad (5.9)$$

Both formulas are based on the partial derivations of the function f with respect to each of the twelve input parameters. The resulting vector contains the function f for each component in X, Y and Z. The result of each partial derivation is multiplied by the standard deviation of the corresponding variable and summed up according to the formulas (5.8) and (5.9). Both error estimates are scaled to 68.3% confidence level.

According to the established mobile mapping system the initial parameters are defined by the accuracy information of the system developer as summarized in the table below.

Table 5.1: Accuracy information of used sensors according to system developer information

System	Parameter	Accuracy	Unit
Laser Scanner	Range σ_R :	0.005	m
	Pan Angle σ_Φ :	0.001	°
	Tilt Angle σ_Θ :	0.001	°
Motion Sensor / IMU	Pitch σ_φ :	0.03 / 0.01	°
	Roll σ_θ :	0.03 / 0.01	°
	Yaw σ_ψ :	0.336 / 0.034	°
Lever Arms	$\sigma_{X_{mru-las}}$:	0.001	m
	$\sigma_{Y_{mru-las}}$:	0.001	m
	$\sigma_{Z_{mru-las}}$:	0.001	m
GNSS/IMU	$\sigma_{X_{gps=sXg}}$:	0.02 / 0.01	m
	$\sigma_{Y_{gps=sYg}}$:	0.02 / 0.01	m
	$\sigma_{Z_{gps=sZg}}$:	0.03 / 0.02	m

In the following part of this investigation several effects of different survey configurations will be evaluated. It is for example clear that when the laser scanner in profile scan mode is pointing to the starboard side of the vessel respectively perpendicular to the X-Axis in IMU frame, a uncertainty in roll produce a uncertainty in the Z coordinate of the laser footprint. On the other hand it is also obvious the high uncertainty in yaw / heading measurement creates a uncertainty in the X/Y plane increasing with distance to the sensor.

Following effects respectively influences on the uncertainty will be discussed in more detail:

- Influence of range
- Influence of vertical laser orientation – tilt angle
- Influence of horizontal laser orientation – pan angle
- Comparison between INS and motion sensor accuracies
- Comparison between Gaussian and linear error propagation

It is apparent that with increasing distance from sensor of measurement to point of measurement the uncertainty increases as well. The figure 5.3 below describes distance effects to the uncertainty divided for each component of the 3D coordinate. In this configuration the laser scanner is pointing to starboard with a tilt angle of 60° . As one can see the uncertainty for X and Y starts at $\pm 1\text{cm}$ which is based on the horizontal accuracy of the INS. In contrast to the Y coordinate with $\pm 2\text{cm}$ the X coordinate uncertainty rises up to $\pm 10.5\text{cm}$ at a range of 200m. The reason for this 5 times higher uncertainty is the heading standard deviation of the INS which is less accurate than the roll and pitch values. The height component which is at short distances almost only influenced by the INS height accuracy increases with distance because of the roll and pitch accuracy of the INS.

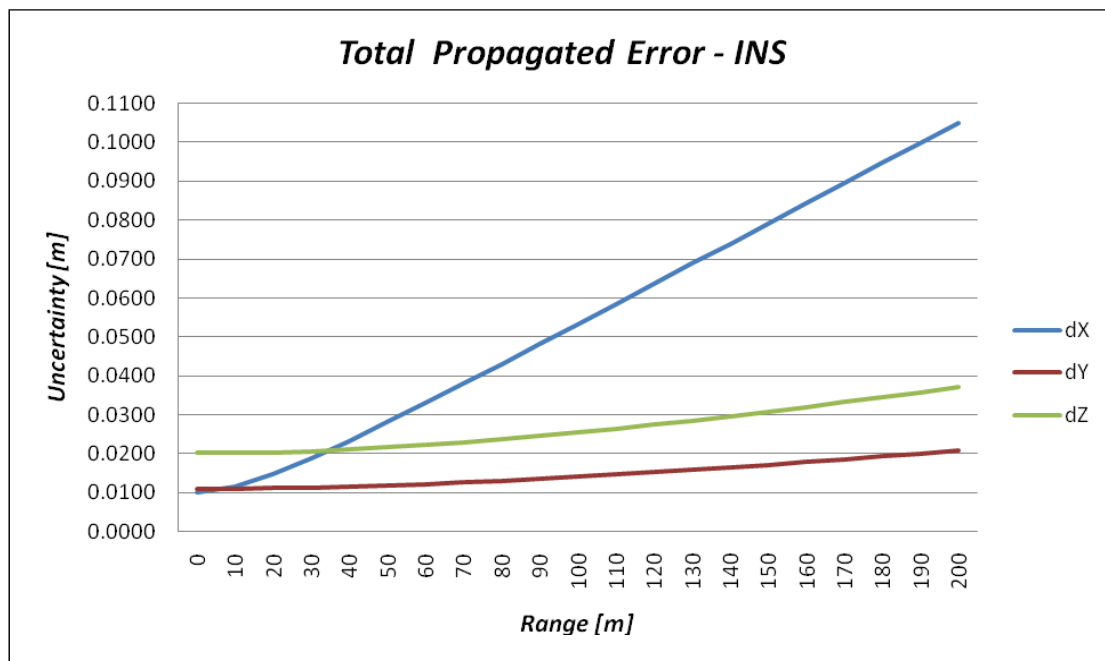


Figure 5.3: Range dependent uncertainty of X, Y and Z coordinates of a laser footprint whereas the laser is oriented perpendicular to the X Axis of the vessel with a tilt angle of 60°

The next figure 5.4 describes the difference in uncertainty between the used GNSS added INS and a common attitude and heading sensor in combination with RTK-GNSS. When comparing the standard deviations of both systems with respect to table 5.1 one can imagine that the uncertainty of the X component is skyrocketing when using a less accurate heading sensor. At ranges up to 200m the X coordinate has got an theoretical uncertainty of more than $\pm 1\text{m}$, which is not acceptable for a mobile laser scanning system although the Y and Z coordinates are on a cm-level uncertainty.

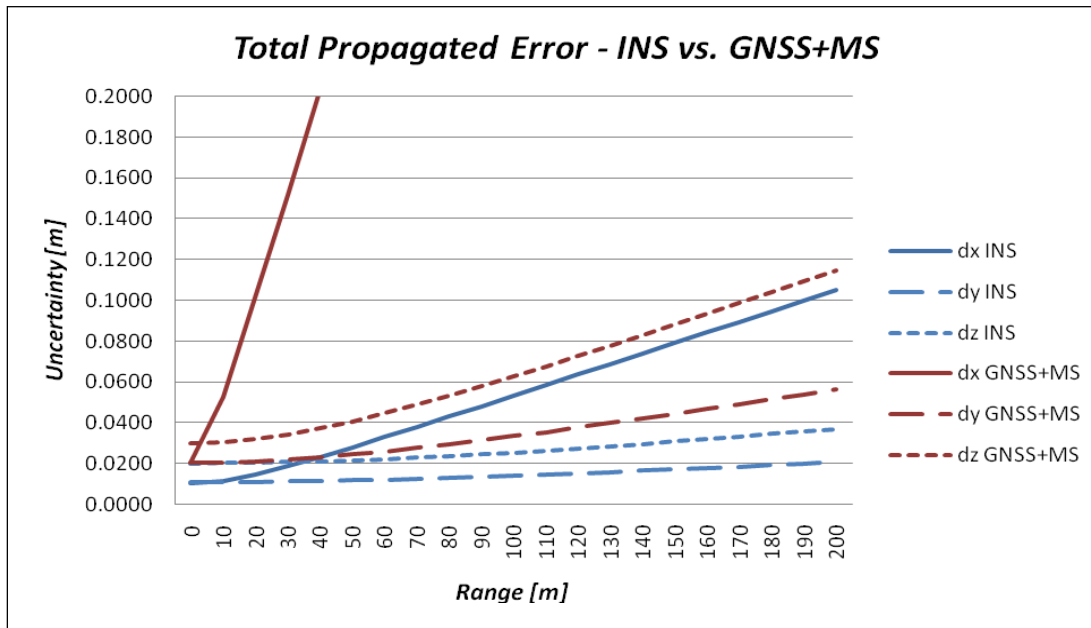


Figure 5.4: Comparison of X, Y and Z coordinate uncertainties of corresponding laser footprint produced by INS and AHRS measurements; The laser is oriented perpendicular to the X Axis of the vessel with a tilt angle of 60°

As a result of the comparison above it is evident that the performance of a mobile laser scanning system stands and falls with the accuracy of heading measurement. For this reason all following considerations are based on INS accuracies.

The figures 5.5 and 5.6 deal with changes in uncertainty based on differences in scanner orientation. When performing mobile laser scanning the scanner is orientated fixed in the horizontal plane that means with a fixed pan angle whereas the rotating polygon mirror deflects the laser beam in vertical direction described by the tilt angle. The tilt angle is defined as shown in figure 5.2 as the angle between the upward pointing Z axis of the laser scanner and the axis of the laser beam and is limited for the RIEGL VZ-400 from 30° to 130° .

As shown in Figure 5.5 the effects of motion and heading uncertainties change with increasing tilt angle. When the laser beam is tilted to 30° a roll angle uncertainty for example has a bigger impact on the uncertainty of a laser footprint's horizontal position than on the vertical height. If the laser beam is almost oriented horizontally the horizontal uncertainty of the laser footprint is almost not influenced by the roll uncertainty.

Generally it can be said that all measurement points of a profile scan have different uncertainties corresponding to their tilt angle which is very similar to bathymetric depth measurements by using a multibeam echosounder.

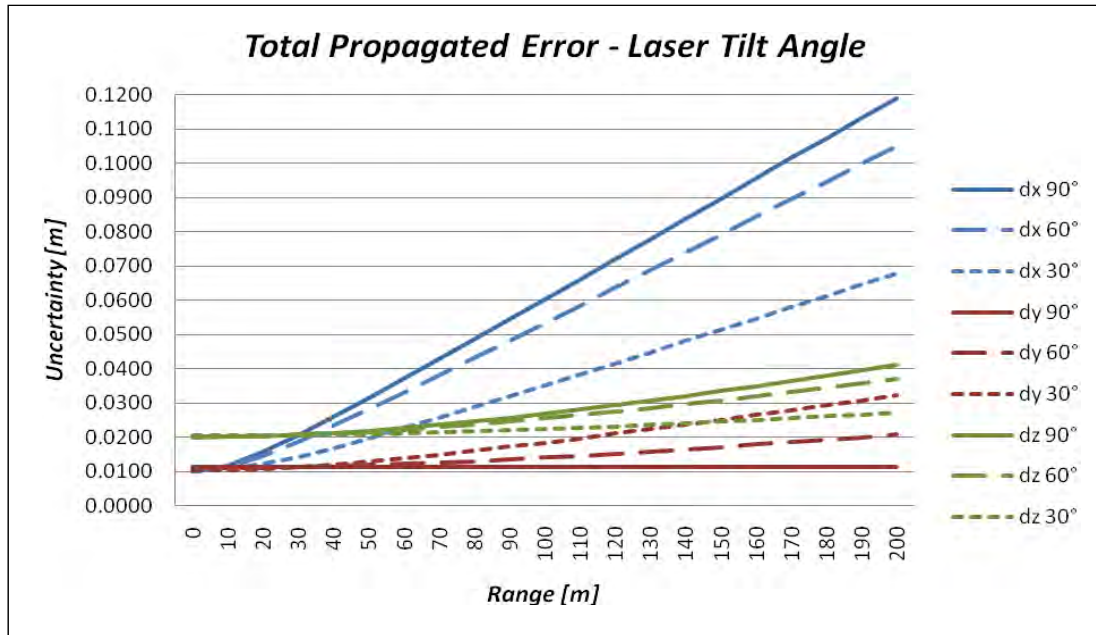


Figure 5.5: Changes in uncertainty of X, Y and Z coordinates depending on the tilt angle of the laser beam; The laser is oriented perpendicular to the X Axis of the vessel means pointing to starboard

As shown above the uncertainty of the X coordinates decreases from almost $\pm 12\text{cm}$ at a range of 200m and a tilt angle of 90° to less than $\pm 7\text{cm}$ at a tilt angle of 30° . In this case the influence of less accurate heading measurements decreases with decreasing tilt angles.

On the other hand it is not unusual to change the horizontal orientation of the laser scanner which is described by the pan angle.

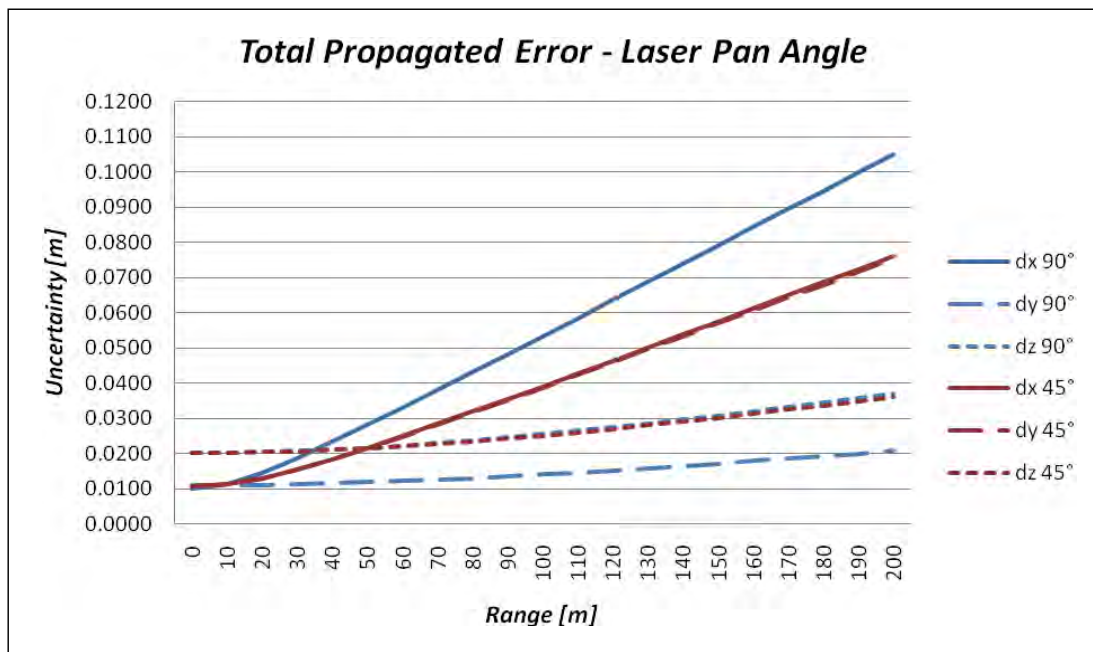


Figure 5.6: Changes in uncertainty of X, Y and Z coordinates depending on the pan angle of the laser scanner; A pan angle of 90° defines a laser scanner orientation directly to starboard of the vessel whereas 45° pan angle means an orientation between starboard and ahead. The tilt angle of the laser beam is set to 60°

When surveying coastal areas or directly at shoreline constructions buildings and other facilities at land are mostly orientated parallel to the waterside. To survey these buildings it is not useful to have the laser scanner oriented perpendicular to the X axis of the vessel because of the grazing angles at the side walls of even these facilities.

As presented in figure 5.6 two different cases are compared with each other. The most common configuration whereas the laser scanner is directly oriented to the starboard side of the vessel produce a non-homogeneous distribution of uncertainties. As discussed before the most critical error source is the heading accuracy of the system. In this configuration the heading uncertainty is completely propagated to the uncertainty of the X coordinate. If the laser scanner is rotated to a starboard ahead orientation with a pan angle of 45° the effect of the heading accuracy is shared by the X and Y uncertainties to equal parts. This configuration doesn't improve the accuracy of the system but the uncertainties in the X-Y plane are homogeneous.

As mentioned before there are two different approaches to estimate errors respectively uncertainties. By definition the Gaussian law of error propagation defines the uncertainty of a mean value which was computed out of several independent parameters and their well known uncertainties. The maximum error threshold is a worst case scenario by taking the absolute value of the individual error threshold of each contained parameter into account. Below figure 5.7 shows the differences between both approaches of error propagation for the X, Y and Z coordinates. The following section of this chapter investigates which of these error estimation approaches does fit better to the true accuracy of mobile laser scanning determined by comparison with a reference dataset.

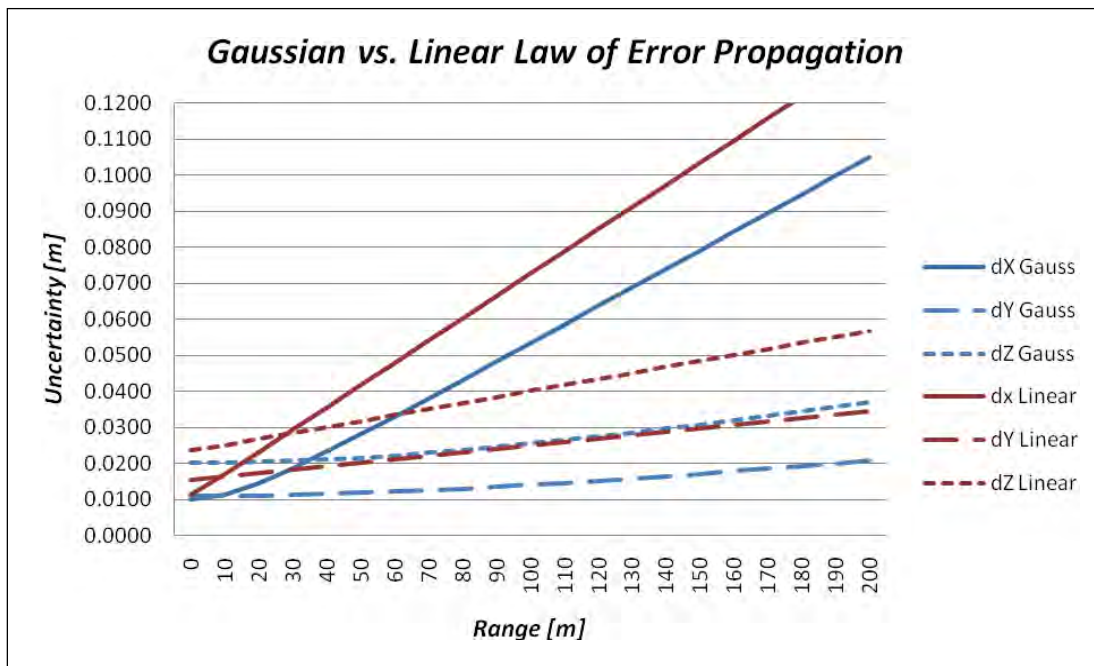


Figure 5.7: Comparison of Gaussian and linear law of error propagation whereas the Gaussian approach defines the uncertainty of the mean value instead of the maximum error threshold of the mean value defined by the linear approach; The laser is oriented perpendicular to the X Axis of the vessel with a tilt angle of 60°

To summarize the uncertainty analysis it is important to mention that the uncertainty computation for the echosounding part is similar to the laser scanning part of a hydrographic mobile mapping system. They differ only in their error sources and error equations and finally in their magnitudes if both are scaled to 95% confidence level as shown in figure 5.8.

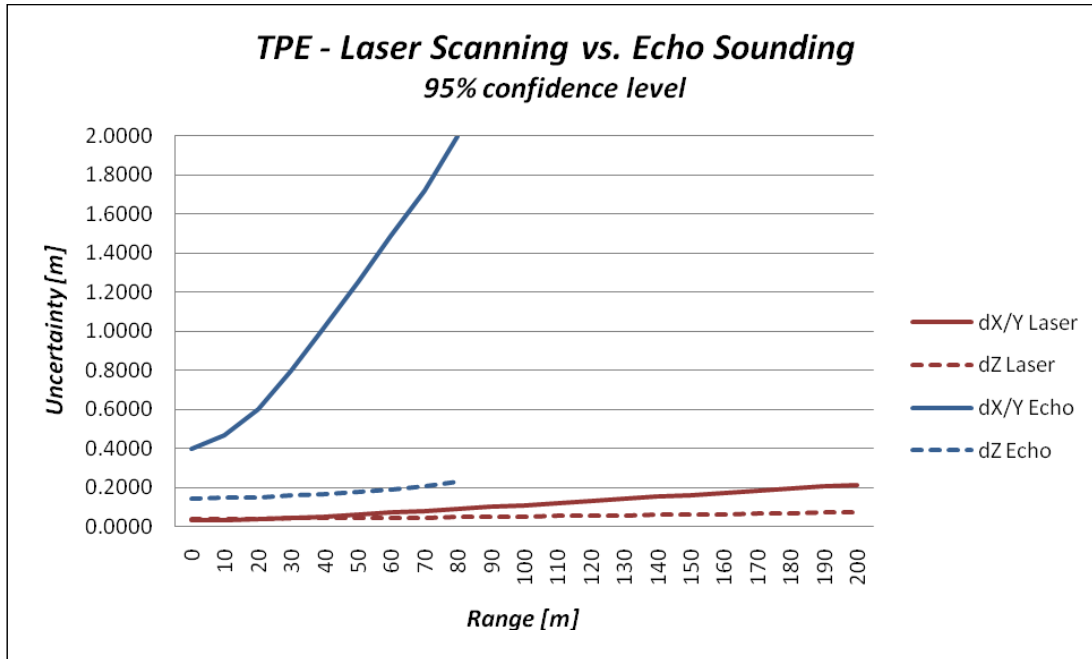


Figure 5.8: Range depending uncertainty of X+Y and Z coordinates of a laser scanning system in comparison with a multibeam echosounding system. Uncertainties are scaled to 95% confidence level.

To improve the horizontal uncertainty of the echosounding system significantly it is necessary to use a high resolution, high frequency multibeam echosounder in combination with a INS. The vertical uncertainty of such a system is mostly influenced by the accuracy of sound speed measurement which is not only needed for the beam forming process but also for the ray tracing of the echo beams.

In contrast to bathymetric uncertainties which are mainly derived from the soundings “huge” footprints the heading accuracy is the Achilles’ heel of the laser scanning uncertainty. Although current INS sensors have improved the heading accuracy by one order in magnitude compared to a common gyro, this error source is still responsible for the performance of such a system. But not only the attitude and heading measurements effect the final uncertainty at a laser footprint but also the accuracy of the positioning system in horizontal and vertical direction raises in significance compared to echosounding.

It was pointed out that all laser points have different uncertainties depending on range, tilt and pan angle, which is also very similar to echosounding. For this reason it can be expected that the TPE will play in future a certain role in mobile laserscan dataprocessing similar to bathymetric data cleaning algorithms. For example during the noise reduction process points with higher uncertainty will be filtered and more accurate data will be kept.

5.2 Reference Measurement

Chapter 5.1 has shown the theoretical capabilities of the established mobile mapping system by the evaluation of the total uncertainty. It has to be kept in mind that the uncertainty computation doesn't take systematic errors into account which can be introduced for example by an inaccurate boresight alignment or gross errors in the lever arms. For this reason the uncertainty of a system is always only a good approximation of the real error.

The only way to evaluate the absolute error of a system is to compare a mobile captured dataset with a reference dataset. This reference dataset should have a higher accuracy compared with the mobile dataset at least by one order in magnitude. Reference datasets can be discrete points from RTK-GNSS or total station measurements, point clouds from for example aerial LIDAR or terrestrial laser scanning. In some investigations a 3D CAD model was used to evaluate the accuracy of mobile recorded datasets.

For this thesis a dataset was created by static terrestrial laser scanning. From different positions on land complex building facades were measured with the same laser scanner which was also used in mobile mode. As shown below in figure 5.9 six fixed reference points (red) were used to registrate the three different scan position (blue). The absolute X and Y coordinates of these points with respect to a local horizontal and vertical reference frame were determined by GNSS measurements, the heights by levelling.

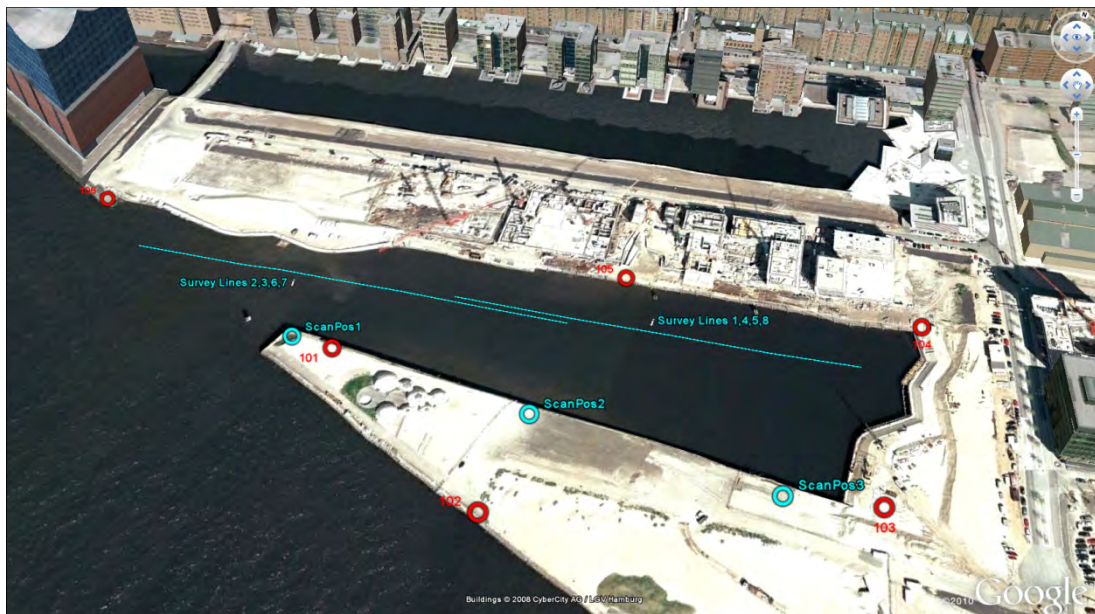
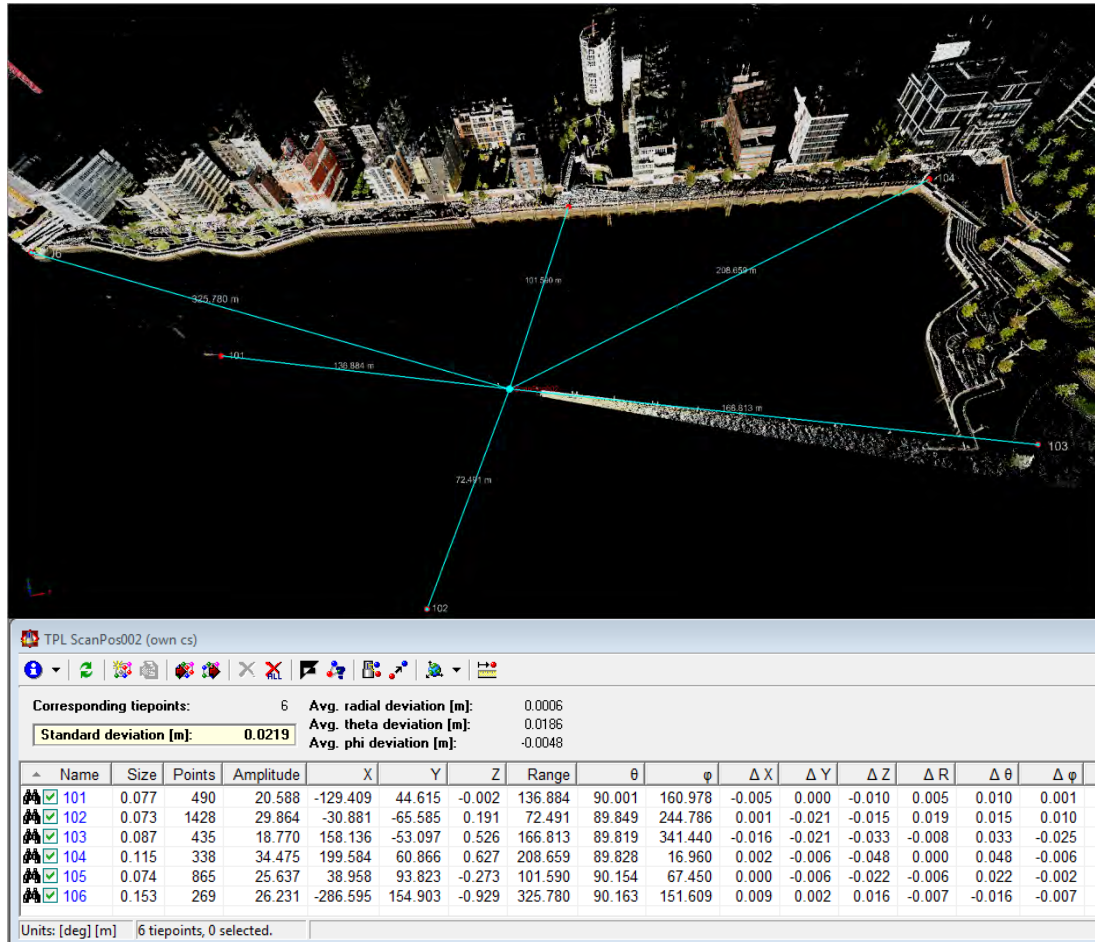


Figure 5.9: Overview of the area used for the reference measurement. Data was collected in a new district of Hamburg, the HafenCity; The tie points (red) for this measurement are spread around the harbor basin Grasbrookhafen whereas the scan positions (blue) are located on the opposite side to house facades; Additionally the eight mobile survey lines are shown (Google Earth)

As result a registered reference point cloud was created. The results of the registration indeed are not as accurate as expected. As shown in figures 5.10 the standard deviation for scan position 2 is around $\pm 2\text{cm}$ which is the highest value of all three scan positions.

The reason for this can be the tie point accuracy in horizontal direction which depends on the accuracy of the used GNSS. However, if we take the scan distances between scan position and tie points into account which are widespread from 70m up to 320m the registration result is still well suited to produce a reference dataset.

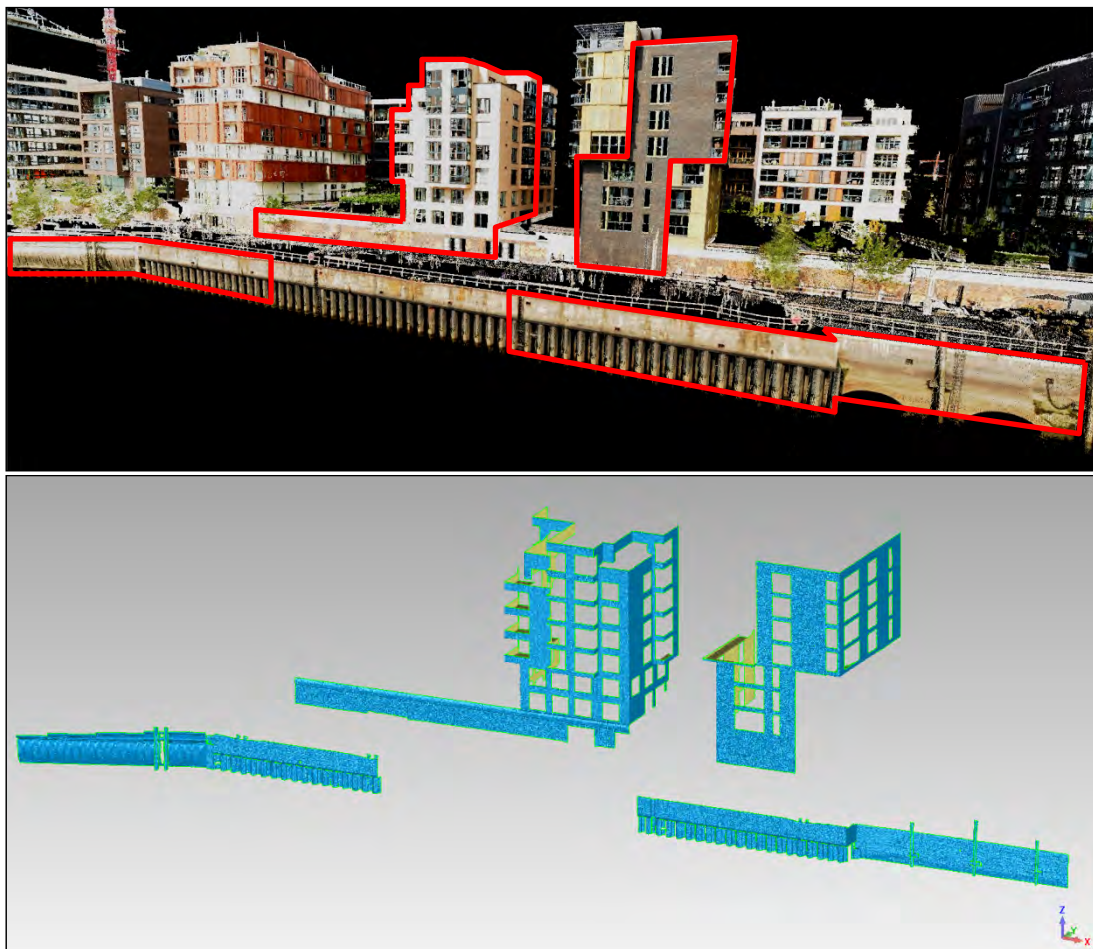


Figures 5.10: Overview of the reference point cloud in true color mode containing scan position 2 and all used tie points including their scan distances (Top); Below the result table of a scan registration done with RiSCAN PRO containing all used tie point points incl. their deviations and the final accuracy of the computation described by standard deviation

Although the reference dataset and mobile captured datasets map the complete esplanade of the northern part of the Grasbrookhafen it is not advisable to compare them completely. Instead objects have to be found in both datasets which are representative for the whole dataset containing not only information about differences in position but also in the height component. It is also important to detect remaining systematic errors in the mobile dataset which mostly depend on the object height respectively the vertical scan angle.

A lot of different empirical accuracy investigations have been performed in the past to compare mobile scanning datasets with reference datasets. HESSE (2007) for example has compared the 3D position of window crosses and also tie points of both datasets. A similar approach was used by GLAUS (2006) where discrete point features were measured by mobile laser scanning but also total station. GLENNIE (2009) has compared sections of roadways measured also by car based mobile laser scanning and as reference by RTK-GNSS in addition with total station.

In his research he has created a longitudinal section of each dataset in order to compare the height component of the profiles. Additional to differences in profiles GLENNIE describes the comparison of elevation models based on grids which were derived from mobile and terrestrial laser scanning point clouds. In another study ALHO et al. (2009) uses even this approach to receive accuracy information from river bank surveys. But similar to GLENNIE these calculations take only the height difference into account to evaluate the accuracy of a mobile system. VENNEGEERTS et al. (2008) have split their accuracy considerations into a comparison of discrete points but also an area based evaluation. For one feature, an almost flat and vertical wall, they tried to evaluate systematic effects in mobile data. For this VENNEGEERTS has created a vertical grid out of the point cloud to compare this grid with a vertical plane. The result of this computation was a difference grid containing the deviations of the mobile dataset from a plane. In this thesis the aim of the accuracy assessment is not to determine deviations between discrete points in mobile and reference data but to give an area based overview of 3D differences. For this reason four objects were selected out of the whole dataset which were presented in figure 5.11.



Figures 5.11: Overview of selected objects used for accuracy evaluation; (Top) The true color coded reference point cloud whereas the selected features are red framed; (Bottom) The selected objects, two buildings and two parts of shoreline constructions are shown as 3D polygon models created with Geomagic

The building objects are well suited for accuracy assessment because on the one hand they contain not only large vertical façade surfaces for horizontal accuracy computations but also horizontal features like superstructures and balconies which can be used to evaluate the vertical accuracy as shown in figure 5.11. On the other hand high objects are needed to check the mobile datasets for systematic in motion data. For example the effect respectively the horizontal error of a pitch bias in the laser scanning system increases with the surveyed object height. The quay wall objects were selected because they contain a lot of small features like the sheet pile structure, piles and bollards for vessel mooring.

As introduced this empirical accuracy analysis consists of three parts. The first section will compare the results of all five processing methods (see chapter 4) in order to select for each software bundle, QPS QINSy and RIEGL RiPROCESS, the most reliable processing solution. The second part will then investigate the inner accuracy respectively the precision of the mobile mapping system by computing the 3D differences between all conducted survey lines. The third and last part deals with the question of absolute accuracy by means of computing differences between the reference and mobile datasets.

5.3 Inner Accuracy between Processing Methods

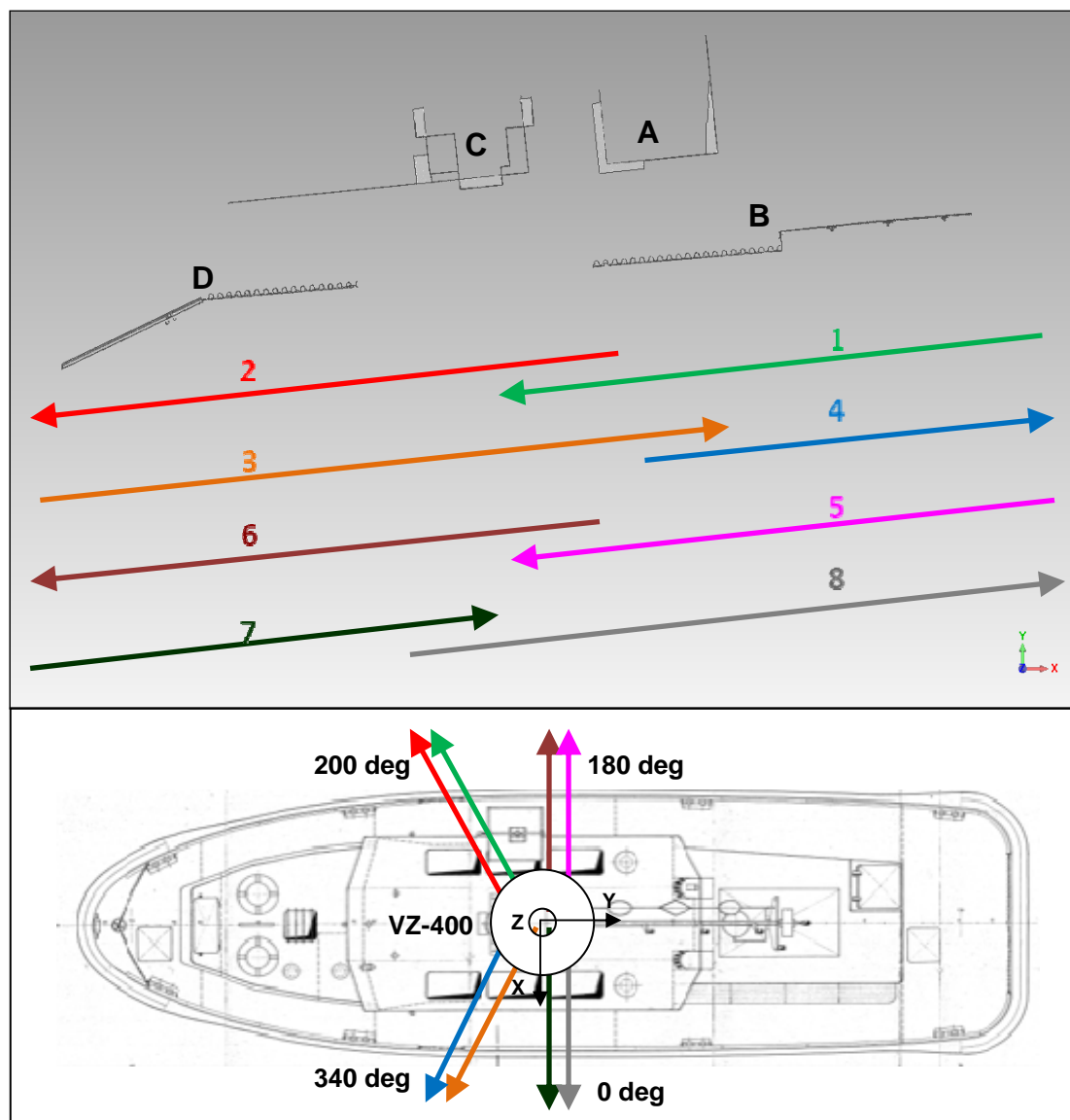
This part of accuracy assessment investigates the inner accuracy respectively the precision of the results produced by all five different processing methods which were described in detail in Chapter 4. The different processing methods and their inherent properties are summarized below.

QINSy Online:	<ul style="list-style-type: none">-contains the results of QINSy boresight alignment respectively the angular misalignments of the laser scanner-quality assured values of lever arms-only online filtered but not quality assured raw data in INS position, motion and scan data-potential latencies in raw data
QINSy Postpro. GNSS:	<ul style="list-style-type: none">-contains the results of QINSy boresight alignment and also quality assured values of lever arms-quality assured data in GNSS position, motion, heading tide whereas all detected latencies are compensated-online filtered data from replay functionality
QINSy Postpro. INS:	<ul style="list-style-type: none">-contains the results of QINSy boresight alignment and also quality assured values of lever arms-post processed and quality assured INS trajectory containing position, height, attitude and heading-online filtered data from replay functionality

RiPROCESS Postpro.: -contains the results of QINSy boresight alignment and also quality assured values of lever arms
 -post processed and quality assured INS trajectory containing position, height, attitude and heading

RiPROCESS Recalib.: -contains the results of the RIEGL scan data adjustment respectively the recalibrated angular laser misalignments
 -contains quality assured values of lever arms
 -post processed and quality assured INS trajectory containing position, height, attitude and heading

The objects A to D were mapped by different survey lines with different scanner orientations as shown below in figures 5.12.



Figures 5.12: (Top) Overview of the survey line configuration in combination with all test objects A-D, whereas in contrast to the figure the survey line-object distances are almost equal. The survey lines were measured with different scanner orientations in order to increase the object information (Bottom).

In this first part of accuracy assessment the 3D polygon models C and D derived from the resulting point clouds of each survey line will be compared with each other separated by processing method. This is carried out in order to find one processing method which produces the most reliable dataset with respect to inner accuracy. For further difference computations the model created by the most reliable processing method will be used as reference. The aim is to find the “best” processing solution for each software bundle (QPS QINSy and RIEGL RiPROCESS).

To create a 3D model out of a point cloud the software Geomagic Studio was used. The workflow in Geomagic can be summarized as follows. After importing the whole point cloud of one survey line the desired point object has to be extracted from the rest. This has to be done manually with the cleaning functionality of the software package. All points which shall to be omitted from the final 3D object like windows, folding shutters, guard railings etc have to be deleted from the dataset. Otherwise the reconstruction of the 3D polygon model becomes extensive. The next step is to mesh the point object which can be described as “...stretching plastic sheeting around a point object and pulling it tight to reveal a polygon surface.” (GEOMAGIC, 2010-1) This new polygon object has to be quality assured and reworked by editing the 3D triangulation if it is not mapping the reality sufficient enough or where unwanted points have created also unwanted triangles. Additional there are a lot of algorithms for example to decrease the number of polygons, smoothing the polygon object or to repair the mesh. For this accuracy analysis none of these algorithms was used. The workflow is depicted in Figure 5.13.

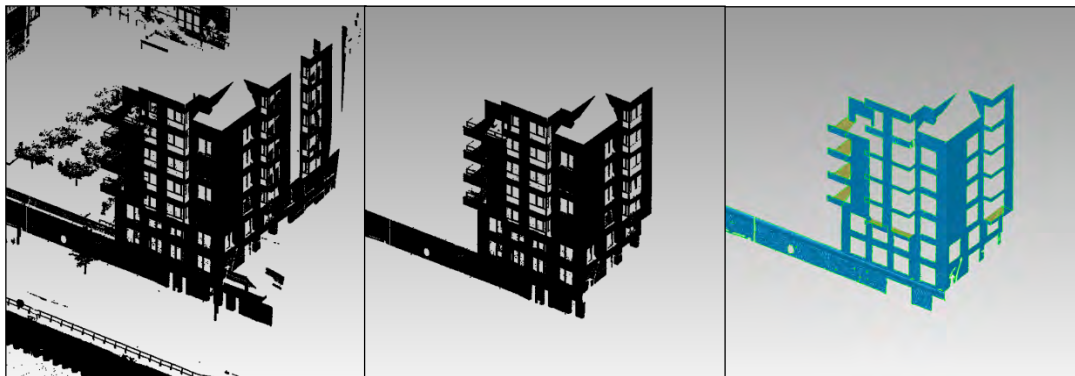


Figure 5.13: Overview of the 3D polygon object production workflow in Geomagic Studio. From the whole point cloud of the survey line (Left) over a precleaned point object (Middle) to the final reworked 3D polygon object (Right).

Overall forty 3D objects were created by applying the workflow described before. With respect to table 5.2 the objects C and D are covered by four survey lines and then processed by five different processing methods.

Table 5.2: Overview of the amount of created 3D objects (left side) and their corresponding differences calculated for each processing workflow separately (right side).

	3D Test Objects C+D				Differences between Survey Lines with respect to Object C+D					
	Line 2	Line 3	Line 6	Line 7+8	Lines 2 / 3	Lines 2 / 3	Lines 2 / 6	Lines 2 / 6	Lines 2/7+8	Lines 2/7
QINSy - Online	pts / polyg	pts / polyg	pts / polyg	pts / polyg	2c / 3c	2d / 3d	2c / 6c	2d / 6d	2c / 7+8c	2d / 7d
QINSy - Postpro GPS	pts / polyg	pts / polyg	pts / polyg	pts / polyg	2c / 3c	2d / 3d	2c / 6c	2d / 6d	2c / 7+8c	2d / 7d
QINSy - Postpro INS	pts / polyg	pts / polyg	pts / polyg	pts / polyg	2c / 3c	2d / 3d	2c / 6c	2d / 6d	2c / 7+8c	2d / 7d
RiPROCESS - Postpro.	pts / polyg	pts / polyg	pts / polyg	pts / polyg	2c / 3c	2d / 3d	2c / 6c	2d / 6d	2c / 7+8c	2d / 7d
RiPROCESS - Recalib.	pts / polyg	pts / polyg	pts / polyg	pts / polyg	2c / 3c	2d / 3d	2c / 6c	2d / 6d	2c / 7+8c	2d / 7d

The differences between corresponding 3D objects are computed with Geomagic Qualify. The most significant capability of Geomagic Qualify from point of accuracy analysis is the 3D comparison algorithm. By defining one dataset as reference and one as test is possible to calculate deviations between both of them. The software offers computation of three different types of deviation.

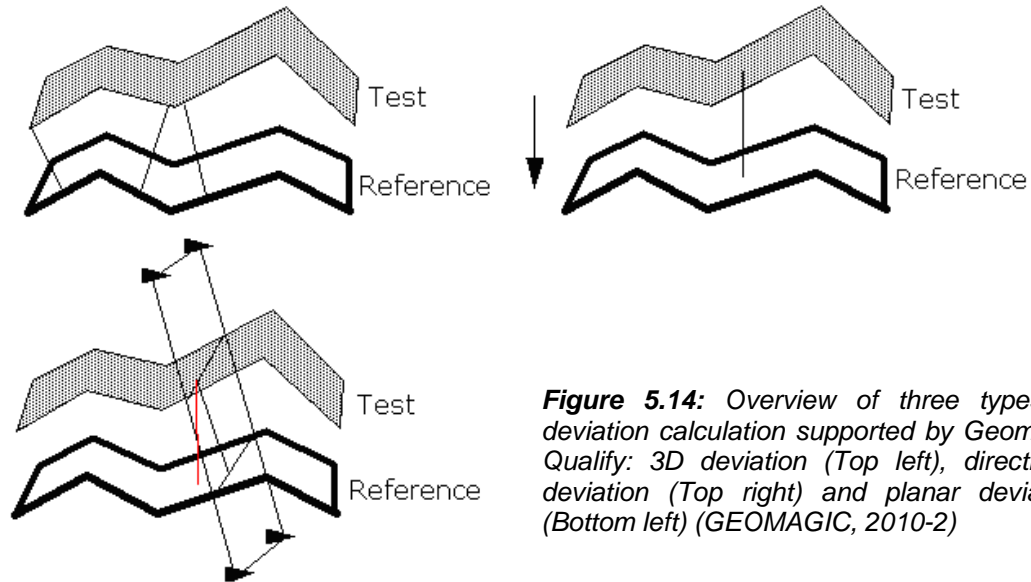


Figure 5.14: Overview of three types of deviation calculation supported by Geomagic Qualify: 3D deviation (Top left), directional deviation (Top right) and planar deviation (Bottom left) (GEOMAGIC, 2010-2)

Once computed the differences are stored as a result model and can be displayed as a color coded object (see figure 5.15). Additional to visual results Geomagic Qualify provides the user with statistical information like minimum, maximum and mean difference, standard deviation of differences and many more. With respect to table 5.2 it is important to mention that all computed differences are based on the 3D deviation algorithm.

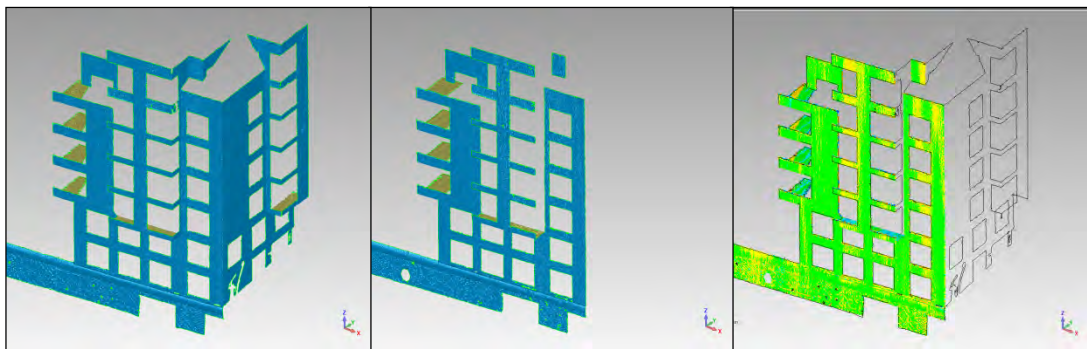


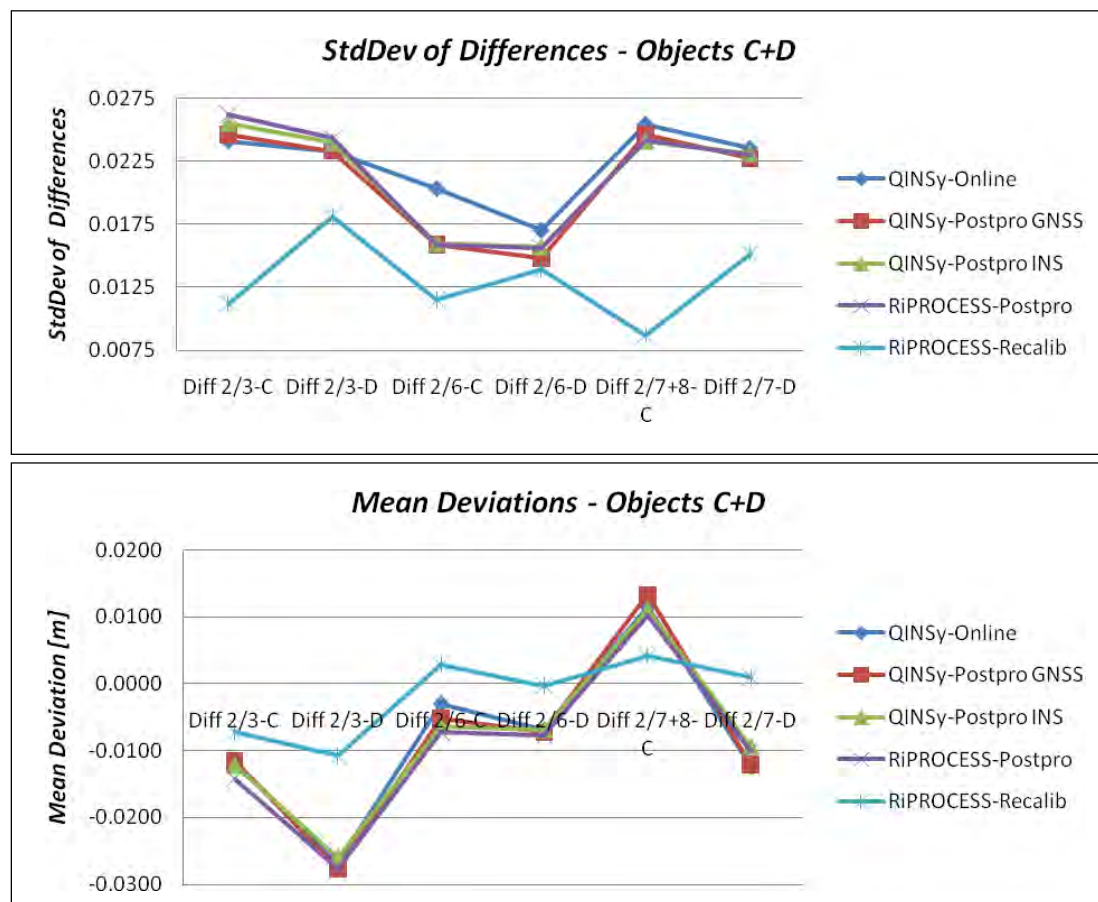
Figure 5.15: Overview of the 3D deviation computation workflow in Geomagic Qualify; The reference object has to be defined (Left) as well as the test object (Middle) to compute 3D deviations displayed as a color coded difference model (Right).

The difference models were created as pictured in figure 5.15 and listed in table 5.2 and their statistical information are summarized in table 5.3. Although these computations are part of chapter 5.4 where the inner accuracy of each processing method will be determined, it is also significant to determine the most reliable processing method which can be used as reference for further investigations. Reliability in this term means small mean differences and standard deviations of computed differences in other words the distribution of differences.

Table 5.3: Main results of 3D object comparison performed with Geomagic Quality; The mean deviations and the standard deviations in meters of calculated differences are significant measures for the inner accuracy of datasets.

Processing Method	Statistics	Object C Diff 2/3-C	Object D Diff 2/3-D	Object C Diff 2/6-C	Object D Diff 2/6-D	Object C Diff 2/7+8-C	Object D Diff 2/7-D
QINSy - Online	Mean Dev	-0.0119	-0.0266	-0.0030	-0.0069	0.0115	-0.0123
	Std. Dev	0.0241	0.0233	0.0203	0.0170	0.0254	0.0235
QINSy-Postpro. GNSS	Mean Dev	-0.0116	-0.0277	-0.0052	-0.0073	0.0133	-0.0121
	Std. Dev	0.0246	0.0233	0.0159	0.0148	0.0246	0.0227
QINSy-Postpro. INS	Mean Dev	-0.0122	-0.0259	-0.0064	-0.0069	0.0110	-0.0094
	Std. Dev	0.0255	0.0240	0.0160	0.0157	0.0241	0.0231
RiPROCESS Postpro.	Mean Dev	-0.0142	-0.0276	-0.0072	-0.0077	0.0102	-0.0101
	Std. Dev	0.0262	0.0243	0.0159	0.0156	0.0242	0.0230
RiPROCESS Recalib.	Mean Dev	-0.0072	-0.0108	0.0029	-0.0003	0.0042	0.0010
	Std. Dev	0.0112	0.0181	0.0115	0.0139	0.0087	0.0152

If one compares the values listed in table 5.3 it is obvious that - except of the processing method “RiPROCESS-Recalibration” - the size of standard deviations and mean deviations depends on the survey line direction of movement. Survey lines 2 and 3 but also 2 and 7/8 are sailed in opposite directions, whereas the lines 2 and 6 are surveyed in same direction which is directly linked to their accuracy values. This effect can be based on not well calibrated angular misalignments of the scanner or in other words on the improved scan data adjustment which was applied to the “RiPROCESS-Recalibration” processing described in chapter 4.3.

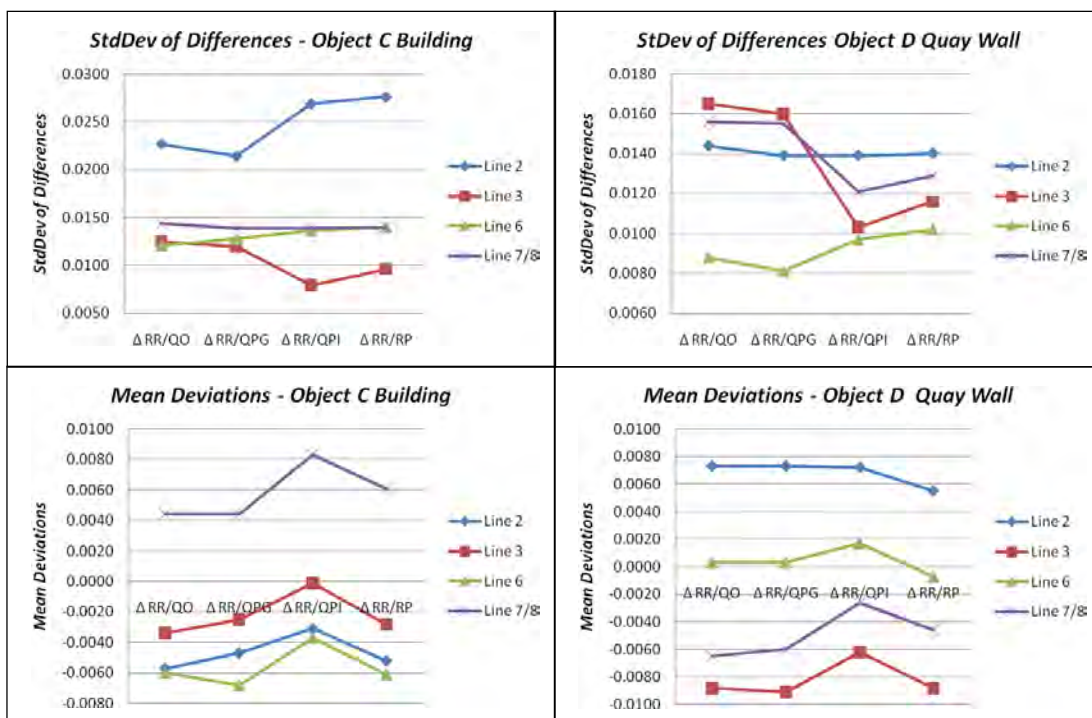


Figures 5.16: Graphical summary of difference calculations. Above the standard deviations and below the mean deviations between the test objects C and D, categorized by processing method.

Although there is no distinction in X, Y and Z deviation it is apparent that the processing method “RiPROCESS-Recalibration” contains the highest precision. While the mean deviations are distributed close to zero, the standard deviations reach as highest value only $\pm 1,8\text{cm}$. The results of all other processing methods are close together and seem to be systematic biased. In the following all other processing methods will be compared against the reference method in order to find the most accurate processing solution for each software package.

Table 5.4: Main results of 3D object comparison performed with Geomagic Qualify; For each affected survey line the 3D object differences of every processing workflow were determined by using RiPROCESS-Recalibration as reference method

Survey Line	Statistics	Object C $\Delta RR/QO-C$	Object D $\Delta RR/QO-D$	Object C $\Delta RR/QPG-C$	Object D $\Delta RR/QPG-D$	Object C $\Delta RR/QPI-C$	Object D $\Delta RR/QPI-D$	Object C $\Delta RR/RP-C$	Object D $\Delta RR/RP-D$
Line 2	Mean Dev	-0.0057	0.0073	-0.0047	0.0073	-0.0031	0.0072	-0.0052	0.0055
	Std. Dev	0.0227	0.0144	0.0214	0.0139	0.0269	0.0139	0.0276	0.0140
Line 3	Mean Dev	-0.0034	-0.0088	-0.0025	-0.0091	-0.0001	-0.0062	-0.0028	-0.0088
	Std. Dev	0.0125	0.0165	0.0120	0.0160	0.0079	0.0103	0.0096	0.0116
Line 6	Mean Dev	-0.0060	0.0003	-0.0068	0.0003	-0.0037	0.0017	-0.0061	-0.0007
	Std. Dev	0.0121	0.0088	0.0128	0.0081	0.0136	0.0097	0.0140	0.0102
Line 7	Mean Dev	0.0044	-0.0065	0.0044	-0.0060	0.0083	-0.0026	0.0061	-0.0046
Lines 7/8	Std. Dev	0.0132	0.0156	0.0133	0.0155	0.0123	0.0121	0.0123	0.0129



Figures 5.17: Graphical summary of difference calculations; Above the standard deviations and below the mean deviations in meter between 3D models, separated by test objects C (Left) and D (Right) categorized by survey line

As shown in figure 5.16 the results of all processing methods except the “RiPROCESS-Recalibration” solution are close together and have only tight differences. Nevertheless the essence of the computations displayed above in table 5.4 and figures 5.17 is that the processing method “QINSy-Postpro INS” creates results which are in general at closest to the reference. For this reason only the 3D objects created out of the processing methods “RiPROCESS-Recalibration” and “QINSy-Postpro INS” will be used for further investigations in chapter 5.4 and 5.5.

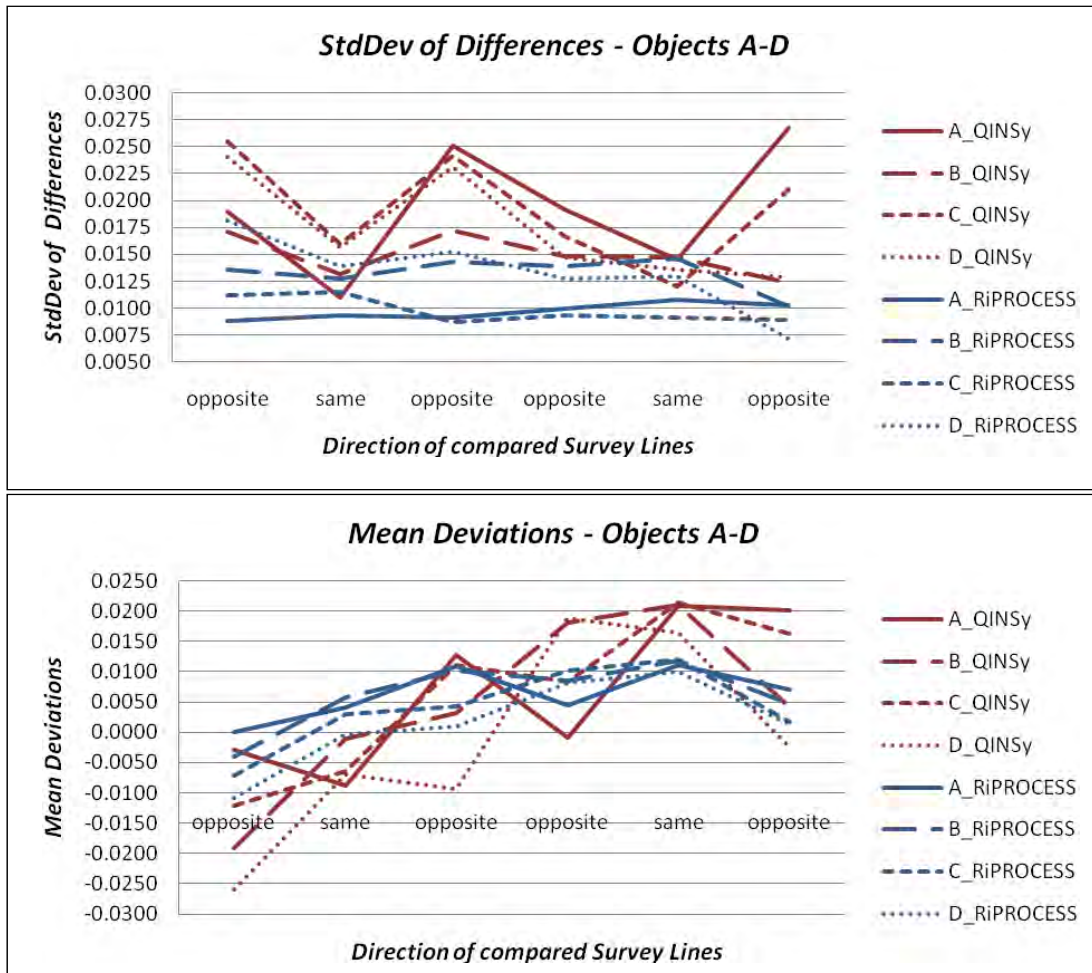
5.4 Inner Accuracy between multiple Survey Lines

Figure 5.12 has shown the measured survey lines in order to map the test objects. Although different scanner orientations have been used the comparison of two corresponding survey lines can provide a measure for the precision of the system. If for example the mapping system contains a systematic bias in motion data, the inner accuracy of two in opposite direction sailed survey lines should be less precise than the accuracy derived from two in same direction surveyed lines. In this chapter the inner accuracy of the mobile scanning system will be evaluated. In order to do so the datasets of each survey line will be compared in every combination with the other ones. This procedure is done separately for the final both processing methods (see chapter 5.3) with all test objects.

Table 5.5: Main results of 3D object comparison performed with Geomagic Qualify. For each test object and both processing methods the 3D object differences between the corresponding survey lines in all combinations.

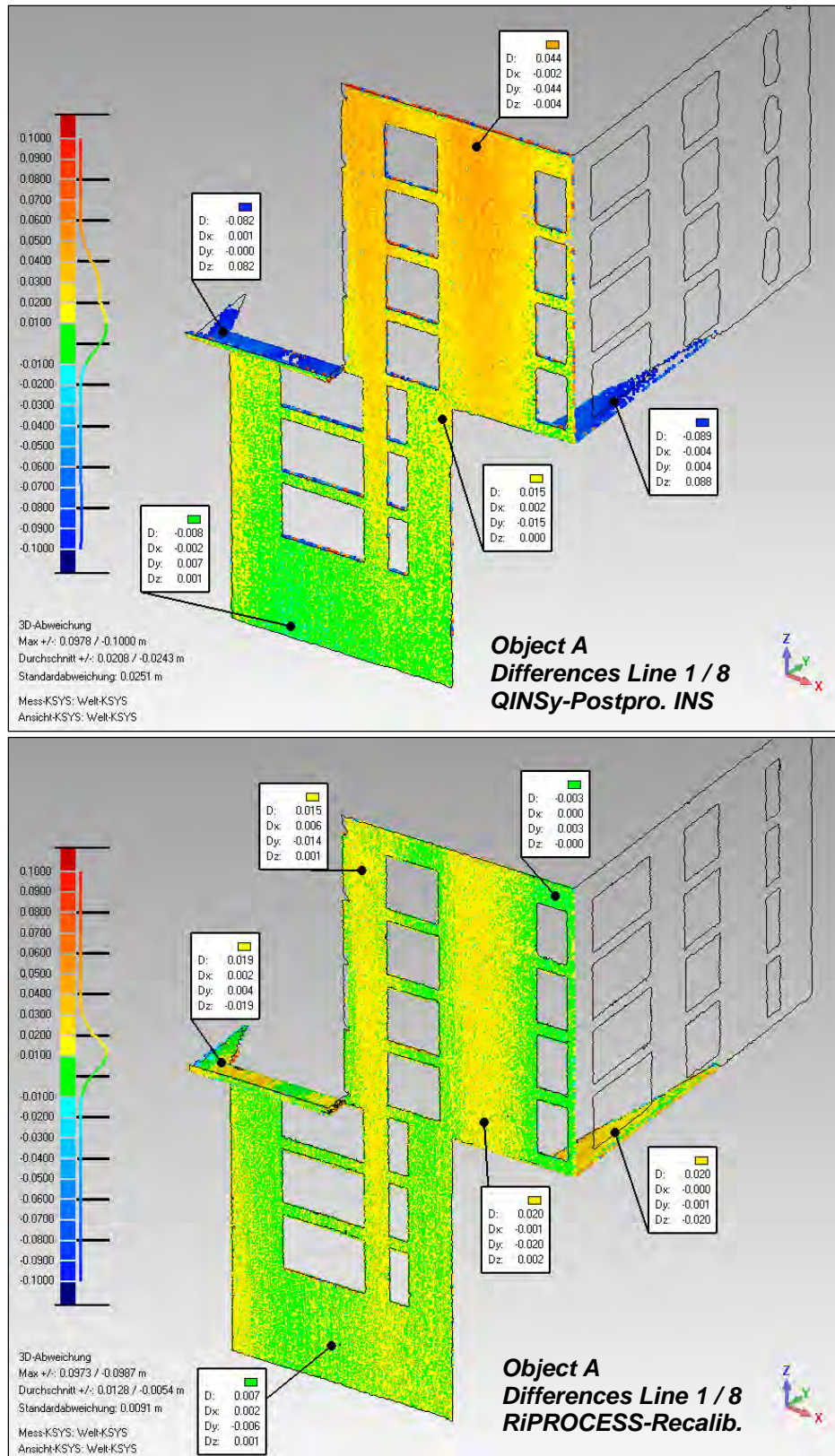
Object	Processing Method	Statistics	Diff 1/3-A	Diff 1/5-A	Diff 1/8-A	Diff 3/5-A	Diff 3/8-A	Diff 5/8-A	Mean
A	QINSy-Postpro INS	Mean Dev	-0.0030	-0.0088	0.0128	-0.0009	0.0208	0.0201	0.0068
		Std. Dev	0.0190	0.0110	0.0251	0.0192	0.0145	0.0267	0.0193
	RiPROCESS-Rekalib.	Mean Dev	0.0001	0.0040	0.0109	0.0044	0.0111	0.0071	0.0063
		Std. Dev	0.0088	0.0093	0.0091	0.0100	0.0108	0.0103	0.0097
B	QINSy-Postpro INS	Diff 1/3+4-B	Diff 1/5-B	Diff 1/8-B	Diff 3+4/5-B	Diff 3+4/8-B	Diff 5/8-B	Mean	
		Mean Dev	-0.0191	-0.0011	0.0031	0.0181	0.0211	0.0041	0.0044
		Std. Dev	0.0171	0.0132	0.0172	0.0148	0.0147	0.0123	0.0149
	RiPROCESS-Rekalib.	Mean Dev	-0.0041	0.0058	0.0102	0.0085	0.0118	0.0046	0.0061
		Std. Dev	0.0136	0.0128	0.0143	0.0139	0.0146	0.0102	0.0132
C	QINSy-Postpro INS	Diff 2/3-C	Diff 2/6-C	Diff 2/7+8-C	Diff 3/6-C	Diff 3/7+8-C	Diff 6/7+8-C	Mean	
		Mean Dev	-0.0122	-0.0064	0.0110	0.0084	0.0214	0.0162	0.0064
		Std. Dev	0.0255	0.0160	0.0241	0.0167	0.0120	0.0210	0.0192
	RiPROCESS-Rekalib.	Mean Dev	-0.0072	0.0029	0.0042	0.0101	0.0120	0.0017	0.0040
		Std. Dev	0.0112	0.0115	0.0087	0.0093	0.0091	0.0089	0.0098
D	QINSy-Postpro INS	Diff 2/3-D	Diff 2/6-D	Diff 2/7-D	Diff 3/6-D	Diff 3/7-D	Diff 6/7-D	Mean	
		Mean Dev	-0.0259	-0.0069	-0.0094	0.0188	0.0164	-0.0025	-0.0016
		Std. Dev	0.0240	0.0157	0.0231	0.0147	0.0136	0.0129	0.0173
	RiPROCESS-Rekalib.	Mean Dev	-0.0108	-0.0003	0.0010	0.0082	0.0099	0.0014	0.0016
		Std. Dev	0.0181	0.0139	0.0152	0.0127	0.0130	0.0072	0.0134

As already expected and confirmed by table 5.5 the precision of the RIEGL processing solution is higher by factor 1.5 than the QINSy solution. Especially between survey lines that were sailed in opposite direction the differences between the 3D models show a higher distribution for the QINSy solution than the RiPROCESS solution. This fact is based on the more reliable calibration method. Whereas the QINSy calibration of the boresight angles is very extensive and based only on subjective and visual decisions of the hydrographer, the scan data adjustment of RIEGL is more reliable because of used least square methods to determine the angular misalignments of the scanner. However both software solutions achieve good results. The inner accuracy of the QINSy solution can be evaluated in average as $\pm 1.8\text{cm}$ in contrast to the RiPROCESS solution with $\pm 1.2\text{cm}$. This accuracy value has to be seen with respect to the sensor-object distances which were spread from 40m up to 60m. Figure 5.18 points the differences of both processing methods respectively their values for inner accuracy. Additionally it has to be kept in mind that the final accuracy value is derived from 3D differences. These three dimensional vectors in space are describing shortest distances from one model to a reference model which were not divided into X, Y and Z components for this considerations.



Figures 5.18: Graphical summary of difference calculations; Above the standard deviations and below the mean deviations between the two corresponding survey lines categorized by test objects A-D; All red colored graphs are derived from the QINSy processing method, all blue graphs from the RiPROCESS processing method

At a closer look to a difference model like shown in figures 5.19 it is easy to identify systematic effects in datasets and to distinguish between horizontal and vertical deviations. The top view of this figures shows the differences between two survey lines sailed in opposite direction processed with QINSy. With increasing object height the deviations increase as well from zero up to almost 5cm. This effect in the Y axis is caused by an erroneous roll angle misalignment of the scanner. At lower object heights which mean laser tilt angles of around 90 degrees even this error source introduces a height error as shown by the large deviations of up to 9cm at the horizontal elements of superstructures respectively balconies. In contrast to this scenario the bottom view of figures 5.19 shows the capabilities of the system when all angular misalignments are determined precisely. The differences are distributed normally which is indicated by the histogram on the left hand side of the figure. Indeed there is still a bias in Y direction of approx. 1 cm but this is just the accuracy of the positioning system. The vertical deviations have decreased to ± 2 cm at maximum which is also the accuracy of the INS height but they oscillate around zero which can be still a dynamic effect in motion data. This has to be investigated in more detail in the next chapter where the mobile datasets are compared to the reference dataset produced by terrestrial laser scanning described in chapter 5.2.



Figures 5.19: 3D difference models derived from survey line 1 and 8 datasets processed by QINSy (Top) and RiPROCESS (Bottom); Because line 8 was surveyed with a scanner orientation of 0 deg (perpendicular to the track axis) only the front façade and some superstructures were detected; The lines 1 and 8 were sailed in opposite directions; The small information boxes display discrete point differences in X, Y and Z directions.

5.5 Absolute Accuracy between Reference and Mobile Data

Chapter 5.4 has shown the capabilities of the mobile scanning system by evaluating the inner accuracy between different survey lines. It was pointed out that the datasets processed with the RiPROCESS solution better than the QINSy datasets. This is based on the differences in used calibration procedures. Nevertheless precision values have been found which describe the repeatability of the measurement system in other words the inner accuracy. In this part of accuracy analysis the mobile datasets will be compared against a reference dataset as introduced in chapter 5.2, which is assumed to be very close to the true value in terms of absolute accuracy. Although both measurements, mobile and terrestrial, are based on laser scanning with the same sensor, it has to be assumed they are independent and not correlated with each other. To determine measures for absolute accuracy again several differences have been computed between the reference dataset and all mobile datasets for objects A to D. Below in table 5.6 the pairs of difference calculation are summarized.

Table 5.6: Pairs of datasets for difference computations; For both processing methods the 3D differences between all test objects and the reference dataset were calculated.

	Differences of Objects A+D							
	Ref / Line 1		Ref / Line 3+4		Ref / Line 5		Ref / Line 8	
QINSy-Postpro INS	Ref / 1A	Ref / 1B	Ref / 3A	Ref / 3+4B	Ref / 5A	Ref / 5B	Ref / 8A	Ref / 8B
RiPROCESS-Recalib	Ref / 1A	Ref / 1B	Ref / 3A	Ref / 3+4B	Ref / 5A	Ref / 5B	Ref / 8A	Ref / 8B
	Differences of Objects C+D							
	Ref / Line 2		Ref / Line 3		Ref / Line 6		Ref / Line 7+8	
QINSy-Postpro INS	Ref / 2C	Ref / 2D	Ref / 3C	Ref / 3D	Ref / 6C	Ref / 6D	Ref / 7+8C	Ref / 7D
RiPROCESS-Recalib	Ref / 2C	Ref / 2D	Ref / 3C	Ref / 3D	Ref / 6C	Ref / 6D	Ref / 7+8C	Ref / 7D

As explained before the 3D difference vectors between reference and test object can be divided into the components X, Y and Z deviation. To determine values for absolute accuracies it is useful to investigate each of them individually instead of taking only the averaged 3D distance into account, because as shown in chapter 5.1 the error propagation differs significantly in X, Y and Z direction. For all computed differences the mean deviations and the standard deviations in X, Y and Z direction have been calculated and summarized in tables 5.7 and 5.8.

Table 5.7: Results of difference computations between A and B reference and test datasets; For both processing methods the results of 3D difference computations are summarized by mean deviations and standard deviations in meter in X, Y and Z direction

Mean Deviations - Object A					
Processing Method	Mean	Δ Ref/1-A	Δ Ref/3-A	Δ Ref/5-A	Δ Ref/8-A
QINSy-Postpro INS	X	-0.0106	-0.0018	-0.0019	0.0006
	Y	0.0052	0.0086	0.0138	-0.0072
	Z	-0.0013	0.0011	-0.0002	0.0034
RiProcess-Recalib	X	-0.0016	-0.0003	-0.0009	-0.0003
	Y	0.0096	0.0104	0.0075	0.0018
	Z	0.0007	0.0008	0.0013	0.0003

Standard Deviations of Differences - Object A					
Processing Method	StdDev	Δ Ref/1-B	Δ Ref/3+4	Δ Ref/5-B	Δ Ref/8-B
QINSy-Postpro INS	X	0.0243	0.0059	0.0065	0.0046
	Y	0.0101	0.0095	0.0101	0.0099
	Z	0.0092	0.0077	0.0058	0.0136
RiProcess-Recalib	X	0.0107	0.0058	0.0039	0.0029
	Y	0.0083	0.0080	0.0079	0.0072
	Z	0.0056	0.0065	0.0072	0.0043

Mean Deviations - Object B					
Processing Method	Mean	Δ Ref/1-B	Δ Ref/3+4	Δ Ref/5-B	Δ Ref/8-B
QINSy-Postpro INS	X	-0.0036	-0.0027	-0.0034	-0.0025
	Y	0.0042	0.0208	0.0041	0.0009
	Z	-0.0007	0.0005	-0.0001	0.0010
RiProcess-Recalib	X	-0.0030	-0.0006	-0.0019	-0.0004
	Y	0.0123	0.0160	0.0064	0.0024
	Z	0.0004	0.0005	0.0005	0.0003

Standard Deviations of Differences - Object B					
Processing Method	StdDev	Δ Ref/1-B	Δ Ref/3+4	Δ Ref/5-B	Δ Ref/8-B
QINSy-Postpro INS	X	0.0088	0.0088	0.0099	0.0086
	Y	0.0092	0.0117	0.0096	0.0096
	Z	0.0036	0.0066	0.0030	0.0053
RiProcess-Recalib	X	0.0073	0.0069	0.0075	0.0062
	Y	0.0077	0.0089	0.0079	0.0068
	Z	0.0040	0.0053	0.0037	0.0028

Table 5.8: Results of difference computations between C and D reference and test datasets; For both processing methods the results of 3D difference computations are summarized by mean deviations and standard deviations in meter in X, Y and Z direction.

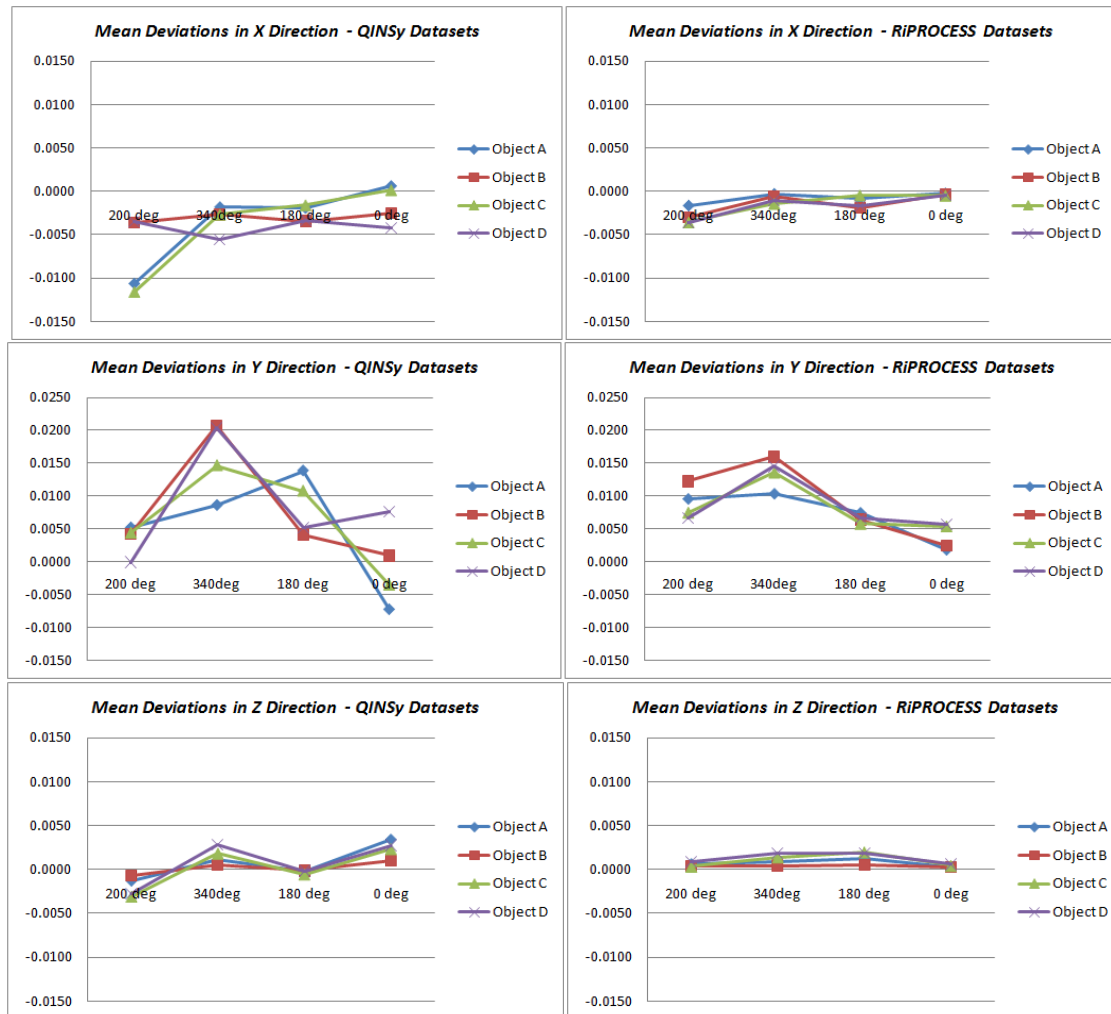
Mean Deviations - Object C					
Processing Method	Mean	Δ Ref/2-C	Δ Ref/3-C	Δ Ref/6-C	Δ Ref/7+8
QINSy-Postpro INS	X	-0.0116	-0.0027	-0.0016	0.0002
	Y	0.0044	0.0146	0.0108	-0.0036
	Z	-0.0031	0.0018	-0.0006	0.0023
RiProcess-Recalib	X	-0.0035	-0.0014	-0.0005	-0.0005
	Y	0.0075	0.0136	0.0058	0.0054
	Z	0.0003	0.0014	0.0020	0.0005

Standard Deviations of Differences - Object C					
Processing Method	StdDev	Δ Ref/2-C	Δ Ref/3-C	Δ Ref/6-C	Δ Ref/7+8
QINSy-Postpro INS	X	0.0248	0.0061	0.0038	0.0039
	Y	0.0122	0.0108	0.0083	0.0097
	Z	0.0124	0.0076	0.0039	0.0086
RiProcess-Recalib	X	0.0077	0.0051	0.0029	0.0025
	Y	0.0075	0.0088	0.0066	0.0057
	Z	0.0044	0.0061	0.0070	0.0031

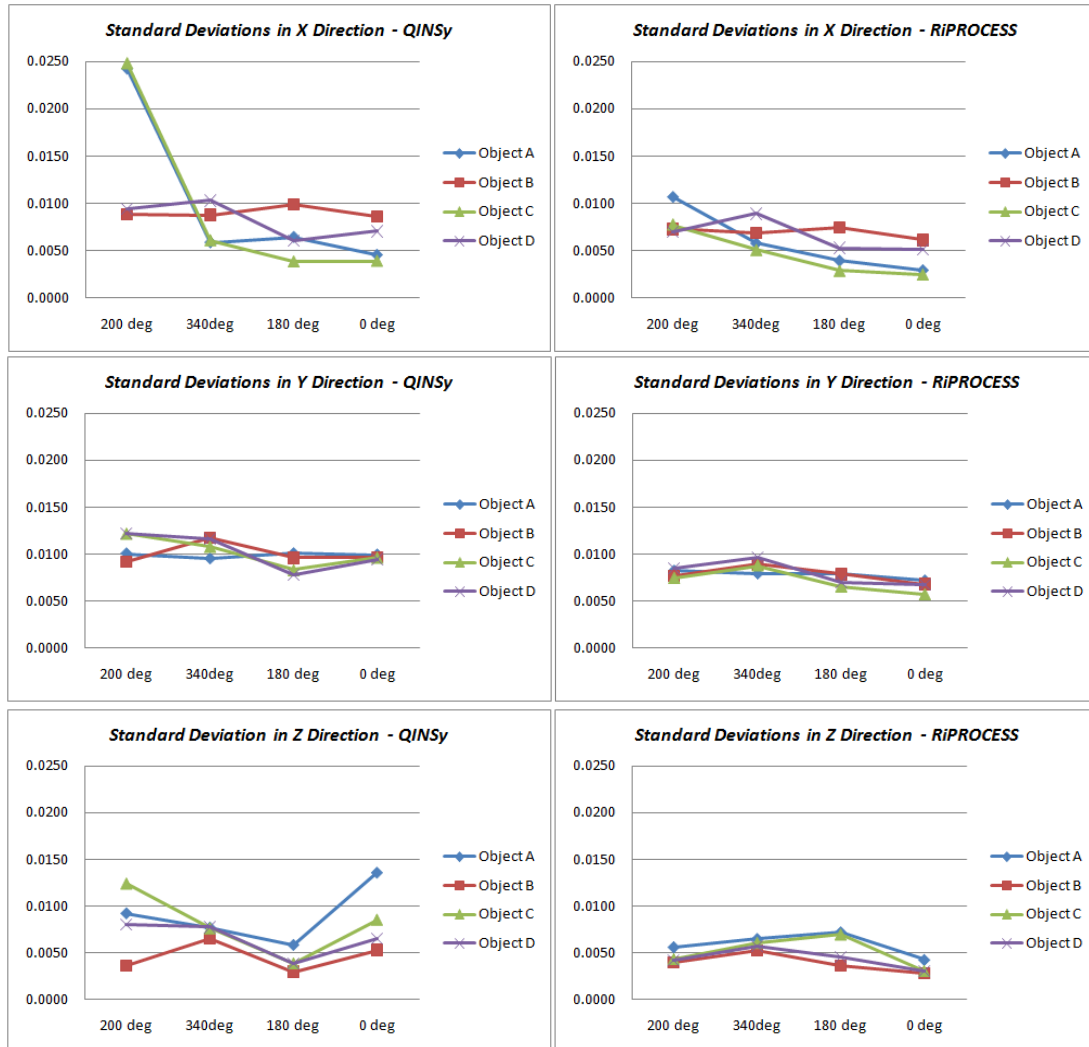
Mean Deviations - Object D					
Processing Method	Mean	Δ Ref/2-D	Δ Ref/3-D	Δ Ref/6-D	Δ Ref/7-D
QINSy-Postpro INS	X	-0.0035	-0.0056	-0.0033	-0.0042
	Y	-0.0001	0.0203	0.0052	0.0076
	Z	-0.0027	0.0028	-0.0002	0.0027
RiProcess-Recalib	X	-0.0036	-0.0011	-0.0016	-0.0005
	Y	0.0066	0.0145	0.0067	0.0056
	Z	0.0009	0.0019	0.0018	0.0006

Standard Deviations of Differences - Object D					
Processing Method	StdDev	Δ Ref/2-D	Δ Ref/3-D	Δ Ref/6-D	Δ Ref/7-D
QINSy-Postpro INS	X	0.0095	0.0103	0.0060	0.0071
	Y	0.0122	0.0117	0.0078	0.0095
	Z	0.0081	0.0078	0.0039	0.0065
RiProcess-Recalib	X	0.0070	0.0089	0.0053	0.0052
	Y	0.0085	0.0097	0.0070	0.0067
	Z	0.0042	0.0058	0.0045	0.0031

To visualize the results, the mean deviations and the standard deviations for each coordinate component are displayed in the figures 5.2 below whereas the graphs are separated for both processing methods.



Figures 5.20: Graphical summary of difference calculations separated for X, Y and Z direction; Mean deviations of QINSy (Left) and RiPROCESS (Right) processed datasets; With reference to a left hand coordinate system the deviations points from the reference dataset to the test dataset



Figures 5.21: Graphical summary of difference calculations separated for X, Y and Z direction; Standard deviations in meter of differences between QINSy (Left) respectively RiPROCESS (Right) processed datasets and reference datasets;

Taken into account the results of chapter 5.4, which point out that the QINSy processed datasets produce noisier results than the RiPROCESS ones because of systematic effects in the boresight alignment, it is clear that the QINSy show a higher distribution around the reference dataset. In spite of this fact none of the datasets exceeds mean deviations to reference of more than 2cm in any direction. Also the standard deviations of the differences reach 2,5cm at maximum.

For further considerations it has to be pointed out that the survey lines were measured with different scanner orientations as depicted in figure 5.12. Each of these survey lines contributes a different amount of accuracy information for X, Y and Z direction as shown in figure 5.22. In contrast to the reference dataset which covers almost the whole building, all mobile datasets map at least the front façade and parts of the horizontal superstructures. For example the dataset where the scanner was oriented perpendicular to the house front doesn't contain any information about the accuracy in X direction because the side walls were not detected by the system. Points of a dataset located on the front façade have reliable information about the accuracy in Y direction but they also deceive a high accuracy in Y and Z direction.

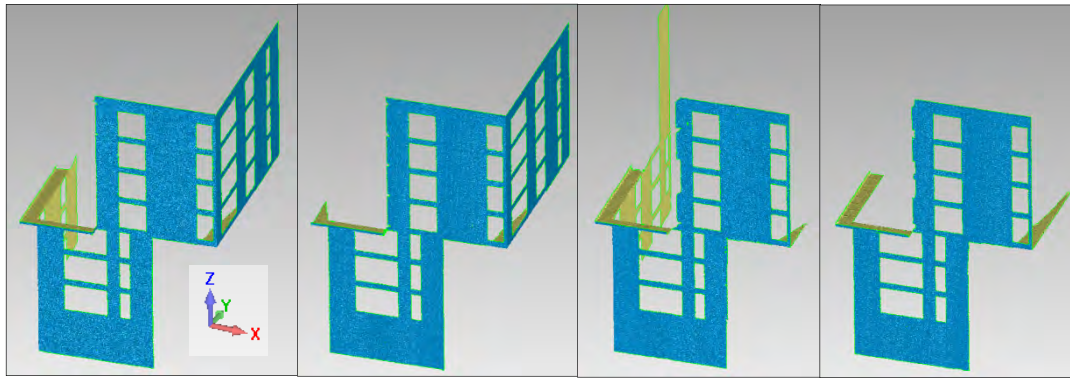


Figure 5.22: 3D models of test object A derived from different source datasets influenced by the scanner orientation; (From left to right) Reference dataset from terrestrial laser scanning, mobile datasets with 200deg, 340deg and 180deg scanner orientation

For this reason the results of table 5.8 which were graphically shown in figures 5.20 and 5.21 are at least good estimates for an absolute accuracy. To receive more reliable, concrete accuracy information each 3D difference model has to be investigated in detail like shown exemplarily in figure 5.23.

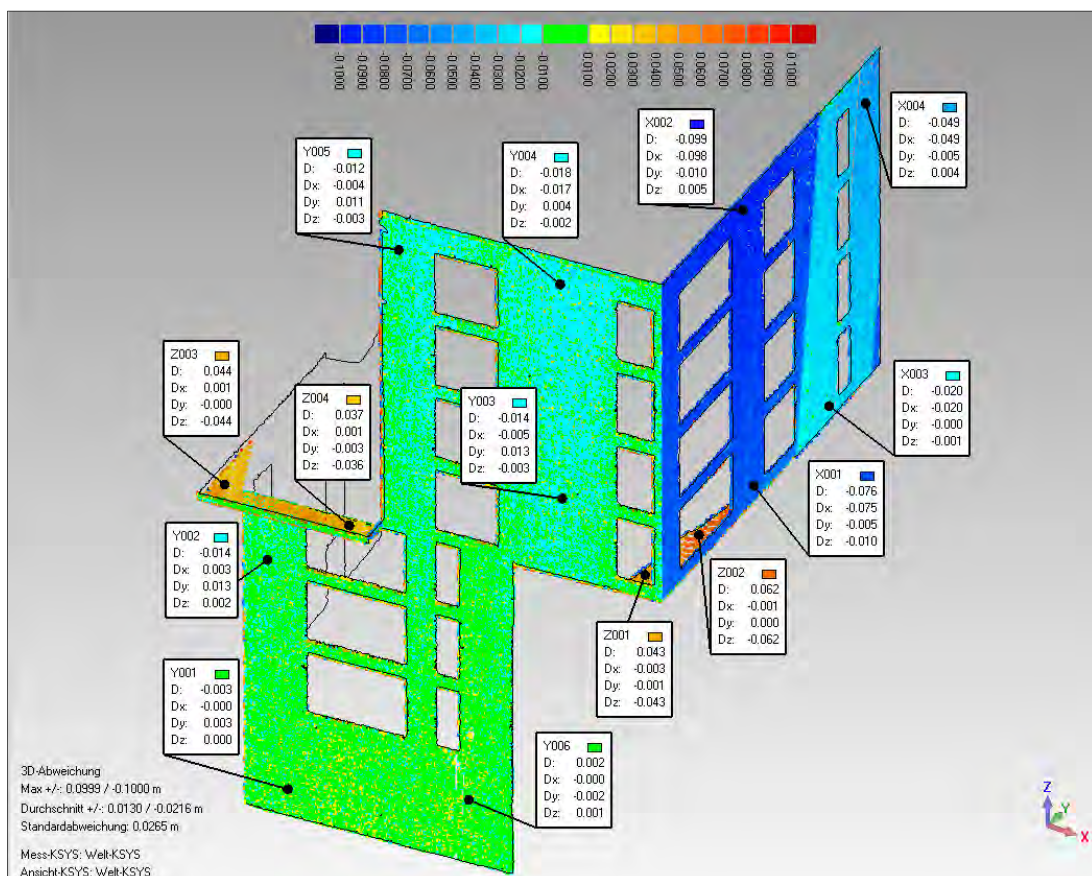


Figure 5.23: 3D difference model derived from survey line 1 with scanner orientation of 200deg; From each detected feature of the building the corresponding coordinate difference can be evaluated by determining the min. and max. deviation

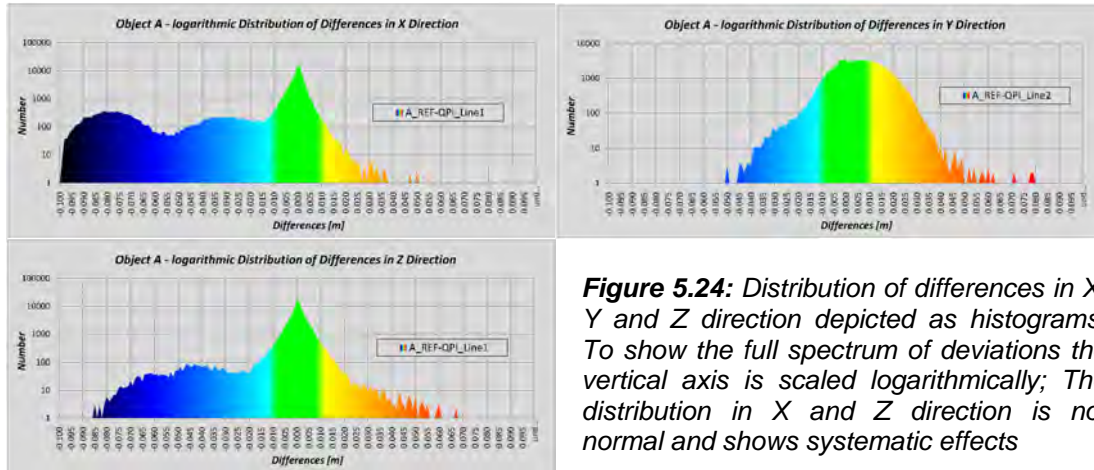


Figure 5.24: Distribution of differences in X, Y and Z direction depicted as histograms; To show the full spectrum of deviations the vertical axis is scaled logarithmically; The distribution in X and Z direction is not normal and shows systematic effects

By comparing the 3D difference model with the corresponding histograms the peaks of deviations can be related with a certain part of the difference model. With reference to figure 5.23 where the deviations at the side wall, which are spread from -7.5cm to -9.8cm (dark blue area) can be found as a peak in the upper left histogram of figure 5.24. A similar situation can be found for deviations in height from -3.6cm up to -6.2cm whereas the mean deviation in height was computed as -0.0013m because only a “few” measurements contribute the true deviation in Z direction. For this reason the pictures of all difference models including their distribution histograms are attached to this thesis as appendix A.5.

To summarize these considerations one can say that from a statistical point of view the datasets of the mobile laser scanning system have mean deviations to the reference dataset of ± 2 cm. But a more realistic value was found by evaluating each difference model. For RiPROCESS datasets area based deviations in X up to ± 3.5 cm, in Y up to ± 2.5 cm and in Z up to ± 3.5 cm were found. The difference models have discovered still remaining systematic effects. Abrupt changes in deviations can be found in every coordinate direction as shown below in figure 5.25. These effects can be caused by a noisy trajectory or by a shaky mounting bracket. But also oscillating structures which can be based on a variable latency in motion data became visible. All of these issues have to be investigated in future work.

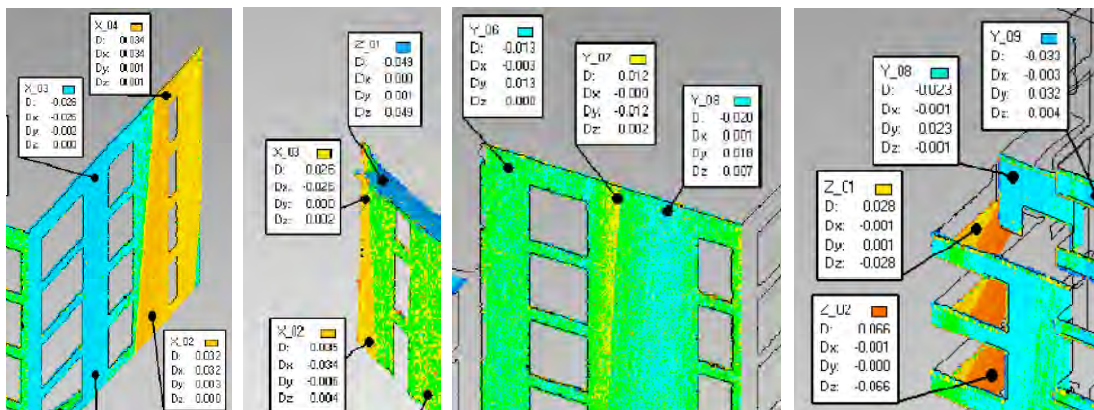


Figure 5.25: 3D difference models discover system effects in mobile datasets; Abrupt variations in X differences (Left), oscillating but also abrupt changes in Y (Middle) and Z direction (Right)

5.6 Summary of Accuracy Considerations

In the chapters 5.1 to 5.5 different approaches were used to evaluate the accuracy of the mobile mapping system with focus on mobile laser scanning. In chapter 5.1 a uncertainty estimation was presented with the result that the heading accuracy of the INS is the weakest link of the accuracy “chain”. The resulting X component of a laser points 3D coordinate therefore contains the highest amount of uncertainty. Different scanner configurations have been taken into account to derive the change in uncertainty for different tilt and pan angles. This first accuracy investigation provides the user of such a mobile system with a good estimate of reachable accuracy.

The next chapter has introduced and explained the reference measurement which was later used to determine a measure for an absolute accuracy. Additionally this reference dataset was the base to define four test objects. For these test objects, two buildings and two parts of quay wall, all further considerations for determining the precision and the absolute accuracy of the mobile laser scanning system were applied to. Chapter 5.3 has compared the different processing methods with each other. The comparison was conducted by computing 3D differences out of 3D models created by Geomagic Studio. As a result the most precise processing method for each software bundle was determined.

The next chapter 5.4 has investigated the inner accuracy or in other words the precision of the both prior selected processing methods. To create a measure for precision the datasets of all survey lines were compared with each other separated for both processing methods. It was shown that the RiPROCESS-Recalib. workflow produce datasets containing the highest inner accuracy compared to the QINSy workflow. The reason for this was found in the less accurate determination of the boresight angles with the validation tool of QINSy.

Whereas the inner accuracy respectively the precision describes the measure how good different correlated datasets match to each other, chapter 5.5 has investigated the absolute accuracy between the reference dataset and mobile datasets. For this consideration the deviations between two corresponding datasets were divided into the three coordinate components X, Y and Z. For each of these components accuracy values were computed, but it was shown that because of statistical reasons the accuracy values are over-averaged and biased. A more realistic approach was then to examine each 3D difference model to find more reliable values for area based deviations. The results were sobering in contrast to calculated statistical values but more similar to the estimated uncertainties. It was confirmed that the X coordinate is based on the most problematic error source, the heading. But in contrast to error estimation the height component Z is not as accurate as expected. Additionally different systematic artifacts based on noisy trajectory and/or variable latency in motion data have been discovered but not yet investigated.

However in general the accuracy and performance of the mobile mapping system is still well suited for a lot of applications which will be shown in the next chapter.

6. Test Surveys and Examples of Multipurpose Products

The chapters 3 to 5 have shown the functionality and the accuracy of the mobile mapping system established for this thesis. But the whole effort to set up such a system is only crowned with success when the system fulfills the requirements of different survey applications. The potential demand on products based on mobile mapping will be discussed from point of a port authority. In this chapter several performed survey projects will be presented and the workflows to derive multipurpose products will be described.

6.1 Building “Dockland” – Object of 3D Port Model

The first presented survey project the “Dockland” building was already introduced in chapter 3.5. This architectural interesting construction was built in 2005 and opened in 2006. The maritime design of this office building is based on the hull of a motor yacht and fits perfectly to the port ambience. Directly located at the northern bank of the river Elbe this building is not only a significant part of the Port of Hamburg’s skyline but has also become a town’s landmark. From point of vessel based mobile mapping Dockland is not only a nice building but also almost completely surrounded by water and therefore predestinated for mobile laser scanning. The survey was performed by several in opposite directions sailed lines whereas the scanner orientation was changed during the survey to map all features of the building as shown in figure 6.1. The laser scanner was configured to measure in high speed mode with maximum object ranges of up to 80 meters whereas the vessel speed was limited to 5 knots per hour at maximum.

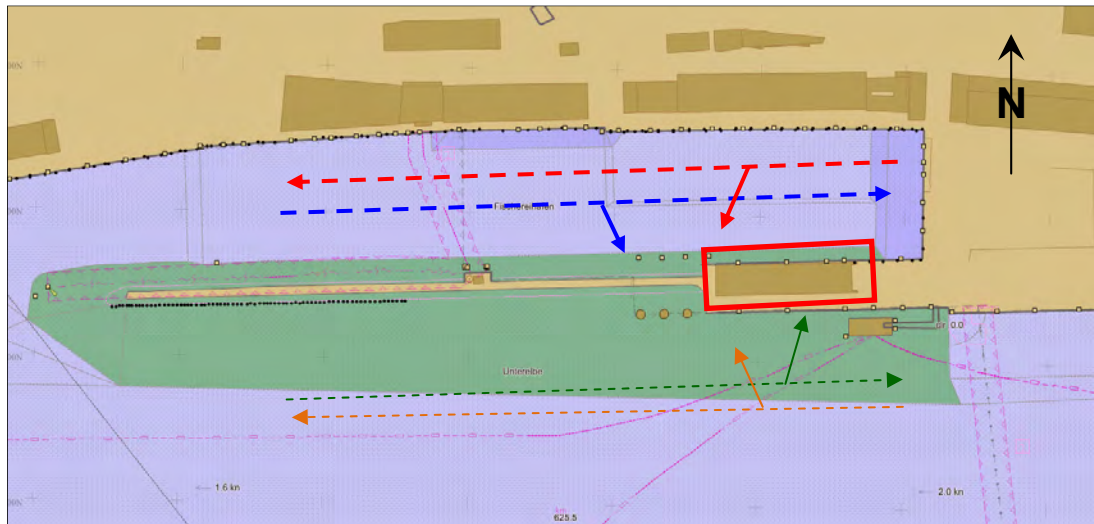


Figure 6.1: Overview of the “Dockland” survey configuration. Several lines north and south of the building were measured with different scanner orientations. The red-marked area in the picture shows the location of the building.

The data was processed with respect to chapter 4.3, which means that the trajectory was post-processed with IXSEA DelphINS and merged with the scan data in RIEGL RiPROCESS. The results were geo-referenced point clouds for each survey line which can be visualized like shown in figure 6.2.

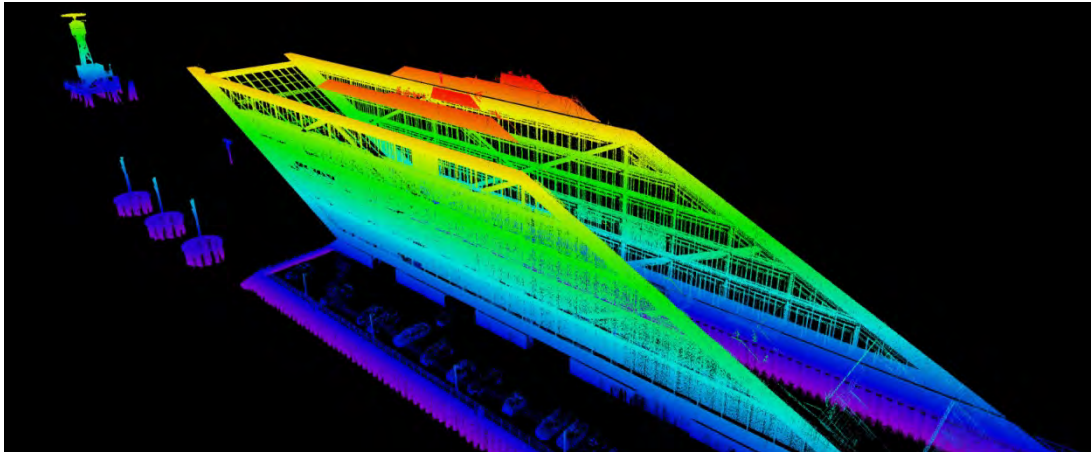


Figure 6.2: Pre-cleaned point cloud of the mapped building Dockland color coded by height.

Although a cleaned point cloud can be already a product from the point of visualization, but it contains millions of points and is not easy to handle. The result of the following proposed workflow is a simple but detailed 3D model of the building which can be used in several applications.

The workflow shown in figure 6.4 and the final 3D model were developed and realized in cooperation with the survey department of the Hamburg Port Authority (HPA) which has provided the tools and the know-how of 3D modeling to this thesis. For 3D modelling the software package TerraScan of the Finnish software developer Terrasolid was used. The point clouds containing X, Y and Z coordinates and intensity values were imported into TerraScan which is a Microstation based laser scan processing tool for airborne and mobile laser scan datasets.

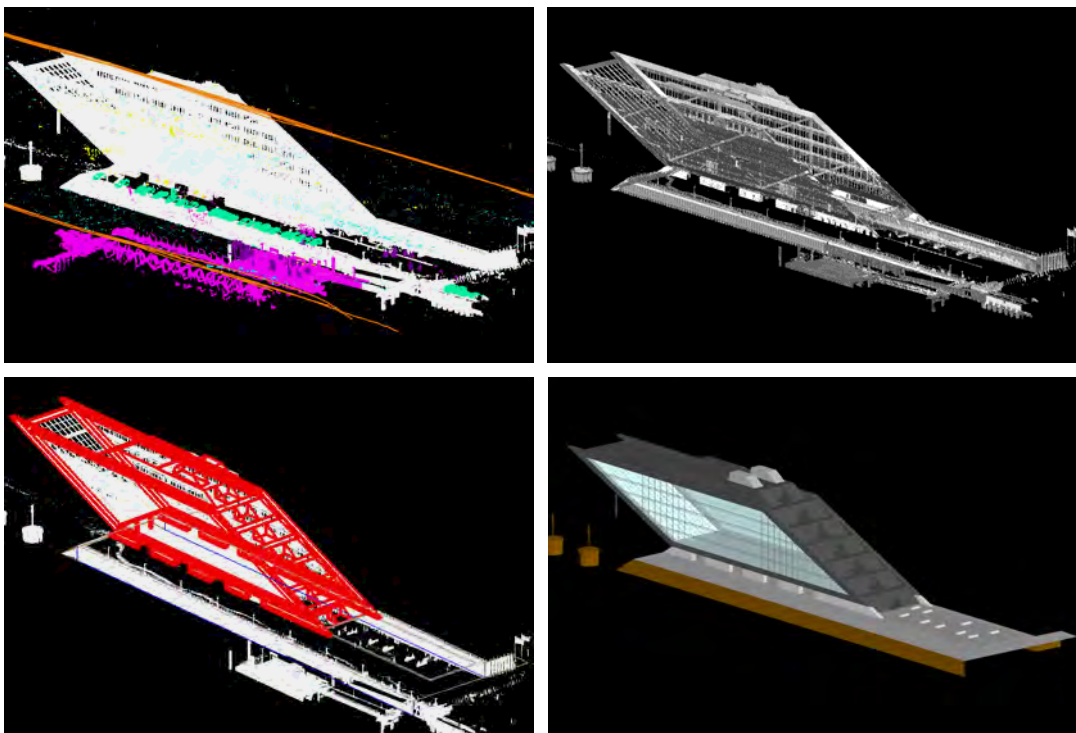


Figure 6.3: Overview of the modeling workflow in Terrasolid TerraScan; From point cloud classification (Top left) over feature digitization to object modeling (Bottom Left)

With respect to figure 6.3 which depicts the steps of the modeling workflow the first procedure is to classify the point cloud by feature type e.g. building, quay wall or bad data in order to manage the huge amount of points. Especially during the digitization process which is the most extensive part of 3D modeling the classification is used to focus only on special parts of the whole dataset. The digitization which can be described as fitting geometric primitives like lines and planes into the point cloud starts with the determination of the rough building shape whereas parallelism and perpendicularity is assumed for this new building. The level of detail which will be remained in the model depends on the point density and the ability to distinguish between different features in the dataset. For this reason the digitization is mostly performed in an intensity or true color coded point cloud which makes differentiations possible.

In the case of the project Dockland the most challenging part was to determine between true and multipath biased data. As one can see in figure 3.23 the building is based on a steel frame with several crossbeams whereas the façades are almost completely glass fronts with a double window structure causing multipath effects. The next steps were to design respectively to build surfaces of the Dockland object based on the digitized vector data and to construct the small features like windows, basement features and dolphins. It is important to mention that the roof structure of the building is derived from airborne laser scanning datasets because of the inherent geometric shadowing effects in mobile terrestrial laser scanning. The final procedure is to set for each surface of the building the color or material to receive a realistic object. Another step can be to texturize the 3D object by using photographs taken during the survey.

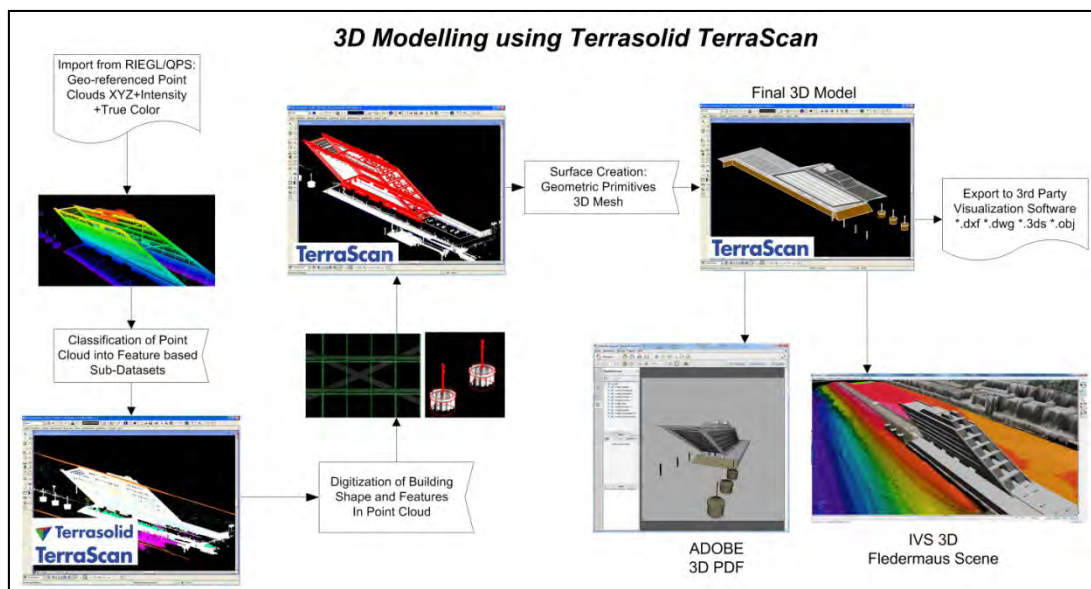


Figure 6.4: Schematic of the modeling workflow in Terrasolid TerraScan; From point cloud classification over feature digitization to 3D mesh generation and feature coloring

The final 3D model can easily be used in different applications to build up for example similar to 3D city models a 3D port model, which can contain not only buildings on land but also 3D bathymetric information, port facilities like quay walls, embankments and aids to navigation.

Figure 6.5 shows a combination of different 3D models based on different source datasets. The purposes for such a port model can be multifarious. Decision making processes like port infrastructure planning can be supported with a 3D overview of the port containing water and land infrastructure in combination with terrain and bathymetric information. Flooding scenarios can be accurately calculated which may be an interesting feature for insurance issues of a risk management. The port model can also be linked with a database containing attributes for each feature which supports a port facility management.

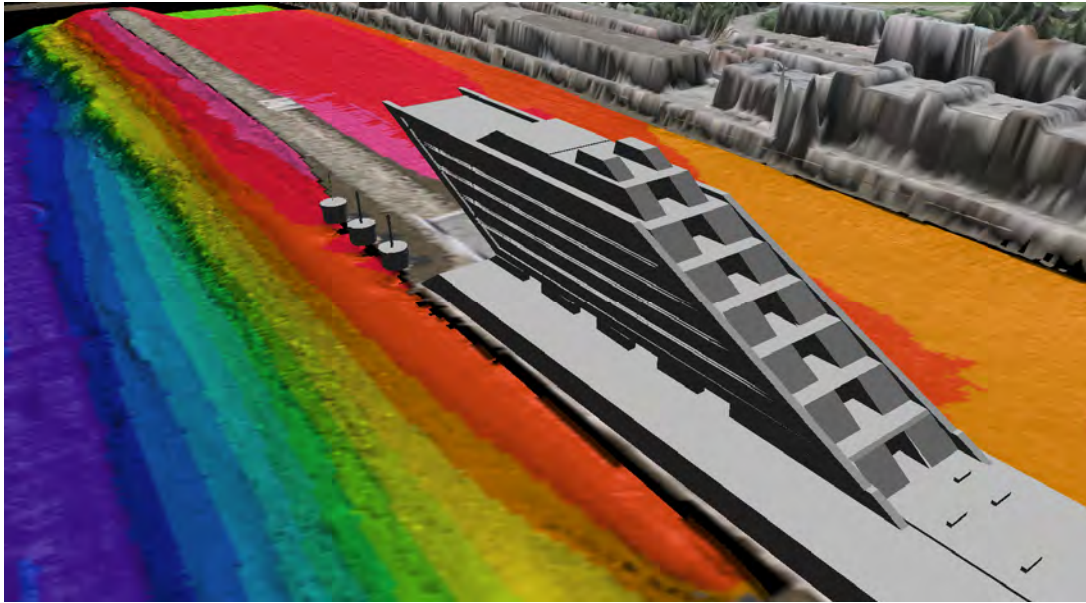


Figure 6.5: Combination of 3D Dockland model, bathymetric 3D model based on multibeam echosounder data, height model and ortho-photo from airborne mapping

Each specialist department can contribute specific datasets like flow model, reference model of the maintained seabed topography, sediment classification data, biologic parameters and many more datasets to this database to create a port information system whereas the topography and bathymetry created by mobile mapping systems are the basis for such a system. For each user the layers of data are combined as required as shown in the pictures 6.6 below. For example the dredging department is mainly interested in current water depths with respect to the reference model and the nautical department additionally needs information about the aids of navigation and all other feature in the water area.

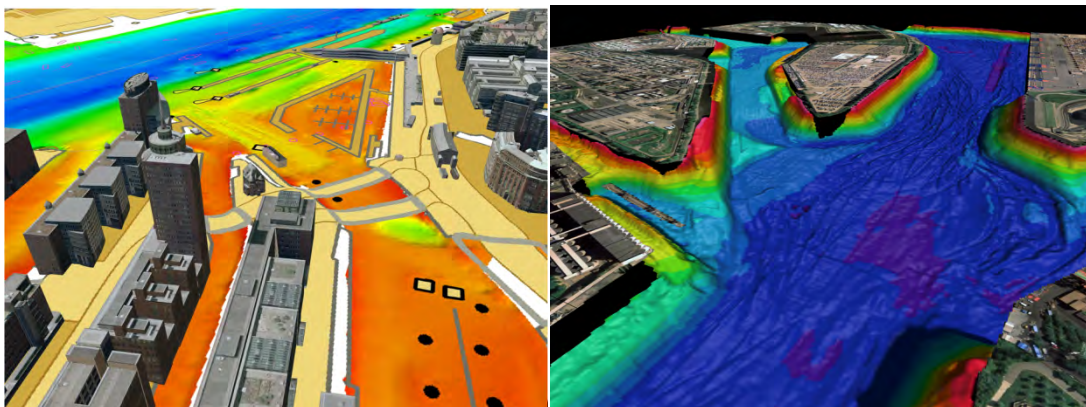


Figure 6.6: Possible data combinations for a port information system; 3D city model with gridded bathymetry and ENC (Left); 3D bathymetry combined with ortho-photos (Right)

6.2 Embankment “Koehlbrand” – Bathymetric Chart

One of the tasks of the hydrographic department of the HPA is to monitor the embankments of the ports waterways. The water areas of Port of Hamburg are optimized to provide always enough under keel clearance for the shipping traffic. Optimization in this context means that the banks of the river Elbe but also the watersides of the many harbor basins are constructed to utilize fully the limited water space in order to handle the increasing vessel traffic. For this reason several kilometers of different quay walls have been built over the last decades. Almost all other water sides are constructed as embankments with well defined cross-sections. These cross-sections were planned and realized to use only relatively small transition areas between the land and fairway to increase the water area which can be used by the vessel traffic. Generally this is done by increasing the slope ratio of such embankments. To improve the stability of the embankments these steep slopes are made up of several pavement layers of different material to avoid instabilities. Because of external causes based on strong erosion effects, vessel groundings or over-dredging activities the stability of steep slopes can be endangered and lead to slope ruptures. These critical damages of the embankment affect not only the safety of navigation in this area but also the stability of buildings and constructions located directly at the waterside.

For this reason the most endangered embankments of the port have to be monitored in certain intervals by hydrographic measurements. The results of these measurements were generally mapped as scaled hydrographic charts containing depth values and depth contours of the surveyed area. By comparing the results of different surveys partial changes of the embankment like subsidences can be detected and potential slope ruptures can be avoided or at least the effects of these damages minimized.

Unfortunately hydrographic echosounding measurements are only able to map the underwater part of the slopes whereas the dry part is of equal importance. To receive the required height information of the slope land surveys have to be performed by using discrete RTK GNSS and tacheometric measurements.

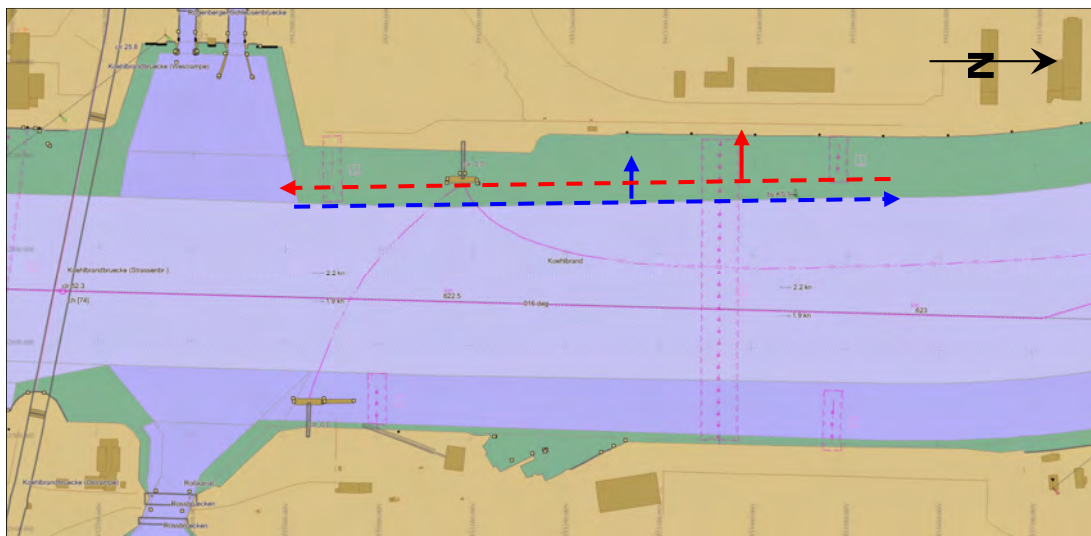


Figure 6.7: Overview of the “Koehlbrand” survey configuration; Two lines in opposite direction were measured for the mobile scanning part whereas the laser scanner was oriented perpendicular to the embankment

To avoid such uneconomic and dangerous surveys from land the laser scanning component of the mobile mapping system is well suited to take over this task. In the frame of this thesis an embankment survey was performed to show the advantages of the combination of multibeam and laser scan measurements. A special area located in the Koehlbrand was mapped and post-processed in order to create a bathymetric chart of the embankment. This chapter describes the workflow from data processing to the final end product the paper chart.

The survey was divided into two sections because of the tide effects in the port. At first the mobile laser scanning was performed during low tide in order to scan also areas which are submerged during high tide. As shown in figure 6.7 two in opposite direction sailed survey lines were measured for the laser scanning part of this survey. The bathymetric measurements were performed time shifted at high water to create an overlapping area with respect to the scan data.

After the survey the results of scanning and echosounding were available as online processed point clouds which allow a first quality assurance in the field. As shown in figure 6.8 both point clouds create a seamless transition between sounding and scanning data with no height differences in the overlapping area. After this first quality control the datasets of echosounding and laser scanning were processed separately whereas the post-processed trajectory was applied to both datasets.

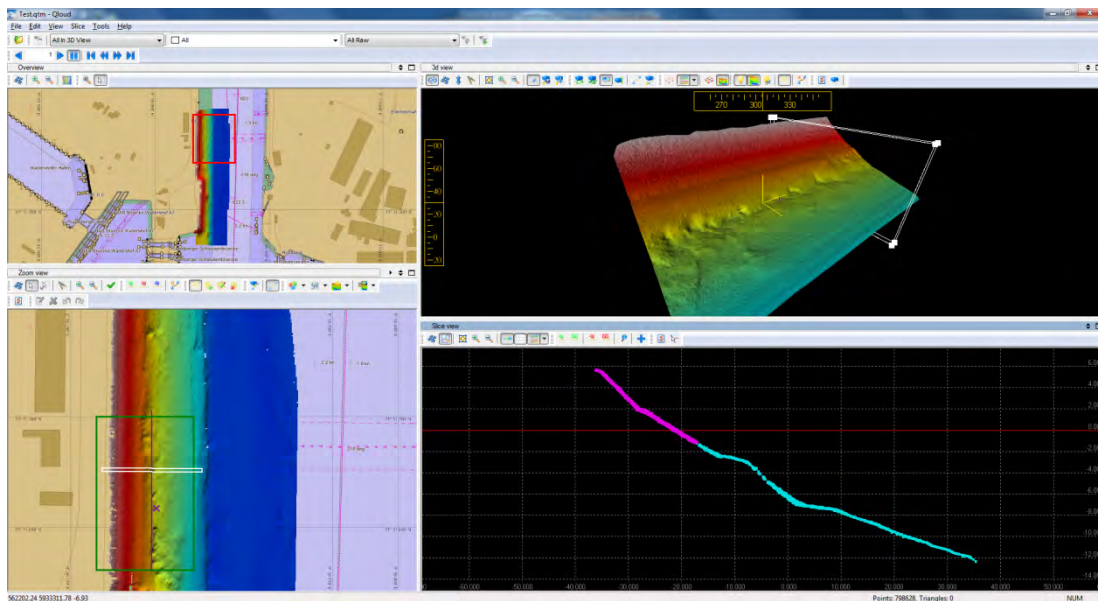


Figure 6.8: Quality assurance directly after the survey with the QPS post-processing tool Qloud; Multibeam and scan data are displayed combined as a depth depended color coded grid (Left); View of a 3D model of a part of the embankment (Top right) and a cross-section showing laser scan data as purple and multibeam data as blue points (Bottom right)

With respect to figure 6.9 the data processing workflow starts with already processed laser scan files in LAS-format which is a public transfer format for LIDAR data and with XTF (eXtended Triton Format) files which contain the sensor raw data for multibeam processing. These files were imported into CARS HIPS&SIPS where the multibeam datasets are merged with the post-processed trajectory to create bathymetric point clouds. The point clouds from the laser and multibeam survey have to be cleaned to get rid of outliers and blunders in multibeam data and unwanted laser scan points from vegetation and adjacent manmade features like buildings, fences or walls.

The cleaned datasets were used to build high resolution bathymetric grids which can be described as regular 2½ dimensional models of the mapped embankment. These grids were imported into CARIS BathyDatabase where depth contours and soundings were calculated.

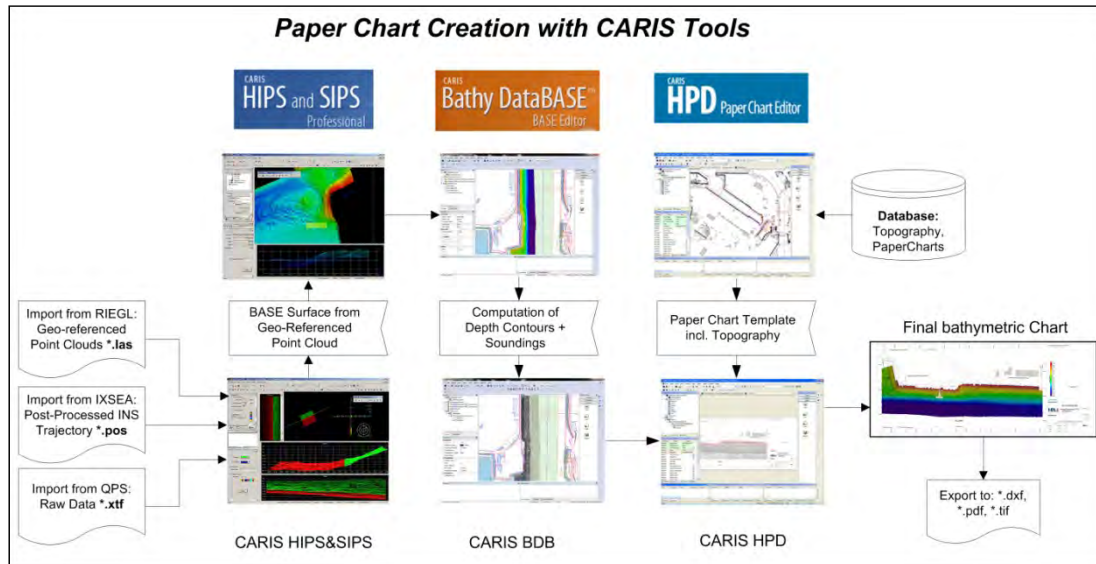


Figure 6.9: Schematic of the paper chart production workflow based on CARIS tools ; From data processing and cleaning in HIPS&SIPS to the final bathymetric chart in HPD.

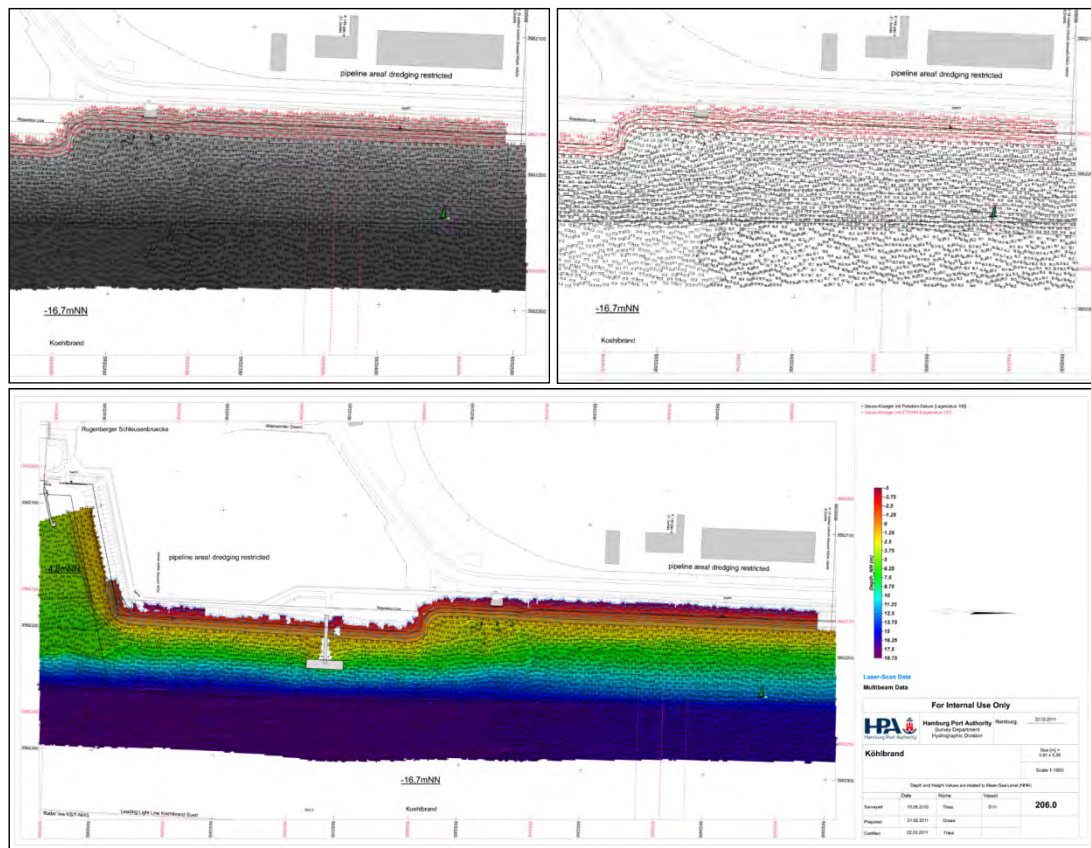


Figure 6.10: The bathymetric chart as an end product of the multibeam and laser scan survey project for embankment monitoring; The soundings based on laser scanning are annotated in red (Top) and complements the multibeam dataset to map the whole steep slope up to the top ground surface

The contours and soundings which were prepared for a special chart scale were imported into the HPD Paper Chart Editor. This product editor is based on a hydrographic database containing topographic and maritime objects of the whole port in S57 format. Additionally all geo-referenced templates of paper charts which cover the port area are stored in this database. The final procedure is to import the bathymetric grid, the depth contours and soundings into the corresponding paper chart template as shown in figure 6.10. Although such bathymetric charts can be printed as the name of the product editor suggests, they usually were used as pdf-documents or geo-tiff images. Usually the bathymetric grids were used in such monitoring applications to create difference models where height differences of two grids of different survey epochs were computed. The resulting chart is just a difference chart containing difference contours and soundings.

As shown in this example the combination of laser scan and multibeam measurements from one mobile platform can partially replace static land survey procedures especially at the transition zone between water and land. The tide effect can be used to create seamless “wet” and “dry” datasets from the deep fairway up to a flood protection facility like a dam or wall. Both datasets complements one another and control each other if they overlap.

6.3 Harbor “Grasbrookhafen” – Electronic Navigational Chart

This chapter describes the creation of a non-official Electronic Navigational Chart (ENC) for a small area in the Port of Hamburg out of topographic laser scan and bathymetric echosounding datasets. As defined by the International Maritime Organization (IMO) ENC means “... the database, standardized as to content, structure and format...” and contains “...all the chart information necessary for safe navigation and may contain supplementary information which may be considered necessary for safe navigation.” Official ENC’s were created by authorized governmental hydrographic offices for the use in type approved Electronic Chart Display and Information Systems (ECDIS). At the moment ECDIS containing official ENC datasets replace old-fashioned sets of paper charts which had to be used in the past for navigation by vessels which are covered by the IMO SOLAS convention. Nowadays ECDIS becomes mandatory for several types of vessels as shown in the table 6.1 below.

Type of Ship	Gross Tonnage	Date of Construction	Start of ECDIS Carriage Requirement
	≥ 500	≥ 07/01/2012	07/01/2012
		< 07/01/2012	07/01/2014
	≥ 3000	≥ 07/01/2012	07/01/2012
		< 07/01/2012	07/01/2015
	3000 - 10000	≥ 07/01/2014	07/01/2014
	≥ 10000	≥ 07/01/2013	07/01/2013
	10000 - 20000	< 07/01/2013	07/01/2018
	20000 - 50000	< 07/01/2013	07/01/2017
	≥ 50000	< 07/01/2013	07/01/2016

Source: Resolution MSC.282(86) Annex 1

Table 6.1: Overview of ECDIS carriage requirements classified by ship type and size based on the latest amendment to SOLAS (HPA)

Not only for SOLAS vessels ENC's become more and more important, also in a port like the Port of Hamburg different public authorities like water police or fire brigade but also private shipping companies which offers harbor tours or ferry trips have a demand on high accurate and detailed electronic charts of the port. Since ENC's are based on IHO S57 datasets almost all third party navigation software packages support this format for navigational purposes. For this reason it is not required to setup a complete ECDIS system with official ENC's which are not designed for special port relevant requirements but to provide customized datasets for the day-to-day business of port companies.

The selected area for this product creation is the harbor basin Grasbrookhafen which was already introduced in chapter 5. The measurements were similar to the survey described in chapter 6.2 split into laser scanning and echosounding part whereas the data acquisition was performed by QPS QINSy. The whole product creation workflow is summarized in figure 6.11 and starts with bathymetric data processing in CARIS HIPS&SIPS where a bathymetric grid respectively a BASE surface was created. This grid was imported into the BASE Manager tool of the BathyDatabase (BDB). By defining the required depth intervals it was possible to compute S57 conform depth areas, depth contours and soundings out of the BASE surface. The laser scan data which were available as geo-referenced point clouds immediately after the survey were directly imported in the BDB. With different available 2D and 3D views it is possible to digitize features in the point cloud whereas the software is directly linked to the S57 object catalogue. Object attributes can directly be defined during the digitization process. All digitized features respectively S57 objects describing the topography, aids to navigation, land and sea areas but also Meta information were then loaded into the CARIS S57 Composer.

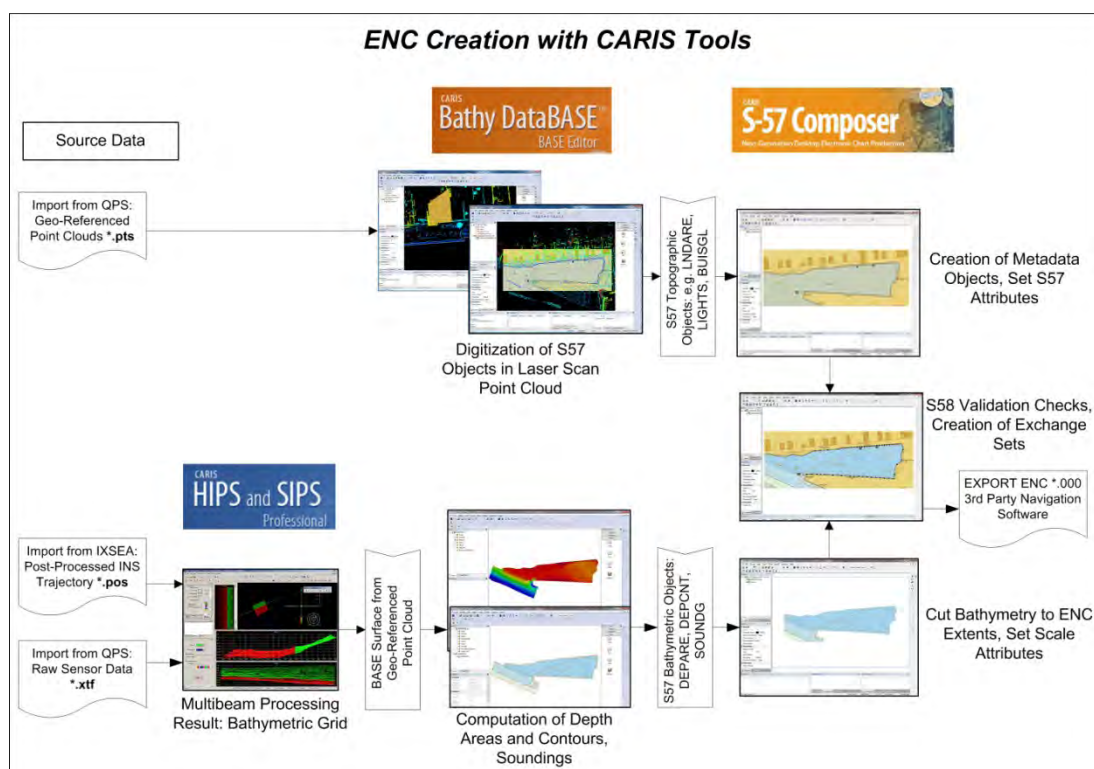


Figure 6.11: Schematic of the ENC production workflow based on CARIS tools; From data processing and cleaning in HIPS&SIPS over S57 object creation in BathyDatabase to the final electronic navigational chart created in the S57 Composer

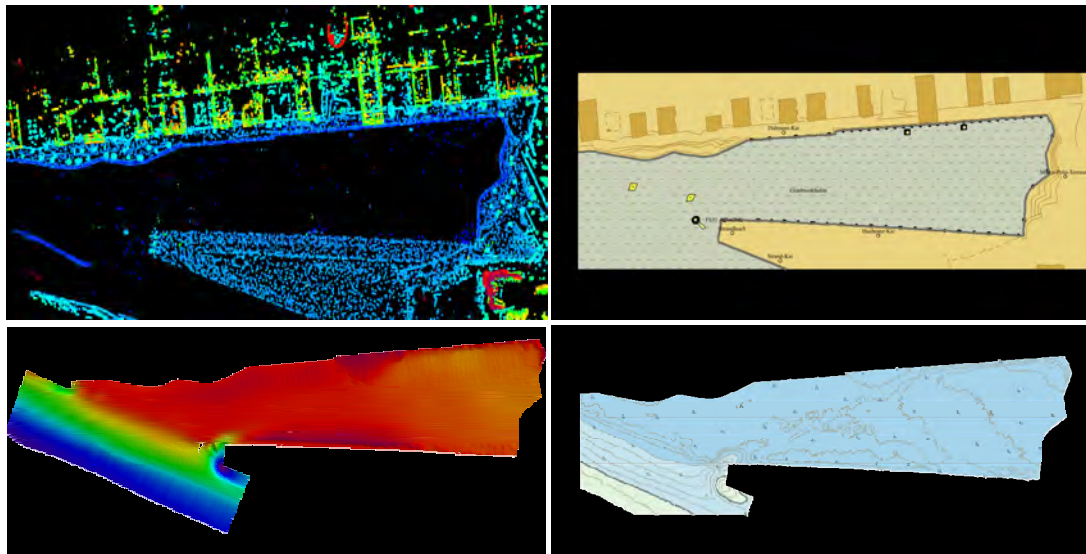


Figure 6.12: Source data and intermediate S57 products of bathymetric and laser scanning measurements; Laser scan point clouds and derived S57 objects (Top); Bathymetric grid and derived S57 depth areas, depth contours and soundings (Bottom)

This ENC production tool merges the intermediate bathymetric and topographic products of the BDB which is displayed in figure 6.12 to create one final ENC cell. The composer allows not only to set all mandatory attributes which for example influence the presentation of the ENC cell but also to check the S57 conformity of the dataset. The created ENC cell of the Grasbrookhafen as pictured in figure 6.13 provides at least decimeter accuracy and is more suited to large scale applications than an official ENC.

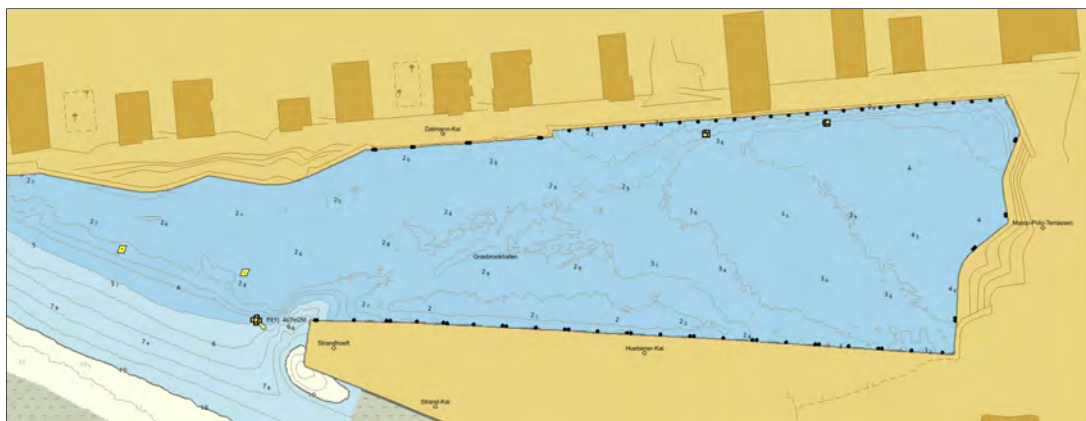


Figure 6.13: Non-official Electronic Navigational Chart ENC of the Grasbrookhafen including topographic and bathymetric information optimized for large scale applications in a port.

The produced ENC can be used for navigational purposes for example on survey vessels, dredgers, port ferries, harbor tour boats and can complement existing official ENC's when the corresponding vessel is not covered by the SOLAS convention. As mentioned in chapter 6.1 such ENC's can be used as base datasets in a port management and information system. The creation of S57 datasets based on mobile mapping measurements is straight forward whereas the digitization is the most time consuming process.

6.4 Summary

It was shown that the results of mobile mapping measurements are not only nice to see but also have several practical purposes. Although several end products were presented in the chapters before there are manifold other practical applications for mobile mapping measurements imaginable. In the following some more possible applications from the point of a port authority were presented.

Especially in the Port of Hamburg a potential route of a vessel is mostly restricted either by water depths or by bridges. The draught and height of a vessel determines the areas in the port which can be reached by a ship at a certain water level. With overall 2500 bridge constructions there is a certain demand on accurate clearance diagrams for the commercial shipping sector. With mobile mapping systems which combine echosounding, laser scanning and camera sensors, source datasets for clearance investigations can be produced easily as shown in figure 6.14. But also the physical condition of a bridge which is of high importance for the operation of this construction can be monitored simultaneously during such a survey.

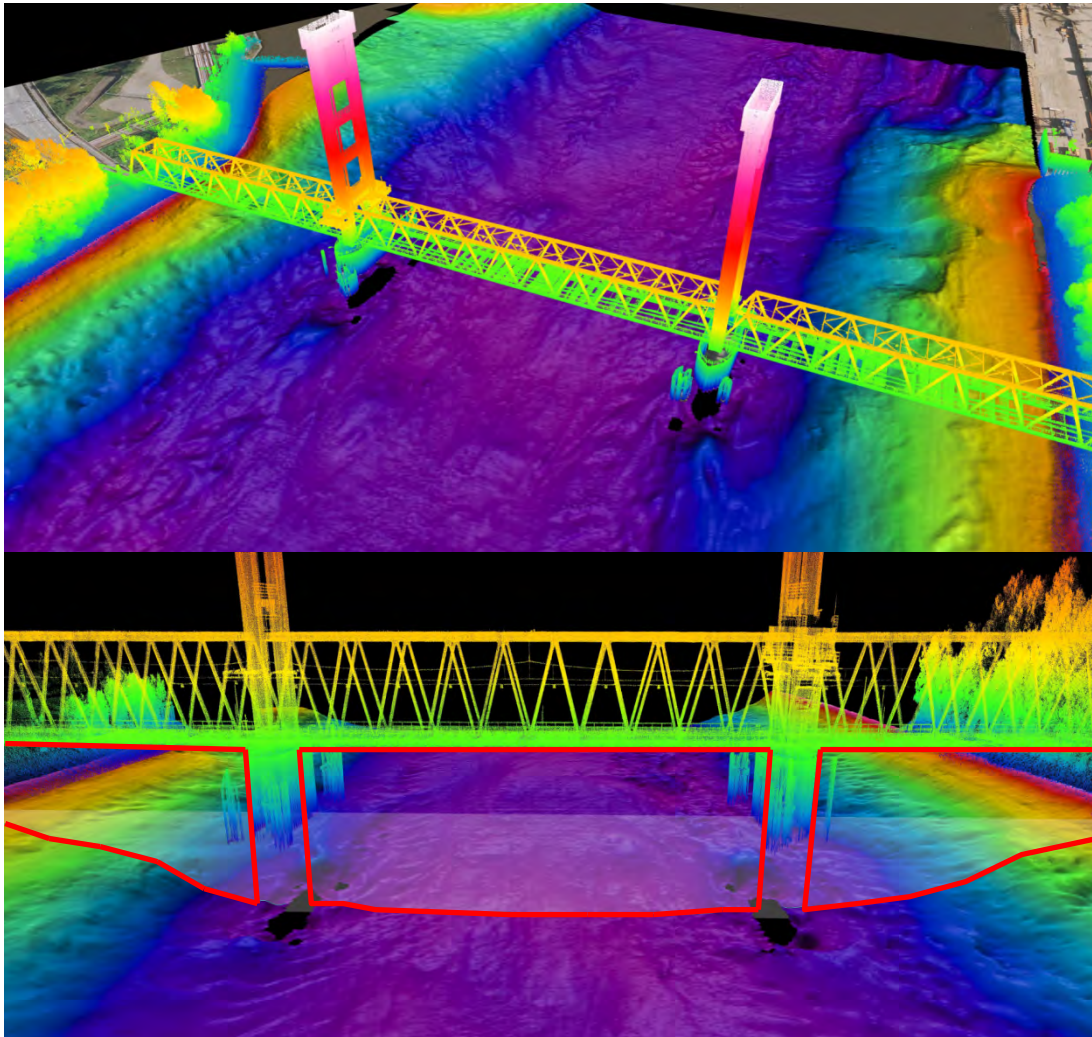


Figure 6.14: Vertical clearance information can be derived from mobile mapping surveys; In this case the Kattwyk Bridge and the surrounding area was surveyed with multibeam echosounder and laser scanner; Vertical clearance diagrams can be produced directly out of the point clouds (Bottom)

With high resolution multibeam echosounders the seabed can be mapped to detect critical erosions at pylons of the bridge which may have an effect on the stability of the bridge. But also the whole construction can be investigated to find damages or deformations caused by vessel collisions.

Another field of work is the monitoring of port facilities like quay walls. At the moment only the seabed topography in front of these constructions are monitored by echosounding methods. But especially for the responsible facility managers the current structural condition and also a temporal change in condition of those buildings are important to plan further maintenance activities.

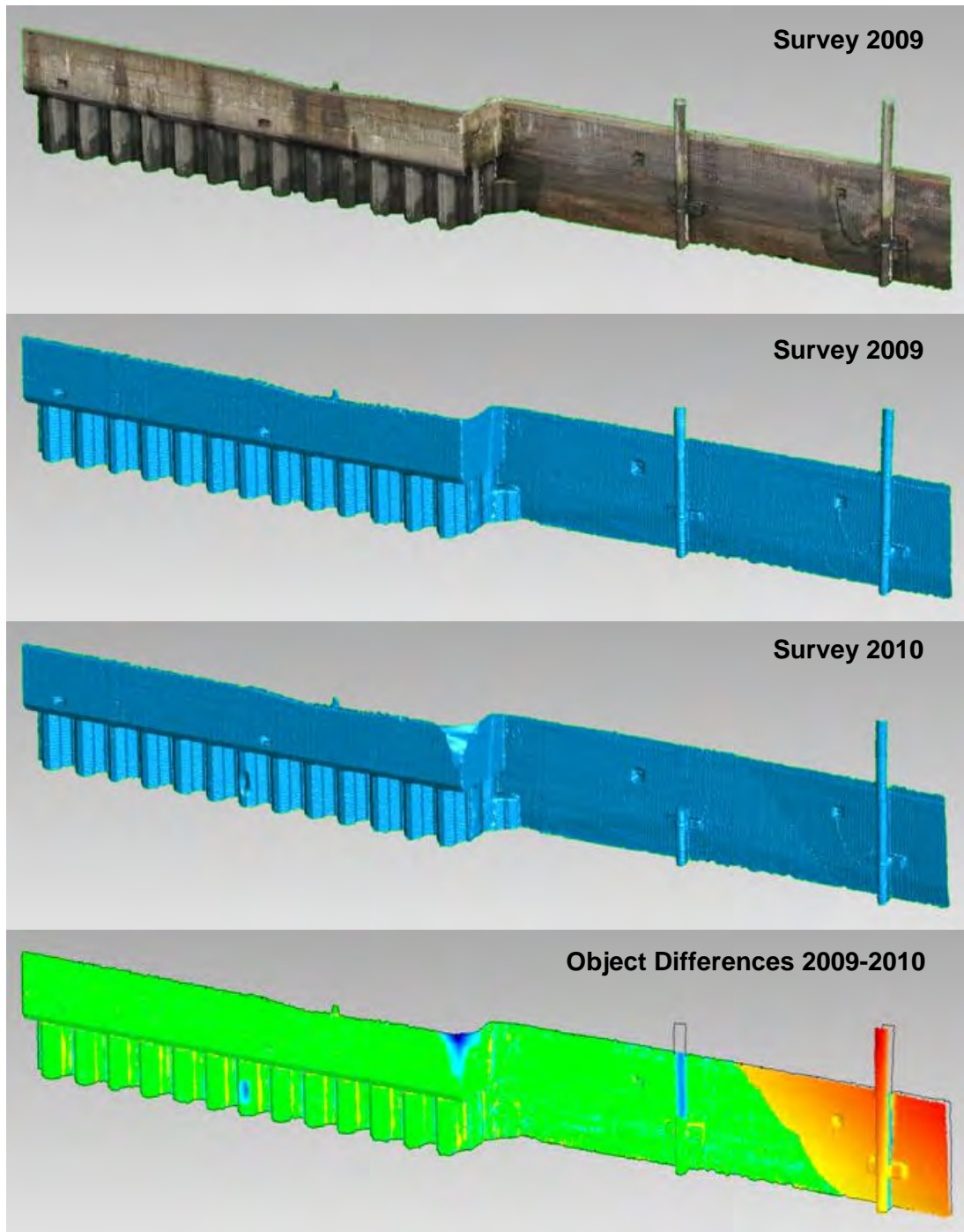


Figure 6.15: Change analysis of a part of an old quay wall; The wall was surveyed in 2009 and again in 2010; The 3D geometric differences are shown as a difference model (Bottom)

In the example shown in figure 6.15 a change analysis was simulated for a part of an old quay wall. Two consecutive surveys from 2009 and 2010 were geometrically compared with each other in order to evaluate physical changes of the construction. The survey from the year 2009 depicts the good condition of the quay wall whereas obvious deformations have occurred before the second survey was performed. The difference model, which displays changes as color coded areas, reveals several small damages like the burst pile, a demolished edge at the beginning of the sheet pile wall and a small buckle in one sheet pile element. The most significant change is the tilted part of the very old brick wall on the right hand side of the difference model. It can be expected that the wall will collapse in the near future caused by earth pressure induced maybe by construction activities at land. Such a change analysis can be used by the responsible authority to lock down this facility immediately and to trigger activities to avoid the collapse of the wall.

Very important results of all monitoring activities are photographs of the current state of the monitored object. Since mapping sensors like laser scanner are generally equipped with high resolution digital cameras the photos taken during the scan procedure cannot only be used to colorize the point clouds or to texturize derived 3D models but also as a stand-alone product. As introduced with google street view the photos can be processed to map the whole port in a "Port View" application. Below in figure 6.16 some selected pictures taken during thesis related survey projects are displayed.



Figure 6.16: Photographs for a potential "Port View" application taken during mobile mapping measurements; Pictures of the west side of the Ellerholz Lock (Top) and the north-easterly part of the Kattwyk Bridge (Bottom)

7. Conclusion and Outlook

The Hamburg Port Authority is responsible for the strategic port planning, the real-estate management, the maintenance of waterway, railway and corresponding land infrastructure and the safety of navigation in the Port of Hamburg. To attend for this duty the HPA improves and further develops port facilities and the whole port infrastructure continuously. Not for no reason the Port of Hamburg is able to handle millions of containers and additionally millions of tons of bulk and mixed cargo. One major task of the HPA's waterway infrastructure is the maintenance of the water depths and corresponding bank constructions in the port. Because of sedimentation and erosion effects in the tide influenced port area the seabed topography changes continuously. This is monitored by the four survey vessels of the hydrographic department of the HPA which perform all-the-year hydrographic measurements to determine the water depths area based in the whole port. Unfortunately hydrographic echosounding measurements are only able to map the underwater part of slopes, embankments, quay walls and other port facilities although the dry part is of equal importance.

In this thesis a survey system has been established, which provide not only kinematic echosounding but also above-water mapping capabilities by using a terrestrial laser scanner in addition to the multibeam echosounder. Terrestrial laser scanners are active, optical measurement sensors which are based on contact-free and area based object detection by using laser devices. These sensors scan automatically the environment either grid based or similar to multibeam echosounders profile based with high speed in order to map the surrounding area as a point cloud.

A multisensor system was configured to provide not only online data processing but also post-processing capabilities. It was shown that the main focus during such an installation should be on accurate time synchronization for all used sensors. But although this was assured in the established system a certain latency in motion data was detected. On the other hand it was pointed out that the spatial relationship between the mapping, positioning and attitude sensors has to be known precisely to setup a proper system. A workflow has been proposed which covers the initial measurement to determine the lever arms in the body system and the calibration procedure to determine the angular misalignments of all contained mapping sensors. It was shown that the visual determination of the angular offsets in the validator tool of QPS QINSy is laborious, time consuming and user depended. Algorithms have to be implemented to compute the calibration parameters automatically like it is realized for multibeam datasets.

To handle the recorded data either in online or in post-processing mode five different processing workflows were presented and compared with each other. It was shown that the online processing produce geo-referenced point clouds in the field which enables to user to make first quality control during data acquisition. The online processed survey results give a good overview of the performance of the system and can be used to fine-tune the survey configuration.

QINSy's post-processing capabilities enables the user to go back to online recorded sensor raw data but also to implement certain external datasets like a post-processed trajectory. With additional data manipulation tools QINSy can be used to improve the measurement result iteratively.

The software RIEGL RiPROCESS combines scanner raw data and external trajectory data to process geo-referenced point clouds. With the automated scan data adjustment RiPROCESS provides a powerful tool to compute the angular misalignments of the mapping sensor out of the scan data. Another advantage of the RIEGL approach is the possibility to process camera data together with laser scan point clouds. It was stated that a combination of both software packages would complement one another's advantages to build the complete mobile mapping processing solution.

The performed accuracy analysis was used to evaluate the accuracy of the mobile mapping system with focus on mobile laser scanning. A uncertainty estimation was presented with the result that the heading accuracy of the INS is the weakest link of the accuracy "chain". In addition to the inner accuracy respectively the precision which describes the measure how good different correlated datasets match to each other, the absolute accuracy between the reference dataset and mobile datasets was investigated as well. By using area based 3D deviation models it was shown that in contrast to statistical methods a more realistic approach was to examine each 3D difference model individually to find reliable values for area based deviations. The results were similar to the estimated uncertainties and it was possible to confirm that the coordinate component which is mostly influenced by the heading accuracy of the system contains a lower accuracy. It was pointed out that the accuracy and performance of the mobile mapping system is well suited for a lot of applications.

Finally several survey projects in the Port of Hamburg were presented and have shown that the results of mobile mapping can be used to create multipurpose products like a 3D port models, bathymetric papercharts or electronic navigational charts and many more. It was shown that the combination of laser scan and multibeam measurements from one mobile platform can partially replace static land survey procedures especially at the transition zone between water and land. The tide effect can be used to create seamless "wet" and "dry" datasets from the deep fairway up to a flood protection facility like a dam or wall. Both measurement methods on one survey platform complements one another in order to support decision making processes for the maintenance of the port infrastructure with high resolution geo-datasets.

Future work is needed to evaluate the performance of laser scanning methods on soft and wet sediments. As the Port of Hamburg is in a tide influenced area especially laser scan measurements on areas which fall dry during low tide have to be tested and evaluated.

Further investigations have to be done from the point of data storage and data handling. At the moment it is possible to produce terabytes of point cloud data but the data management is mostly performed only file based. Database solutions have to be developed to handle the amount of point clouds and to provide interfaces to product creation tools.

I List of Figures

2.1	Principle of one-dimensional propagation of sound waves as a function of time (LURTON, 2010).....	6
2.2	Physical principle of piezoelectricity and the realization of this effect in a transducer (LURTON, 2010)	7
2.3	Principle of measurement of a singlebeam echosounder (LURTON, 2010)	7
2.4	Principle of measurement of a multibeam echosounder (LURTON, 2010)	9
2.5	Relationship between measured variables of a multibeam echosounder (LURTON, 2010)	10
2.6	Principle of measurement of a terrestrial laser scanner (GORDON, 2008)	11
2.7	Fields of application for terrestrial laser scanners (ELING, 2009)	12
2.8	Direct time-of-flight measurement principle (HESSE, 2007)	13
2.9	Multiple target capability of laser scan systems (RIEGL, 2010)	14
2.10	Amplitude-modulated continuous wave measurement principle (HESSE, 2007)	15
2.11	Principle of dynamic incremental encoding by measuring the phase shift (MÖSER et al., 2000)	16
2.12	Examples of parallel and serial binary codes for angle encoding (SCHULZ, 2007).....	17
2.13	Relationship between spherical and cartesian coordinates with respect to the scanners own coordinate system (ELING, 2009)	18
2.14	Classification of laser scan devices by the field of view (HESSE, 2007).....	18
2.15	Classification of laser scanning devices by deflection system (HESSE, 2007)	19
2.16	Types of reflection and different scenarios of laser beam – object geometry (JUTZKI, 2007)	20
2.17	The free gyroscope (TETLEY, CALCUTT, 1988)	21
2.18	Precession of a gyroscope (FAA, 2008).....	22
2.19	Principle of a bottom heavy north seeking gyro (TETLEY,CALCUTT,1988)	23
2.20	Principle of a precessing gyro only influenced by the gravity and a gyro damped by an external torque (TETLEY, CALCUTT, 1988)	23
2.21	Example of gyro damping by using the principle of communicating vessels (TETLEY, CALCUTT, 1988)	24
2.22	The Sagnac Interferometer (WIKIPEDIA, 2011).....	25
2.23	Principle of measurement of a ring laser gyroscope and a fiber optic gyroscope (GROVES, 2008)	26
2.24	Configuration of a common inertial measurement unit IMU (GROVES, 2008).....	27
2-25	Schematic of the IXSEA Kalman filter (IXSEA, 2009)	28
2.26	Schematic of a possible mobile mapping system and an example of a practical realization of an car based MMS (RIEGER et al., 2008).....	30

LIST OF FIGURES

2.27	Different approaches of time synchronization between GNSS, laser scanner and external sensors (HESSE, 2007)	31
2.28	Geo-referenced scan data and corresponding trajectory (STUDNICKA et al., 2007)	32
2.29	Example of the results of an combined forward and backward Kalman filter (IXSEA, 2010)	33
2.30	Relationship of different reference frames used in mobile mapping applications (GRÄFE, 2007)	34
2.31	The mobile mapping system Road-Scanner (GANDOLFI et.al., 2008).....	36
2.32	The mobile mapping system mini-UAV (JAAKKOLA et.al., 2010)	37
2.33	The mobile mapping system Bay-Hydrographer (VAN RENS et.al., 2007).....	38
3.1	Survey vessels “Deepenschriewer I – IV” of the HPA.....	39
3.2	Survey boat “Level A” of the NIAH	40
3.3	RIEGL VZ-400 laser scanner	41
3.4	Z+F IMAGER 5006h laser scanner	41
3.5	TSS MAHRS-Surface attitude and heading sensor	41
3.6	IXSEA OCTANS attitude and heading sensor	42
3.7	IXSEA HYDRINS inertial navigation system	42
3.8	TRIMBLE SPS851 GNSS receiver	42
3.9	RESON Seabat 8101 multibeam echosounder.....	43
3.10	Sensors for mobile mapping mounted on a single bracket on the roof of the “Deepenschriewer III”	43
3.11	Schematic of interfaced sensors	44
3.12	User interfaces of RIEGL VZ-400, IXSEA HYDRINS, TRIMBLE SPS851	45
3.13	„Deepenschriewer III“ on slipway and lever arm determination in water.....	46
3.14	Determination of lever arms by initial measurement	47
3.15	Angular misalignments between IMU frame and vessels coordinate system (IXSEA, 2009).....	48
3.16	Determination of the heading misalignment of the IMU with respect to the vessels coordinate system	49
3.17	IMU reference measurement to determine angular offsets in roll and pitch direction between the IMU and the vessels reference frame	50
3.18	Calibration procedure for determination of roll and pitch boresight angles ...	51
3.19	Calibration procedure for determination of roll and pitch boresight angles with the Validator tool of QPS QINSy.....	52
3.20	Calibration procedure for determination of heading misalignment.....	53
3.21	Calibration procedure for determination of second heading misalignment ...	55
3.22	Position offset between three reversely sailed survey lines	56
3.23	Motion artifacts in point clouds of the survey project “Dockland”	57
3.24	Cross section of the “Dockland” façade with compensated latency	58
3.25	The geometrical relationship between range, vertical angular stepwidth, vessel speed and the resulting horizontal and vertical point spacing	59
3.26	Considerations on laser point density for the RIEGL VZ-400 system	60

4.1	A partial overview of the QINSy settings file used for mobile mapping	62
4.2	A possible configuration of the QINSy online user interface	63
4.3	QINSy controller for scanner RIEGL VZ-400 and camera NIKON D700.....	63
4.4	QINSy logfile of controller / scanner communication.....	64
4.5	Schematic overview of QINSy online processing	64
4.6	QINSy Analyze tool to evaluate and edit sensor raw data	66
4.7	QINSy Analyze tool to filter noisy sensor raw data.....	66
4.8	Schematic overview of the QINSy post processing workflow.....	67
4.9	Comparison of the height component of the trajectory determined with GNSS, INS online mode and INS post-processing mode	68
4.10	Schematic overview of the QINSy post processing workflow using post- processed INS trajectory	69
4.11	Transformation matrices to define the lever arms and angular misalignments in RIEGL RiPROCESS	70
4.12	User interface of RiPROCESS after post-processing.....	70
4.13	Schematic overview of the RIEGL post processing workflow.....	71
4.14	Spatial relationship between two corresponding planar surfaces (RIEGER et.al. 2009).....	72
4.15	Plane search and matching parameters for scan data adjustment	73
4.16	Results of a scan data adjustment computation.....	73
5.1	Uncertainty of a soundings position and depth in water depths of 20 meters for the survey system "Deepenschriewer III" (THIES, 2007)	79
5.2	The scanners own coordinates system (RIEGL, 2009)	80
5.3	Range dependent uncertainty of a laser footprint.....	83
5.4	Comparison of uncertainties of corresponding laser footprints produced by INS and AHRS measurements	84
5.5	Changes in uncertainty of a laser footprint depending on the tilt angle of the laser beam.....	85
5.6	Changes in uncertainty of a laser footprint depending on the pan angle of the laser scanner	85
5.7	Comparison of Gaussian and linear law of error propagation	86
5.8	Comparison of range depending uncertainty for laser scanning and multibeam echosounding.....	87
5.9	Overview of the area used for the reference measurement	89
5.10	Overview of the reference point cloud in true color mode	90
5.11	Overview of selected objects used for accuracy evaluation	91
5.12	Overview of the survey line configuration in combination with all test objects	93
5.13	Overview of the 3D object production workflow in Geomagic Studio	94
5.14	Overview of three types of deviation calculation in Geomagic Qualify	95
5.15	Overview of the 3D deviation computation workflow in Geomagic Qualify...	95
5.16	Graphical summary of difference calculations for precision determination ..	96
5.17	Graphical summary of difference calculations for test objects C and D	97
5.18	Graphical summary of difference calculations for multiple survey lines	99

LIST OF FIGURES

5.19	3D difference models derived from different survey lines	100
5.20	Graphical summary of difference calculations for absolute accuracy determination – Mean deviations	102
5.21	Graphical summary of difference calculations for absolute accuracy determination – Standard deviations.....	103
5.22	3D models of test object A derived from different source datasets influenced by the scanner orientation.	104
5.23	3D difference model derived from survey line 1 with scanner orientation of 200deg	104
5.24	Distribution of differences in X, Y and Z direction as histograms.....	105
5.25	3D difference models discover systematic effects in mobile datasets	105
6.1	Overview of the “Dockland” survey configuration.....	107
6.2	Pre-cleaned point cloud of the mapped building “Dockland” color coded by height.....	108
6.3	Overview of the modeling workflow in Terrasolid TerraScan	108
6.4	Schematic of the modeling workflow in Terrasolid TerraScan	109
6.5	Combination of 3D Dockland model and bathymetric 3D model.....	110
6.6	Possible data combinations for a port information system.....	110
6.7	Overview of the “Koehlbrand” survey configuration	111
6.8	Quality assurance directly after the survey with the QPS post-processing tool Qcloud.....	112
6.9	Schematic of the paper chart production workflow based on CARIS tools .	113
6.10	The bathymetric chart as an end product of the multibeam and laser scan survey project for embankment monitoring	113
6.11	Schematic of the ENC production workflow based on CARIS tools.....	115
6.12	Source data and intermediate S57 products of bathymetric and laser scanning measurements	116
6.13	Non-official Electronic Navigational Chart ENC of the “Grasbrookhafen” ...	116
6.14	Vertical clearance information derived from mobile mapping surveys	117
6.15	Change analysis of a part of an old quay wall.....	118
6.16	Photographs for a potential “Port View” application.....	119

II List of Tables

2.1	Overview of different laser scanning systems differentiated by the distance measurement method (Schulz, 2007)	12
2.2	Overview of different laser scanning systems differentiated by the deflection system (Schulz, 2007).....	19
2.3	Biases for common gyroscopes and accelerometers distinguished by IMU grade (Grove, 2008).....	27
2.4	Different potential sensors of a mobile mapping system (Hesse, 2007)	30
2.5	Different coordinate reference frames in mobile mapping applications (Gräfe, 2007)	33
2.6	Overview of developed and published mobile mapping systems classified by mobile platform (Hesse, 2007)	35
3.1	Results of the heading misalignment computation	49
3.2	Results of the first boresight angle calibration procedure.....	54
3.3	Results of the second boresight angle calibration procedure.....	54
3.4	Combined results of both boresight angle calibration procedures.....	55
4.1	Results of the scan data adjustment	74
4.2	Final evaluation of determined angular misalignments	74
5.1	Accuracy information of used sensors according to system developer information.....	82
5.2	Overview of created 3D objects and their corresponding differences	94
5.3	Main results of 3D object comparison separated for each processing method.....	96
5.4	Main results of 3D object comparison separated for each survey line	97
5.5	Main results of 3D object comparison separated for each test object and both remaining processing methods.....	98
5.6	Pairs of datasets for difference computations	101
5.7	Results of difference computations between reference and test datasets separated for test objects A and B	101
5.8	Results of difference computations between reference and test datasets separated for test objects C and D	102
6.1	Overview of ECDIS carriage requirements (HPA, 2010).....	114

LIST OF TABLES

III Bibliography

[ALHO et al., 2009], Alho, P., Kukko, A., Hyypä, H., Kaartinen, H., Hyypä, J., Jaakkola, A. (2009), *Application of boat-based laser scanning for river survey*, in Earth Surface Processes and Landforms, Vol. 31, Department of Geography, University of Turku, Finland

[BOWDITCH, 1995], Bowditch, N. (1995), *The American Practical Navigator - An Epitome of Navigation*, 1995 edn, National Imagery and Mapping Agency, Bethesda, USA

[CALDER, 2003], Calder, B.R. (2003): *Automatic Statistical Processing of Multibeam Echosounder Data*, Int. Hydro. Review, Vol. 4, No. 1, New Hampshire USA

[ELECTRICLY, 2011], Free Tutorial Electronics and Robotics (2011), *Absolute Optical Encoders*, <http://electricly.com/tag/optical-encoder/> (accessed 01 Feb. 2011)

[ELING, 2009], Eling, D. (2009), *Terrestrisches Laserscanning für die Bauwerksüberwachung*, Dissertation, Fakultät für Bauingenieurwesen und Geodäsie, Deutsche Geodätische Kommission der Bayerischen Akademie der Wissenschaften, Munich, Germany, pp. 13-18

[FAA, 2008], Federal Aviation Administration (2008), *Instrument Flying Handbook*, http://www.faa.gov/library/manuals/aviation/instrument_flying_handbook/ (accessed 02 Feb. 2011)

[FABECK, 1980], Fabeck, W. v. (1980), *Kreiselgeräte*, Vogel-Verlag, Würzburg, Germany

[GANDOLFI et al., 2008], Gandolfi, S., Barbarella, M., Ronci, E., Burchi, A. (2008), *Close Photogrammetry and Laser Scanning using a Mobile Mapping System for the High Detailed Survey of a High Density Urban Area*, ICWG V/I Integrated systems for mobile mapping, Bologna, Italy

[GEOMAGIC, 2010-1], Geomagic (2010), *Geomagic Studio – Online Help*, Online Help, Durham, USA

[GEOMAGIC, 2010-2], Geomagic (2010), *Geomagic Qualify – Online Help*, Online Help, Durham, USA

[GLAUS, 2006], Glaus, R. (2006), *Kinematic Track Surveying by Means of a Multi-Sensor Platform*, Dissertation, Swiss Federal Institute of Technology, Zurich, Switzerland, pp. 141-162

[GLENNIE, 2009], Glennie, C. (2009), *A Kinematic Terrestrial LIDAR Scanning System*, Article Transportation Research Board of National Academies, USA

[GORDON, 2008], Gordon, B. (2008), *Zur Bestimmung von Messunsicherheiten terrestrischer Laserscanner*, Dissertation, Fachbereich Bauingenieurwesen und Geodäsie, Technische Universität Darmstadt, Germany, pp. 19-34

BIBLIOGRAPHY

- [GRÄFE, 2007], Gräfe, G. (2007), *Kinematische Anwendungen von Laserscannern im Straßenraum*, Dissertation, Fakultät für Bauingenieur- und Vermessungswesen, Universität der Bundeswehr München, Germany, pp. 21-55
- [GREWAL, WEILL, ANDREWS, 2007], Grewal, M. S., Weill, L. R., Andrews, A.P. (2007), *Global Positioning Systems, Inertial Navigation and Integration*, 2nd edn, John Wiley & Sons, Hoboken, USA
- [GROVES, 2008], Groves, P. D. (2008), *Principles of GNSS, Inertial, and Multisensor Integrated Navigation Systems*, 1st edn, Artech House, Boston, USA
- [HARE et al., 1995] Hare, R., Godin, A., MAYER, L. A., (1995) *Accuracy Estimation of Canadian Swath and Sweep Sounding Systems*, Technical Report, Canadian Hydrographic Service, New Brunswick, Canada
- [HARE, 2001], Hare, R. (2001), *Error Budget Analysis for NAVOCEANO Hydrographic Survey Systems*, Final Report for Task 2 FY 01, Hydrographic Science Research Center, University of Southern Mississippi, USA
- [HESSE, 2007], Hesse, C. (2007), *Hochauflösende kinematische Objekterfassung mit terrestrischen Laserscannern*, Dissertation, Deutsche Geodätische Kommission der Bayerischen Akademie der Wissenschaften, Munich, Germany, pp. 14-71
- [IXSEA, 2009], IXSEA (2009), *PHINS – User Guide*, Technical Manual, Paris, France, pp. I2-I13
- [IXSEA, 2010], IXSEA - IXBLUE Company (2010), *Delph INS – IXSEA INS post processing software*, IXESA Presentation, Paris, France
- [JAAKKOLA, 2010] Jaakkola, A., Hyyppä, J., Kukko, A., Yu, X., Kaartinen, H., Lehtomäki, M., Lin, Y. (2010), *A low-cost multi-sensoral mobile mapping system and its feasibility for tree measurements*, Article in press ISPRS, Masala, Finland
- [JUTZKI, 2007], Jutzi, B. (2007), *Analyse der zeitlichen Signalforn von rückgestreuten Laserpulsen*, Dissertation, Institut für Photogrammetrie und Kartographie der Technischen Universität München, Munich, Germany, pp. 7-17
- [KAHMEN, 1997], Kahmen, H. (1997), *Vermessungskunde*, 19th edn, Walter der Gruyter, Berlin, Germany
- [LI, 1997] Li, R. (1997), *Mobile Mapping - An Emerging Technology For Spatial Data Acquisition*, Article, in 'Photogrammetric engineering and remote sensing', 1997, vol. 63, no. 9, pp. 1085-1092
- [LURTON, 2010], Lurton, X. (2010), *An Introduction to Underwater Acoustics – Principles and Applications*, 2nd edn, Springer, Chichester UK
- [MANSION, 2010], Mansion, R. (2010), *Laser Scanning and video recognition*, ENSIETA Final Year Project Report, Amsterdam, Netherlands
- [MÖSER et al., 2000], Möser, M., Müller, G., Schlemmer, H., Werner, H. (2000), *Handbuch Ingenieurgeodäsie - Grundlagen*, 3rd edn, Herbert Wichmann Verlag, Heidelberg, Germany

- [RIEGER et al., 2008], Rieger, P., Studnicka, N., Ullrich, A. (2008), „*Mobile Laser Scanning*“ *Anwendungen*, RIEGL Article, Horn, Austria
- [RIEGER et al., 2009], Rieger, P., Studnicka, N., Pfennigbauer, M. (2009), *Boresight alignment method for mobile laser scanning systems*, RIEGL Article, Horn, Austria
- [RIEGL, 2009], RIEGL Laser Measurement Systems (2009), *RIEGL VZ-400 - Technical Documentation*, Technical Manual, Horn, Austria, pp. 7-104
- [RIEGL, 2010-1], RIEGL Laser Measurement Systems (2010), *RiPROCESS Data Processing Software for RIEGL Scan Data*, User Manual, Horn, Austria
- [RIEGL, 2010-2], RIEGL Laser Measurement Systems (2010), *RiWORLD Geo Referencing Software for RIEGL Scan Data*, User Manual, Horn, Austria
- [SCHULZ, 2007], Schulz, T. (2007), *Calibration of a Terrestrial Laser Scanner for Engineering Geodesy*, Dissertation, ETH Zurich, Switzerland, pp. 7-22 / 87-108
- [SMITH, 2003], Smith, S. M., (2003), *The Navigation Surface a Multipurpose Bathymetric Database*, Master Thesis, New Hampshire, USA
- [STUDNICKA et al., 2007], Studnicka, N., Rieger, P., Ullrich, A. (2007), „*Mobile Laser Scanning*“ *Key Features and Applications*, Presentation Intergeo2007, Horn, Austria
- [TETLEY, CALCUTT, 1988], Tetley, L., Calcutt, D. (1988), *Electronic Aids to Navigation*, 1st edn, Hodder & Stoughton, London, UK
- [THIES, 2007], Thies, T. (2007), *Optimierung von hydrographischen Auswerteprozessen am Beispiel der Hamburg Port Authority*, Diploma Thesis, Hamburg, Germany
- [VENNEGEERTS et al., 2008], Vennegeerts, H., Martin, J., Becker, M. Kutterer, H. (2008), *Validation of a kinematic laserscanning system*, in *Journal of Applied Geodesy*, Vol. 2-2008, Germany
- [VAN RENS et al., 2007], van Rens, A., Brennan, R., Antonio, S., Canter, P., (2007) *Surface Imaging Capabilities on Marine Hydrographic Vessels*, Article US-HYDRO 2007, USA
- [WANG, JIN, 2010], Wang, J., Jin, F. (2010), *Precision Estimation of a mobile Laser Scanning System*, in *Survey Review*, Vol. 42, pp. 270-278, Shandong, China
- [WDR, 2007], Westdeutscher Rundfunk (2007), *Schüsse ins Wasser - Rückblick zum Todestag von Alexander Behm*, <http://www.wdr.de/themen/kultur/stichtag/2007/01/22.jhtml> (accessed 23 Jan. 2007)
- [WIKIPEDIA, 2011], Wikipedia–Die freie Enzyklopädie (2011), *Sagnac Interferometer*, <http://de.wikipedia.org/wiki/Sagnac-Interferometer> (accessed 02 Feb. 2011)

BIBLIOGRAPHY